Biomimetic Design of Nucleic Acid/Protein-Based Nanomaterials

By

Julio Cesar Bernal-Chanchavac

A Dissertation Presented in Partial Fulfillment
of the Requirements for the Degree
Doctor of Philosophy

Approved October 2023 by the
Graduate Supervisory Committee:

Nicholas Stephanopoulos, Chair
Jeremy Mills
Anne Jones

ARIZONA STATE UNIVERSITY

December 2023

ABSTRACT

In recent years, researchers have employed DNA and protein nanotechnology to develop nanomaterials for applications in the fields of regenerative medicine, gene therapeutic, and materials science. In the current state of research, developing a biomimetic approach to fabricate an extracellular matrix (ECM)-like material has faced key challenges. The difficulty arises due to achieving spatiotemporal complexity that rivals the native ECM. Attempts to replicate the ECM using hydrogels have been limited in their ability to recapitulate its structural and functional properties. Moreover, the biological activities of the ECM, such as cell adhesion, proliferation, and differentiation, are mediated by ECM proteins and their interactions with cells, making it difficult to reproduce these activities *in vitro*.

Thus, the work presented in my dissertation represents efforts to develop DNA and protein-based materials that mimic the biological properties of the ECM. The research involves the design, synthesis, and characterization of nanomaterials that exhibit unique physical, chemical, and mechanical properties. Two specific aspects of the biomimetic system have been to include (1) a modular protein building block to change the bioactivity of the system and (2) to temporally control the self-assembly of the protein nanofiber using different coiled coil mechanisms. The protein nanofibers were characterized using atomic force microscopy, transmission electron microscopy, and super-resolution DNA Point Accumulation for Imaging in Nanoscale Topology. The domains chosen are the fibronectin domains, Fn-III$_{10}$, Fn-III$_{9\text{-}10}$, and Fn-III$_{12\text{-}14}$, with bioactivity such as cell adhesion and growth factor binding.

To extend this approach, these cys-nanofibers have been embedded in a hyaluronic acid scaffold to enable bioactivity and fibrous morphologies. Nanofiber integration within the HA gel has been shown to promote tunable mechanical properties and architectures, in addition to promoting a temporal display of the protein nanofibers. The hydrogels were characterized using scanning electron microscopy, mechanical compression testing, and fluorescence microscopy. The findings in this dissertation highlight the promise of biomimetic DNA and protein nanomaterials as a versatile approach for developing next-generation materials with unprecedented properties and functions. These findings continue to push the boundaries of what is possible in nanotechnology, leading to new discoveries that will have a significant impact on society.

DEDICATION

To my family and to the friends that have become family, my success has been deeply rooted in the constant love and support that you all have provided me with.

ACKNOWLEDMENTS

First and foremost, I want to say thanks to the endless support and love that my Mom and Dad have provided me with throughout graduate school. Everything that I have accomplished goes to you because you both have worked so hard to give me the opportunity to thrive in this hectic world. For that, I owe my success to you both and will always strive to make you both happy and proud to call me your son. To my siblings, Rebeca, Raquel, Michael, Valeska, and Kevin, thanks so much for being there and providing endless laughs, good times, and unconditional love through my existence. Special shoutout to Michael, AKA "Tank". You've been one of the closest people in my life and I know that I will be able to rely on you.

I would also like to thank my committee members and scientific mentors during my tenure here at Arizona State University. To Dr. Nicholas Stephanopoulos, I have been able to grow to a mature scientist under your guidance. You have always been there to answer my questions whenever I barged into your office to ask a question. You provided me with endless support, engaging conversation, and multiple moments of laughter. You have invested so much time and effort into my growth and have always been excited about my research. To Drs. Anne Jones and Jeremy Mills, thanks so much for being there when I need to grow professionally. Anne, you have provided me with a different perspective on how to approach my science and without your help to refine "my story," I would not be the same writer and presenter that I am today. To Jeremy, thank you for providing the laid-back vibe to my research. Without your down-to-earth take on research, graduate school would have been the unpleasant atmosphere that people loathe. So, thank you for providing me with that perspective of academia.

I want to say thanks to my best friends, Drew, Ben, Griffin, and Rocky. You give have been the homies since day one. Life would NOT be the same without you guys. I know there has been some distance between us, but I have no doubt that I can count on any one of you guys for support when I need it. Also, to Rhino and Midge, WE DA MAMBAS.

To the friends that I made along the way during graduate school, specifically Jesse, Casey, Mubark, Jordyn, Matthew, Berta, and Al-Amin, thanks so much for providing happiness, laughter, and time well spent when we all needed it. Especially to you, Casey, you have been the BEST partner that I could ask for. Thanks for your relentless support, I love you. I know that I have formed a life-long friendship with each of you and I'm excited about the experiences that we have yet to embark on together.

I would like to say thanks to my labmates. We have spent so much time together during my five years in the Stephanopoulos lab. Specifically, to Al-Amin. I am glad I could always count on you see grab a brew, to alleviate my complaints, and to just kick the dirt around. To Yang, thanks SO MUCH for all the help that you provided me throughout the years. You were like my lab mom, always being there when I needed help. To Minghui, thanks for all your help throughout the years, your expertise in DNA nanotechnology helped me beyond words. To Justin, thanks for your energy, your sense of calm, and your fresh take on life rejuvenated my science and I am glad I got to spend the last two years guiding you to be the scientist that you are today. To Abhay, thanks for being the companion in the lab that I can always ask for help with and to share scientific anguish. Lastly, thanks to Tara and Alex, for your help in bringing me into the lab. I would have been absolutely lost without your guidance and friendship.

TABLE OF CONTENTS

Page

LIST OF FIGURES

Figure page

Figure page

Figure Page

CHAPTER 1

INTRODUCTION TO PROTEIN AND DNA NANOTECHNOLGY AND THEIR APPLICATION FOR THE CONSTRUCTION OF BIO-INSPIRED MATERIALS

Portions adapted with permission from: Bernal-Chanchavac, Al-Amin, M., and Stephanopoulos, N., "Nanoscale Structures and Materials from the Self-Assembly of Polypeptides and DNA." *Current Topics in Medicinal Chemistry*, 2022, 22,8. 699-712.

1.1 Nanotechnology

The field of nanotechnology has revolutionized mankind's ability to measure, manipulate and manufacture matter at the nanoscale. The birth of the field is accredited to American physicist and Nobel Laureate Richard Feynman, where in his talk, in 1959, *There's Plenty of Room at the Bottom*, he postulated the manipulation of manner at the atomic scale.[1] However, it was not until 15 years later that a Japanese scientist, Norio Taniguchi coined the term "Nanotechnology," which emphasized single-atom or single-molecule manipulation.[2] The field saw a major advancement during the development of the scanning tunneling microscope by Gerd Binning, which allowed for the visualization of surfaces at the atomic level.[3] Through the implementation of nanotechnological techniques, scientists have enabled the development of novel tools and applications in the fields of physics, chemistry, and biology, all rooted around the manipulation of matter at the scale of 1-100 nm.

Since the development of the field, scientists have implemented two distinct methods to fabricate nanomaterials, through a "top-down" or a "bottom-up" approach, each

giving rise to their own structural benefits across multiple length scales. The use of the "top-down" approach to develop nanomaterials is achieved by using precise engineering tools to break down a bulk material to realize nanoscale particles. Tools such as nanolithography can be implemented to generate the desired nanomaterial through electron beam etching.[4] However, through this approach, the surface properties of the material cannot be controlled, giving rise to altered material properties.

To alternative approach is through the "bottom-up" construction of nanomaterials through the self-assembly of atoms or molecules. Chemical synthesis is an approach to develop atoms or molecules that create bulk material or that can be used as building blocks for more precise nanomaterials. In addition to chemical synthesis, self-assembly can be used to allow for molecules or atoms to self-organized into precise nanomaterials through complementary chemical and physical interactions.[5] Self-assembled nanomaterials have the benefit of precise composition and facile production. However, the ability to engineer molecules and atoms to spontaneously arrange themselves into well-defined materials continues to be challenging.

The interactions that dictate molecular self-assembly are weak, noncovalent interactions such as hydrophobic interactions, hydrogen-bonding, van der Waals interactions, and electrostatic interactions. Although each of these interactions are individually weak, their collective interactions dictate the structural conformation of all biological macromolecules and control their interactions with other molecules. However, the ability to replicate the architectural complexity that is seen in nature has proven to be difficult. This challenge is due to the difficulty in predicting the entropic and enthalpic

contributions of each of these non-covalent interactions. To overcome this challenge, the principles of self-assembly need to be understood.

Biomimicry has been an emergent field that has facilitated the understanding and development of self-assembled nanomaterials made through biomolecules. This rapid development is ascribed to the plethora of examples that Nature has provided, composed of a variety of biomolecules such lipids, polypeptides, and oligonucleotides. In addition to the large variety of self-assembled structures seen in Nature, these self-organized structures are often associated well-defined functionality.[6] By drawing inspiration from these functional nanomaterials, the construction of biomimetic nanomaterials can be achieved with entirely new functions.[6, 7]

Nanomaterials fabricated through biomolecules offer various benefits such as a favorable sub-cellular scale, they are inherently biocompatible due to their respective building blocks, and are easily tractable due to the advancements of chemical biology. Due to these benefits, these nanomaterials have been useful for therapeutic applications.[8] Of the biomolecules that can be used to construct nanomaterials, peptides and proteins are powerful building blocks imparting a wide variety of function. Nature has utilized peptides and proteins to construct materials such as collagen, spider silk, and keratin. The self-assembly of peptides and proteins is mediated through a complex set of interactions, driven mainly through hydrophobic and electrostatic interactions. Therefore, it is much more difficult to predict how a polypeptide sequence folds. However, over the recent decade, much progress has been made, experimentally and computationally, on how peptides and

proteins self-assemble. As a result, the study and implementation of protein self-assembly creates the subfield of protein nanotechnology.

1.2 Protein Nanotechnology

Proteins make up the most versatile structural polymers that are known. The importance of proteins is derived from their critical functions in biology. Due to their versatile function and diverse set of structural conformations, the design and fabrication of self-assembled protein and peptide materials has allowed for materials to be generated that match or even surpass the functions of the living world. The vast range of assembling properties stem from their building blocks, namely the twenty amino acids. The chemical diversity of proteins is endowed from the side chains on each amino acid, ranging from hydrophobic, charged, nucleophilic and aromatic side chains. The chemical niches of each side chain also promote the propensity of polypeptides to fold, giving rise to various secondary, tertiary, and quaternary structural motifs. Although the protein folding problem[9, 10] has made significant headway due to the development of AlphaFold[11] and RoseTTaFold,[12] it still remains difficult to design protein-based materials with well-defined parameters from the bottom-up. However, Nature has provided plenty of examples of sequence-specific structural motifs that scientists have been taking advantage of to push the limits of protein nanotechnology.

The most commonly exploited proteins structural motifs are alpha helical coiled coils, beta sheets, and collagen triple helices.[13] Through these motifs, researchers have been able to generate one-dimensional (1D) nanofibers, two-dimensional (2D) nanosheets, and three-dimensional (3D) hydrogel scaffolds.[13, 14] From a protein material perspective,

the coiled coil is one of the simplest motifs that has been extensively studied due to its ubiquitous nature.[15] For a structural context, the coiled coil structure is comprised of two- or more α-helices (Figure 1.1 A).[16] The programmability of these motifs are dictated through a repeating heptad domain of hydrophobic (**h**) and polar (**p**) residues in a **hpphppp**. The heptad repeat is typically represented as $gabcdef_n$, where *n* is the number of repeated heptads and *a*-*g* represent the amino acid positions on a heptad wheel diagram (Figure 1.1 B). The main driving force for coiled coil self-assembly is hydrophobic packing, where the *a* and *d* positions typically consist of hydrophobic amino acids. The tight knob-in-hole type packing of the *a* and *d* residues allows for effective exclusion of water.[16] The stabilization of the coiled coil is further mediated through favorable electrostatic interactions in the *e* and *g* positions (Figure 1.B). The coiled coil helical arrangement is stabilized through complementary charge interactions whereas like-charges resulting in destabilization. Through the careful study of the heptad repeat pattern, coiled coils have been routinely used for *de novo* design through careful design principles (Figure 1.1 C).[17-22]

In addition to well-understood design principles, the physical parameters of the structural motif are understood to the extent of being used as a precise nanoscale building block. In terms of the structure of the coiled coil, the α-helices are arranged in a supercoiled manner to compensate for staggered arrangement of helices for efficient hydrophobic packing. For context, the helical pitch of a straight α-helix, there is a helical rise of 0.54 nm/helical turn. As a result, for a dimeric coiled coil, the helices results in a more gradual translation pitch of 1.034 nm from every seventh side chain, exhibiting a helical pitch angle of 20° with a helical rise of 3.64 residues/turn.[16, 23] These dimensions stem from the

structural parameters of a simple α-helix, where each pitch consist of seven residues, which exhibit a rotation of 100°/turn, allowing for a helical pitch rotation of 700°. In addition to the helical rotation, the α-helix displays a helical rise of 0.15 nm/residue and 3.6 nm/turn, yielding a helical pitch of 0.54 nm/turn.[24-26] These nanometer-level parameters effectively allows for the coiled coil motif to be used to effectively construct nanomaterials with nanometer resolution.

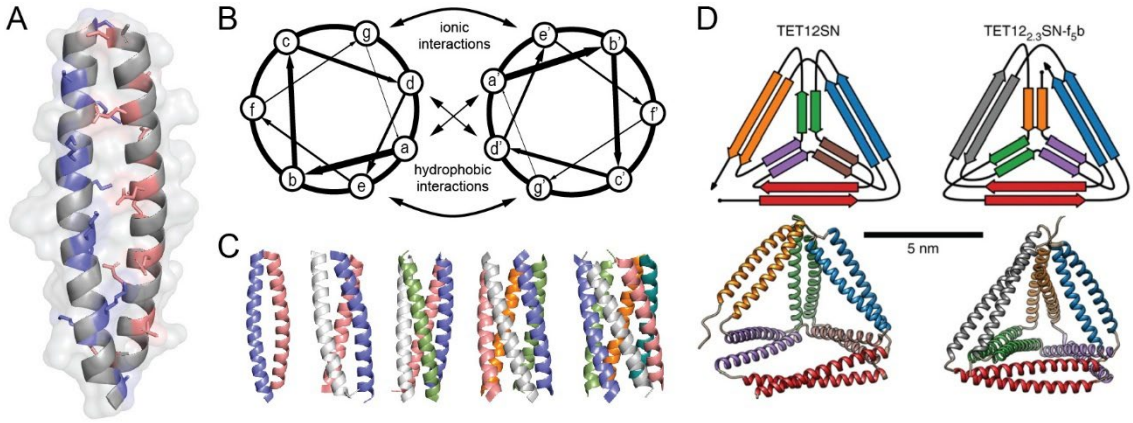

Figure 1.1. Coiled coil motif and representative nanostructures. A) A homodimeric, parallel coiled coil structure. **B)** Heptad wheel diagram representing key amino acid positions in a dimeric coiled coil. **C)** Different oligomeric coiled coil structures. **D)** Designed polypeptide to self-assemble into a coiled coil tetrahedron. Reprinted with permission from H. Gradišar et al.[40]

The ability to generate coiled coil-based nanomaterials has been facilitated by the synthetic tractability of these nanoscale building blocks. The use of solid-phase peptide synthesis has allowed researchers the ability to generate highly functionalized coiled coil peptides. For example, multiple oligomeric forms of the coiled coil have been functionalized with metal-chelating groups to allow for metal bio sites to be engineered into the protein motifs.[27] Due to the precise localization of amino acid resides in the protein structure, the metal coordination site can be rationale engineered. Other researchers have

introduced a photochemical handling on the assembly of coiled coil through the modification of an azobenzene moiety.[28] Through the crosslinking of the *i* and *i*+7 positions with the azobenzene moiety, the assembly can be controlled through a photoswitchable transition between the *cis*- and *trans* state of the azobenzene. Lastly, through selective point mutations of the peripheral residues on the coiled coil motif, water-soluble helical barrels can be engineered with precise pore sizes.[29] These barrels have been exploited to generate synthetic ion channels[30] and to act as receptors to selectively bind to small molecules of interest.[31] As showcased, the field of coiled coil engineering continues to push the boundary of natural systems by increasing their functionality.

In addition to extensive functionality, the fundamental self-assembly of the coiled coil has been routinely exploited to generate a wide variety of nanofiber systems. Approaches include the use of "sticky-ends", analogous to sticky-end DNA hybridization but through engineered amino acids residues on the *b*, *c*, and *f* positions of a dimeric coiled coil pair.[32] This approach led to the formation of individual fibrils which matured to wider bundled fibers, with a width of 20 nm or more and spanning several hundred nanometers. A similar approach was used, where the surface charge of a pentameric coiled coil bundle was exploited to promote nanofiber formation and subsequent gelation.[33] This approach was extended to promote the retention of a small molecule within the coiled coil domain, which highlights the potential use of these materials for therapeutic applications. Lastly, further chemical approaches, like a common bioconjugation thiol-ene click reaction, have been implemented to generate ultra-rigid coiled coil nanofiber.[34, 35] This approach was extended through electrospinning, which allowed superior tensile mechanical properties, rivaling other protein fiber materials. These examples have highlighted a few approaches

of exploiting the self-assembly of coiled coils to generate materials with optimal material properties.

Recently, researchers have extended the capabilities of the coiled coil mode of self-assembly to introduce a reversible mechanism into the motif. This reversible mechanism, namely coil displacement, was pioneered by the Seitz lab, where they implemented a heptad "toe-hold," allowing for effective coil displacement.[36] The process was demonstrated with a three-heptad system, forming a stable coiled coil complex. The additional heptad toehold and subsequent binding of the displacement process allowed for a more energetically favorable four-heptad coiled coil complex. The use of coiled coil displacement was implemented by the Freeman lab, where a four-heptad coil was chemically anchored onto a glass surface, which subsequently bound to its three-heptad complement exhibiting a cellular adhesion Arginine-Glycine-Aspartate (RGD) peptide and an unbound heptad.[37] This approach facilitated the cellular adhesion of Human foreskin fibroblasts on the coil-coated surface. However, through the addition of the displacement peptide, the bioactive coil peptide was removed from the surface, preventing the fibroblasts from adhering onto the glass surface. One of the last highlights for reversible assembly of the coiled coil motif was through an engineered coiled coil hairpin.[38] The coiled coil segment was varied from two heptads, two and a half heptads, and three heptads, demonstrating that binding affinity of these coils. To implement reversible self-assembly, the complementary coils were linked with a 17-mer ligand that binds to a CREB-binding protein (CBP). Without the CBP present, the coil peptide would spontaneously form an intramolecular coiled coil. However, once the CBP was added into the solution, the CBP would bind to the 17-mer ligand and force open the coiled coil complex. These examples

have demonstrated the continuous engineering efforts to introduce further functionality to the coiled coil motif.

Thus far, the ability to design advanced function and utility to the coiled coil motif has been a successful method to construct a wide variety of nanomaterials. However, coiled coil-based nanomaterials often exhibit similar pitfalls as other peptide systems, which is the inability to construct monodispersed, anisotropic nanostructures. Significant efforts from the Jerala lab have enabled the first example of these kind of structures, through the folding of polypeptides into more complex, wireframe structures (Figure 1.1 D).[39, 40] The designed, self-assembled protein cages, termed coiled coil protein origami (CCPO), were engineered through orthogonal coiled coil peptides. These peptides were fused together into a single polypeptide chain, where the self-assembly between the coiled coil dimers would enable the intramolecular folding of the desired nanocage. The engineering of these structures was through a topological Eulerian trail, where the polypeptide folding path along the edge of the polyhedron enables to connection of two vertices by exactly two connections. This folding path was enabled through the ability of coiled coil to self-assemble in an anti-parallel manner or through a parallel manner.[41-46] This approach was extended by the *in vitro* and *in vivo* fabrication of these polypeptide tetrahedra, enabling these constructs with biomedical potential due to their lack of cytotoxicity.[40] However, these CCPO constructs still remain limited to their symmetry. On the other hand, another biomolecule, namely deoxyribonucleic acid (DNA), has shown tremendous potential as a nanoscale building block.

1.3 DNA Nanotechnology

DNA was first envisioned as a nanoscale building block by Nadrian Seeman in 1980's.[47] Seeman's initial inspiration was provided by M.C. Escher's *Depth*, where he envisioned a 3D DNA scaffold that could designed to host proteins-of-interest for structural determination *via* X-ray crystallography. Through this vision, a continuous effort of 40 years has enabled the field of DNA nanotechnology to flourish. The understood rules of self-assembly of DNA have been exploited by researchers to develop nanostructures with unmatched structural complexity and versatile function.

DNA is another well-suited biomolecule for the bottom-up construction of nanomaterials because its physical properties have been exhaustively characterized. For instance, the predictability DNA self-assembly is derived from its canonical base pairing, where adenine (A) pairs with thymine (T) and guanine pairs with cytosine (C), to form a right-handed double stranded helix. The self-assembly of DNA through complementary, hydrogen-bonded, base pairs was first reported by Watson and Crick, who used X-ray diffraction data provided by Rosalind Franklin to characterize the helical structure of DNA.[48] Further physical studies demonstrated that the single stranded biopolymer consisted of deoxyribose sugars connected through a negatively-charged phosphate backbone, connecting each nucleobase.

The physical form of the DNA double helix is comprised of two strand, where each strand has a canonical directionality, where the two helices self-assemble in an anti-parallel manner, with the 5'-end hybridizing to the 3'-end of the complementary strand, forming the right-handed helix.[49] The 5'-end refers to the 5'-hydroxyl position on the deoxyribose

sugar directly connected to the phosphate group, whereas the 3'- end refers to the 3'-hydroxy group on the terminal deoxyribose sugar. The stability and the *programmability* of the DNA duplex is derived from the hydrogen bonding pattern of each nucleobase. For the C/G base pair (bp), three hydrogen bonds stabilize the interaction, whereas A/T base pairs exhibit two hydrogen bonds. Thus, the stabilization energy of the C/G base pair is ~50 % higher than that of the A/T base pair (Figure 1.2 B).[50] The most common conformation of the DNA duplex is B-form DNA, which exhibits well-defined atomic parameters that make DNA well-suited for precise structural engineering at the molecular level.[51] For B-form DNA, one helical rise is equivalent to 3.4 nm, where there are 10.5 bp per helical turn (Figure 1.2 A).[47] As such, each base pair implements a 34.3° turn and

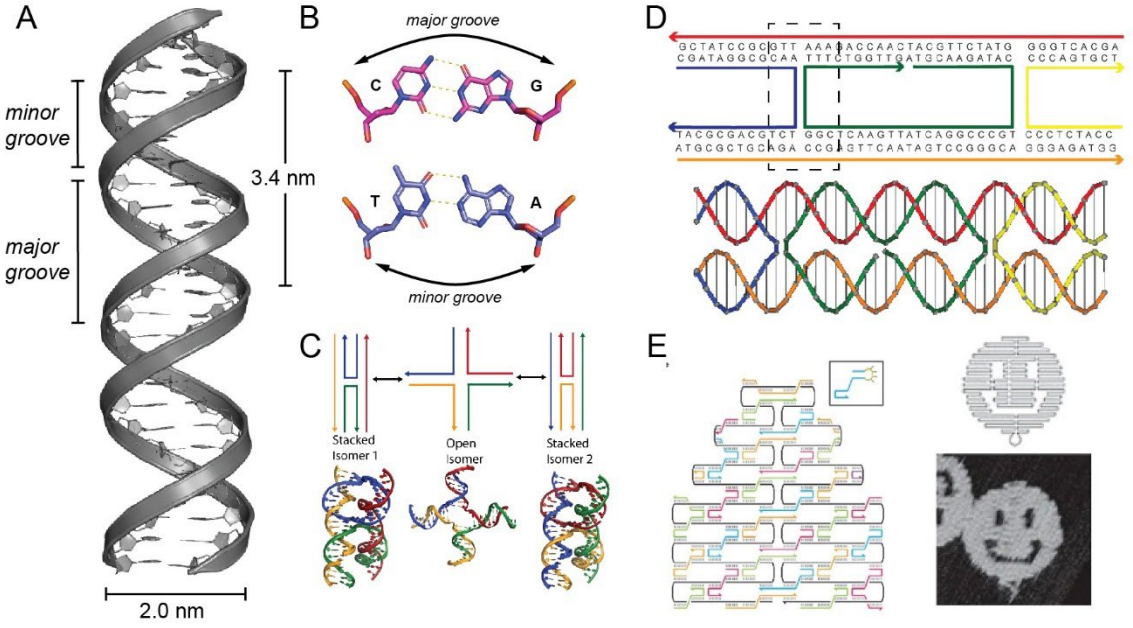

Figure 1.2 Overview of DNA nanotechnology. A) Schematic of DNA double helix. **B)** Watson Crick base pairing of the four nucleotides featuring their orientation in the helix. **C)** 2D and 3D representation of the fundamental building block the Holliday junction. **D)** 2D and 3D representation of a DX tile. Dotted black line showing incorporated Holliday junction. **E)** Schematic of the assemble of DNA origami from M13 scaffold and staple strands yielding a 2D smiley face.[68]

induces a helical width of 2.0 nm. These nanometer-level parameters enable the fabrication of complex nanostructure through geometric principles.

To reinforce the structural stability of the DNA duplex, other biological DNA structures were pursued to construct higher ordered structures with additional rigidity. More specifically, inspiration to form rigid crossover regions, where one strand connects two distinct duplexes, was derived from the Holliday junction (HJ).[52] The Holliday junction is a native four-arm junction that occurs during genetic recombination.[53] The junction is comprised of four different strands, where two bases from each strand interact at the crossing point (Figure 1.2 C).[53-55] Through this cross-over motif, the Holliday junction provides a means to impart mores structural stability and more complex dimensionality into designed DNA nanostructures.

One major achievement for DNA nanotechnology was the design of the *immobile* Holliday junction in 1983 by Seeman.[56] The introduction of asymmetric sequences that flank the eight junction bases facilitated the formation of an immobile Holliday junction. The sequence asymmetry effectively circumvented the sliding effect that was present in the Holliday junction for genetic recombination. Based on the eight junction bases and four canonical nucleotides, 36 possible immobile junction sequences exist to construct junction points for DNA nanotechnology.[57] Following the design of the immobile HJ, Seeman rationalized that sticky-end cohesion can be implemented into immobile HJ for construction of arrays and lattices.[58] Seeman and co-workers also envisioned methods to increase the structural complexity of these junction points through the design of multi-armed junctions ranging from three- to eight-arm branch points.[59-61] In this manner,

researchers have been able to assemble complex wireframe nanostructures in two- and three-dimensions.[62-64]

To circumvent the lack of rigidity of the stand-alone HJ motif, a tile structure was engineered, namely the double cross-over (DX) tile, consisting of two helices connected by two HJs to minimize the structural flexibility (Figure 1.2 D).[65] Through this approach, the first example of a 2D crystalline lattice composed of DX tiles was demonstrated.[66] This work signified a major advancement in the field of higher-ordered crystalline assemblies composed of DNA. However, the periodic arrangement of the arrays did not provide an avenue to generate highly addressable and functional anisotropic structures.[67]

The lack of anisotropic structures was addressed by Rothemund in 2006 through the development of DNA origami.[68] DNA origami allows for the construction of larger DNA nanostructures (>100 nm) due to the building block being implemented. This methodology required the use of a large, 7249-nucleotide DNA viral scaffold extracted from the M13 bacteriophage. Similar to the paper origami technique that inspired its name, this large viral DNA segment is folded into a desired 2D shape by short, complementary DNA "staple" strands (Figure 1.2 E). Due to the unique/non-repeating DNA sequence of the M13 scaffold strand, the staple strands are highly addressable. The lack of repetitive sequences expands the designer space to facilitate a multitude of 2D DNA origami structures to be designed. The designer space was expanded in three dimensions by the Shih lab, where the helices were arranged in a honeycomb pattern to facilitate optimal spatial arrangement of both the scaffold and the staple strands.[69] The realm of 2D and 3D

DNA origami rapidly expanded by the development of design software to aid in origami prototyping.[70]

As the field progressed, more elaborate ways were devised to create DNA nanostructures. Such an approach was demonstrated by the Shih lab, where they developed curved DNA origami.[71] This approach was demonstrated by strategically placing base deletions or additions to take advantage of the helical rotation of the DNA duplex. An alternative approach to construct large 3D DNA nanostructures was designed by the Shih and Yin labs, where a multitude of short oligonucleotides comprising of 32 bases were implemented as "bricks".[72] These bricks can be used to assemble large DNA nanostructures, without the need to reroute the M13 scaffold and generate a whole new set of staple strands. In this approach, the DNA bricks exhibit a unique sequence comprised of four, eight-base sticky end that can be used to anneal to a neighboring brick with a 90° rotation. As a result, the modular way that these DNA bricks were designed, a plethora of 3D DNA nanostructures can be created while keeping the same set of DNA "voxels." Lastly, the Yin and Yan lab demonstrated that 2D origami can be assembled using a long, single-stranded DNA strand that can intramolecularly fold through the implementation of parallel crossovers.[73] The use of parallel crossovers was critical to the self-assembly process in order to avoid kinetic entanglement of the scaffold. This approach was also demonstrated with RNA, highlighting the versatility of the routing design. These methodologies have exemplified the potential of DNA to be used as a powerful building block to construct a wide range of precise nanostructures. However, these methods provide a means for construction but fail to introduce dynamic modes of self-assembly.

The ability to dynamically control the self-assembly of DNA nanostructures has been shown through a wide variety of stimuli, such as oligonucleotide triggers, proteins, light, and metal-ions, to name a few. One of the most common methods to control dynamics is through DNA strand displacement.[74] The first example of such a dynamic reaction was shown by Yurke *et al.* where they demonstrated that DNA could undergo multiple cycles of hybridization and toehold reactions.[75] Through this powerful method, a set of DNA tweezers were shown to undergo multiple cycles of "open" and "closed" stated through two orthogonal DNA fuel strands. The mechanism has undergone extensive study, to enable well-define stability and kinetics of DNA, RNA and DNA: RNA strand displacement.[76, 77] The DNA tweezer has seen other methods of actuation such as photo-inducible actuation through the use of DNA-caged 6-nitropiperonyloxymethyl (NPOM) groups, preventing DNA hybridization.[78] Once irradiated with 365 nm light, the cages would be removed, allowing for the opening of the DNA tweezer. Lastly, the use of dynamic protein interactions with DNA nanostructures has been extensively used. Such examples have highlighted the use of enzymatic degradation and transcriptional cycles to regulate the formation of DNA nanotubes,[79] to control the opening of DNA drug delivery vehicle,[80] and to use a DNA force spectrometer to measure nucleosome-nucleosome interactions.[81]

The design space of DNA nanotechnology has been extensively explored and continues to emphasize the ability of DNA to generate nanomaterials with complex structure and immense function. To this end, DNA nanotechnology enabled the creation of DNA nanomaterials with a wide range of geometric parameters, diverse shapes, and sizes, and can be applied to a plethora of research fields.[82] DNA nanotechnology has been

implemented in research fields such as biosensing, biophysics, nanoelectronics, synthetic biology, regenerative medicine, and drug delivery.[83-87] Briefly, several successful applications of DNA nanotechnology have been demonstrated through increasing functionality of DNA nanostructures for targeted cell delivery,[80, 87, 88] biomolecular scaffolding,[89-91] and dynamic materials.[92-96]

Although the ability of DNA to create complex nanomaterials is unmatched, DNA in this context still lacks inherent functions other than a structural building block. As such, the ability for DNA nanotechnology to be effectively implemented in a biological context is limited by several factors. For instance, the anionic nature of the phosphate backbone implements a high energetic cost for assembly due to charge-charge repulsion between two adjacent backbone helices.[67] To mitigate these repulsive effects, DNA nanostructures are routinely constructed in high cationic salt buffers ($\geq$ 12.5 mM Mg^{2+}). However, such high divalent salt concentrations deviate from the magnesium concentration found in biological environments. In addition, the anionic nature of these constructs poses issues during cellular uptake.[97] Furthermore, DNA nanostructures are susceptible to nuclease degradation. Ultimately, to aid in the successful integration of DNA nanostructures in *in vivo* applications, these shortcomings need to be addressed. However, these limitations can be overcome through the development of hybrid biomolecules.

1.4 Peptide Oligonucleotide Conjugates

The synthesis of peptide oligonucleotide conjugates has combined the chemical functionality of amino acids and the structural benefits of nucleic acids to usher in the ability to generate novel hybrid materials with unprecedented structure and function.

Researchers have implemented two distinct methods to generate hybrid peptide oligonucleotide materials, using either favorable electrostatic interactions or generating covalent peptide oligonucleotide conjugates. The synthesis of covalent conjugates is the approach that is most often used due to the unpredictability of non-covalent self-assembly. Although the field is still in its infancy, this approach has been successfully applied in various avenues of research such as protein mimics,[98, 99] gene therapeutics,[100-106] templated protein and peptide synthesis,[107, 108] used for imaging tools,[109, 110] biomaterials,[111-114] the formation of nanowires,[115] and as hybrid scaffolds,[116-119] to name a few examples.

The most common avenue uses a two-step synthetic approach, where each DNA and peptide component is individually synthesized, modified, and subsequently conjugated together to produce the peptide oligonucleotide conjugate. The covalent linkage between these two biomolecules often requires the use of a heterobifunctional linker, or the functionalization of the DNA or peptide with a bio-orthogonal functional group. Selecting the type of bifunctional linker often depends on the functional groups that are present in the biomolecule-of-interest or how site-specific the bioconjugation needs to be. For examples, bis-NHS (N-hydroxysuccinimide) esters are often employed for the covalent crosslinking for free amine group.[120] However, such an approach lacks site-specificity due to the promiscuous nature of free amines on the surface of various peptides and proteins. Other methods, such as the use of a Succinimidyl-4-(*N*-maleimidomethyl)cyclohexane-1-carboxylate (SMCC) linker enables the conjugation of an amine group (through the NHS reactive group) and a thiol group (through the thiol-ene click reaction).[107, 121-123] However, in order to implement this approach, a single cysteine needs to be present on the peptide to ensure site specificity. In addition, azide-alkyne click reactions are often used due to their

optimal thermodynamic and kinetic properties.[124] To aid in ease of conjugation, researchers have even applied standard coupling techniques such as DCC[100, 125] or NHS-EDC[104, 126] coupling to obtain their desire conjugate. However, care must be taken when choosing a specific conjugation route to ensure ease of functionality, site-specificity, and functional group stability.

A versatile method for the synthesis of peptide oligonucleotide conjugates is through bio-orthogonal click chemistry, which exhibit optimal kinetics and regiospecificity.[127] Two most commons click reactions are the copper-assisted azide-alkyne cycloaddition ("copper click") or the strain-promoted azide-alkyne cycloaddition (SPAAC) ("copper-free click"). Copper click has been successful in generating POCs, however, some difficulty arises due to the large steric effect between the DNA and the peptide components.[128] More often, researchers employ the copper-free click method due to the ease of coupling and their facile introduction of each reaction group in the biomolecules through avenues such as noncanonical amino acid incorporation and through cyclooctyne addition on the oligonucleotide.[98, 112, 129, 130] Other bio-orthogonal reactions have been explored and have generated successful conjugates, such as oxime-thiazolidine formation,[131] enzymatic ligation,[126, 132] and thiol-ene reactions.[133-136]

Due to the well-studied self-assembly rules, the coiled coil has been routinely used for the assembly of higher-order hybrid nanostructures. One of the first examples of *structurally* integrating coiled coils with DNA was the construction of a filamentous virus-like particle reported by Stupp and coworkers in 2013.[137] The researchers designed a mushroom- like coiled-coil peptide nanostructure that bound to, and encapsulated, double

stranded (ds) DNA using electrostatic interactions. The peptide nanostructure was rationally designed in a three-component manner, where the bulk structural component consisted of an α-helical peptide that oligomerized into a heptameric coiled coil. Secondly, DNA binding was facilitated by the addition of a positively charged spermine unit on the *N*-terminus. Lastly, a polyethylene glycol (PEG) brush was added at the *C*-terminus of the peptide to aid in solubility of the peptide as well as to control the higher-order assembly through steric exclusion interactions. The programmable nature of DNA allowed the researchers to control the length of the "artificial virus," whereas the incorporation of the PEG brushes modulated the persistence length of the overall assembly.

A few years later, the Jensen lab reported the first example of a peptide-DNA conjugate that implemented the coiled coil to create a protein mimic.[98] The design involved covalently conjugating three distinct oligonucleotides to a peptide that self-assembled into a homotrimeric coiled coil (Figure 1.3 A). The oligonucleotides were designed to form a triplex structure, which was shown to synergistically enhance the assembly of the coiled coil by placing the peptides in close proximity. The effect of this peptide-DNA assembly was an unprecedented thermal stability of the coiled-coil, with enhanced alpha helicity as shown by circular dichroism, as well as enhanced resistance to elevated pH. The results emphasized that the DNA triplex motif was an effective molecular scaffold to propagate the self-assembly of the coiled coil motif.

Recently, two groups pioneered the integration of the coiled-coil motif into DNA nanotechnology using covalent peptide-DNA conjugates. Both approaches used coils to drive the assembly of DNA origami structures, albeit with different end goals. The first

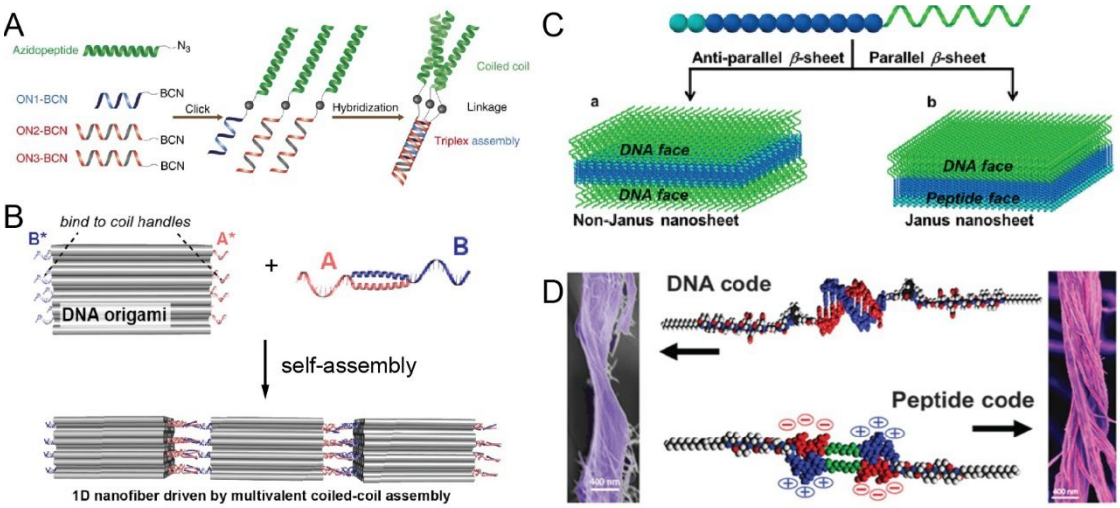

Figure 1.3 Hybrid peptide-oligonucleotide nanomaterials. A) The first example of a covalent coiled-coil peptide-DNA conjugate. Reprinted from Lou et. al.[98] Copyright 2016, Springer Nature. **B)** DNA origami cuboid structures were used to create one-dimensional nanofibers through coiled coil interactions. Reprinted with permission from Buchberger et. al.129 Copyright 2020, American Chemical Society. **C)** Fabricated Janus nanosheets through β-sheet peptide-DNA conjugates. Reprinted with permission from Albert et. al.[141] Copyright 2021, Wiley-VCH Verlag GmbH & Co. KGaA. **D)** The assembly of DNA-peptide amphiphile conjugates gives rise to supramolecular fibers. The hierarchical association of these fibers can be mediated through DNA hybridization or electrostatic peptide interactions. Adapted from Freeman et. al.[143] Reprinted with permission from 2018 AAAS.

example by the Turberfield and Woolfson labs utilized DNA origami to quantify the dissociation constants of a *de novo* designed coiled-coil pair.[138] The distinguishable (by TEM) dimerization of origami structures allowed the researchers to estimate the dissociation constants of the coiled-coil, which are typically too low to deduce from traditional techniques. A key benefit of the DNA origami structures was that they allowed the coil peptides to be displayed in a multivalent manner and probe the effect of avidity on the binding constant. This precise stoichiometric control emphasized the benefits of DNA nanotechnology to display peptide motifs in a spatial manner with molecular precision.

The multivalency of coiled-coil peptides on DNA origami was also employed by the Stephanopoulos lab, which utilized this motif to polymerize DNA origami cuboids

(Figure 1.3 B).[129] The one-dimensional nanoarray was propagated through a coiled-coil interface, where the multivalent display of the coil peptides was shown to increase the extent of filamentous growth. One of the elegant features of the design was that it allowed for hierarchical assembly, depending on which peptides were anchored onto the faces of the DNA cuboids. Lastly, the use of a robust cuboid nanostructure allowed for one-dimensional nanofibers to exhibit a high persistence length. Both approaches mentioned above took advantage of the highly programmable nature of DNA origami to affect the overall assembly of the coiled-coil motif in a way not possible with other molecular scaffolds.

Turning to a different helical peptide motif, the Conticello and Ke labs demonstrated the use of the collagen triple helix as a modular building block to construct stacked nanoarrays of DNA origami sheets.[139] The collagen mimetic peptide (CMP) scaffold was rationally designed in a triblock fashion, where the central core consists of the proline-hydroxyproline- glycine (POG) repeat canonical to collagen, flanked with positively charged proline-arginine-glycine (PRG) repeats. The assembly of the positively charged CMP allowed the triple helix to bind to DNA origami structures through electrostatic interactions. The synthetic peptides, by contrast, allowed for the inter-origami spacing in the array to be modulated by extending the central POG core. Additionally, the authors were able to demonstrate hierarchical assembly by changing the dimensions of the DNA origami scaffolds. The example demonstrates the first example of CMPs being integrated into DNA nanotechnology through noncovalent interfaces, but to date there are no examples of *covalent* CMP-DNA conjugates and the type of materials that can be developed from such hybrid molecules.

Alongside the coiled-coil motif, β-sheet peptides are another well-studied structural motif that has been implemented into DNA nanotechnology. Unlike coiled coils, however, β-sheet peptides do not have design rules that lead to monodisperse structures. By contrast, β-sheet peptides allow molecular designers to control the orientation of molecular stacking, either in a parallel or anti-parallel fashion, as well as guide the overall morphology of the assembled structures, such as nanofibers or nanosheets.[140] The Park lab elaborated on their previous approach to develop Janus nanosheets utilizing phenylalanine-rich peptides conjugated to DNA.[141] Their initial result of a Janus nanosheet was derived from the peptide design, which favored a parallel β-sheet orientation (Figure 1.3 C). The orientation of the parallel β-sheets was further corroborated using computational modeling and molecular dynamics, which highlighted that this arrangement was the most energetically favorable conformation. The researchers extended their design by synthesizing DNA-peptide-DNA conjugates, which allowed them to create dual-addressable Janus nanosheets. The DNA handles allowed the researchers to independently modify either side of the Janus nanosheet with complementary oligonucleotides, which they demonstrated using gold nanoparticle-labelled DNA strands. Their ability to control the manipulation of each face of the Janus nanosheets was further demonstrated by enzymatic assays. Due to the molecular-level control of orientation of biomolecules, such as enzymes, the authors were able to demonstrate enhanced catalytic capabilities on their Janus nanosheet using glucose oxidase and horseradish peroxidase.

The benefit of designer DNA-peptide conjugates is that researchers can incorporate non-canonical chemical motifs into these hybrid biomolecules. One major class of such conjugates is peptide-DNA amphiphiles, which consist of a polar headgroup with a non-

polar motif. These types of molecules typically self-assemble into high-aspect ratio nanofibers, where the non-polar group collapses to form the fibrous core and the polar headgroups are displayed on the exterior of the nanofiber.[142] It was not until 2018 that the Stupp lab demonstrated the first example of DNA-peptide amphiphilic conjugates to construct supramolecular networks.[143] The conjugate was composed of a long, hydrophobic carbon tail, whereas the peptide and DNA components acted as the hydrophilic components (Figure 1.3 D). The unique hybrid biomolecule resulted in supramolecular bundles of fibers with tunable properties. The group demonstrated that the morphology of the fibers can be tuned based on the nature of the interaction, including both DNA hybridization but also entirely unrelated motifs, like electrostatic interactions between charged peptides. Not only could the morphologies of the structures be manipulated, but the fibers could also be crosslinked through DNA hybridization. The authors highlighted the benefit of these synthetic biomolecules by incorporating peptide nucleic acid (PNA) handles into these materials. The interaction of a PNA-terminated fiber with a DNA-terminated fiber resulted in twisted fibers. By modulating the number of base pairs in the hybridized fibers, the pitch of the twisted fibers could be tuned accordingly. Furthermore, DNA strand displacement could be used to reverse the hybridization (and thus the bundling), or to restore it after displacement. The molecular control of fiber formation was ultimately shown to result in morphological changes in cortical astrocytes in a reversible fashion, demonstrating their responsiveness to the underlying matrix nanostructure and paving the way for dynamic DNA nanostructures to be used in tissue engineering and regenerative medicine.

1.5 Dissertation Overview

This dissertation will describe the work that has been carried out throughout my doctoral studies relating to the field of DNA and protein nanotechnology. This chapter has offered an overview of the current state of the field, from the design and application of each of these forms of nanotechnology. The introductory chapter provides a necessary foundation to understand the importance and scope of the work that will be discussed in the following chapters. These chapters will elaborate on a few subcomponents of the field of biomimetic ECM materials, ranging from fibrous materials, dynamic materials, and the biomechanical properties of these materials.

Specifically, Chapter 2 will discuss the design and construction of reversible protein nanofibers that are mediated through the coiled coil. Two distinct approaches have been shown to develop nanofibers on the micron scale, such a disulfide-mediate approach and a protein complementary system. In addition, this nanofiber platform implements two distinct modes of reversibility, allowing for a handle to the self-assemble of the fibrous platform. In addition, the design incorporated a module approach, allowing for a few different proteins with distinct functionality to be incorporated in the biomimetic nanofiber platform. Both of these nanofiber approaches have been characterized through atomic force microscopy (AFM), transmission electron microscopy (TEM), and "DNA Points-Accumulation for Imaging Nanoscale Topography" (PAINT). The chapter also highlights the challenges when trying to design and implement a protein nanofiber platform.

Chapter 3 discussed the integration of the self-assembled protein nanofibers into a biomaterial scaffold. With the Cys-rich protein nanofibers, the nanofibers were

incorporated into a hyaluronan-based scaffold through photocrosslinking. This mechanism has shown the ability to allow for a wide range of mechanical stiffnesses to be achieved *while* allowing for the reversible removal of the protein nanofibers to be retained. Different types of biomaterial architectures have been highlighted and these hydrogels have been characterized through fluorescence microscopy, scanning electron microscopy (SEM), compression testing, and rheology.

Chapter 4 shifts gears to highlight the self-assembly of thermal stable protein thin films. The approach implements a hyperstable protein filament, γPFD, which has been modified through genetic fusion to display coil peptides. Designed coiled coil-DNA crosslinkers were introduced to generate DNA-protein thin films, where the assembly of these 2D arrays was shown to be reversible through either DNA strand displacement or nuclease degradation. These films have been characterized through AFM and TEM to highlight the tight arrangement of these protein filaments into large, micron-sized arrays.

Chapter 5 implements a cysteine-containing-mutant of the γPFD filaments to incorporate filamentous character into hyaluronan- and PEG-based hydrogel systems. This approach was successful at incorporating fibrous morphologies into each non-fibrous scaffold while being able to modulate the mechanical properties of the resulting gels. This approach highlights a facile method to incorporate a fibrous morphology into biomaterial scaffold, which can be difficult to do. The incorporation of the γPFD filaments have been characterized by compression testing, SEM and fluorescence microscopy.

To conclude, Chapter 6 will summarize all the work that has been completed in previous chapters and offer a perspective of the future work and implications of each

individual study. Although many of these projects discussed in this dissertation outline novel ways to integrate the utilize of protein-DNA hybrid nanomaterials to realize unprecedented function, these approaches require further studies to enable their complete potential.

CHAPTER 2

SELF-ASSEMBLY OF FIBRONECTIN DOMAINS MEDIATED THROUGH THE COILED COIL

2.1 Introduction

Efforts to create well-defined biomimetic nanofibers that mimic the fibrous morphology in the ECM have been successful.[144, 145] However, there are specific elements to reported designs that do not completely recapitulate the nature of the ECM, such as reversibility and the ability to modulate the bioactivity of these nanofibers in a spatiotemporal manner. Currently, there have been studies to create biomimetic nanofibers that are well-supported with biological studies *in vitro* and *in vivo*. For example, the Stupp lab has pioneered the field of peptide amphiphiles, whose self-assembly is mediated through hydrophobic packing of a lipid tail, while the periphery of the nanofiber is decorated with hydrophilic peptides. [144, 146] These peptide amphiphiles have been designed to display bioactive peptides and have been shown to exhibit remarkable bioactivity. For example, the neurite-promoting laminin epitope IKVAV, was introduced onto the peptide amphiphiles; neural stem cells plated on surfaces of these nanofibers differentiated preferentially into neurons, and astrocyte differentiation was suppressed.[147] However, one of the major drawbacks to this system is that the assembly is static, meaning that the peptide amphiphiles cannot be disassembled, resulting in a constant bioactive signal. In addition, these amphiphiles are synthetic constructs, deviating from natural components typically found in the ECM.

Other approaches to form biomimetic nanofibers have been pioneered by the Hartgerink lab, utilizing collagen mimetic peptides (CMPs) to result in nanofiber

assembly.[148] The benefit for such an approach is due to the native presence of collagen in the ECM. Through modifications to these CMPS, different bioactivity can be achieved through these biomaterials, exhibiting bioactivity as well as a canonical and fibrous morphology. One such example utilized the same IKVAV epitope on a CMP to promote nerve regeneration *in vivo*.[149] Due to the fibrous nature of the CMPs and their ability to form hydrogels, CMPs have been a successful platform for biomimetic ECM materials. However, once again, the nature of the nanofibers and the bioactive signal is still static and cannot be reversed.

In order to overcome these limitations of dynamics, the Stupp lab was able to generate a peptide amphiphile system where the user has a defined control on the extent of bundling.[143] The system involved the use of peptide amphiphiles that exhibited complementary binding, either through electrostatic peptide domains or through DNA hybridization. The use of DNA hybridization allowed for the nanofiber bundles to be reversed. The use of these bundled fibers exhibited reactive phenotypical behavior for cortical astrocytes, compared to the unbundled fibers. This example highlights the importance of dynamic self-assembly, especially in a biological context. The only downside to such a platform is that the *fiber* formation is non-reversible. The dynamics are only attributed to the extent of bundling, limiting such a platform for complex, dynamic biomimetic ECM nanofibers.

In efforts to develop a nanofiber platform that can recapitulate both a fibrous morphology as well a completely reversible platform, a protein-based system was devised that can incorporate each of these elements in addition to controlling the bioactivity,

depending on the protein used. The protein nanofibers consist of self-assembled domains of fibronectin, which is a natural occurring protein in the ECM. The domains chosen for the research project are Fn-III$_{10}$, Fn-III$_{9\text{-}10}$, and Fn-III$_{12\text{-}14}$, where the bioactivity consists of a Arginine-Glycine-Aspartate (RGD) epitope for cell adhesion,[150] for both the Fn-III$_{10}$, Fn-III$_{9\text{-}10}$ domains, and growth factor binding for the Fn-III$_{12\text{-}14}$ domain.[151] Ultimately, the goal is to create a fibrous biomaterial matrix that can be reversibly polymerized to modulate the presentation of bioactive signals and/or bulk mechanical properties. In this way, it should be possible to design biomaterial scaffolds that can direct cell behavior in ECM-mimetic, dynamic ways.

The self-assembly of these protein building blocks exploits two orthogonal coiled coil peptide pairs; the EK/KE[138] and P3/P4[39] pair, where the P3 and EK coils will be fused onto the N- and C-terminus of each protein building block, respectively. The proteins were polymerized by introducing the complementary coils, Cys-P4 and KE-Cys, where the coils have terminal cysteines on the N- and C-terminus of the coils, respectively. The coiled coil protein complex then polymerizes via disulfide formation to yield a 1-D protein nanofiber.[152] The polymerized protein fibers can subsequently be broken down to monomers by reducing the disulfide linkages using molecules like TCEP. We also introduced an alternative mechanism, namely coil displacement to reverse protein assembly by creating another Cys-coil, termed KE-3H-Cys, where this coil will bind to only three heptads onto the protein, displaying a peptide "toehold".[36, 37] The resulting coiled coil protein complex can be displaced with the complementary synthetic displacement peptide corresponding to four complete heptads, imparting programmable degradation to the material. The nanofiber composition can also be tuned by swapping out the existing

proteins with different bioactive domains. The resulting biomimetic platform will find applications in research fields such as fundamental biology (probing ECM-cell interactions) and tissue engineering.

2.2. Results and Discussion

2.2.1 Plasmid Construction and Expression of the Fibronectin Domain and the Synthesis and Characterization of the Peptide Linker

To create a biomimetic nanofiber platform, I chose the tenth type III domain of fibronectin ($FN(10)_{III}$), because it displays the classic cell-adhesive RGD epitope present in this domain.[111, 153] As such, fibers of this protein can mediate cell-surface interactions, for both adhesion and migration/differentiation. To control the assembly of the fibronectin domain, two orthogonal coiled coil pairs were used, namely the P3/P4[39] and EK/KE[138] pair due to their nanomolar affinity and more neutral electrostatic character. To avoid post-expression modifications (e.g. covalent conjugation) of the protein, the monomeric protein

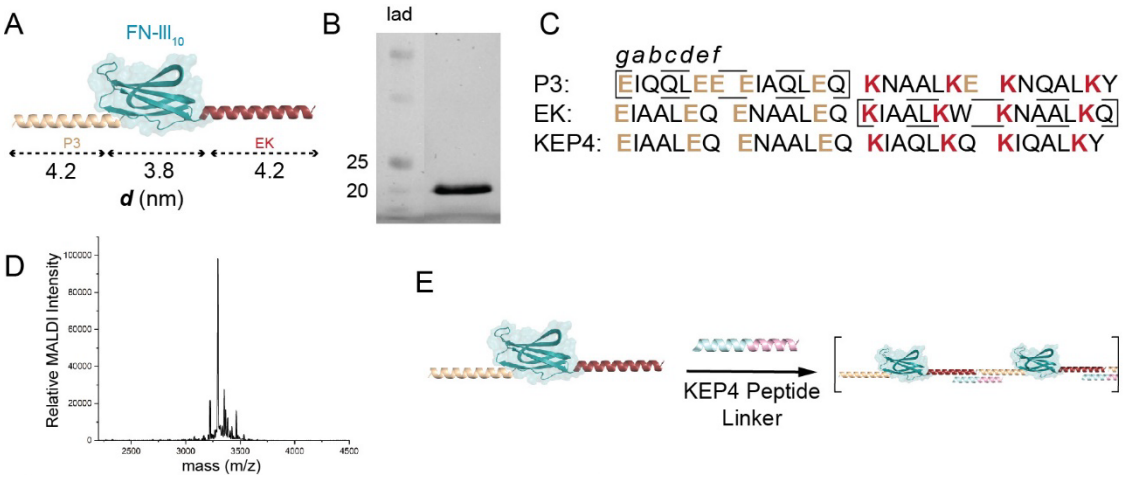

Figure 2.1 Initial design of the protein nanofibers with accompanying characterization. A) A schematic representing the fusion protein, P3-$Fn(10)_{III}$-EK. **B)** SDS-PAGE gel representing the purified protein, with a mass of 18.57 kDa. **C)** Peptide sequences of the coils used for the inital design. **D)** Mass spectrum of the KEP4 peptide linker. **E)** Schematic for the peptide-mediated 1-D protein nanofiber.

vector was assembled using Gibson assembly and incorporated into a pQE-80L vector.[154] The protein design consisted of the P3 peptide fused on the N-terminus and the EK peptide at the C-terminus to yield P3–FN(10)$_{III}$–EK (Figure 2.2 A). The plasmid for the fusion

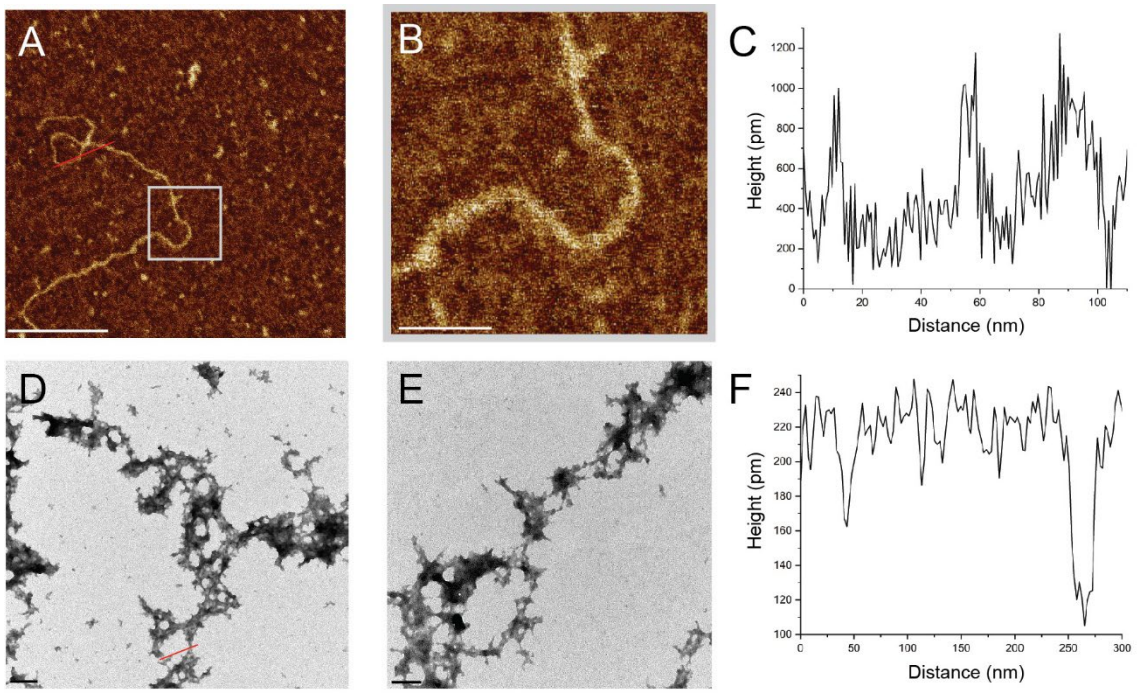

Figure 2.2. Unannealed nanofiber assembly through the peptide linker approach. **A, B)** AFM micrographs of the protein nanofiber without an annealing step. Scale bar = 200 nm. for A. Scale bar = 50 nm for B. **C)** Height profile of the protein nanofiber in panel A. **D, E)** TEM micrographs of the unannealed protein nanofibers. Scale bar = 200 nm for D. Scale bar = 100 nm for E. **F)** Height profile of the nanofiber in D.

protein was transformed into *E. coli* and expressed at 37 °C overnight. The resulting culture was lysed, and the supernatant was purified via affinity and ion-exchange chromatography. The protein fractions were characterized via denaturing sodium dodecyl-sulfate polyacrylamide gel electrophoresis (SDS-PAGE) and the resulting pure protein was consolidated and dialyzed into 1x phosphate buffer saline (PBS), pH = 8.0, overnight (Figure 2.1 B).

To promote the polymerization of the fusion protein monomer into one-dimensional (1-D) nanofibers, a peptide "splint" was designed to connect two monomers together. The peptide linker "KEP4" was designed to bind to the two last heptads of the EK coil on the protein and the first two heptads of the P3 coil (Figure 2.2 C). The peptide was synthesized via standard solid-phase peptide synthesis (SPPS). Additionally, the peptide was purified by reverse-phase high-performance liquid chromatography (RP-HPLC) and characterized by matrix-assisted laser desorption ionization (MALDI) spectrometry (Figure 2.2 D).

Once the biomolecular components were achieved in high purity, the assembly of the two components were probed with atomic force microscopy (AFM) and transmission electron microscopy (TEM). Initially, the two components were added in a one-pot

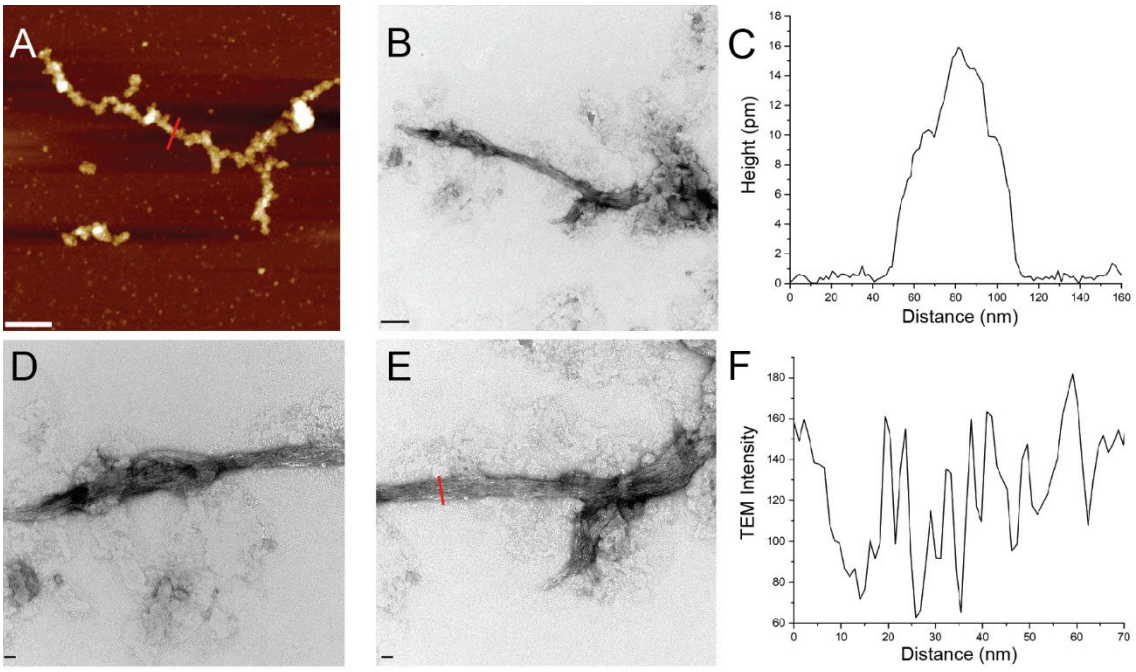

Figure 2.3 Annealed nanofiber assembly through the peptide linker approach. A) AFM micrograph of the protein nanofiber an annealing step. **B)** TEM micrograph of the protein nanofiber with an annealing step. **C)** Height profile of the nanofiber in A. **D,E)** Zoomed-in TEM micrographs of the protein nanofiber in B. **F)** Width profile of the protein nanofiber in E. Scale bar = 200 nm.

assembly, without any annealing conditions, to examine the extent of self-assembly. Under ambient conditions overnight, AFM revealed undefined protein assemblies (Figure 2.3 A,B) with some background protein. The initial micrograph indicated a short filament, exhibiting a certain level of flexibility (Figure 2.3 B), and present at a low population. Based on the height profile, the fibers were flattened on the dry surface, representing a height of about one nanometer (Figure 2.3 C). In addition, the width of each filament measured out to be 6.9 nm, which is larger than the expected width, but can account for due to the flattening of the protein on the surface as well as a tip broadening due to AFM acquisition.

By negative-stain TEM analysis, the unannealed sample looked fibrous in nature, where some areas appeared bundled/aggregated but other areas seemed like single filaments connecting the bundled areas (Figure 2.3 D,E). Upon measuring the fibers, the thin filament that was measured has a width of 7.2 nm, whereas the larger area has a width of 21.6 nm. From these measurements, the thin fiber is still wider than the expected width of the fiber. Due to the nature of TEM imaging, the width should correspond well with the expected dimensions. Therefore, the width of the thin filament suggests bundling/aggregation of the protein filament. For the larger filament, the width suggests a larger degree of bundling, indicating non-specific self-assembly.

Due to the lack of well-defined protein nanofibers, the components were subjected to an annealing protocol to probe whether additional thermal energy would result in more well-defined protein nanofibers. The annealing protocol consisted of incubating the sample at 37 °C for 10 minutes and then a gradual decrease to 12 °C, with a ramp rate of 0.5 °C/30

min. Once the ramp was completed, the sample was incubated at 4 °C until the sample was ready for imaging. Remarkably, under AFM, the nanofibers resulted in larger nanofibers, with lengths of a few microns, a width of 64.0 nm, and a height profile of 15.4 nm (Figure 2.3 C). Due to the topological output of AFM micrographs, the topology of the nanofibers seemed amorphous and granular. However, under TEM imaging, there were a few types of assemblies seen. Once again, similar undefined nanofibers were seen as a majority population but there were other instances where large bundles of nanofibers were seen, with lengths of up to tens of microns (Figure 2.3 B,D,E). Under close inspection, the bundled nanofibers exhibited well-oriented fibers. Taking a closer examination of the width of each fibril in the larger bundle, the width measured to be 2.3 nm, which corresponds nicely to the expected width of the protein nanofiber. Based on these micrographs, the results suggest that the annealing protocol allows for each protein fibril to co-assemble into nicely aligned fibers through favorable electrostatic interactions. These results highlight the effect of thermal annealing to these protein nanofibers compared to the protein nanofiber bundles seen in the unannealed approach.

However, the complete understanding of why these fibers bundle is still unclear. To obtain better control of self-assembly, peptide and protein titrations were done to see if a component in excess would result in more well-defined bundled nanofibers. In a series of titrations, where the peptide or the protein was in either one-fold, two-fold, or three-fold excess, only the condition where the protein was in three-fold excess relative to the peptide, resulted in large, bundled nanofibers (Figure S2.4).

Typically, well-ordered self-assembly systems require strict equivalence of each component into the system. In contrast, it is unclear as to why the protein nanofibers bundle with an excess of the protein in solution. Due to the lack of ability to simulate protein assembly, better understanding of this self-assembly process is unobtainable. In addition, the presence of the nanofibers was scarce, and the results were consistently irreproducible. As a result, the design of the nanofiber system was optimized to achieve more reproducible results.

We next explored a new design, using disulfide chemistry to promote the polymerization of the fibronectin domain. The disulfide strategy provides a few key benefits compared to the initial approach such as full complementary interactions between the coils in the system, the disulfide bond is reversible (which may enable longer polymerization and avoidance of kinetic traps), the peptides needed for this system are more synthetically feasible, previous systems have used this approach to promote polymerization,[152] and lastly, the approach can allow for a highly modular platform.

The second design utilizes the same fusion protein but to promote polymerization, complementary cys-coils are added into the protein solution. For the design, the P4 coil has a cysteine on the N-terminus of the peptide and the KE coil has a terminal cysteine on the C-terminus of the peptide (Figure 2.4 A). After an overnight incubation, the resulting nanofibers were visualized under AFM. Surprisingly, the redesigned approach resulted in many protein nanofibers on the mica surface, with lengths around a micrometer in size (Figure 2.5 A). The height profile revealed that the fibers had a width of 6 nm. The width

discrepancy with the expected fiber diameter (2.9 nm) can be due to the tip-broadening effect. On AFM, the nanofibers appeared to be clustered together.

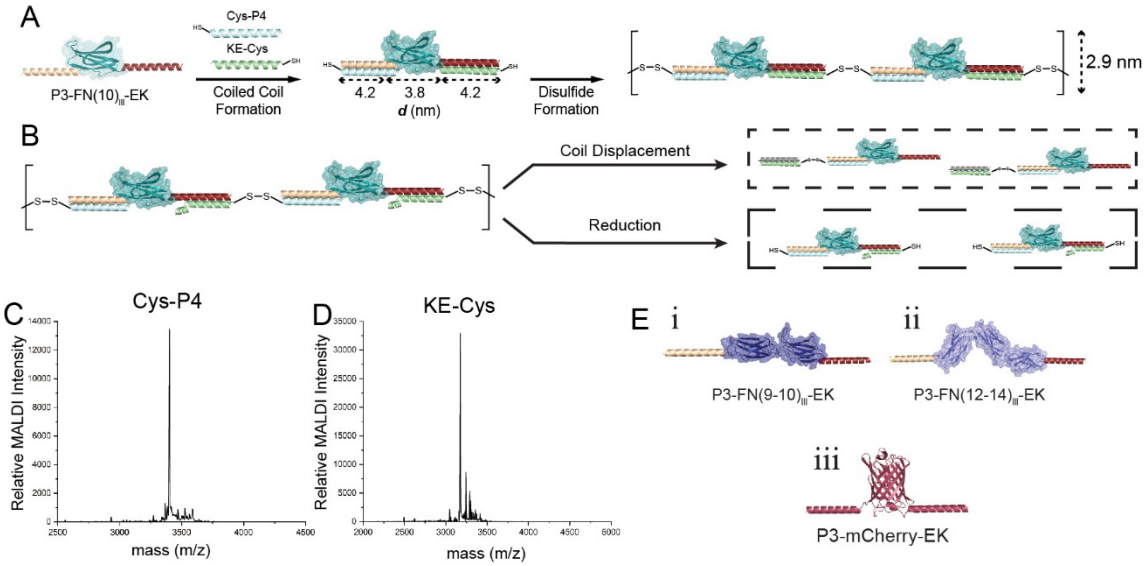

Figure 2.4 Disulfide-mediated protein nanofibers with initial characterization. A) Schematic for protein nanofibers mediated through cysteine-coils. **B)** Schematic highlighting the two modes of reversible self-assembly; coil displacement and chemical reduction. **C, D)** The mass spectra for the cysteine-coils. **E)** The modular design of the peptide-protein nanofiber system allows for the incorporation of a variety of protein domains. The protein domain (i) will add stronger cell adhesive bioactivity. The protein domain (ii) will allow for PDGF and VEGF binding to promote cell growth and differentiation. The protein domain (iii) will serve as a fluorescent tag.

With this new design in hand, we decided to explore a variety of different fibronectin domains, such as FN(9-10)$_{III}$ (ii), FN(12-14)$_{III}$ (iii), and a fluorescent protein, mCherry (iv). The benefit of such a modular protein nanofiber system is that the bioactivity of the nanofibers can be changed, depending on the biological question. In this case, FN(9-10)$_{III}$ can be incorporated to increase the binding affinity of the nanofibers to cell surface integrins.[112, 150] To have a better control of stem cell differentiation, FN(12-14)$_{III}$ nanofibers can be used due to the binding of a wide variety of growth factors. [151, 155] In the last instance, a fluorescent protein can aid in the characterization of the protein nanofibers through

fluorescence microscopy. In addition, the fluorescent protein can be “doped” in to create a hybrid fluorescent *and* bioactive protein nanofiber.

After cloning, expression, and purification, the proteins were self-assembled with cysteine coils (Figure S1). Based on the AFM micrographs, protein nanofibers readily formed (Figure 2.5 A-D). For the FN(9-10)$_{III}$ domain fibers, the fibers appeared to be spread out, extending across the surface of the mica. The population of the nanofibers as well seemed to be abundant on the surface. In addition, the AFM height profile revealed nanofibers with widths of 7.61 nm, with a height of one nanometer. These dimensions line up nicely with the expected dimensions of the nanofiber (similar to the FN(10)$_{III}$ dimensions), taking account surface effects of air mode acquisition. For the FN(12-14)$_{III}$ domain fibers, the fibers were also spread out, extending onto the mica surface. The height profile of the fibers on AFM revealed nanofibers with a width of 6.37 nm and a height of 1.3 nm. These values once again correspond nicely to the expected dimensions of the nanofibers and are congruent with the other dimensions measured with the other fibronectin fibers.

Lastly, the final protein nanofiber variant that was assembled was the mCherry nanofibers. Under AFM, the fibers initially appeared much wider than the fibronectin fibers, which is to be expected due to the larger size of the mCherry protein (~32 kDa). The nanofibers also appeared more rigid, based on the curvature and looping of the nanofibers, in contrast to the fibronectin fibers. The height profile of the mCherry nanofibers revealed a width of 12.43 nm and a height of 1.2 nm. The width of the nanofibers was about double the width of the fibronectin fibers but with a similar height profile. Due to the dimensions

of the mCherry protein (4.8 nm vs. 2.9 nm for $FN(10)_{III}$, the width was expected to be 4.9 nm so there is a large discrepancy to the width profile. However, the width discrepancy can be due to the air mode acquisition under AFM, similar to the width profiles of the fibronectin nanofibers.

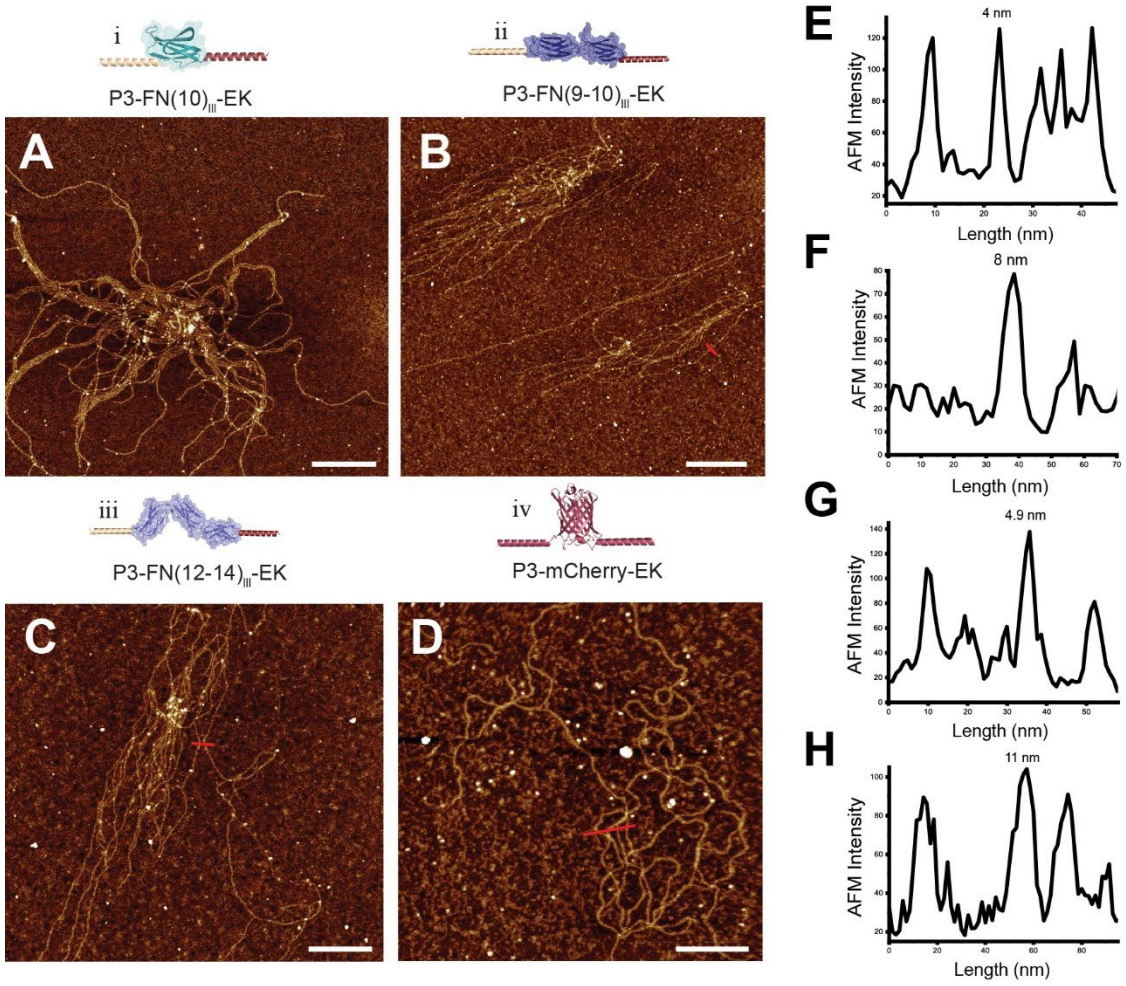

Figure 2.5. Characterization of all the disulfide-mediated protein nanofiber variants. A) Air mode AFM micrograph of protein domain (i) nanofibers. Scale bar: 200 nm. **B)** Air mode AFM micrograph protein domain (ii) nanofibers. Scale bar: 250 nm. **C)** Air mode AFM micrograph protein domain (iii) nanofibers. Scale bar: 200 nm. **D)** Air mode AFM micrograph protein domain (iv) nanofibers. Scale bar: 200 nm. E) Height profile of the nanofibers in panel A. **F)** Height profile of the nanofibers in panel B. **G)** Height profile of the nanofibers in panel C. **H)** Height profile of the nanofibers in panel D.

Under TEM, protein nanofibers were seen but more dispersed in nature (Figure 2.6 A). The $FN(10)_{III}$ domain fibers under TEM measured to be around 3.8 nm in width,

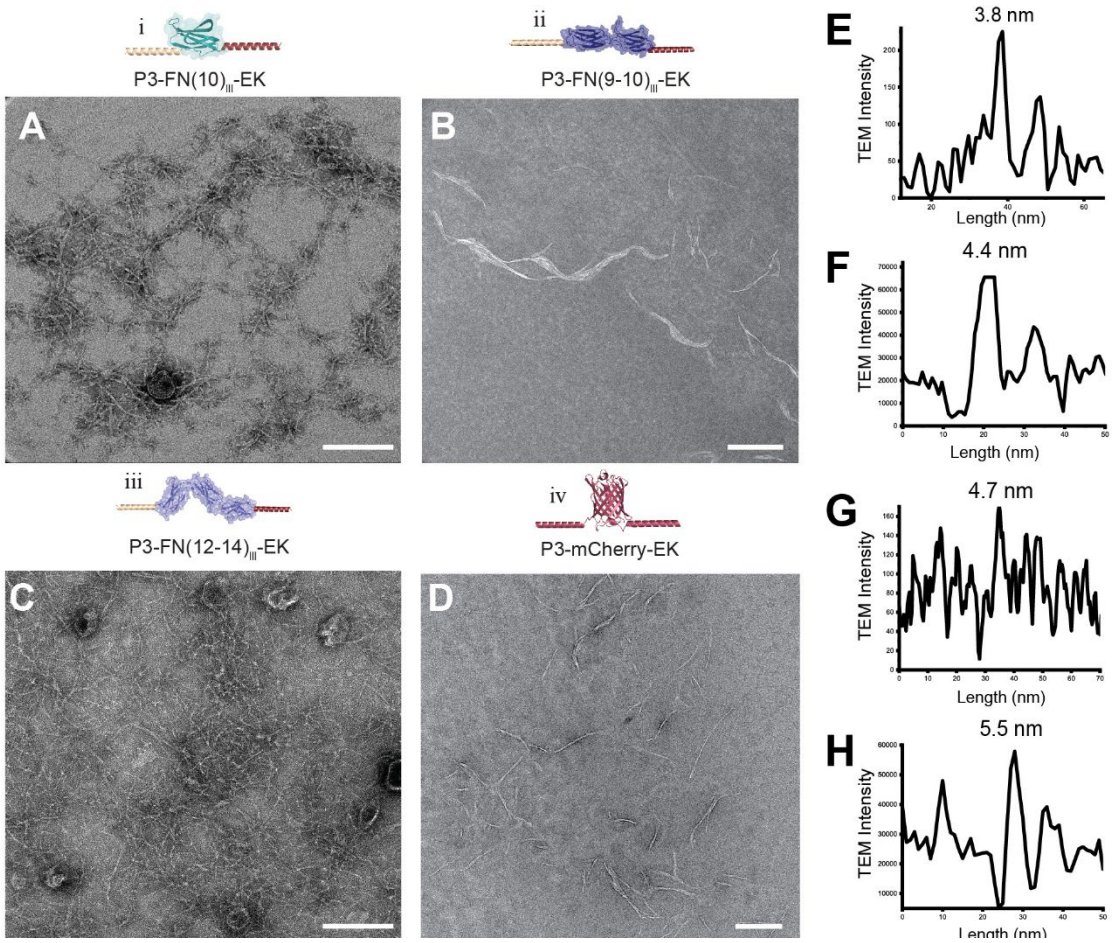

Figure 2.6. TEM Characterization of all the disulfide-mediated protein nanofiber variants. A) Negative-stain TEM micrograph of protein domain (i) nanofibers. Scale bar: 200 nm. **B)** Negative-stain TEM micrograph of protein domain (ii) nanofibers. Scale bar: 500 nm. **C)** Negative-stain TEM micrograph of protein domain (iii) nanofibers. Scale bar: 200 nm. **D)** Negative-stain TEM micrograph of protein domain (iv) nanofibers. Scale bar: 200 nm. **E)** Width N analysis of the nanofibers in panel A. **F)** Width analysis of the nanofibers in panel B. **G)** Width analysis of the nanofibers in panel C. **H)** Width analysis of the nanofibers in panel D.

corresponding better with the expected width of the protein compared to the AFM micrographs (Figure 2.6 E). The lack of clustering under TEM indicates that the clustering seen on the AFM may be due to surface effects and possibly due to air mode imaging. However, under TEM, there were areas where the nanofibers seem to coil around each other. The overall population of the fibers were much greater compared to the isolated fiber clusters seen on AFM, indicating better assembly than initially expected.

For the FN(9-10)$_{III}$ domain nanofibers, TEM characterization indicated well-formed nanofibers (Figure 2.6 B). However, compared to the FN(10)$_{III}$ domain fibers, the nanofibers seemed to be more bundled, indicating possible higher-order assembly. The width measurements revealed a width of 4.4 nm, getting closer to the expected dimensions of the nanofiber (Figure 2.6 F). The measurement was more precise compared to the AFM height profile due to higher resolution of the structures. For the FN(12-14)$_{III}$ domain nanofibers, the nanofibers completely covered the TEM grid, indicating a high population of nanofibers (Figure 2.6 C). The mat of nanofibers was the best display of self-assembly compared to all the other nanofibers imaged. Width analysis of the nanofibers resulted in the nanofibers having a width of 4.7 nm (Figure 2.6 G). These measurements, as well as all the other fibronectin nanofibers gave widths of ~4.5 nm, indicating good agreement between each sample type.

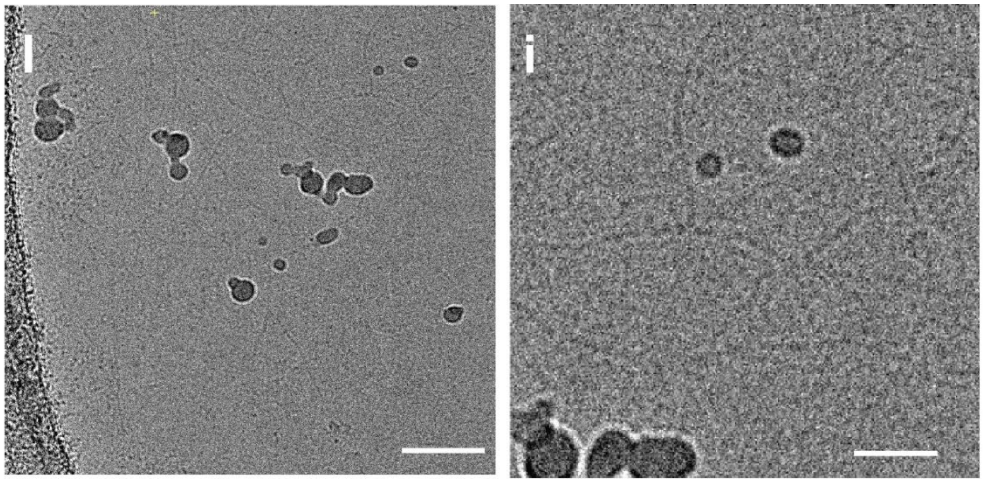

Figure 2.7. Cryo-TEM Characterization of the 12-14th domain disulfide-mediated protein nanofibers. A cryo-TEM micrograph showing protein domain (iii) nanofibers. Scale bar: 50 nm. (i) Zoom-in image of the area in Fig 2.7 A. Scale bar: 25 nm.

Lastly, for the mCherry nanofibers under TEM, the fibers were in high abundance, with a visible decrease in curvature and bending compared to the fibronectin fibers (Figure

2.6 D). Due to the wider nature of the mCherry protein, the increase in width might result in stiffer fibers. However, it is difficult to conclude without persistence length measurements. The resulting nanofibers were measured, and the width was 5.5 nm (Figure 2.6 H). The width of these is higher than that of the fibronectin variants, which is to be expected. Also, the width of these is much closer to the expected dimensions of the protein building block.

To further verify how the nanofibers were in solution, the nanofibers were analyzed under cryogenic conditions (Figure 2.7 A,B). In the resulting cryo-TEM micrograph the nanofibers appeared to be well-dispersed without the clustering or supercoiling structures seen in the dry-deposition techniques. The absences of these artifacts indicate robust assembly. The lack of bundling indicates that these fibers are well dispersed in solution.

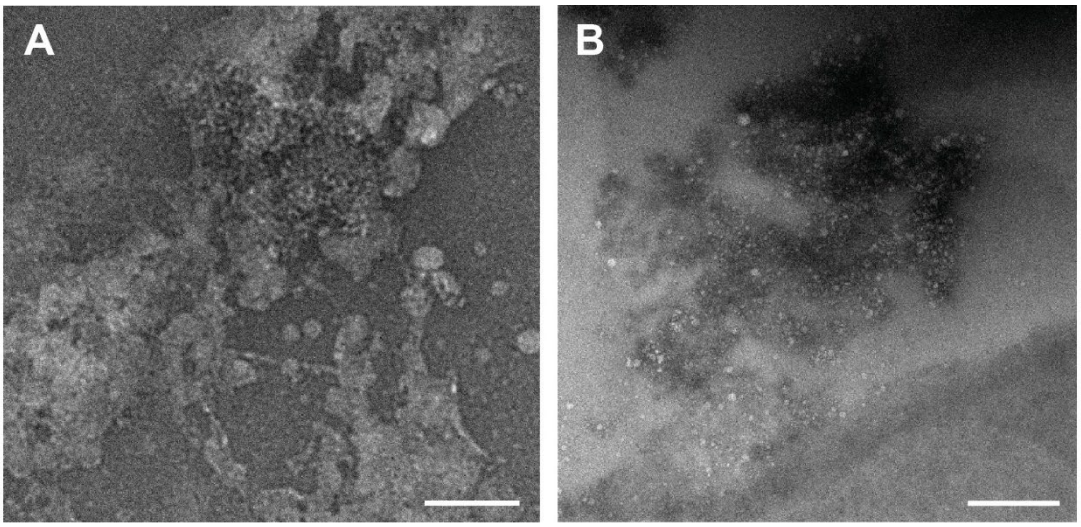

Figure 2.8. TEM Characterization of nanofiber DTT reduction. A) Negative-stain TEM micrograph of the reduced protein domain (i) nanofibers. Scale bar: 100 nm. **B)** A negative-stain TEM micrograph of reduced protein domain (iii) nanofibers. Scale bar: 600 nm.

However, further structural details are limited due to the low contrasting ability of the

protein domains. Other avenues can be taken to increase the elemental contrast of these nanofibers, either with metal nanoparticle or even DNA.

To highlight the reversibility of the protein nanofibers, two protein nanofiber variants were chosen, $FN(10)_{III}$ and $FN(12\text{-}14)_{III}$, due to the abundant and well-dispersed nanofibers seen under TEM. Upon addition of 10 mM Dithiothreitol (DTT) for 30 minutes, to reduce the disulfides, there were no nanofibers seen under TEM, only areas of aggregated protein (Figure 2.8 A,B). Due to the absence of nanofiber morphology on the TEM grid, it highlights the reversibility of these nanofibers under reducing conditions.

2.2.3 Design of an All-Protein-based Nanofiber System

Building off the success of the disulfide-mediated fiber formation, we explored other avenues in order to simplify the nanofiber platform in addition to overcoming the downsides to the previous approach. In detail, the previous approach allowed for reproducible fibers to be formed but the directionality (i.e. which "end" of the protein, N- or C-terminus, formed by the disulfide for the growing end) of each monomer incorporation could not be controlled. Additionally, the system requires synthetic peptides, which increased the number of molecular species in solution. To simplify this approach, the complementary coils to the P3-$FN(10)_{III}$-EK fusion protein were genetically fused to the same $FN(10)_{III}$ domain creating KE_3H-$FN(10)_{III}$-P4 (Figure 2.9 A).[156, 157] The coil on the N-terminus has 3 heptads (3H) that are complementary to the EK coil, leaving a free heptad for coil displacement.

Similar to the disulfide approach, four protein variants were tested to show the modularity and ease of protein nanofiber assembly (Figure 2.5 B-E). Simple incubation of

the two proteins overnight at room temperature promoted the self-assembly to form fibers.

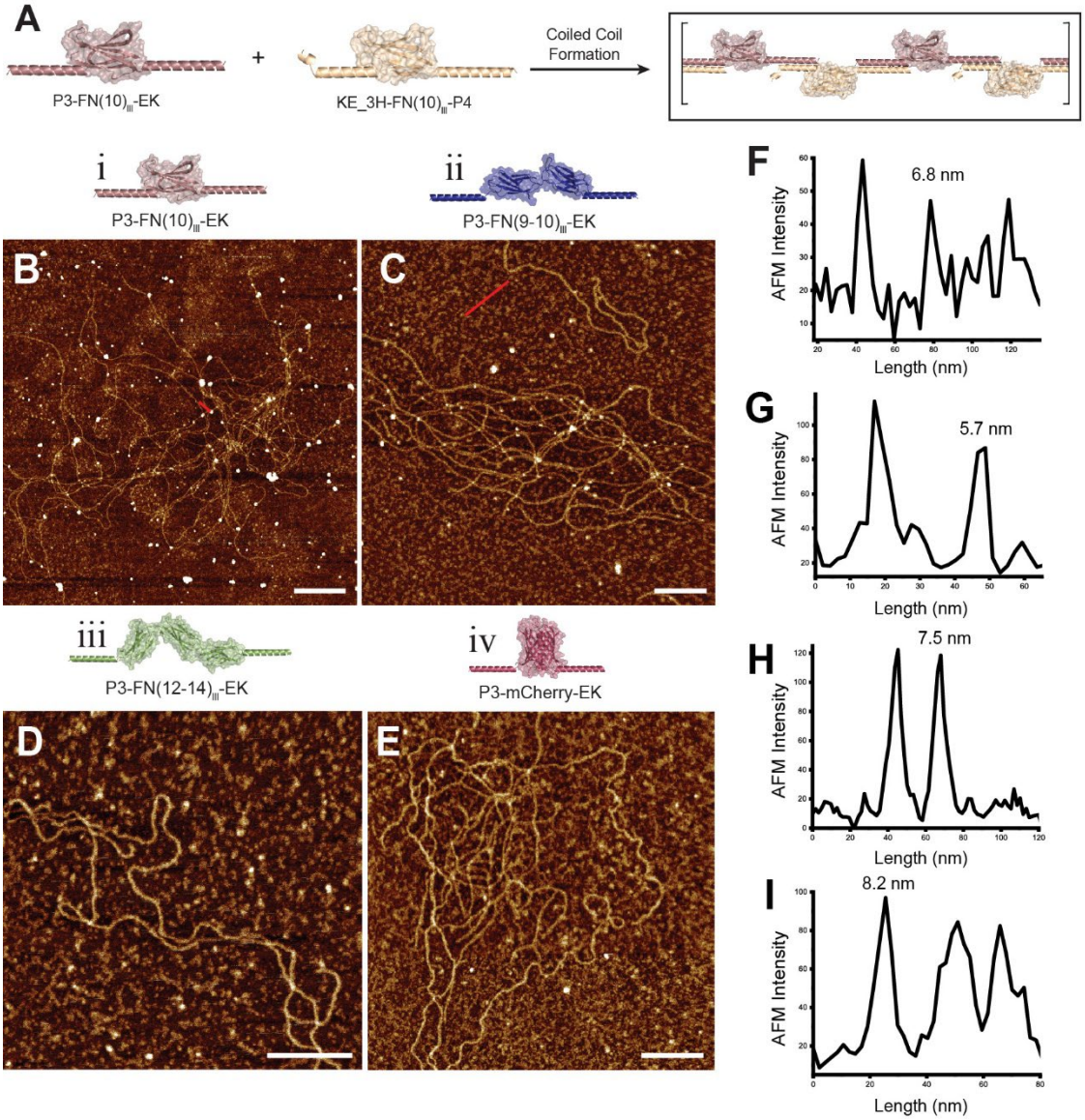

Figure 2.9. Characterization of the complementary protein nanofiber variants. A) Air mode AFM micrograph of protein domain (i) nanofibers. Scale bar: 200 nm. **B)** Air mode AFM micrograph protein domain (ii) nanofibers. Scale bar: 250 nm. **C)** Air mode AFM micrograph protein domain (iii) nanofibers. Scale bar: 200 nm. **D)** Air mode AFM micrograph protein domain (iv) nanofibers. Scale bar: 200 nm. **E)** Height profile of the nanofibers in panel A. **F)** Height profile of the nanofibers in panel B. **G)** Height profile of the nanofibers in panel C. **H)** Height profile of the nanofibers in panel D.

Additionally, the incorporation of these two proteins is mediated precisely to form an *ab* block copolymer. This precise control of each protein species in the polymer provides a

versatile method to form nanofibers, especially if more orthogonal coiled coil pairs are used. In contrast to the first approach with synthetic peptides, this approach allows for the directionality of the proteins due to the parallel orientation of the coiled coil pairs used in this system.

Under AFM, this "protein complement" system (as we term it) allowed for all these fusion proteins to self-assemble, yielding fibers with lengths up to a few micrometers in size. For the $FN(10)_{III}$ nanofiber variant, the system formed these long, spread out nanofibers. Based on the height profile, the width of the protein nanofibers was 5.6 nm with a height of 1.4 nm. Although many nanofibers were observed on the surface, they were fairly aggregated, similar to the disulfide-mediated system. For the $FN(9\text{-}10)_{III}$ nanofiber variant, the nanofibers seemed to be more clustered but well formed. The height profile of the nanofibers revealed a width of 9.2 nm with a height of 1.6 nm. The last fibronectin variant, the $FN(12\text{-}14)_{III}$ nanofibers, formed readily but from the initial micrograph, appeared to be more flexible. Based on the height profile of the nanofibers, the height was revealed to be 7.1 nm with a height of 1.1 nm. All the fibronectin variants exhibited similar width profiles compared to their disulfide counterparts. However, the height of the nanofibers in the latter system appears to be higher, indicating less flattening on the surface possibly due to more robust packing/assembly.

For the mCherry variant, a large number of nanofibers was observed though they were entangled with one another. In addition, the fibers seemed to have more curvature to them, similar to their disulfide counterpart, suggesting that the mCherry nanofibers are more flexible compared to the thinner fibronectin nanofibers. The height profile of the

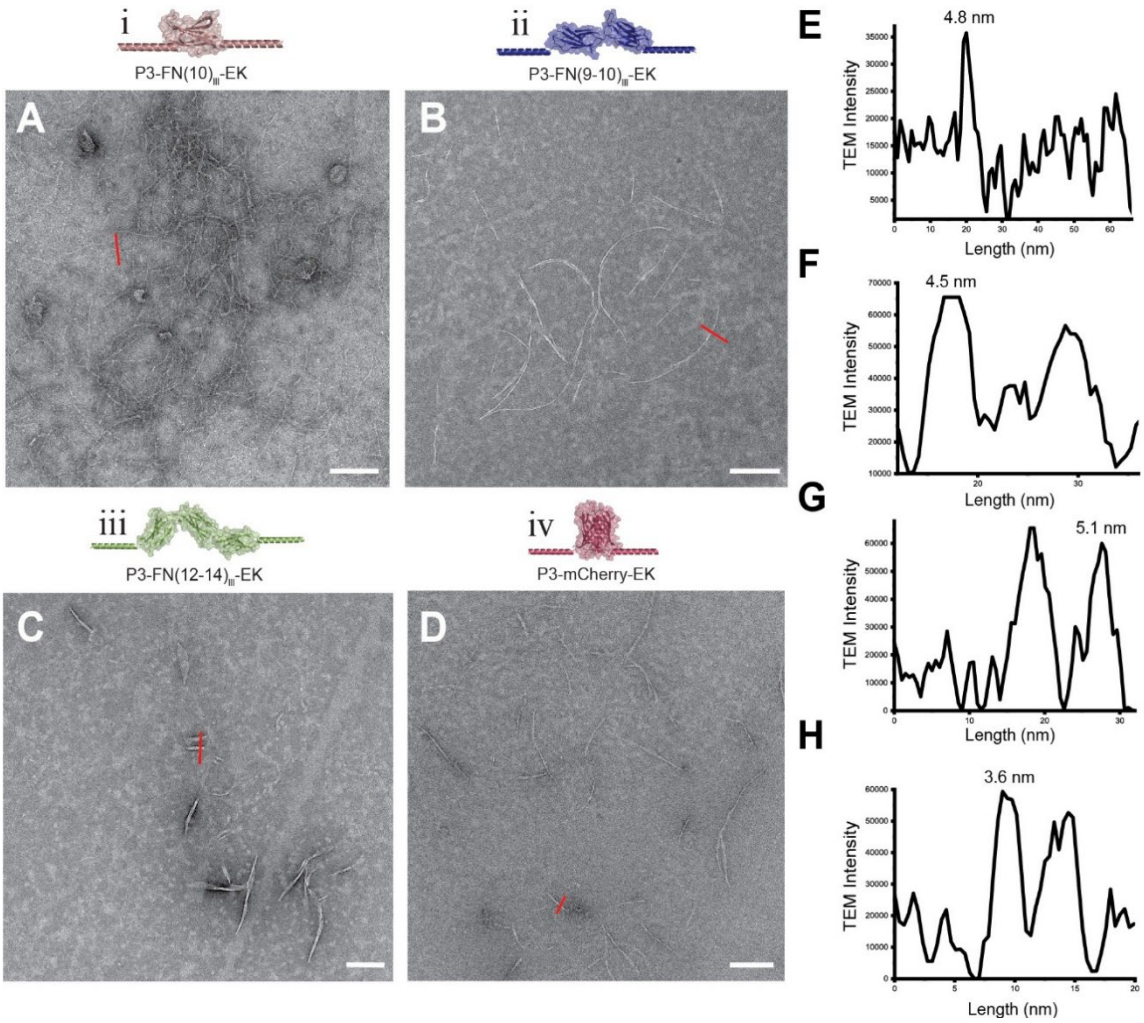

Figure 2.10. TEM Characterization for all protein variants with the protein complement system. A-D) Negative-stain TEM micrograph of protein domain (i-iv) nanofibers, respectively. Scale bar: 200 nm. **E)** Width profile of the protein nanofibers in panel A. **F)** Width profile of the protein nanofibers in panel B. **G)** Width profile of the protein nanofibers in panel C. **H)** Width profile of the protein nanofibers in panel D.

nanofibers revealed a width of 8.6 nm with a height of 910 pm. The width of these nanofibers is in more agreement with the expected dimensions of the nanofiber, but the height seems to be smaller compared to the fibronectin nanofibers. The height may indicate that the nanofibers are more prone to compression, possibly due to the β-barrel structure of mCherry. To note, variant (*iv*) allowed for a hybrid nanofiber consisting of both a bioactive and fluorescent protein.

After each of the variants were characterized under AFM, each nanofiber variant was characterized by negative-stain TEM. Once again, all the nanofiber samples seemed more dispersed and less clustered compared to the AFM micrographs. For the $FN(10)_{III}$ nanofiber variant, the nanofibers formed readily, and the population of nanofibers seemed to be more abundant as compared to AFM (Figure 2.10 A). The width of the nanofibers was 3.94 nm, which was closer to the expected width compared to the measurement obtained from the AFM micrographs (Figure 2.10 E). For the $FN(9\text{-}10)_{III}$ nanofiber variant, the nanofibers were more dispersed and more straight/stiffer compared to fibers imaged under AFM (Figure 2.10 B). Width measurements revealed a width of 2.8 nm, which is very close to the expected width of the nanofibers (Figure 2.10 F). Once again, the TEM measurements were more accurate as compared to the measurements obtained from AFM. For the $FN(12\text{-}14)_{III}$ nanofiber variant, the fibers seemed more dispersed and stiffer compared to the fibers under AFM (Figure 2.10 C). In addition, there was some minor bundling/cohesion between fibers seen under TEM that wasn't apparent under AFM. The width measurements revealed a width of 3.7 nm, which was close to the expected width of the nanofibers (Figure 2.10 G). For all of the fibronectin variants, TEM revealed dispersed and abundant nanofibers, appearing much stiffer compared to the nanofibers seen under AFM.

Lastly, for the mCherry sample under TEM, the fibers were observed in high abundance with a visual decrease in curvature and bending compared to the fibronectin fibers (Figure 2.10 D). These stark changes in nanofiber morphology were also apparent in the disulfide-mediated mCherry nanofibers. Due to the wider nature of the mCherry protein, the increase in width might result in stiffer fibers. However, it is difficult to

conclude without persistence length measurements. The resulting nanofibers were measured, and the width was 4.52 nm (Figure 2.10 H). The width of these is higher than that of the fibronectin variants, which is to be expected due to the larger size of the protein. Also, the width of these is much closer to the expected dimensions of the protein building block.

With the design of the KE_3H-FN(10)$_{III}$-P4 fusion protein, the complementary protein nanofiber system can still allow for reversible assembly due to the peptide toehold on the N-terminal coil. To explore this, a synthetic displacement peptide (EK Displacement) was synthesized and titrated with the hybrid FN(10)$_{III}$/mCherry nanofiber to see if the EK Displacement peptide would be effective enough to disrupt nanofiber assembly. Without the displacement peptide, the length distribution of the protein nanofibers ranges from 0.5µm to 3.5 µm (Figure 2.11 E).

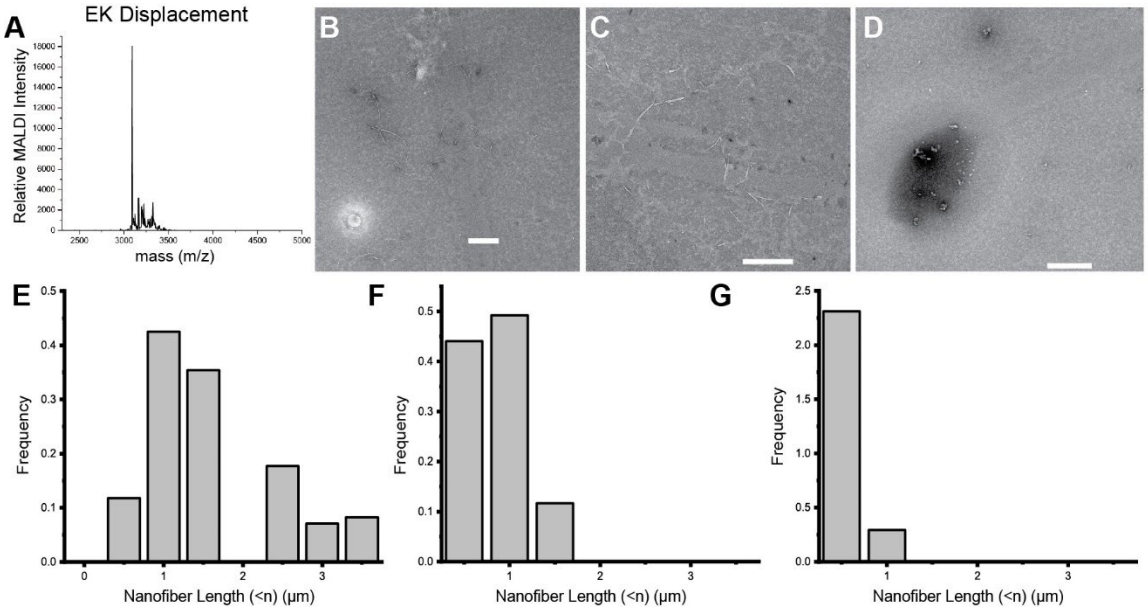

Figure 2.11. Protein nanofiber displacement characterization. A) Mass spectrum of the EK Displacement peptide. **B-D)** Displacement of mCherry protein complement nanofibers with 5x, 30x and 50x displacement peptide, respectively. Scale bar: 500 nm. **E-G)** Fiber length histograms for mCherry nanofibers with 0x, 5x, and 30x displacement peptide.

To start, the EK Displacement peptide was added to the nanofiber solution at a 5 molar excess to the KE_3H-FN(10)$_{III}$-P4 fusion protein, which resulted in shorter nanofibers under TEM (Figure 2.11 B). With the displacement peptide present at a five-molar excess, the length distribution ranges from 0.1 μm to 1.5 μm, which decreases the length distribution by more than half, compared to the initial length distribution. Increasing the displacement peptide to be at a thirty-molar excess, resulted in significantly shorter nanofibers (Figure 2.11 C). The resulting nanofiber length distribution was less than one micrometer, indicating a large decrease in the overall length distribution (Figure 4.7 G). Finally, at fifty molar excess, no nanofibers at all were seen on the TEM grid, indicating that all of the nanofibers present in solution were displaced (Figure 2.11 D).

Previous examples of coil displacement (with synthetic peptides alone) indicate that the coil displacement should be efficient, occurring at a 1:1 molar ratio.[37] However, in these experiments, the protein nanofiber displacement requires up to a 50 molar excess, indicating a less efficient process. These result hint towards either low affinity of the displacement peptide to the protein, or that the overall kinetics of the process might be slower than that of free, accessible peptides. These nanofibers are quite long, which might indicate that the size of these nanofibers might be reducing the kinetics of the displacement reaction. In another view, since these nanofibers are quite "sticky" (as seen by their aggregation under some conditions), the displacement peptide might be interacting with the nanofibers non-specifically. In this regard, the displacement peptide would need to be present at a much higher concentration to promote efficient binding to outcompete any non-specific interactions occurring in solution. Nonetheless, the process works

successfully, and it represents the first examples of coil displacement occurring with protein systems.

To visualize the nanofibers with another technique, we turned to “DNA Points Accumulation for Imaging in Nanoscale Topology” (DNA-PAINT), for super-resolution fluorescence microscopy. The use of DNA-PAINT requires a nanostructure that displays a docking strand (21 nucleotides) to which the fluorescently modified imaging strand (7 nucleotides) can transiently bind, resulting in fluorescent “blinking” needed for point accumulation and super-resolution reconstruction. In this regard, one of the cysteine-bearing peptides (Cys-P4) was modified on the C-terminal end with an azidolysine for copper-free click chemistry with a DBCO-modified oligonucleotide (Figure 2.12 A). To ensure quality imaging in a buffer reservoir over an extensive period of time, the other polymerization peptide (KE-Cys) was modified on the N-term with biotin, to ensure surface immobilization on a streptavidin-modified glass surface (Figure 2.12 A). The new peptides that are necessary for DNA-PAINT imaging represent a set of highly modified peptides with diverse functions, from the ability to promote polymerization of the protein through disulfide formation, the ability to allow for DNA hybridization, and the ability for surface mobilization.

In addition to super-resolution microscopy, the DNA-modified protein nanofibers can then be further self-assembled in a hierarchical manner through the addition of a DNA splint (Figure 2.12 B). By introducing an DNA oligonucleotide that can splint two DNA-protein nanofibers, then it allows for the hybrid nanofibers to bundle, in a programmable (and potentially reversible) manner. Based on this design, the splinting of two nanofibers

can be achieved through a complementary oligonucleotide that exhibits two-repeating sections of the DNA sequence on the protein nanofiber. In this manner, the protein nanofibers can be positioned in close proximity (Figure 2.12 C).

Towards this goal, both modified biomolecules were synthesized, where DNA-peptide conjugate was synthesized through copper-free click chemistry, and the biotin-

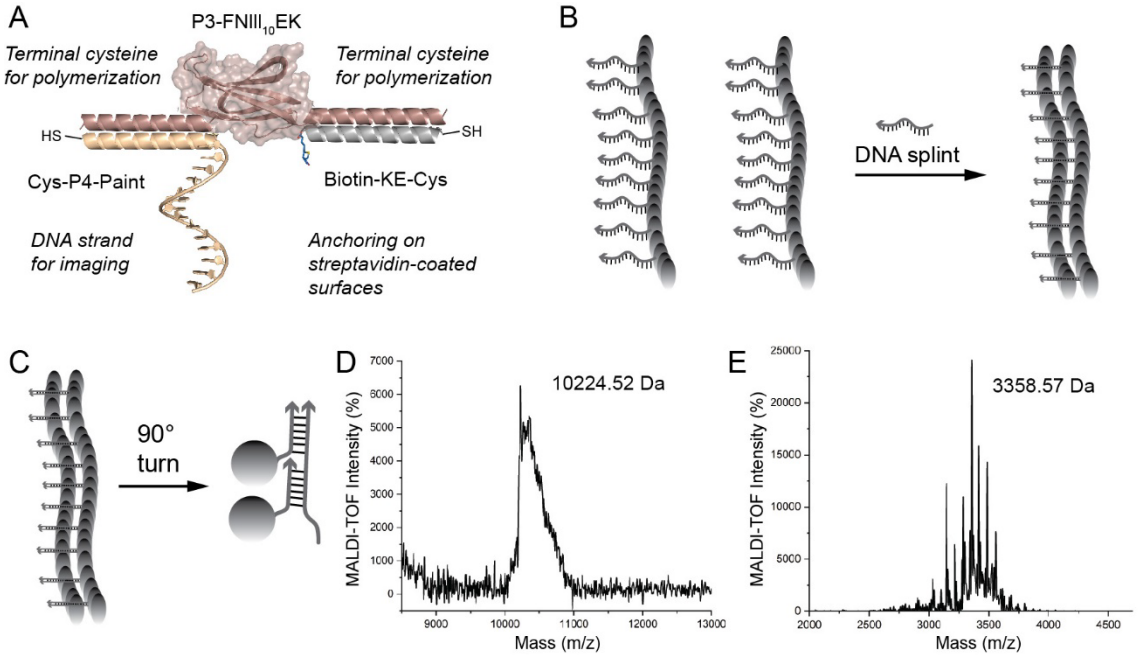

Figure 2.12. DNA modification of the disulfide-mediated protein nanofibers. A) Cartoon schematic representing the DNA and biotin modifications of the cysteine peptides used for protein polymerization. **B)** Cartoon schematic highlighting the hybridization of two protein-DNA nanofibers through a DNA splint. **C)** Cartoon schematic highlighting the orientation of the DNA-protein nanofibers upon splinting. **D)** Mass spectrum of the Cys-P4-Paint conjugate. **E)** Mass spectrum of the biotin-KE-Cys peptide.

peptide was directly modified on the solid-phase peptide synthesizer. For the DNA-peptide conjugate, once synthesized, it was purified and characterized through MALDI-TOF mass spectrometry. The reaction never resulted in a visible precipitation, indicating that there was no side reaction being produced. The resulting mass spectrum of the conjugate revealed an observed mass of 10224.5 Da, which is close to the expected mass of 10014.9

Da (Figure 2.12 D). In our experience, peptide-DNA conjugates do not ionize well on the mass spectrometer, resulting in a broad peak. In this regard, the trend remains true where the resulting mass peak was broad but still revealed a mass that is indicative of the peptide-DNA conjugate.

For the biotin-KE-Cys peptide, the modification was done on solid-phase, promoting efficient coupling on the resin in which the peptide was synthesized on. However, an issue that arose was due to the poor solubility of the biotin in DMF. Due to the poor solubility, only a small amount was to dissolve in the DMF, resulting in poor coupling yields. The poor coupling yield was observed on the chromatogram but due to sufficient separation, the biotin-peptide was able to be purified in pure manner. The resulting pure peptide was characterized by MALDI-TOF, yielding an observed mass of 3358.6 Da, which is close to the expected mass of 3416.0 Da. In the future, to avoid this issue with poor coupling, an NHS-Biotin should be used to aid in the solubility of the compound in DMF. However, based on the successful synthesis of each of these peptides, the self-assembly of this new approach was tested.

Each of the peptides that were previously used were completely replaced with the newly modified peptides with $Fn(10)_{III}$, resulting in all the protein complexes exhibiting a DNA docking strand and a biotin tag. The resulting self-assembled structures were initially characterized with air-mode AFM, as previously done with the peptide/protein-based system. An initial wide-field AFM scan was conducted, which revealed the formation of the protein nanofibers at a high efficiency (Figure 2.13 A). The DNA-protein nanofibers were well-scattered on the mica surface, without any large clustering or aggregation seen.

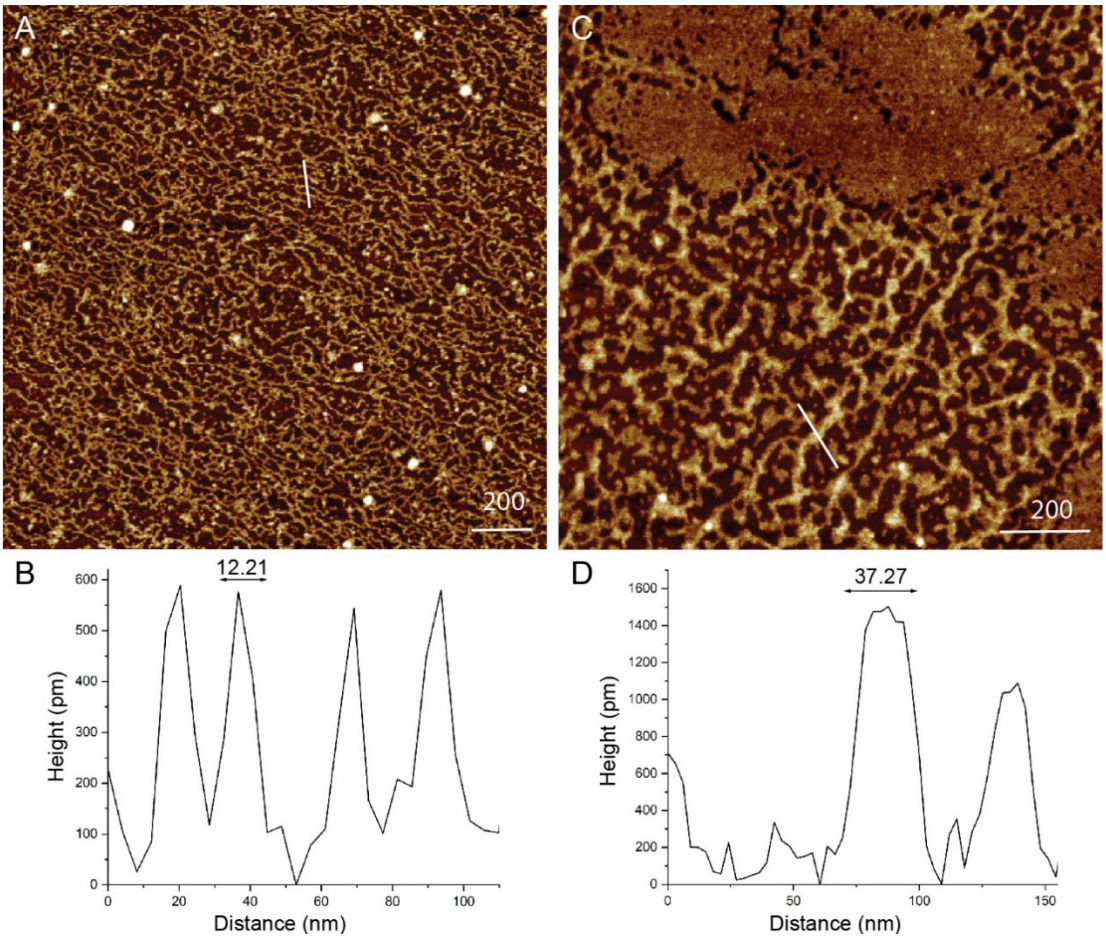

Figure 2.13. AFM analysis of the disulfide-mediated DNA-Fn protein nanofibers. **A)** AFM micrograph of the DNA-Fn(10)$_{III}$ protein nanofibers. Scale bar = 200 nm. **B)** Width analysis of the micrograph in (**A**). **C)** Zoomed-in AFM micrograph of the DNA-Fn(10)$_{III}$ protein nanofibers. Scale bar = 200 nm. **D)** Width analysis of the micrograph in (**C**).

Additionally, the nanofibers did not cluster together, as seen in previous AFM micrographs of just the peptide/protein nanofiber system. The increase in dispersity or even high affinity to the mica surface may arise due to the DNA tag on the nanofiber. A DNA handle should allow for better binding to the mica surface, which may result in better AFM data acquisition.

To better understand the physical dimensions of these new nanofibers, a width measurement of these nanofibers was taken, which is represented in the white line in the

AFM micrograph. The width measurement revealed well-defined, high-intensity peaks highlighting the adequate dispersity of the nanofibers on the surface (Figure 2.13 B). The average width of these peaks was 12.2 nm with a height of ~ 600 pm. The width is about a two-fold increase in width compared to the same nanofibers without the DNA handle (6 nm). The DNA handle is 21 nucleotides long, which represents an expected width of 7.14 nm, assuming a double-stranded helix and completely straightening of the helix. However, the DNA handle is ssDNA and could collapse, which would shorten the expected length of the DNA handle. On top of that, the measurement is not accounting for the width broadening due to AFM acquisition artifacts. Therefore, taking to account a possible length of 3.67 nm (half the width of the same length of double stranded DNA), 3 nm of width broadening due to AFM acquisition (from previous AFM measurements), and 2.9 nm for the width of the fibronectin domain, that would result in an expected with of 9.6 nm, which is relatively close to the observed width dimensions. The height profile highlights protein flattening on the mica surface, due to air mode AFM acquisition.

By scanning other regions of the sample, there were some nanofibers that seemed to be bundled together, where smaller filaments are seen penetrating into the bundle and filaments extruding from the bundled area (Figure 2.13 C). Although these filaments and bundles are well-dispersed on the surface, the bundles represent an instance of possible hierarchical packing, due to the DNA modification on these protein nanofibers. To obtain a better picture of the bundled area, width measurements were taken, which is represented by the white line on the AFM micrograph. The width measurement revealed that the bundled fiber had a width of 37.27 nm with a height of 1.5 nm. The width of the bundled fiber is approximately three times as large as the measured individual filaments (~ 36.63

nm) whereas the height profile also represented a height which was approximately three times as large as the individual filaments. Due to the agreement in the width and height measurements, the data could be due to the bundled fiber containing at least three of the individual filaments that have been self-packed into larger fibers. The other peak that was measured adjacent to the bundled fiber has a width of ~12 nm, indicating the inhomogeneous nature of the sample, where the sample consists of individual filaments and bundled filaments to larger fibers.

Due to the successful formation of the DNA-protein nanofibers, these DNA-$Fn(10)_{III}$ nanofibers were imaged using a Total Internal Reflectance Fluorescence (TIRF) microscope for super-resolution DNA-PAINT imaging in collaboration with the Hariadi Lab at Arizona State University. With the help of Dr. Prathamesh Chopade, the sample preparation consisted of thoroughly washing a glass cover slip with isopropanol and plasma cleaned to ensure complete removal of any surface debris. To follow, the surface was treated with BSA-biotin in a flow chamber made with double sided Kapton tape, to effectively modify the surface with biotin. After biotin modification, the surface was exposed with tetrameric streptavidin to ensure that the biotin-labeled nanofibers can be anchored on the glass surface. After subsequent washing steps, the DNA-protein nanofibers were flowed onto the glass slide, subsequently washed, and then anchored with and incubated with an oxygen-scavenging solution and the imaging strand, using Cy3 for the fluorophore in these experiments. Once incubated, the buffer chamber was sealed with epoxy and allowed to solidify before data acquisition. Once dried, the samples were taken over to the TIRF microscope for data acquisition.

For data acquisition, 10000 frames were acquired over a period of 15 minutes. After data processing, which involves the localization of well-defined peaks, and the rendering of the localized peaks, a TIRF micrograph was obtained which appeared to have multiple nanofibers scattered across the glass surface (Figure 2.14 A). Based on the scale bar, each of these nanofibers had a length of around ~1 μm, which corresponds well with previously measured filaments. However, many of the nanofibers in the micrograph seemed aligned, which might be due to poor drift correction. In this regard, only fibers that deviated from the straight line and were parallel to one another were chosen for further analysis. A closer look at one of the nanofibers on the surface revealed three nanofibers in close proximity to one another, ranging in length from 500 nm to 1.5 μm (Figure 2.14 B). Each of these nanofibers seem to exhibit segmentation, indicating some of the protein monomer "units" to be resolved using this technique. To obtain a better insight on these segmented blocks, a length measurement was done on the larger fiber, where a vector was placed alongside the length of the nanofiber. The resulting measurement revealed incremented peaks, with the peaks occurring at intervals around ~ 60 nm. In addition, each peak had an average width of 35.78 nm. To understand these measurements better, it is important to look back

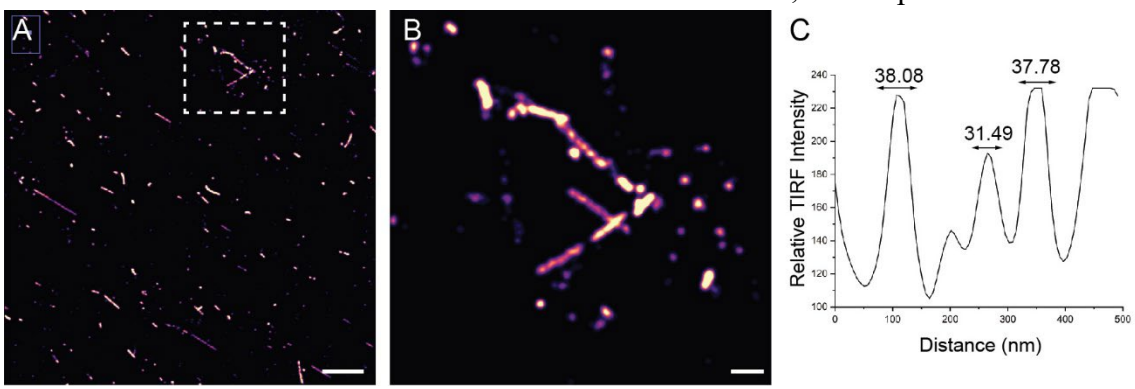

Figure 2.14. DNA paint analysis of the disulfide-mediated DNA-Fn protein nanofibers. A) TIRF micrograph of the DNA-Fn(10)$_{III}$ protein nanofibers. Scale bar = 1 μm. **B)** Zoomed-in TIRF micrograph of the DNA-Fn(10)$_{III}$ protein nanofibers. Scale bar = 200 nm. **C)** Width analysis of the micrograph in (**C**).

at the expected dimensions of the protein complex. The width of the protein complex is 12.4 nm. Based on this expected length, the segmentation occurring at ~60 nm represents a repeating unit that is too large to be each protein complex. One possibility is that the DNA handle is not providing sufficiently localized blinking, resulting in a broadening of the peak distribution, decreasing the resolution of the obtained imaged. The resulting DNA-PAINT images provide a promising initial set of images that highlights the benefit of the DNA handle for super-resolution imaging of these DNA-protein nanofibers. However, these imaging conditions need to be optimized to resolve each protein complex in the nanofiber.

After the DNA-paint images, the DNA-protein nanofibers were tested for programmable crosslinking. Based on the single DNA sequence that is displayed on the DNA-protein nanofibers, the simplest way to promote DNA-induced bundling was to have a complementary sequence that contains two repeats of the complementary sequence on the nanofiber. In addition, the complementary crosslinker had a seven-base toehold, providing the potential to reversible the possible hierarchical bundling. Based on this design, the complementary crosslinking strand was added to a 1 μM solution of the protein nanofibers, at an equimolar ratio. Due to the sample that was previously made, the protein nanofiber that was crosslinked only displayed 50% of the Cys-P4-Paint conjugate, allowing for 50% of the nanofiber to be decorated with a DNA handle. The resulting solution was annealed from 37 °C to 12 °C over a period of 10 hours and held at 4 °C until the sample was ready to be imaged. The sample was annealed at these low temperatures to avoid any potential denaturation of the protein-of-interest. In this regard, the anneal might be "incomplete" due to the lack of complete thermal denaturation of the crosslinked strand.

However, based on the sequence and the temperature, the sequence should not exhibit any secondary structure which might perturb the effective crosslinking ability.

The sample was initially taken over to the AFM to obtain a topological understanding of the crosslinked sample. With a wide-field scan of the sample, the sample exhibited more clustered features to it as compared to the sample that has not been treated with the crosslinker (Figure 2.15 A). The wide-field scan revealed dispersed, individual filaments but also areas that appeared to be like aggregates of the protein nanofiber, with an apparent increase in the height profile. Throughout the surface, there was features that appeared to be intertwined filaments.

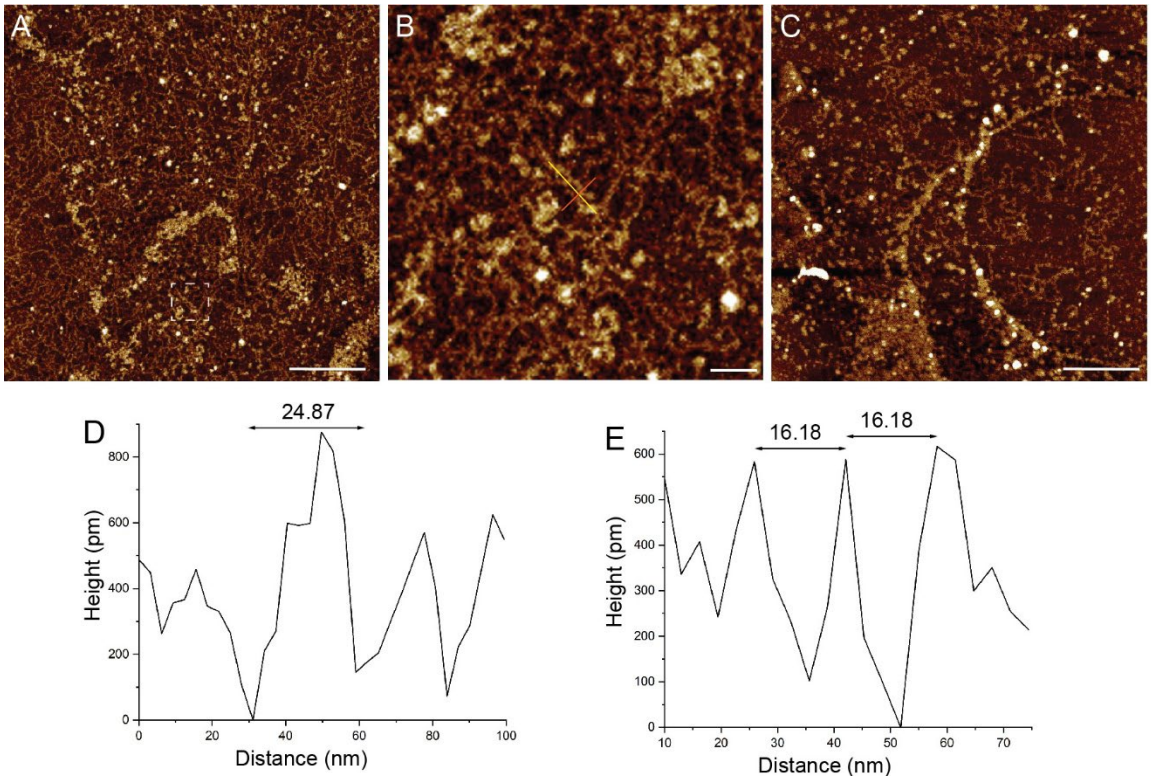

Figure 2.15. AFM analysis of the splinted disulfide-mediated DNA-Fn protein nanofibers. A) AFM micrograph of the crosslinked DNA-Fn(10)$_{III}$ protein nanofibers. Scale bar = 240 nm. **B)** Zoom-in AFM micrograph on crosslinked nanofibers. Scale bar = 50 nm. **C)** AFM micrograph of the crosslinked DNA-Fn(10)$_{III}$ protein nanofibers, highlighting the different morphologies seen on the mica surface. Scale bar = 240 nm. **D)** Width analysis of the nanofiber in (**B**). **E)** Length analysis of the nanofiber in (**B**).

To obtain a better understanding of the intertwined filaments, a zoom-in was taken, which appeared to be two filaments that were overlapping, in a helical manner (Figure 2.15 B). Due to the overlapping, the intertwined filaments were measured to obtain more physical measurements of their interactions. The first measurement was represented by the orange line, which measures the width of the observed structure. The width measurement revealed a width of 24.9 nm (Figure 2.15 D). The width measurement is wide enough to be two filaments that are entangled, based on the width of the filaments that were measured on the previous AFM (Figure 2.13 A). In this regard, the width measure indicates a structure that is twice as wide as one individual filament. The other length measurement, represented by the yellow line, provide evidence of repeated domains and potential helicity, due to each height peak being equally spaced at 16.2 nm. The spacing closely corresponds with the length of the protein complex (~ 12 nm), indicating that the observed structure is two filaments together, crosslinked at an interval of the length of the protein complex. However, due to the crowding of the sample area, other repetitive domains could not be highlighted. If there were multiple regions that showed continuous intertwined filaments at a similar length repeat, then that would have further indicated the crosslinking of the protein nanofibers at well-defined intervals.

The same sample was scanned in other regions to potentially obtain other instances of the crosslinked filaments (Figure 2.15 C). The other micrograph revealed multiple individual filaments scattered across the mica surface with many instances of aggregation. The micrograph depicts a crowded region and lacks clear examples of crosslinked filaments. The inefficient crosslinking may be due to the length of the crosslinker. Since the crosslinker consists of a length of 50 bases, then the thermal anneal does not efficiently

provide enough thermal energy to allow for thermodynamically stable products. As a result, the observed sample might indicate fibers that are kinetically trapped. The kinetically trapped species may be due to the multi-valency of the protein nanofiber and the strength of binding between each duplex (21 bps). As the DNA crosslinker is added into solution, the DNA-protein crosslinked are immediately crosslinked without proper hybridization. As for the kinetically trapped species, these species might be intertwined filaments, intense aggregates, or even cases where the filaments are not crosslinked at all. In any case, all of these species are depicted by the AFM micrographs that were obtained from the sample.

To corroborate some of the structures seen under the AFM, the same sample was taken over to the TEM and visualized with negative staining. Under TEM, many examples were seen of large, bundled fibers, which seemed to be segmented (Figure 2.16 A). In addition to the segmentation, the fibers had a length of several microns. These lengths far exceed the lengths of the protein nanofibers without the addition of the DNA. The increase in length and due to some areas that appear to be quite straight, it is possible that the DNA handle on these protein nanofibers promote a higher stiffness and increase the ability of the protein nanofibers to grow too much longer lengths. However, lengths measurement would need to be conducted to compare the length distribution of both species.

By taking a closer look at the segmented regions of the DNA-protein nanofiber, a zoomed-in TEM micrograph revealed nicely defined bundles that are seen through the length of the nanofiber (Figure 2.16 B). The length of these bundles was measured to be

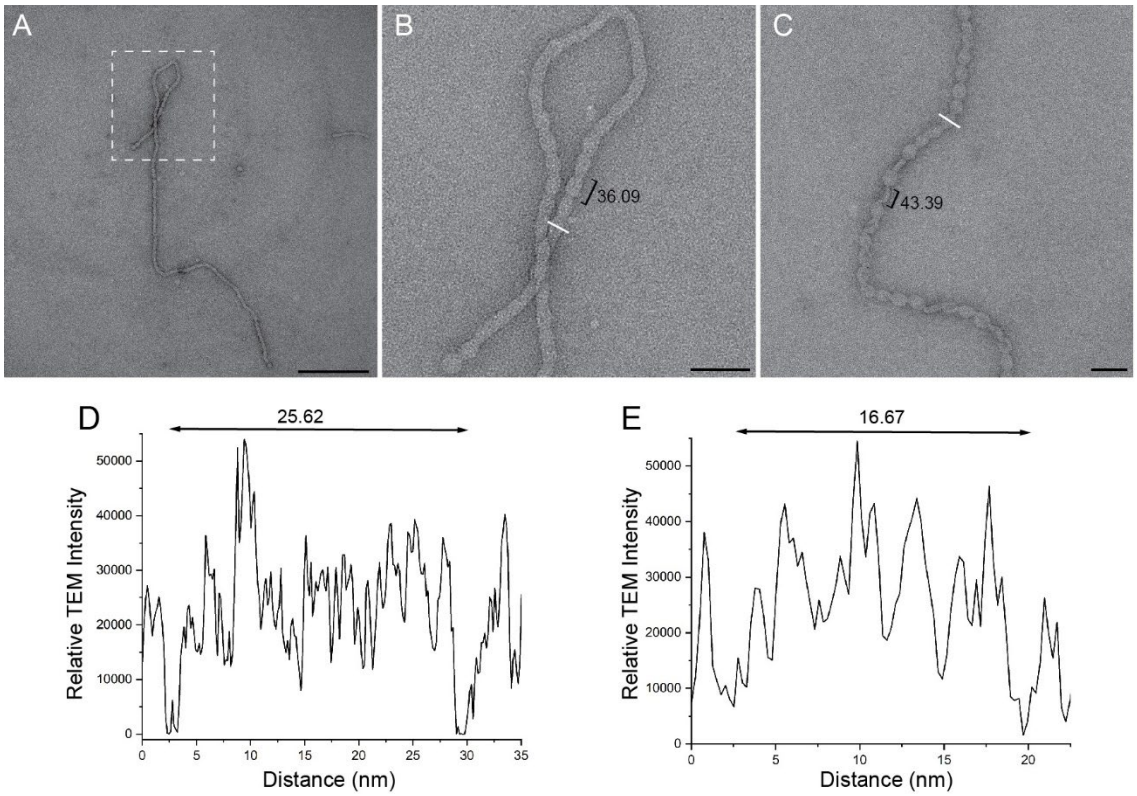

Figure 2.16. TEM analysis of the crosslinked disulfide-mediated DNA-Fn protein nanofibers. A) TEM micrograph of the crosslinked DNA-Fn(10)$_{III}$ protein nanofibers. Scale bar = 500 nm. **B)** Zoom-in TEM micrograph on crosslinked nanofibers. Scale bar = 100 nm. **C)** TEM micrograph of the crosslinked DNA-Fn(10)$_{III}$ protein nanofibers, highlighting the helicity seen in these crosslinked DNA-protein nanofibers. Scale bar = 100 nm. **D)** Width analysis of the nanofiber in (**B**). **E)** Width analysis of the nanofiber in (**C**).

36.1 nm, which is about three times the length of a single protein complex. The measurement indicates that the crosslinking is occurring at an interval of at least two protein monomers, which corresponds well with the percentage of the doped in DNA-peptide conjugate (50%). However, is it peculiar that each bundle is at a similar interval. If the peptide-DNA conjugate is doped in at 50%, the peptide would assemble and disperse in a random manner, not evenly spaced out.

In addition to the interesting interval spacing, there were regions in the bundles nanofiber that did not exhibit any bundling and remain as a straight fiber. It is unclear as

to why there would be no bundling in this region if there are two filaments are crosslinked together. In the case where two filaments are not crosslinked, there should at least be some void space in between each filament, representing two individual filaments. However, this is not what is observed. In terms of the width of the bundled protein nanofiber, the width measurement revealed a width of 25.6 nm, which corresponds well with the expected width of two individual filaments and corresponds well with the bundled filaments seen under AFM (Figure 2.16 D).

Lastly, another TEM micrograph revealed another bundled nanofiber, with an observed spacing of 43.4 nm (Figure 2.16 C). The observed bundled nanofiber also had areas where there was imparted helicity throughout the fiber, indicated by the curvature and turning of some of the individual bundles. Due to the turning of some individual bundles, there appeared to be some bundles which had a morphology with a divot or hole in the middle. Additionally, due to the turning of some of the individual nodules, some appeared to be completely on their sides, providing an area with a thinner width compared to the previously measured width of 25.6 nm. In this respect, a nodule that was on its side was measured and the measurement revealed a width of 16.7 nm (Figure 2.16 E). The width is distinctly thinner compared to the previous measurements, indicating a much wider x-axis length and a thinner y-axis width.

The observed helicity may represent a novel case of artificial helicity imparted on protein nanofibers, perhaps due to the modification of DNA. The reason for the imparted helicity is unclear but one can speculate that the helicity may be due to unfavorable electrostatic repulsion. It is possible that the dense, local negative charge on the DNA-

protein filaments, once crosslinked, becomes too unfavorable and resulting in turning of each protein monomer to minimize the repulsive electrostatic interactions. In this case, helicity may provide an avenue for such a stabilized structure. However, taking a closer look at the helical fiber, the helicity is not continuous, nor does it demonstrate specificity towards right-handedness or left-handedness. There are areas in the fiber that exhibit both right- and left-handedness, indicating lack of chirality and more of a random helicity. Due to the lack of handedness, the pitch could not be obtained through physical measurements of the TEM micrograph. Altogether, the crosslinked DNA-modified protein nanofiber yielded a novel structure, where apparent helicity is imparted to the crosslinked fiber. It is important to note that there were no observed structures that represented multiple filaments bundled together. Based on the physical measurement of these interesting fibers, it appears that the crosslinking only resulted in at most two individual filaments being crosslinked together.

To ascertain whether another DNA-protein nanofiber construct would result in a similar morphology as the DNA-FN(10)$_{III}$ nanofibers, the DNA-mCherry nanofibers were assembled and characterized in a similar manner. Similar to the FN variant, the DNA-mCherry nanofibers were assembled with Cys-P4-Paint conjugate. Once the components were allowed to incubate overnight, the sample was imaged with air-mode AFM. A wide-field AFM micrograph revealed well-dispersed nanofibers on the mica surface, where there were visible clusters of nanofibers (Figure 2.17 A). As compared to the mCherry nanofibers without the DNA modification, the nanofibers seemed more well-dispersed on the surface, which may be due to more efficient binding to the mica surface. Taking a closer look at the nature of the nanofibers on the surface, the surface was covered with the nanofibers, where

individual filaments and even filaments with larger widths were seen. The nanofibers seemed to form an extensive web-like network on the surface.

To obtain more physical measurements of the nanofibers, a width measurement was taken with respect to the white line in the AFM micrograph. The resulting measurement indicated two distinct species of fibers on the surface, where a bundled region was seen with a width of 39.8 nm and another thinner filament with a width of 13.3 nm. The thinner

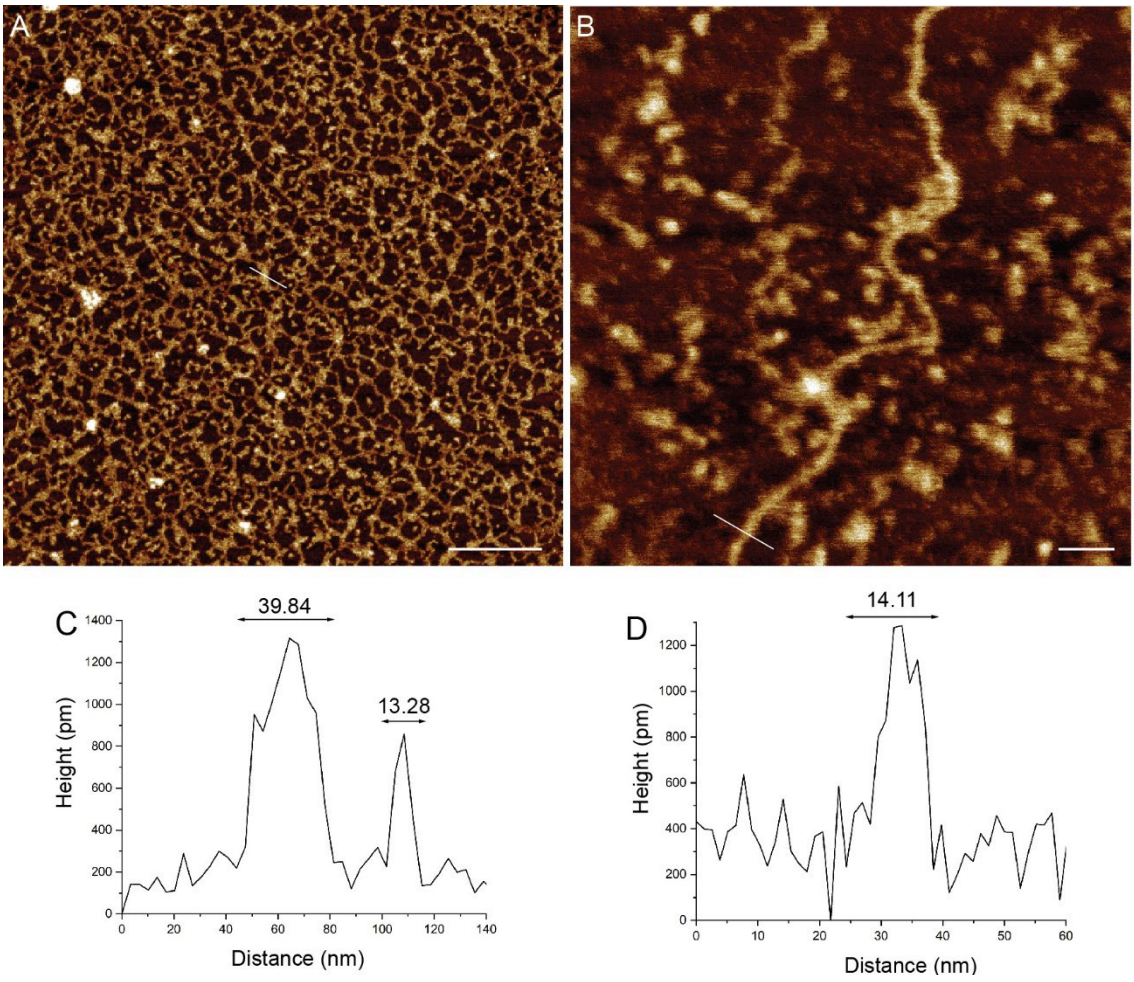

Figure 2.17. AFM analysis of the disulfide-mediated DNA-mCherry protein nanofibers. A) AFM micrograph of the DNA-mCherry protein nanofibers. Scale bar = 250 nm. **B)** Zoomed-in AFM micrograph of the DNA-mCherry protein nanofibers. Scale bar = 50 nm. **C)** Width analysis of the nanofiber in (**A**). **D)** Width analysis of the nanofiber in (**B**).

filament most likely indicates an individual filament, where the measurement closer aligns with the width that was observed for the DNA-FN nanofiber. In addition, the height profile revealed a height of 800 pm. The individual filament is a bit wider than the DNA-FN nanofiber, approximately by one nanometer. The slight change in width is derived by the larger protein building block being used in this particular system. Additionally, the large, bundled fiber was approximately three times as wide as the individual filament, indicating some potential induced-bundling due to the DNA handle on the nanofiber. Due to the bundling, the larger bundled fiber had a higher height profile, with a measured height of 1500 pm. The induced packing may be due to the negative charge on the DNA backbone where it can pack the protein in the middle of the bundle, leaving the DNA exposed on the surface of the bundle nanofiber to reduced surface charge. However, without a close look at these bundled areas, it is difficult to say why there is some induced bundling occurring in these samples.

Other scans of the same sample resulted in an AFM micrograph with a singular DNA-protein nanofiber (Figure 2.17 B). The nanofiber ranges in length surpassing several hundred nanometers and there is little curvature seen in the nanofiber. To obtain more physical measurements of the singular nanofiber, the width was measured, yielding 14.1 nm (Figure 2.17 D). This measured width is approximately three nanometers wider than the mCherry nanofiber without the DNA component. The additional three nanometers parallel the measurements in the DNA-FN measurements, where it was stated the ~3.5 nm is half the theoretical length of the DNA strand, assuming a double-stranded character. Due to the single stranded nature of the DNA strand, then ~3 nm is reasonable. Altogether, the

AFM micrographs depict the ability for the DNA-mCherry constructs to readily form nanofibers.

Due to the successful formation of nanofibers, the same sample was analyzed by super-resolution DNA-PAINT imaging. Compared to the DNA-FN nanofibers, these DNA-mCherry nanofibers were subjected to a collection of 45,000 frames, over a period of 30 min. The increase in frame account was increased to improve the signal to noise ratio, in hopes of improving the resolution of the acquired images. In addition to the increase in frame count, an internal standard was used to improve the drift correction issue that was seen with the DNA-FN DNA-PAINT images. The internal standard that was used was a rectangular origami structure, with 9 docking sites, which have been showed previously in the lab to improve drift correction. Once all the frames were acquired, the images were localized, processed and rendered to obtain a wide-field of view of the resulting DNA-PAINT experiment (Figure 2.18 A).

The resulting image revealed more fibrous-like structures, compared to the previous DNA-FN images, without the poor drift correction. Through the same, the rectangular origami standard was seen with a few localized spots, indicating suitable localization of the acquired image. In addition to the DNA origami, there were multiple nanofibers seen on the surface with lengths ranging from several hundred nanometers to a few microns in length. Throughout the wide-field image, there were multiple instances of nanofiber morphology, compared to previously obtained fluorescence images of the nanofiber. One observed nanofiber that was ~3 μm in length, which is highlighted by the white box in the micrograph. Taking a closer look at this species revealed a bundled

nanofiber, with thin striations throughout the entire length of the fiber (Figure 2.18 B). The thin striations indicate that individual filaments are bundling together, corroborating some of the bundled fibers seen under AFM. In addition, the striations revealed three distinct filaments bundled together, which further corresponds well with the AFM measurements. By taking some physical measurements of the DNA-PAINT fiber, the measurement revealed an individual filament with a width of 13.2 nm, which is in close agreement with the width that was measured for a single filament under AFM (Figure 2.18 C). As a result, both techniques indicate induced bundling of individual DNA-mCherry filaments, where the bundles contain three distinct filaments with a width of ~13 nm.

Due to the successful formation and characterization of the DNA-mCherry nanofibers, the DNA-induced crosslinking was tested with this system as well. Similarly, to the DNA-FN nanofibers, only 50% of the Cys-P4-Paint conjugate was used for the crosslinking, mainly due to material limitations. Therefore, once these samples were

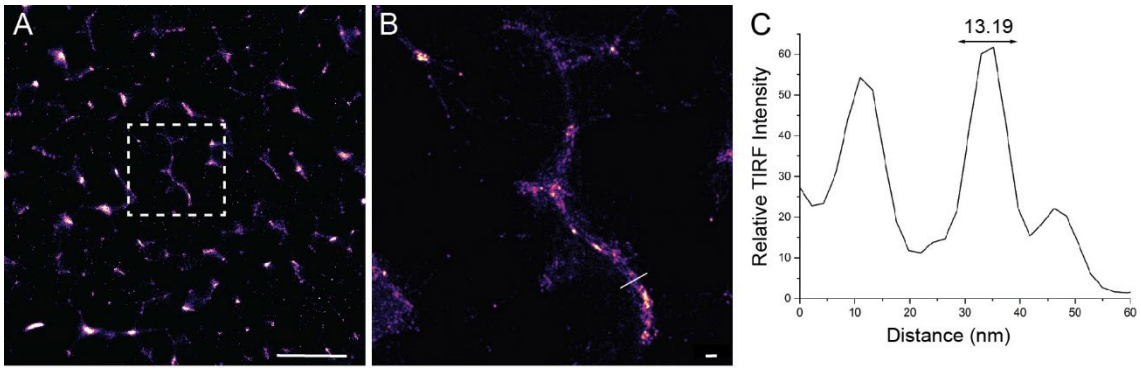

Figure 2.18. DNA paint analysis of the disulfide-mediated DNA-mCherry protein nanofibers. A) TIRF micrograph of the DNA-mCherry protein nanofibers. Scale bar = 2 μm. **B)** Zoomed-in TIRF micrograph of the DNA-mCherry protein nanofibers. Scale bar = 50 nm. **C)** Width analysis of the micrograph in (**B**).

allowed to effectively assemble overnight, the nanofibers were crosslinked with an

equimolar amount of the DNA splint and thermally annealed from 37 °C to 12 °C and allowed to rest at 4 °C until the fiber were imaged.

After the nanofibers were annealed, the sample was analyzed initially with air-mode AFM. An initial wide-field AFM scan revealed more pronounced structure with large height profiles compared to the non-crosslinked AFM micrographs (Figure 2.19 A). Throughout wide-field scan, there were also many individual filaments seen on the mica surface, exhibiting a smaller height profile compared to the initial "bundled" fibers. There was a region that showed distinct filaments clustered together. As a result, these filaments

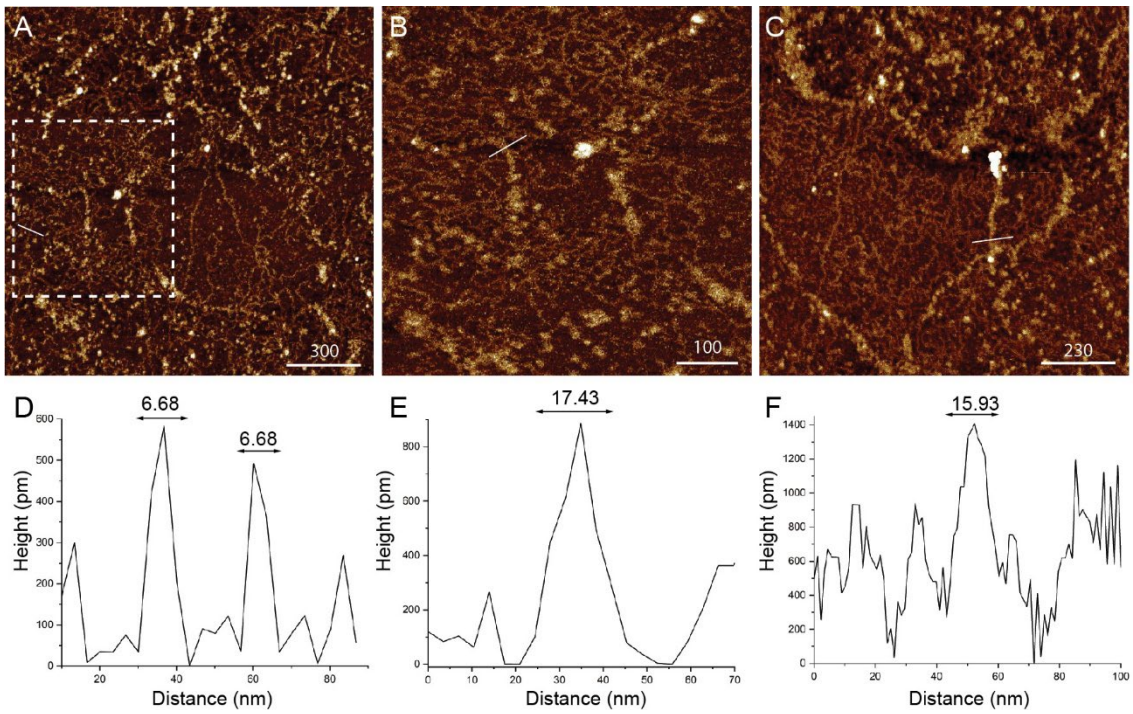

Figure 2.19. AFM analysis of the crosslinked disulfide-mediated DNA-mCherry protein nanofibers. A) AFM micrograph of the crosslinked DNA-mCherry protein nanofibers. Scale bar = 300 nm. **B)** Zoomed-in AFM micrograph of the crosslinked DNA-mCherry protein nanofibers. Scale bar = 100 nm. **C)** AFM micrograph of the crosslinked DNA-mCherry protein nanofibers. Scale bar = 230 nm. **D)**Width analysis of the nanofiber in (**A**). **E)** Width analysis of the nanofiber in (**B**). **F)** Width analysis of the nanofiber in (**C**).

were measured, where the measuring vector is represented by the white line in the

micrograph. The resulting measurement revealed two filaments with widths of 6.7 nm (Figure 2.19 D) with a height profile of about 600 pm. These nanofibers are thinner compared to the filaments measured by the previous AFM and DNA-PAINT measurement. However, these measurements closely correspond to the width of just the mCherry nanofibers (5 nm). The measurements might indicate a few fibers that are not modified with the DNA-handle, resulting in a thinner width.

Another larger bundled fiber appeared near the individual filaments that were measured. Therefore, a zoom-in scan was taken with respect to the white box in the micrograph. By taking a zoom-in scan, a caterpillar-like fiber was seen on the surface, which appeared to have some segmented regions (Figure 2.19 B). The bundled fiber was observed along with many instances of individual fibers, scattered across the mica surface. Measuring the width of the nanofiber yielded 17.4 nm, which is twice as wide as the previously measured individual filaments (Figure 2.19 E). In the case where the previously measured filaments in Fig. 2.19 D indicate the mCherry fibers without DNA, then then a bundled nanofiber would have a width of ~13 nm plus about 5 nm, taking account for the appended DNA. In this case, 17.4 nm is in good correspondence to this expected width, although it might be a bit thinner compared to the expected width. However, one thing to note is that the height profile remains the same as the individual filaments, with a height profile of about 900 pm. The height profile is slightly larger, but if these filaments were bundled, then one would expect at least a two-fold increase in the height profile.

By scanning other regions of interest, larger structures were seen on the mica surface, which deviate from the non-crosslinked nanofibers (Figure 2.19 C). The AFM

micrograph revealed many filaments scatted on the surface of the mica. However, a large fiber was seen in the middle of the micrograph, which has a comparatively wider width and a more pronounced height profile. In addition to the pronouced features of this fiber, the fiber semed to span the entire length fo the micrograph, starting from the bottom middle and then spanning to the top right of the micrograph, which would indicate a length of ~1.5 μm. To probe this structure more closely, a width measurement was taken in respect to the white line in the micrograph.

The resulting width profile revealed a distint peak with a width of 15.9 nm, which is in close agreement with the previously measurement fiber in Fig. 2.19 B. Once again, the measurement can take into account the width of the individual protein nanofiber with the width of the DNA linker. In addition to the larger width, the fiber has a height profile of 1400 pm, which is close to a three-fold increase in the height profile compared to the measured individual filaments, indicating a certain degree of bundling, resulting in the observed height increase.

To observed these changes in structural morphology, the sample was taken over to the TEM. Upon deposition of the sample on the TEM grid and with subsequent negative staining, the TEM micrographs revealed segmented and bundled fibers, similar to the structures seen in the crosslinked DNA-FN fiber sample (Figure 2.20 A). The TEM micrograph reveals a fiber, where both segmentation *and* curvature are seen. The curvature in the micrograph indicates possible helicity, which would further confirm the imparted helicity due to the DNA crosslinker. To take a close examination at the bundled fiber, a zoom-in was taken in respect to the white box in the micrograph.

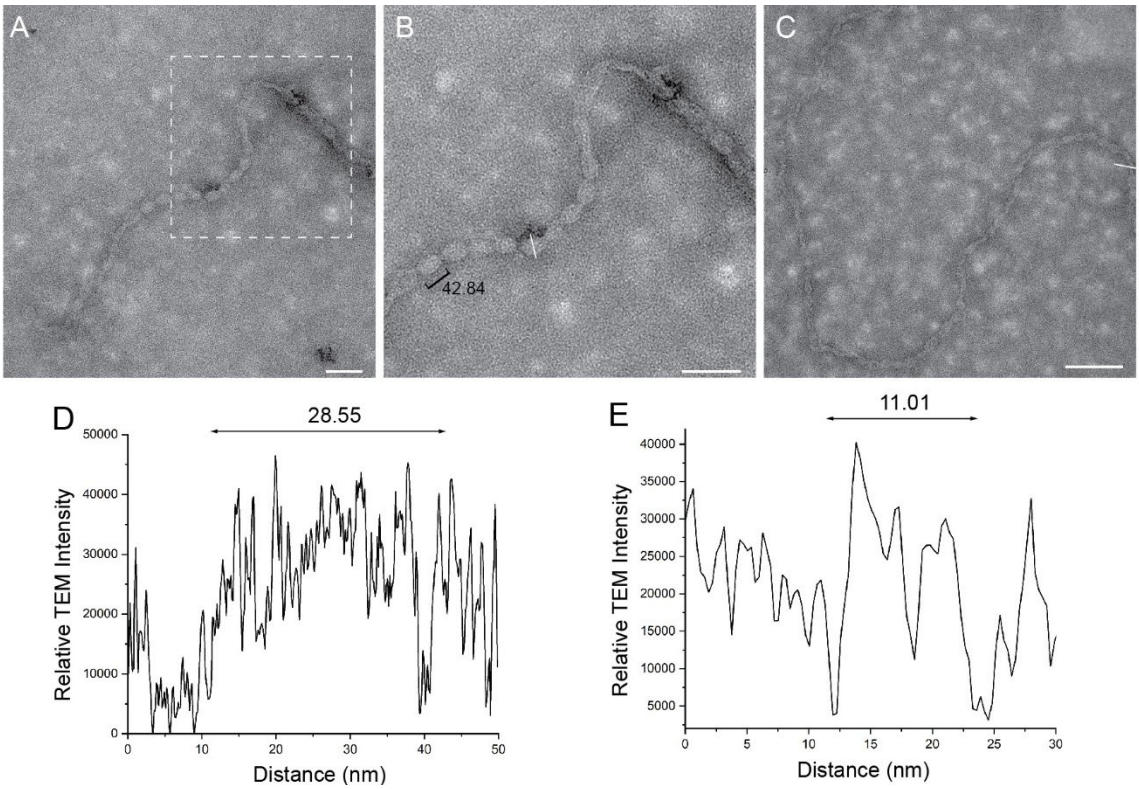

Figure 2.20. TEM analysis of the crosslinked disulfide-mediated DNA-mCherry protein nanofibers. A) TEM micrograph of the crosslinked DNA-mCherry protein nanofibers. Scale bar = 100 nm. **B)** Zoom-in TEM micrograph on crosslinked nanofibers. Scale bar = 100 nm. **C)** TEM micrograph of the crosslinked DNA-mCherry protein nanofibers, highlighting the helicity seen in these crosslinked DNA-protein nanofibers. Scale bar = 200 nm. **D)** Width analysis of the nanofiber in (**B**). **E)** Width analysis of the nanofiber in (**C**).

The zoom-in revealed the bundling to a higher degree, where the bundling was measured to occur at an interval of 42.8 nm (Figure 2.20 B). This interval, based on the width of the protein complex, represents at least three repeats of the protein complex, which would make sense due to the 50% DNA modification of this specific sample. To further corroborate the crosslinking of two individual filaments, the width of the bundle was measured. The width measurement revealed a width of of 28.6 nm, which can encompass the width of two individual filaments and corresponds well with the previously measured bundles fiber for the FN system (25.6 nm). The discrepancy between the DNA-FN bundled fiber and the DNA-mCherry bundled fiber is about 2.9 nm, which can accomdate the

change in width for the size of FN compared to the size of mCherry. Although the measurements deviate slightly, these relative conistency in morphology of these bundled fibers with two completely different proteins, prepared on different days, using the same peptide-DNA linkers is striking.

Aside from the width measurement of the bundled fibers, the length of each of these segmented areas were measured to have an average length of 42.8 nm. Based on the length of the protein complex, the segmentation measurement indicates that the bundling is occuring roughly every three protein units. This spacing could be accounted for by the 50% incorporation of the Cys-P4-PAINT conjugate. The spacing is also longer compared to the segmented spacing seen in the DNA-FN system, where the spacing was 36.09 nm. However, the difference in segmentation length is small (6.75 nm) and can be reasonably accounted for the difference in size of the proteins used.

To get a better understanding of the structural morphology of the DNA-protein bundles fibers, another area of the grid was imaged. A large, bundled nanofiber was discovered with a length of ~3.3 μm. The nanofiber exhibited similar segmented morphology, indicating that this type of unique morphology is consistent with the previously obtained images. There were also multiple instances of curvature within the nanofiber, reinforcing the idea that the DNA-induced crosslinking imparts some artificial helicity to these DNA-protein nanofibers. Additionally, there was a portion of the nanofiber that seemed to be completely on its side. Therefore, a measurement was taken to obtain a width measurement. The width measurement of each nodule on its side was measured to be 11 nm. From this, the dimensions of the bundled fiber is 28.5 nm x 11 nm x 3.3 μm.

The width measurement is actually smaller than the width of the DNA-FN bundled nanofibers (16.7 nm), which is a bit odd, due to the large protein components but since the exact angle of measurement cannot be determined, than it is difficult to say that the width measurments truly capture the width of the nanofiber.

Overall, due to the consistency of the morphology of the bundled nanofibers for both the FN and the mCherry variants, appears that the DNA crosslinking provides a way to introduce hierarchical assembly into these hybrid nanofiber systems. From the morphologies that are seen, this approach has allowed for artificial helicity to be incorporated into a protein-based system, which represents a new category of hybrid biomolecular building materials. Future studies will explore other DNA crosslinkers, as well as reversibly controlling hierarchical nanofiber assembly via strand displacement.

2.3 Conclusion

The results highlighted in this chapter demonstrate the ability of the coiled coil motif to generate protein nanofibers on a micrometer scale. The approach successfully implemented two distinct coiled mechanisms for protein polymerization, where synthetic cysteine-modified peptides and the complementary coils directly fused on to another protein domain both resulted in protein assembly into long nanofibers. These mechanisms allowed for the polymerization of four distinct proteins, three of which are fibronectin domains, which will in turn enable a wide range of bioactivity. Under AFM and TEM, the nanofibers are well-dispersed but are subjected to surface effects from either the mica or the copper grid which can either distort the morphology or promote aggregation. Cryo-EM grid enabled visualization of dispersed nanofibers in solution. Lastly, these systems were

also shown to be amendable to chemical and biochemical "triggers" for their depolymerization.

To extend the functionality of these protein nanofibers, the KE-Cys peptide was further functionalized with a DNA handle. The addition of the DNA handle was successfully conjugated to the peptide and allows the protein nanofibers to be decorated with a DNA handle. The DNA decoration facilitated the super-resolution imaging of these fibers using DNA PAINT and allowed for these structures to bundle in a hierarchical manner. Ultimately, these self-assembled protein nanofibers systems demonstrate methods to develop long, reversible, and modular protein nanofibers. The system has the capability to be implemented in a biomaterial platform to probe the effects of different bioactive proteins domains, biomechanical stiffness, and hierarchical assembly through DNA.

2.4 Methods and Materials

Plasmid Construction and Mutant Library Design. All primers and oligonucleotides were purchased from Integrated DNA Technologies, Inc (Coralville, IA). The gene for P3-FN(10)-EK fusion protein was inserted in the pQE-80L plasmid by Gibson Assembly, a standard molecular cloning technique.[154] The primers used for the Gibson assembly are denoted in Appendix A S2. The constructed plasmid was transformed into *E. coli* DH5α competent cells, from New England Biolab Inc. USA (Rowley, MA) for plasmid amplification. The plasmids were purified via a mini prep by Qiagen (Hilden, Germany). After plasmid purification, all the mutant constructed were verified via Sanger DNA sequencing. The correctly sequenced plasmid was then transformed into BL21 (DE3) cells, from New England Biolab Inc. (Rowley, MA) and then used for protein expression. The

transformed cells were grown in 1x Luria Bertani (LB) broth at 37 °C containing 100 g/mL carbenicillin to an OD600 = 0.6-1.0. Once the optimal OD level was reached, the culture was then induced with 1.0 mM isopropyl-D-thiogalactopyranoside (IPTG) (SigmaAldrich, St. Louis, MO) and allowed to grow overnight at 18 °C.

Protein Purification and Characterization. The overnight culture was harvested by centrifugation at 4200 rpm for 10 min. The cell pellets were resuspended in 15 mL of lysis buffer containing 25 nM Tris pH = 8.0, 150 mM NaCl and 0.1 mM EDTA, and lysed using sonication. In addition, 100 µL of 100 mM PMSF, 50 µL DNase l (10 mg/mL) and 50 µL lysozyme (10 mg/mL) were added to the lysis solution. Following sonication, the cell lysate was centrifuged at 15,000 rpm for 30 min to remove cell debris. The supernatant was loaded onto a Ni-NTA 1 mL HisTrap HP column (GE Healthcare, USA) and rinsed with 10 column volumes of 50 mM Tris pH = 8.0, 300 mM NaCl, and 10 mM imidazole to removed nonspecifically bound molecules. Each mutant protein was eluted with a 40-column volume stepwise gradient, using an elution buffer composed of 50 mM Tris, pH = 8.0, 150 mM NaCl, and 500 mM imidazole. The stepwise gradient consisted of 10 column volumes of 10% of the elution buffer and then a linear gradient from 10%-100% elution buffer over 30 column volumes. The peak fractions were then analyzed via SDS-PAGE, and the fractions containing our protein-of-interest were consolidated and placed in a 10 kDa molecular weight cutoff (MWCO) dialysis membrane and dialyzed overnight at 4 °C against 1 L of 50 mM Tris-HCl buffer with 0.5 mM EDTA, pH = 8.0. The resulting sample was then concentrated using an Amicon-10 kDa (Millipore Sigma, USA) cutoff filter.

Peptide Synthesis and Characterization. Peptides were obtained using solid phase peptide synthesis (SPPS) on a CEM Liberty Blue instrument. Synthesis was performed on a solid phase Rink-Amide resin (0.78 mmol/g) at a 0.1 mmol scale, using a standard Fmoc protocol and deprotected in 20% piperidine in DMF. Amino acids, coupling agents, N,N'-Diisopropylcarbodiimide (DIC) and Oxyma, were added in a 10-fold molar excess. Crude peptides were cleaved by shaking the resin by in a solution containing trifluoroacetic acid (TFA), triisopropylsilane (TIPS), and water in a ratio of 95:2.5:2.5 for 3.5 h. The resin was washed with TFA and concentrated under nitrogen. The solution was then added to 40 mL of cold diethyl ether to precipitate the peptide. The solution was centrifuged at 4200 rpm for 10 min, the supernatant was removed, and the pellet was allowed to dry overnight. The dried pellet was dissolved in a mixture of water and acetonitrile (50:50) and 0.1% TFA. Peptides were purified via reverse phase chromatography on a Waters HPLC using a Phenomenex column with C18 resin. A linear gradient was generated using water/acetonitrile + 0.1% TFA, from 10% to 100% acetonitrile over 50 minutes. Peak fractions were collected based upon their absorbance at 230 nm and tested for purity by MALDI-TOF mass spectrometry on a Bruker Microflex LRF MALDI using α-cyano-4-hydroxycinnamic acid matrix (Sigma). Pure fractions were pooled and lyophilized, and peptides were stored at -20 °C until use.

Protein Nanofiber Assembly Using Peptide Linkers. The fusion protein was added to the peptide linker at a 1:1 molar ratio in a 1x phosphate buffer at a pH = 8.0. The unannealed samples were allowed to incubate on the benchtop overnight without any additional perturbations. For the annealed samples, the annealing protocol consisted of incubating the sample at 37 °C for 10 minutes and then a gradual decrease to 12 °C, with a ramp rate of

0.5 °C/30 min. Once the ramp was completed, the sample was incubated at 4 °C until the sample was ready for imaging.

Protein Nanofiber Assembly Using Cys-Coils. The fusion protein was added with the Cys-peptides at a 1:1 molar ratio in a 1x phosphate buffer at a pH = 8.0. The samples were allowed to incubate on the benchtop overnight without any additional manipulation before imaging.

Protein Nanofiber Assembly Using The Protein Complement. The fusion proteins were mixed at a 1:1 molar ratio in a 1x phosphate buffer at a pH = 8.0. The samples were allowed to incubate on the benchtop overnight without any additional manipulation before imaging.

Atomic Force Microscopy (AFM) Characterization. All AFM micrographs were collected within 24 h of sample preparation. AFM micrographs were captured on a Veeco DI MultiMode V instrument in air using scan assist mode with SCANASYST-AIR tips (Bruker). 2 µL of sample were deposited on freshly cleaved mica followed by the addition of 2 µL of 0.2 M NiCl and incubation for 30 seconds. Next, 56 µL of 1x 50 mM Tris, pH=8.0 was added and the sample was allowed to incubate for 3 mins. The buffer was blown off and washed with 60 µL of Nanopure water to remove excess salts.

Transmisison Electron Microscopy (TEM) Characterization. All TEM micrographs were collected within 24 h of sample preparation. 5 µL of the protein nanofibers were adsorbed onto a glow discharged formvar stabilized carbon type-B, 400 mesh copper grid (Ted Pella, 01814-F), at a concentration of 500 nM, and allowed to incubate for 2 mins. The buffer was wicked off, washed twice with 5 µL of 50 mM Tris, pH = 8.0 and quickly

wicked off. Lastly, the grid was stained twice with 5 μL of a 2% uranyl acetate stain for 20 s and quickly wicked off. The samples were imaged on a Talos L120C TEM with 120 keV.

CHAPTER 3

INTEGRATION OF SELF-ASSEMBLED PROTEIN NANOFIBERS INTO A BIOMATERIAL SCAFFOLD

3.1 Introduction

One of the major goals of regenerative medicine is to replace and repair damaged tissue with functional engineered tissue.[158-160] The success of engineered tissue *in vitro* relies on synergistic relationships with viable cell types, synthetic matrices, and a multitude of biomolecular and biomechanical cues.[161-163] Ideally, cells are obtained from patients, but cell cultures from human origin remains a challenge due to accessibility and life span.[164] To overcome this challenge, stem cells have been a promising therapeutic avenue. MSCs have been rigorously studied due to their extensive self-replication and their ability to differentiate into osteoblasts, chondrocytes, adipocytes, and nerve cells with various artificial and natural matrices.[165-167] The successful use and differentiation of MSCs is heavily dependent on the biomechanical cues of the matrix as well as the spatiotemporal display biochemical cues.[168, 169]

To emulate the native ECM of various therapeutic cell lineages, 3D artificial niches have been developed through biomimetic hydrogels.[170-174] This focus to more complex and user-defined biomaterials has been due to large influence of biomaterials to regulate and dictate stem cell fate.[175] These specific factors include biomaterial stiffness, surface adhesion, and biochemical cues, amongst others.[176-178] All of these factors compose the stem cell microenvironment, and it is an active area of research to discover how each of these factors control stem cell fate.[179, 180] Key focuses of the stem cell microenvironment have been on secreted biochemical signals, such as growth factors,[181] cell-to-cell

interactions, mediated through proteins such as β-catenin,[182, 183] and lastly, through integrin binding to the extracellular matrix.[184, 185] As a result, many avenues for biomaterial development can be studied to obtain greater insight on how to control stem cell differentiation.

To focus on one of the aspects of the stem cell fate, stem cell interactions with engineered extracellular matrix have shown significant progress. However, many biomimetic hydrogels remain limited in their biochemical and biomechanical complexity which can result in lack of reproducibility and non-user defined differentiation. Hyaluronic acid (HA) is a promising hydrogel scaffold due to its biological relevance and chemical tunability.[186-189] It can also be crosslinked by functionalizing it with norbornene groups (to yield "NorHA"), via radical-initiated thiol-ene click reactions, which can encapsulate cells while maintaining their bioactivity. [178, 190, 191] Due to the versatility of the photopolymerization process of NorHA, the biochemical complexity can be tuned in a spatiotemporal manner. Through this process, a range of biochemical complexity can be achieved but this process has remained limited to bioactive peptides. Therefore, a more biomimetic approach would involve the introduction of more protein-based components.

To increase the protein content of a biomaterial, the previous nanofiber approach described in Chapter 2 was incorporated in to the NorHA system. Through this approach, we combine the benefits of the NorHA (e.g. biocompatibility, bulk material synthesis, control of synthesis) while incorporating a self-assembled, bioactive, protein nanofiber to impart novel functionality to cells therein. Due to the ease of radical photopolymerization, the terminal ends of the protein nanofiber system, mediated through disulfides, can be

covalently tethered to the NorHA scaffold, allowing for protein nanofibers to be crosslinked within the scaffold. In addition, due to the reversibility of the nanofiber system, the assembly of the nanofibers can be temporally controlled, through chemical and biochemical inputs. Lastly, due to the benefits of photopolymerization, the protein nanofibers can be defined, allowing for further spatial complexity to be achieved. Altogether, the incorporation of the self-assembled protein nanofibers systems into the photocrosslinked NorHA scaffold allows for the introduction of bioactive protein domains, that can be controlled in a spatiotemporal manner. Ultimately, this approach paves the way for engineered biomaterials to start to rival the biochemical and biomechanical complexity of the ECM.

3.2. Results and Discussion

3.2.1 Photochemical Integration of Self-Assembled Protein Nanofibers into a Hyaluronan Scaffold

To create an ECM biomimetic biomaterial, the protein nanofibers that were developed were incorporated into a hyaluronan-based scaffold. Hyaluronan-based biomaterials have seen a lot of recent advances in biomimetic biomaterials due to the natural presence of hyaluronic acid in the ECM and the ease of functionality.[186-189, 191] From this, a norbornene-modified hyaluronan (NorHA) scaffold was used to take advantage of the terminal cysteine residues of the protein nanofibers.

In this fashion, the terminal cysteine residues can be conjugated to the NorHA scaffold utilizing thiol-ene photoclick chemistry (Figure 3.1A).[190] Due to the high density of reactive norbornene functional groups on the HA scaffold (~92%, in material provided

by the Holloway lab), additional crosslinkers, such as DTT, can be used to modulate the mechanical stiffness of the platform. In addition, due to the use of photochemistry,

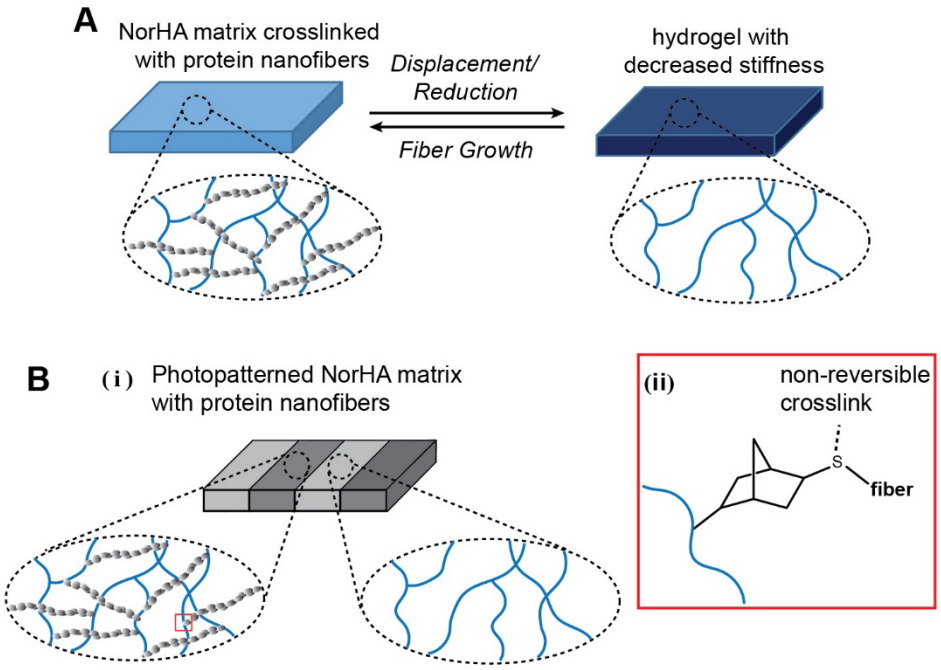

Figure 3.1. Nanofiber incorportation into a hyaluronan scaffold. A) Self-assembled nanofibers incorporated into a NorHA scaffold, with the removal of the nanofiber crosslinks. **B) (i)** Photopatterned nanofibers to allow for a spatial display of bioactive protein nanofibers. (**ii**) Zoom-in on the non-reversible, chemical modification of the NorHA matrix with a thiol-coil handle.

nanofibers can be photopatterned to create a spatial display of bioactivity (Figure 3.1B).

The first attempt to incorporate the protein nanofibers was to create an entire hydrogel with the fibers dispersed throughout the NorHA scaffold. The NorHA was dissolved with the protein nanofibers in a PBS solution at a 0.4 mg/mL (0.4 wt%) and photocrosslinked for 4 min in a silicone mold. The resulting gel was firm enough to manipulate but appeared to still be fairly soft (Figure 3.2 A). The mechanical properties of the resulting NorHA gel were measured using a compression test, and from the strain vs. stress curves, the gel exhibited a storage modulus of 6.8 kPa (Figure 3.2 B,E). In comparison, the addition of DTT (0.1 equivalence relative to the norbornene functional

groups) resulted in a much stiffer gel, with a higher compression modulus of 10.3 kPa (Figure 3.2 D-E). From these two different gel compositions, the approach highlights a method to modulate the mechanical stiffness while keeping the amount of bioactive protein in the gel the same.

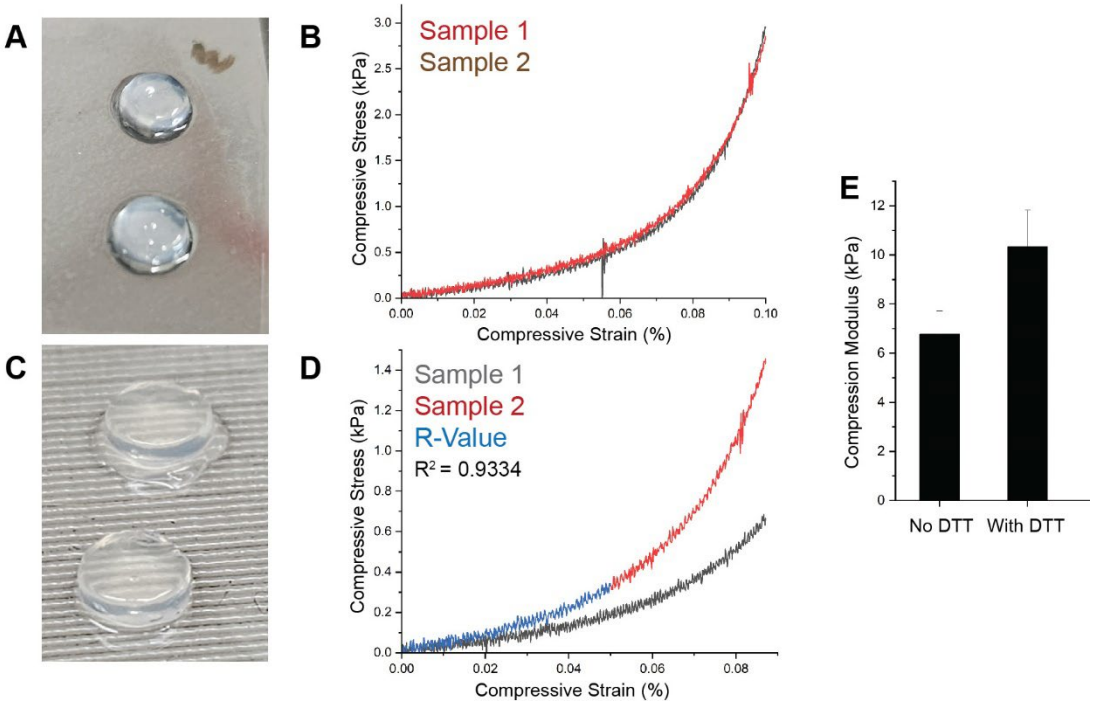

Figure 3.2. Mechanical analysis of the Fibronectin-NorHA hydrogels. A) Image of protein nanofibers-NorHA hydrogel. **B)** Compressive stress vs strain curve of the gel in panel (**A**). **C)** Image of the DTT-doped protein nanofiber-NorHA hydrogel. **D)** Compressive stress vs strain curve of the gel in panel (**D**). **E)** The compression modulus of the hydrogels in panel (**B, D**).

To expand the versatility of the protein nanofibers, the disulfide-linked mCherry fibers were incorporated into the NorHA platform. This protein makes it particularly easy to visualize the fiber incorporation using fluorescence microscopy. In this respect, the first sample that was tested consisted of mCherry protein nanofibers with NorHA and without the addition of DTT (Figure 3.3 A). This approach highlights the ability of the disulfide-mediated protein nanofiber to photochemically crosslink the norbornene groups on the HA. We hypothesized that if the free terminal cysteines are exposed, then the photochemically

crosslinking of the thiol groups to the norbornene groups would allow for allow for efficient crosslinking to the scaffold, due to the length of the overall protein nanofibers. Through this photoinitiated process, the protein nanofibers can be covalently embedded, allowing for a tunable and reversibly fibrous biomaterial. In addition, this process evades the use of using small molecule thiol compounds to allow for the gelation of the NorHA scaffold. The added benefit of avoiding the use of the small molecule dithiol also prevents the reduction of the disulfide-mediated nanofibers. Through mechanical testing, such as compression testing and rheology, as well as fluorescent microscopy, the extent of crosslinking and the spatial display of the nanofibers can be explored.

Using a concentration of 15 μM of the mCherry monomers, the protein nanofibers were mixed with the lyophilized NorHA and gently vortexed to allow for complete solvation of the NorHA. Afterwards, photoinitiator I2959 was added to the solution. 32 μL of the solution was added into 30 μL silicone wells for the formation of disc-shaped gels. The crosslinking process involved irradiation of the gels with UV light, for 4 min, at a lamp power of 10 mW. After the exposure to UV light, the gels were removed from the mold and inverted on their respective coverslips to visually determine the structural stability of the nanofiber gels. Upon removal, the gels were visibly pink, due to the native color of the mCherry proteins, and were much softer and rounder compared to the DTT-crosslinked NorHA hydrogels (Figure 3.3 A). Due to the color retention in the resulting gels, it can be concluded that the nanofibers were physically captured within the NorHA scaffold. Due to the relative stability of the nanofiber gels, the mechanical properties of the gels were tested.

Initially, the gels were probed using a mechanical compression tester. The robustness of the gels allowed for facile placement of the gels on the instrument. Four of the same sample gels were tested, monitoring their strain vs. stress (Figure 3.3 B). Out of the four samples, three of the gels resulted in similar curves, stopping at a similar stress percentage, at about 0.08% - 0.11%. The resulting compressive stress that was recorded by the instrument ranged from the lowest of about 3 kPa to the highest value of about 12 kPa.

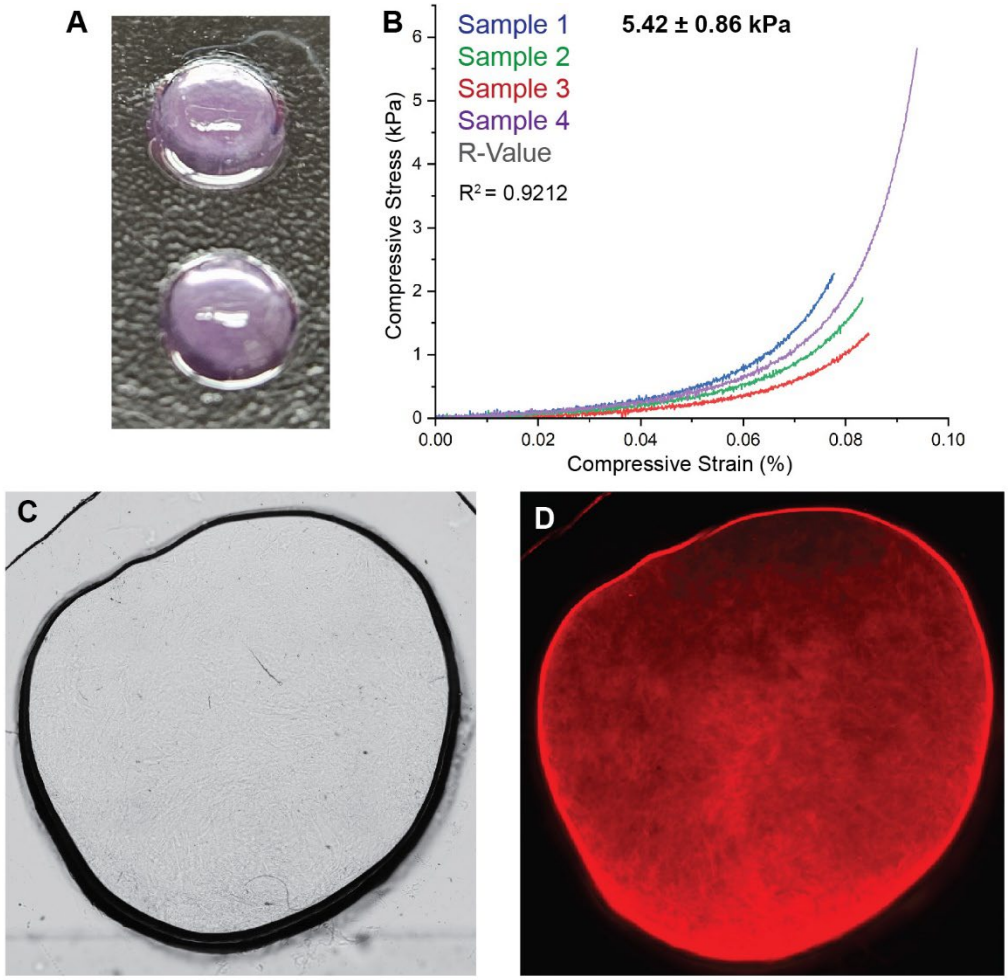

Figure 3.3. Incorporation of fluorescent nanofibers into the NorHA scaffold. A) Image of protein nanofibers-NorHA hydrogel. **B)** Compressive stress vs strain curve of the gel in panel (**A**). **C)** Bright field microscopy image of the gel in panel (**A**) at a magnification of 4x. **D)** Fluorescence microscopy image of the gel in panel (**A**) using the TRITC channel at a magnification of 4x.

The were two samples that resulted in measured compressive stress at about 6 kPa. Upon

measuring the stress vs. strain curves, we processed data to obtain the specific compression moduli for each of the gels and obtained an average value of 5.4 ± 0.9 kPa. The resulting modulus of the mCherry proteins nanofiber gels crosslinked with the NorHA scaffold, *without* the addition of DTT, resulted in a similar modulus to the fibronectin fiber gel from Figure 3.2.

After the mechanical testing of these gel samples, the samples were examined by fluorescence microscopy to monitor the spatial distribution of these nanofibers. Due to the inherent fluorescence of these protein nanofibers, fluorescence microscopy can be used to monitor the protein incorporation of these samples, which is not nearly as straightforward as for the fibronectin variants. Under bright field imaging, the gel looked uniform without any large blemishes that would interfere with fiber incorporation (Figure 3.3 D). To obtain a better understanding of the spatial distribution of the protein nanofibers, the gel was analyzed using the TRITC channel. Under the TRITC channel, the gel displayed well-distributed fluorescence, indicating that the sample did not extensively aggregate, of the fluorescent nanofibers (Figure 3.3 E). On the fluorescence micrograph, there are regions of high fluorescence intensity and areas with lower fluorescence. The disparity seen in the fluorescence signal may be due to uneven distribution of the nanofibers in the gel which may arise from the viscosity of the pre-gel solution precluding complete mixing.

To obtain better control of the distribution of the protein nanofibers in the gels, a second sample type was fabricated, comprised of a "base" layer composed of NorHA crosslinked with DTT and then a top layer that was composed of the mCherry nanofibers and NorHA, without the addition of DTT. Through this manner, the nanofibers can remain

localized towards the top of the gel. In addition, the use of a base may even modulate the mechanical properties of the hydrogel by controlling its crosslinking via DTT concentration. The fabrication involved creating a solution of dissolved NorHA, DTT, and I2959, and allowing this initial solution to crosslink into the mold with 4 min of UV irradiation. After the initial gel was formed, a solution of the mCherry nanofibers, NorHA, and I2959 was added on top of the gel and crosslinked for an additional 4 min. After this second irradiation, the gels can be removed from the mold and kept on the glass coverslip.

The resulting gel with its stiffer foundational gel was a much more stable cylindrical material, exhibiting far better robustness compared to gels made with the protein nanofibers alone (Figure 3.4 A). Due to the two-layer design, the photograph reveals a top "base" layer, with a translucent, cloudy color to it, with a bottom pink layer, due to the color of the nanofibers embedded into the gel scaffold. These gels were visually stiffer compared to the first mCherry gels, making them appear taller than the gels in Figure 3.3 A. After these gels were made, compression testing was performed to determine the compression modulus of the two-layer system. The measurements revealed better reproducibility compared to the previous system (Figure 3.4 B). The compressive strain ranged from 0.12% to 0.16% indicating a larger change in length of the material upon the compressive stress. In addition, the compressive stress that was obtained from these values ranged from 13 kPa to 17 kPa, highlighting a much stiffer stress range compared to the previous system. The higher compressive stress indicates the ability for the dual-layer material to withstand a higher compressive strain, with the respective strain, before mechanical failure. Through these strain vs. stress curves, the sample type resulted in a compression modulus of 11.1 ± 4.00 kPa. This measured compression modulus represents more than a two-fold increase

in the compression modulus compared to just using the protein nanofibers to crosslink the NorHA. The increase in compression modulus is likely due to the addition of the DTT crosslinked bottom layer, allowing for a higher compression modulus due to an increase in crosslinking in one of the layers. The increase in stiffness highlights how these two layers result in synergistic mechanical properties, allowing the lower, stiffer layer to affect the compression modulus of the top, softer layer, whereas the top layer provides the bioactive protein nanofibers.

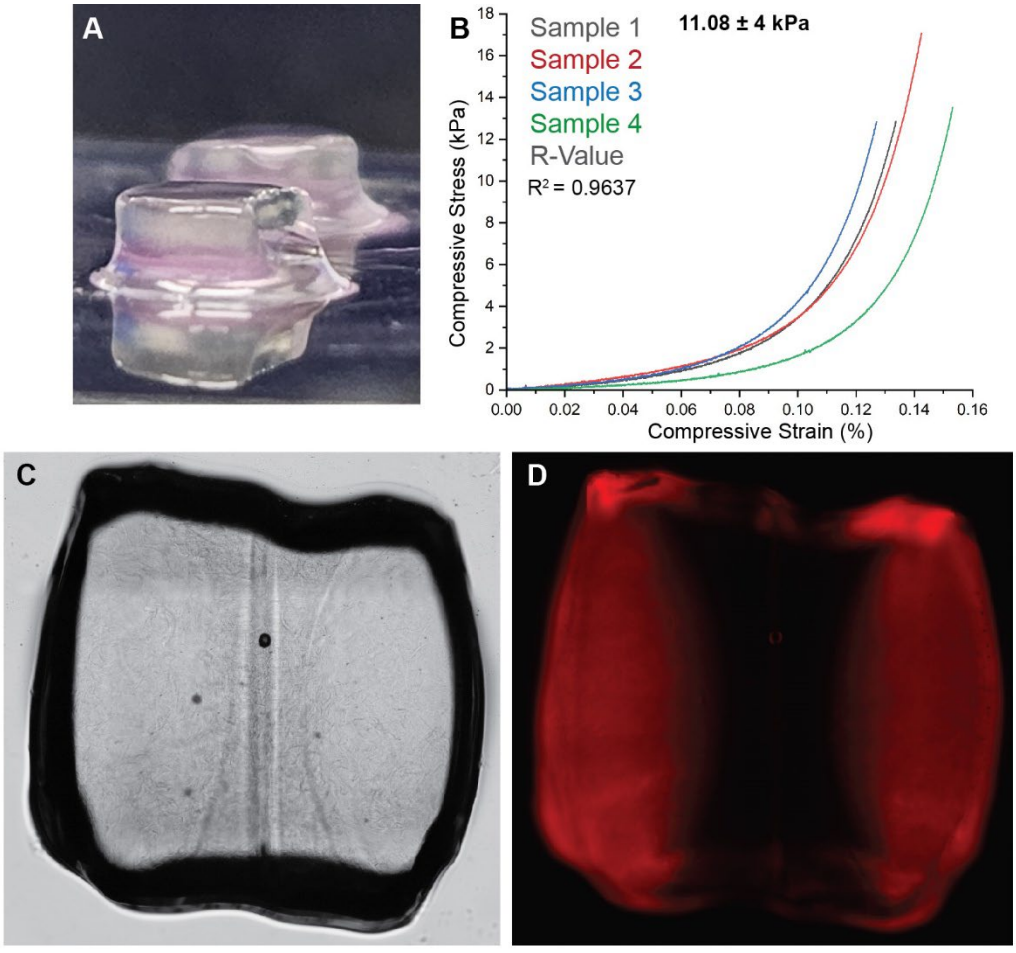

Figure 3.4. Two-layer fabrication of fibrous mcherry-NorHA gels. A) Image of the two-layer protein nanofiber-NorHA hydrogel. **B)** Compressive stress vs strain curve of the gel in panel (**A**). **C)** Bright field microscopy image of the gel in panel (**A**) at a magnification of 4x. **D)** Fluorescence microscopy image of the gel in panel (**A**) using the TRITC channel at a magnification of 4x.

After performing the mechanical testing, the gel samples were analyzed using a fluorescence microscope the probe how well the layering was and if the sample was truly partitioned into two specific NorHA compositions. The layering was imaged after cutting the gel in half to obtain a cross-section of the material, where the non-fibrous layers were pushed together and imaged. For the dual-layered sample type, under bright field, there was a clear line dividing the DTT and non-DTT crosslinked layers (Figure 3.4 D). There was a meniscus partitioning the DTT-crosslinked layer from the fibrous NorHA layer. The meniscus that separates these two layers may be due to surface tension collapse when the first layer was photocrosslinked. If the surface tension is high enough, the surface of the DTT-crosslinked layer would collapse to form a "well". Due to this surface collapse, the introduced fibrous layer should fill in the void and allow for that meniscus to be seen and trapped during photocrosslinking. There was some bright-field diffraction of light, which may be due to the fibers in the top layer, however, these diffraction spots were visible throughout the gel, indicating that these diffraction lines are derived from the NorHA scaffold.

To obtain a better understanding on the dual-layered composition, the gel was analyzed using the TRITC channel in the fluorescence microscope. Under fluorescence imaging, there were two distinct layers that were fluorescent, whereas the bottom non-fiber layers didn't exhibit any fluorescence and very little bleed through (Figure 3.4 E). In addition, the meniscus that was observed under bright-field imaging was also seen, reinforcing the idea of surface collapse, which is then filled in by the top layer. The layer also displays good dispersion of the fluorescent fibers throughout the top layer. There are not many areas that exhibit little fluorescence or areas that exhibit high fluorescence,

indicating that this approach can provide a means to display highly localized nanofibers on the surface of a NorHA gel. The better distribution of the fibers may be due to the smaller volume needed for gelation. Due to the smaller volume, simple vortexing or pipetting can provide a means for the nanofibers to distribute well in solution. From the fluorescence image, the results show that the fibers can be well layered and covalently trapped to a layer that results in little bleed through to the bottom layer due to diffusion.

Lastly, to further localize the protein nanofibers in the NorHA gel scaffold and to modulate the mechanical properties of these fibrous gels potentially further, another sample type was devised. This new sample type consisted of a bulk NorHA gel, crosslinked with DTT while a solution of protein nanofibers is deposited on the surface of the gel. In this fashion, the immediate surface can display a mesh of protein nanofibers, without the fibers being embedded in a gel scaffold, allowing for complete interactions between the fibers and the cell of interest. This approach also reduced the amount of protein nanofibers that needs to be added, since only a thin layer (sufficient for cell adhesion) is needed.

The fabrication of the gel involved 32 μL of a NorHA solution, DTT, and I2959. An entire gel was UV irradiated for 4 min to form a stiff gel. Once the base of the gel was formed and still in the silicone mold, the coverslip was removed and a solution of the mCherry nanofibers was deposited on the surface. Due to the size of the gels, 5 μL of the protein nanofibers at a concentration of 15 μM was deposited on the surface. Following deposition, the gel was further UV irradiated for 4 mins at a power of 10 mW. The resulting gels were removed from the mold and kept on the glass slide for digital imaging.

The gels appeared much stiffer compared to the two previous sample types and there was no visible pink layer, indicating the lack of a bulk layer incorporating mCherry nanofibers (Figure 3.5 A). These gels were immediately tested using a compression tester. The strain vs. stress curve revealed that each of these gel samples behaved similarly and were consistent (Figure 3.5 B). The recorded strain % of these samples ranged from 0.14% to 0.16%, representing a narrow range of strain percentage. The corresponding compressive stress that was recorded ranged from 80 kPa to 120 kPa, which is a large

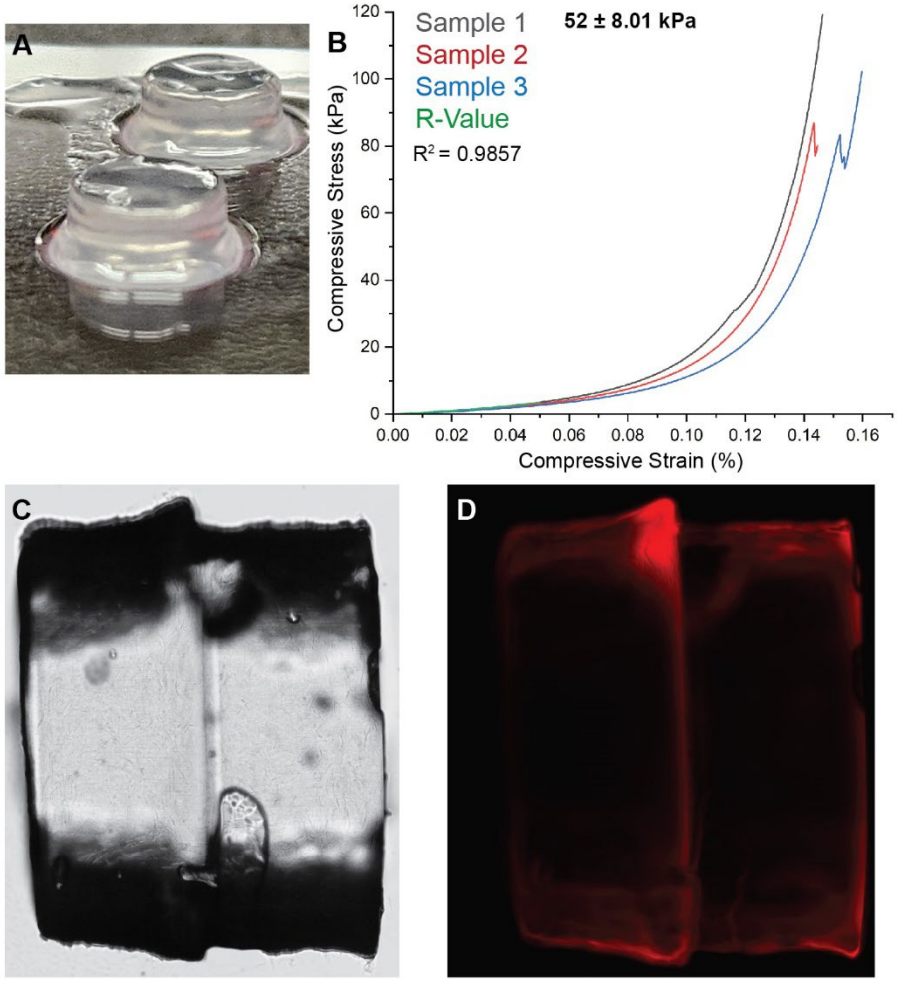

Figure 3.5. Fabrication of a thin layer of mCherry protein nanofibers on a NorHA hydrogel. A) Digital image of protein nanofibers-NorHA hydrogel. **B)** Compressive stress vs strain curve of the gel in panel (**A**). **C)** Bright field microscopy image of the gel in panel (**A**) at a magnification of 4x. **D)** Fluorescence microscopy image of the gel in panel (**A**) using the TRITC channel at a magnification of 4x.

increase in the observed compressive stress compared to the previous two sample types. The compression moduli for each of these gel samples were calculated using the information derived from the compression tester. The average compression modulus for the sample type was calculated to be 52.00 ± 8.01 kPa. This is the highest compression modulus for each of the types of NorHA gels made. The increase in compression modulus is almost a ten-fold increase in the compression modulus from the nanofiber-only NorHA gel, and more than a three-fold increase compared to the two-layer approach. The observed increase in compression modulus is due to DTT-based crosslinking of the bulk gel, resulting in an increase in the number of crosslinks as well as a dramatic decrease in the length of the crosslinker.

To take a closer look within the material, the gel was cut in half to obtain a cross-section. The cross-sectioned gel was taken over the fluorescence microscope and first analyzed using bright-field microscopy. The previous compression seen in the softer gels or the meniscus of the two-layer gel were not visible in the bright-field micrograph of the thin layer gel, highlighting the stiffness of the gel as well as the homogeneity of gel (Figure 3.5 D).

To confirm the surface decoration of the NorHA gel with protein nanofibers, the gel was imaged under the TRITC channel with the fluorescence microscope. The fluorescence micrograph revealed two thin layers of red fluorescence on an edge of each half of the cross-sectioned gel (Figure 3.5 E). The layer was measured to span up to 50 μm in thickness, indicating a dense mat of fibers coated on the surface. Based on these measurements, and due to the 5 nm width of these nanofibers, indicating a layer of

approximately 10,000 nanofibers in thickness. However, this does not account for the influence of the diffraction limit, which might decrease the calculated number of nanofibers on the surface. In addition, the clear thin layer represents a method with little bleed through, indicating reasonable control over fiber modification on the NorHA scaffold. The clear line further enforces the idea of covalent crosslinking with an easy method for fiber distribution analysis through fluorescence.

Due to the successful incorporation of the protein nanofibers into the NorHA scaffold, the next logical step was to test out the reversibility of the nanofiber assembly into these gel scaffolds. Therefore, both the reduction mechanism and the peptide displacement mechanism were tested to see if the protein nanofibers can be dissolved from the NorHA scaffold. To increase the versatility of this method, a hybrid nanofiber was used, where the $FN(10)_{III}$ consisted of 50% of the protein mass and the other 50% consisted of the mCherry protein. In this fashion, the resulting structures would incorporate both a fluorescent *and* a bioactive signal. For this, two sets of samples were fabricated, where the base NorHA, crosslinked with DTT, was formed and 5 μL of the 15 μM protein nanofiber solution was deposited on top of the gel. One of the sample sets were used as a control, where they were only washed with 1x PBS, whereas the other sample set was treated with 10 mM TCEP overnight and subsequently washed with 1x PBS.

The gels were first images using bright-field microscopy, to ensure that the gels were well-formed (Figure 3.6 A,C). From the bright-field images, both the control gel (top gels) and the treated sample were nicely formed gels without major blemishes that would complicate the fluorescence imaging. There were a few bubbles that were trapped in the

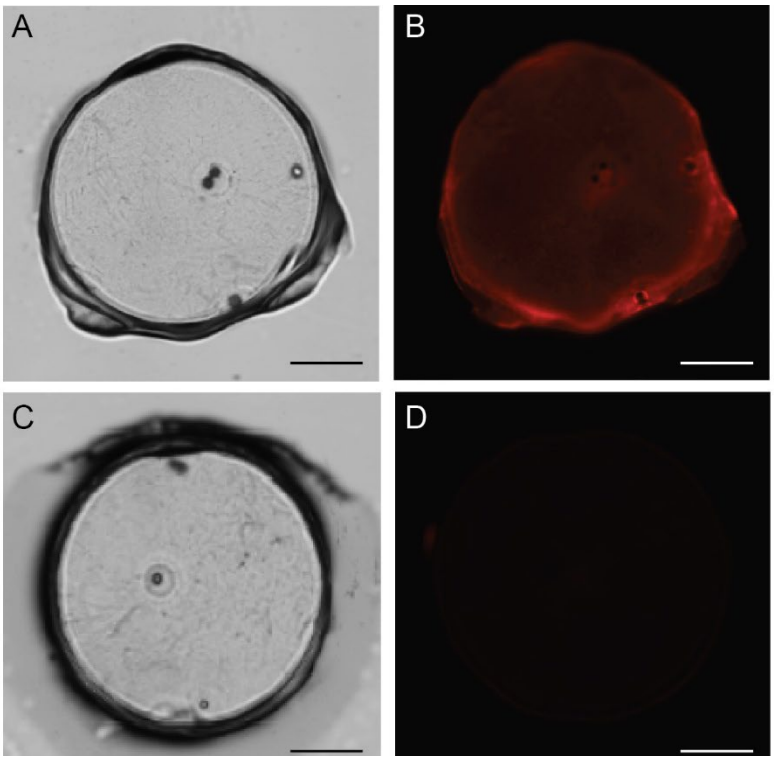

Figure 3.6. Fluorescence microscopy analysis of the reduced mCherry-Fn(10)$_{III}$ nanofibers in the NorHA scaffold. A) Bright-field micrograph of the NorHA gel embedded with the mCherry-Fn(10)$_{III}$ nanofibers without the addition of 10 mM TCEP. **B)** Fluorescence micrograph of the NorHA gel embedded with the mCherry-Fn(10)$_{III}$ nanofibers without the addition of 10 mM TCEP. **C)** Bright-field micrograph of the NorHA gel embedded with the mCherry-Fn(10)$_{III}$ nanofibers with the addition of 10 mM TCEP overnight. **D)** Fluorescence micrograph of the NorHA gel embedded with the mCherry-Fn(10)$_{III}$ nanofibers with the addition of 10 mM TCEP overnight. Scale bars = 1 mm.

gels, which served as benchmarks for the fluorescence imaging but did not interfere with the fluorescence signal. Once the state of the gels was captured, then the TRITC channel was used to capture the fluorescence signal of each gel. For the control gel, there was a clear fluorescence signal throughout the entire gel, indicating that fluorescence nanofibers were effectively incorporated into the hydrogel and that the distribution is homogeneous. However, for the TCEP-treated sample, there was little to no fluorescence that was detected by the fluorescence microscope, indicating that the protein nanofibers were effectively dissolved from the gel and removed from the porous hydrogel. The successful removal of

the fluorescence signal indicates two key conclusions. The first is that the hydrogel allows for efficient diffusion to occur within the gel, to allow for the small molecule reductant to interpenetrate and successfully reduce of the disulfide-mediated protein nanofibers. Secondly, the results indicate that the porosity of the hydrogel is large enough to allow for the dissolved protein monomers to efficiently diffuse *out* of the hydrogel. In this regard, the reduction treatment of these protein nanofibers allows for an efficient method to dissolve the protein nanofibers within the gel, which in effect, allows for the temporal removal of a biochemical signal.

Due to the successful dissolution of the protein nanofibers in the NorHA scaffold with the chemical reductant, the peptide displacement was subsequently tested. To test this method, similar sample sets were made for the chemical reduction experiment. The NorHA was crosslinked with DTT and then a mat of fibers was deposited on the surface of the hydrogels. The gel was first imaged under the fluorescence microscope to determine the extent of coating and fluorescence signal. After, the sample was incubated with a solution of the displacement peptide and allowed to incubate overnight. After incubation, the sample was subsequently washed with PBS. Once the sample was washed, the sample was analyzed using a fluorescence microscope.

The first experiment consisted of the protein fiber gels being treated with 100 μM of the displacement strand, in a total solution of 400 μL. Due to the volume of the solution, the amount of the displacement peptide was quite high. Once the sample with a mat of fibers was treated with the peptide solution, the resulting fluorescence micrograph indicated a little change in the overall fluorescence signal compared to the original

fluorescence (Figure 3.7 A,B). Most of the reduction in fluorescence was seen on the periphery of the gel, where high amounts of initial fluorescence were seen. However, to obtain a better comparison, there was an area of the gel that was formed a small mass island, creating an intense red "loop" around the gels in the respective micrograph. This loop maintains a similar amount of fluorescence before *and* after peptide displacement, indicating that the displacement reaction was inefficient.

Due to the inefficiency of the peptide displacement to work at that specific concentration, the peptide concentration was increased to 250 μM. At this point, the peptide is 17 times the original peptide concentration that was added to the surface of the gel, highlighting the level of excess of the displacement peptide. Therefore, by subjecting the gel to the previous set of conditions, the gel was analyzed the day after incubation under the fluorescence microscope. The gel that was treated with the displacement peptide showed a discernible decrease in the fluorescence signal, where more of the gel features were seen due to the signal decrease (Figure 3.7 D). The original gel showed a few areas of high fluorescence intensity, where the periphery of the gel showed a broad, red band of fluorescence (Figure 3.7 C). Upon treatment with the displacement peptide, more of the peripheral broad band was diminished, highlighting the ability of the displacement peptide to displace some of the protein nanofibers on the gel.

To push the displacement reaction even further, the concentration of the peptide was increased to 0.5 mM, which represents a 33-fold excess of the displacement peptide relative to the protein nanofiber concentration on the surface of the hydrogel. Once the gel

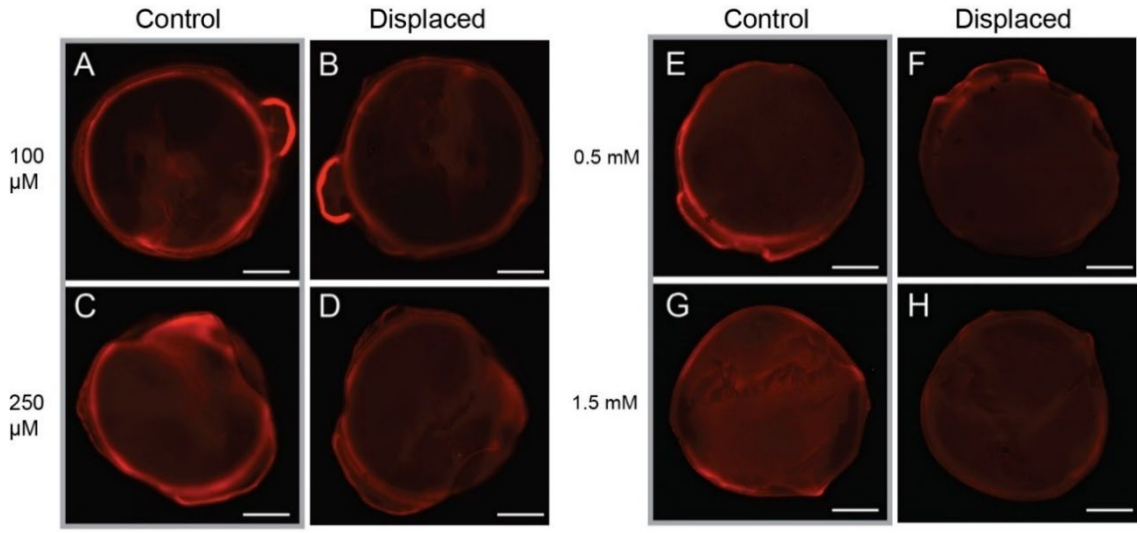

Figure 3.7. Fluorescence microscopy analysis of the displaced mCherry-Fn(10)$_{III}$ nanofibers in the NorHA scaffold. A) Fluorescence micrograph of the NorHA gel embedded with the mCherry-Fn(10)$_{III}$ nanofibers without the addition of the displacement peptide. **B)** Fluorescence micrograph of the NorHA gel embedded with the mCherry-Fn(10)$_{III}$ nanofibers with the addition of the displacement peptide. **C)** Fluorescence micrograph of the NorHA gel embedded with the mCherry-Fn(10)$_{III}$ nanofibers without the addition of the displacement peptide. **D)** Fluorescence micrograph of the NorHA gel embedded with the mCherry-Fn(10)$_{III}$ nanofibers with the addition of the displacement peptide. **E)** Fluorescence micrograph of the NorHA gel embedded with the mCherry-Fn(10)$_{III}$ nanofibers without the addition of the displacement peptide. **F)** Fluorescence micrograph of the NorHA gel embedded with the mCherry-Fn(10)$_{III}$ nanofibers with the addition of the displacement peptide. **G)** Fluorescence micrograph of the NorHA gel embedded with the mCherry-Fn(10)$_{III}$ nanofibers without the addition of the displacement peptide. **H)** Fluorescence micrograph of the NorHA gel embedded with the mCherry-Fn(10)$_{III}$ nanofibers with the addition of the displacement peptide. Scale bars = 1 mm.

was fabricated, the sample was imaged with the fluorescence microscope to determine the extent of nanofiber modification. The gel appears to have a thin coating of nanofibers, based on a light fluorescence signal in the center of the hydrogel (Figure 3.7 E). However, there were bright regions of fluorescence on the periphery of the gel, highlighting some of the morphological features of the edges of the gel. After treatment with the displacement peptide overnight, the gel was imaged again under the TRITC channel. The resulting gel shows a remarkable decrease in the fluorescence signal, where most of the high-intensity

signal on the periphery of the gel was depleted (Figure 3.7 F). In addition, the gel boundaries are becoming more difficult to distinguish, highlighting the increase in efficiency for the peptide displacement reaction.

However, due to the remaining fluorescence signal in the gel, a further experiment was tested to dramatically increase the peptide displacement concentration. The peptide displacement concentration was increased to 1.5 mM, which represents a 100-fold excess of the displacement peptide relative to the protein nanofiber concentration on the surface. As stated before, the NorHA gel was fabricated and crosslinked and subsequently modified with the protein nanofibers. Once modified, the gel was imaged to visualize the extent of modification. The resulting fluorescence signal revealed an even distribution of fluorescence on the surface of the gel, where there were some parts on the periphery of the gel that showed a high fluorescence signal but not much as some of the previous gels (Figure 3.7 G).

After treatment with the displacement peptide, there was a major reduction in the fluorescence signal, removing some of the pronounced morphological features that was seen in the previous fluorescence micrograph (Figure 3.7 H). The reduced fluorescence signal was still homogeneously dispersed throughout the gel but some of the features were lost due to the reduction in signal. For example, the previous crevice that was highlighted in the preceding micrograph is almost completely dark upon the displacement treatment, indicating that at a 1.5 mM concentration of the displacement peptide, the protein nanofibers are being displaced in a dramatic fashion. However, due to the small retention in the fluorescence signal, further studies need to be conducted to ensure complete removal

of the fluorescence signal similarly to the reduction experiment. The main drawback of increasing the peptide displacement concentration is the large amount of the peptide. The inefficiency may be derived from non-specific electrostatic interactions of the peptide with the HA scaffold. These can be reduced by using a charged peptide that exhibits repulsion with the HA gel but can effectively bind to the toehold heptad. Therefore, more optimizations are needed to ensure complete success of the displacement reaction.

We next turned to other avenues of material characterization for these protein nanofiber-NorHA systems. In the regard, the protein nanofibers that are completely embedded, similarly to the gels made in Figure 3.3, were analyzed under the scanning electron microscope (SEM) to image the physical embedding of the nanofibers within the NorHA scaffold. To do this, the protein nanofibers that were embedded with the nanofibers were chemically fixed to ensure that they maintain their physical stability for SEM processing. The physical treatment involved a period of incubation with 4% paraformaldehyde, which allows for any surface exposed amino groups to be covalently tethered tougher, ensuring chemical stability. [192] Once the gel was chemically fixed, it was washed three times with PBS and then buffer exchanged to ethanol over a series of sequential dilutions. Once the gels were exchanged into an ethanol solvent system, the ethanol was removed, and the gels were allowed to dry under vacuum overnight. However, one of the main drawbacks to this system is structural compression due to flattening of the material under vacuum. As a result, most of the structural integrity of the gel was lost but its biochemical composition remains the same. As a result, the porosity of the native gel cannot be determined but the embedded fibers can still be visualized.

Once the gel was prepared, the sample was sputter coated with carbon and analyzed under the SEM. The first SEM micrograph that was obtained was a wide-field micrograph which depicts multiple layers of the hydrogel in addition to the texture interior of the gel (Figure 3.8 A). There was a thick, smooth layer on the right side of the micrograph, which represents the surface of the hydrogel. The micrograph also presents a cross-sectional view of the hydrogel, highlighting the interior morphology of the gel. Zooming in to this region revealed a shelf of the NorHA scaffold where many flakey microstructures were seen (Figure 3.8 B). There are no smooth areas in the micrograph, depicting that the surface features of the nanofiber-NorHA scaffold is decorated with flake-like and fibrous-type features. Due to the fibrous nature of some of the surface features, another zoom-in was taken of this specific area. By taking a closer look at the surface features at a magnification of 38,000 X, the flake-like features of the gel were revealed to be bead-like structures that are compressed together (Figure 3.8 C). There are other areas in the gel that highlight the beads of the NorHA system, but they are entangled by these fibrous connections. These areas depict an extensive fiber network that interconnects multiple regions of the gel. These structures suggest the presence of the protein nanofibers, which create the extensive network throughout the NorHA scaffold.

To further examine the filamentous nature of the gel, a closer zoom-in was obtained with a magnification of 70,000 X, which revealed thin filaments extending throughout the entire area, where most of the filaments seem to be interlinked by small nodules, presumably composed of NorHA (Figure 3.8 D). Most of the filaments seemed to be thin, where the width of each filament seemed to be consistent based on an initial observation.

To obtain more reliable width measurements, three areas that exposed parallel filaments

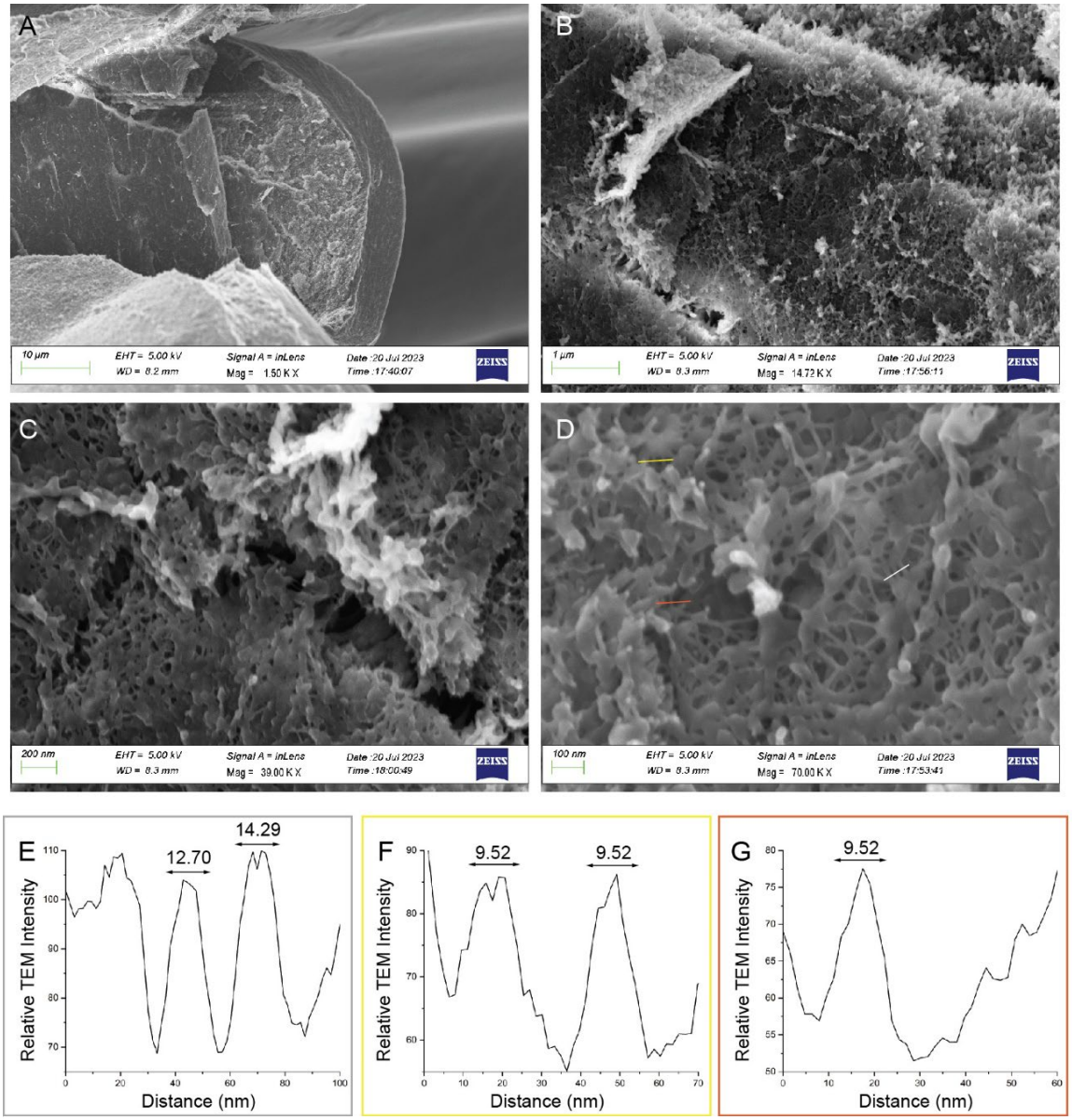

Figure 3.8. SEM analysis of the NorHA hydrogel embedded with mCherry-Fn(10)III nanofibers. A) Wide-field SEM micrograph of the microscale features of the mCherry-Fn(10)$_{III}$ nanofiber NorHA hydrogel. **B)** SEM micrograph of the mCherry-Fn(10)$_{III}$ nanofiber NorHA hydrogel. **C)** SEM micrograph of the mCherry-Fn(10)$_{III}$ nanofiber hydrogel highlighting the fibrous incorporation of the protein filaments in the scaffold. **D)** A zoomed-in SEM micrograph of the mCherry-Fn(10)$_{III}$ nanofiber NorHA hydrogel revealing the fibers dispersed throughout the hydrogel. The lines depict the sections that were measured in the width traces below. **E)** Width profile of the mCherry-Fn(10)$_{III}$ nanofibers in (**D**), traced with the white line. **F)** Width profile of the mCherry-Fn(10)$_{III}$ nanofibers in (**D**), traced with the yellow line. **G)** Width profile of the mCherry-Fn(10)$_{III}$ nanofibers in (**D**), traced with the orange line.

were measured, which are indicated by the lines in the micrograph. The first measurement is indicated by the white line in the micrograph, where three filaments are seen. The measurement revealed two clear peaks, where the third peak was disrupted by background intensity (Figure 3.8 E). The two peaks measured out to be 12.7 nm and 14.3 nm, which are relatively close to one another and deviate from the expected width by ~8 nm. The second measurement was taken along the yellow line, which resulted in two clear peaks, both at a width of 9.5 nm (Figure 3.8 F). This width measurement is close to the expected width of the protein nanofibers and deviates from the expected width by ~4.6 nm, which can be accounted for by the carbon coating. Lastly, the last area that was measured is indicated by the orange line, which measures one distinguishable peak (Figure 3.8 G). The resulting measurement revealed a peak that had a width of 9.5 nm, which has the same width as the previous two filaments, highlighting the width consistency of these filaments. Overall, the average width of the measured filaments was 11.1 nm, which is ~6 nm from the expected width of the protein nanofibers. Due to the few nanometers that are deposited on to the gel sample during carbon sputter coating, these measured widths seem plausible for the expected protein nanofibers. The consistency between these filaments also indicates the nature of a well-defined filament that is dispersed within the NorHA scaffold.

3.3 Conclusion

The ability to incorporate protein nanofibers into a NorHA hydrogel has been successfully demonstrated in this chapter. Three different hydrogel architectures were demonstrated, each providing different levels of mechanical stiffnesses. The full inclusion of the protein nanofibers with the gel without an additional small molecule crosslinker resulted in a compression modulus of ~5 kPa. The two-layer approach resulted in a

compression modulus of 11 kPa and the thin layer approach resulted in compression modulus of 52 kPa. As a result, the compression modulus range achieved from this protein nanofiber system spans over 47 kPa, proving plenty of room to fine tune the mechanical properties of the gel.

In addition to a range of mechanical properties, the NorHA gel showed the ability to reversibly display the protein nanofibers through the incubation of DTT and the displacement peptide. Although the incubation of DTT resulted in complete dissolution of the protein nanofibers, the displacement mechanism was inefficient at dissolving the protein nanofibers. Further work is needed to optimize the peptide displacement process. Lastly, these different protein nanofiber architectures were characterized by SEM to highlight the fibrous inclusion of the nanofiber within the NorHA scaffold. Altogether, these photopolymerization of NorHA with the protein nanofibers provide an excellent tool to develop a protein-based, nanofiber hydrogel system that can be implemented with cellular studies. These efforts pave the way to understand how a spatiotemporal display of bioactive, protein nanofibers regulate cellular activity.

3.4 Methods and Materials

Norbornene-functionalized Hyaluronic Acid (NorHA) Synthesis. NorHA for gel construction was provided by the Holloway lab. Their protocol for making it is as follows: Sodium hyaluronate (HA, Lifecore Biomedical, 60 kDa) was converted to its tetrabutylammonium salt (HA-TBA) using the Dowex 50 x 200 ion exchange resin, frozen, and lyophilized and characterized with ^{1}H NMR (Bruker). HA-TBA carboxylic acid groups were then modified with norbornene groups via amidation with 5-norbornene-2-

methylamine (Tokyo Chemical Industry), anhydrous dimethyl sulfoxide (DMSO), and benzotriazole-1-yl-oxy-tris-(dimethylamino)-phosphonium hexafluorophosphate (BOP) under nitrogen at room temperature for 4 h. The reaction was quenched with cold water, purified via dialysis (SpectraPor, 6–8 kDa molecular weight cutoff) for 7 days at room temperature, frozen, and lyophilized. The degree of modification was ~92% as measured by ^{1}H NMR (Bruker).

NorHA Hydrogel Fabrication. Hydrogels were fabricated with 4 wt % of NorHA macromer in phosphate-buffered saline (PBS). NorHA with approximately 92% norbornene functionalization was dissolved in PBS containing a non-degradable dithiol crosslinker (1,4-dithiothreitol), and 0.05% w/v photoinitiator (Irgacure-2959). DTT was added a stoichiometric molar ratio of 0.2:1 thiol to norbornene functional groups, leaving 80% of the original norbornene groups available for photoconjugation. The pre-gel solution was transferred into a custom cylindrical acrylic mold (SYLGARD 184, Dow), covered with a glass slide, and crosslinked via ultraviolet (UV) light at 10 mW/cm^2 (Omnicure S1500, 320–390 nm) for 4 min.

To embed protein nanofibers throughout the NorHA hydrogels, NorHA was completely dissolved with the protein nanofibers at a concentration of 15 μM. Once dissolved, 0.05 wt% of photoinitiator I2959 in PBS was added into the solution. The solution was pipetted into the custom silicone mold and exposed to UV light (10 mW/cm^2) for 6 min. The mold was removed to retrieve the fabricated gel. The gel was washed with three rounds of PBS to ensure removal of non-crosslinked material.

Secondly, to create a the dual-layered hydrogel, NorHA was completely dissolved in 1x PBS and vortexed. DTT was added at a 0.2 equivalents (relative to the norbornene groups), and 0.05 wt% of photoinitiator I2959 in PBS was added into the solution. The solution was pipetted into the custom silicone mold and exposed to UV light (10 mW/cm^2) for 3 min. Once photocrosslinked, a NorHA solution dissolved with the protein nanofibers at a concentration of 15 μM and 0.05 wt% of photoinitiator I2959 in PBS was added on top of the gel. The solution was exposed to UV light (10 mW/cm^2) for 4 min. The mold was removed to retrieve the fabricated gel. The gel was washed with three rounds of PBS to ensure removal of non-crosslinked material.

Thirdly, to create the thin layer of protein nanofibers on the NorHA hydrogel, NorHA was completely dissolved in 1x PBS and vortexed. DTT was added at a 0.2 equivalents (relative to the norbornene groups), and 0.05 wt% of photoinitiator I2959 in PBS was added into the solution. The solution was pipetted into the custom silicone mold and exposed to UV light (10 mW/cm^2) for 4 min. Once photocrosslinked, 5 μL protein nanofibers at a concentration of 15 μM was deposited on top and exposed to UV light (10 mW/cm^2) for 3 min. The mold was removed to retrieve the fabricated gel. The gel was washed with three rounds of PBS to ensure removal of non-crosslinked material.

Hydrogel Mechanical Property Characterization. Shear and compression mechanical properties were assessed at room temperature immediately after gelation using cylindrical samples approximately 4.8 mm in diameter and 2 mm in height. Shear mechanical properties were assessed with increasing frequency using a dynamic mechanical analyzer (DMA) (Mettler Toledo, DMA1) with a 10 mm diameter parallel plate geometry and a 2

mm gap distance. Oscillatory frequency sweeps were performed from 1 to 10 Hz with 1% strain. Shear storage and loss modulus was plotted as a function of frequency for each individual HA hydrogel concentration (1.5, 2, 2.5, 3, and 4% w/v NorHA, $n = 3$).

Compression mechanical properties were assessed at room temperature immediately after gelation using a benchtop mechanical testing machine (Instron Materials Testing System Series 5943, 50 N load cell) in unconfined compression. Compression was performed at 24% strain per minute and the compressive modulus was calculated from the initial linear region of the stress vs strain curve. The compressive modulus was determined for each individual HA hydrogel construct.

Temporal Displacement of Protein Nanofibers on the NorHA Hydrogels. For the washed NorHA hydrogels that have been modified with a thin layer of protein nanofibers, the modified gel was imaged under bright-field and fluorescence microscopy (Leica DMI6000 B). Once characterized, for both the TCEP reduction and the peptide displacement, the gel was incubated with the reversibility stimulus, (TCEP, 10 mM and EK Displacement peptide; 150 μM – 1.5 mM) and allowed to shake at room temperature overnight. After incubation, the gels were washed three times with PBS and imaged with bright-field and fluorescence microscopy.

Scanning Electron Microscopy Characterization. The protein nanofiber-embedded NorHA gel was prepared in two fashions: through an ethanol replacement protocol followed by subsequent dehydration, or through lyophilization. For the ethanol buffer exchange, the hydrogel was washed three times with 1x, PBS, at a pH = 7.4, and aspirated. Once washed, the gel was incubated with 400 μL of 4 % paraformaldehyde (Electron

Microscopy Sciences) dissolved in 1x PBS, pH = 7.4, and allowed to be fixed for 20 mins. Once fixed, the gel was washed three times with 1x, PBS, at a pH = 7.4, and aspirated. The PBS buffer was then exchanged into 100% ethanol over serial dilutions (10%, 20%, 30%, 50%, 70%, 95%, and 100%), where the gel was incubated in each buffer system for 10 mins. After the buffer exchange, the ethanol was removed, and the gel was dehydrated under vacuum overnight.

For the lyophilization preparation, the hydrogel was washed with 1x PBS, at a pH = 7.4, and flash frozen in a slurry of dry ice in 100% ethanol. Once frozen, the gels were immediately transferred into a lyophilizer and lyophilized for 4 h. The samples were promptly removed to prevent structural compression, and were sealed and stored.

For each dried sample, the sample was immobilized on an SEM stub through double-sided carbon tape. Once immobilized, the sample was sputter coated with carbon using a carbon sputter coated. Once the samples were sputter coated, the samples were analyzed using secondary electron detection using a Zeiss Auriga Focused-Ion Beam Scanning Electron Microscope. The sample was analyzed with an electron voltage of 5 KeV.

Energy-Dispersive Spectroscopy-Scanning Electron Microscopy Characterization. For the sputter coated hydrogel samples, the samples were initially imaged using a Zeiss Auriga Focused-Ion Beam Scanning Electron Microscope at an electron voltage of 5 KeV. Once an optimal area was found, the electron voltage was increased to 20 KeV and subsequently analyzed with an Oxford X-Max Energy Dispersive X-ray Spectrometer (EDS). The elemental composition was obtained, where the Carbon, Nitrogen, Oxygen,

and Sulfur signals were the main elements of focus. The data was acquired using the Oxford AZTec App.

CHAPTER 4

REVERSIBLE ASSEMBLY OF THERMOSTABLE DNA-PROTEIN NANOFIBERS

4.1 Introduction

Biomimetic material development has seen a dramatic rise in production and fabrication due to the elegant architectures seen in Nature.[193] These natural, complex structures give rise to a plethora of function, including suitable traits such as superior mechanical properties while maintaining a lightweight profile.[194] Structurally speaking, many of the diverse traits of biologically derived materials are due to the biological nanoscale components that compose these materials, namely proteins. However, one of the main challenges in the field of biomimetic material development is deciphering how the nanoscale components affect the macroscale properties of biological materials. Therefore, a mesoscale outlook is necessary to understand how the nanoscopic components can be understood and applied to generate macroscale materials with optimal material properties.

The field of protein-based materials has seen some success where highly efficient and mechanically strong materials have been developed. Researchers have utilized a variety of approaches to develop these bio-inspired materials, from directed evolution,[195, 196] systematic design of monomers for materials with predicted material properties, [197] *de novo* designed protein materials,[198] hybrid protein-DNA based materials,[199] and lastly, protein-composites.[200] Through these efforts, materials with remarkable properties have been developed, such as supersonic shock-absorbing materials,[201] highly elastic and tough hydrogels,[202] to strong waterproof adhesives.[203] However, many of these approaches revolve around the construction of 3-D materials, not 2-D materials.

Protein thin films have their own unique set of properties in Nature, such as S-layer-mediated cell protection, adhesion, and aggregation,[204] to hydrophobin thin films which reduce the surface tension of water.[205] Besides the natural uses of protein thin films (PTF), PTFs can be used artificially for the coating of biomedical devices to facilitate the integration to the body,[206] for the synthesis of metal nanoparticle 2D arrays,[207] and for anti-fouling,[208] to name a few. However, the subtle development of protein-based thin films poses many challenges due to confining the growth of the protein-based material in two dimensions, the challenging approach for scalable production, and for the retention of bioactivity in protein building blocks.

To combat one of the issues of protein material fabrication, regardless of dimensionality, researchers have incorporated hyperstable proteins to generate protein-based materials. For example, a hyperstable protein cage, TF55β, which was derived from *Methanocaldococcus jannaschii*, a thermophilic anaerobe, was engineered to form a protein thin film for the precise fabrication of Ni-Pd and Co-Pd alloy thin films.[207] Not only has the methanogen provided a useful protein cage for material fabrication but it also had provided researchers with a filamentous protein, gamma-prefoldin (γPFD), which is a protein chaperone used to stabilize endogenous proteins in extreme conditions (Figure 4.1 A, B).[209] Besides the native use of γPFD, researchers have utilized the thermostable filament to generate geometric protein assemblies,[210] conductive metalloprotein nanowires,[211] and various other hydrogel systems.[212-214] However, the use of γPFD remains limited in terms of generating two-dimensional thermal stable protein thin films. Even further, the reversible assembly of thermal stable protein thin films have not been demonstrated.

To this end, a reversible thin film approach has been designed utilizing γPFD as the main protein building block, where the self-assembly of the filamentous protein is dictated through coiled-coil interactions. In order to allow for coiled-coil interactions to promote the self-assembly of γPFD into thin film assemblies, the γPFD was genetically fused with a KE coil to allow for hierarchical assembly. This approach was utilized in a similar manner to promote the complementary self-assembly of γPFD-KE into hydrogels at high concentrations (i.e., 5 wt%). [212] However, to control the self-association of these filaments *and* to control the self-assembly through DNA hybridization, the protein was kept at a low concentration and was non covalently modified with a DNA handle through coiled coil interactions (figure 4.1 C).

By allowing the γPFD-KE to be non-covalently modified with DNA through the KE-DNA conjugate, it is possible to avoid the tedious task of post-modification of γPFD through standard bio-conjugation techniques. In addition, the self-assembly of the γPFD-KE filaments can be reversibly controlled through DNA strand displacement (Figure 4.1 D). Through this approach, the nature of the crosslinker can be tailored, from a traditional one-dimensional DNA duplex to a more complex two-dimension crosslinker through the use of a DNA tile (Figure 4.1 E). The use of two different crosslinkers allows for the extent of crosslinking to be modulated through a multi-valent display of the KE coil. With these two distinct crosslinkers, it has been shown that the γPFD-KE filaments can be self-assembled into two-dimensional arrays which can be reversed through DNA strand displacement or through enzymatic digestion. Ultimately, this strategy highlights the benefit of DNA modification of γPFD filaments to control their assembly and promotes the fabrication of thermal stable hybrid protein two-dimensional arrays.

4.2. Results and Discussion

4.2.1 DNA Crosslinking of Prefoldin-KE Filaments

Previous strategies to assemble γPFD structures through coiled coils have involved the utilization of completely complementary coils fused on to the γPFD monomer.[212] Due to the four-heptad design of the genetic fusion, the protein filaments resulted in complementary self-assembly and gelation at a concentration of 2 wt%. Due to the high

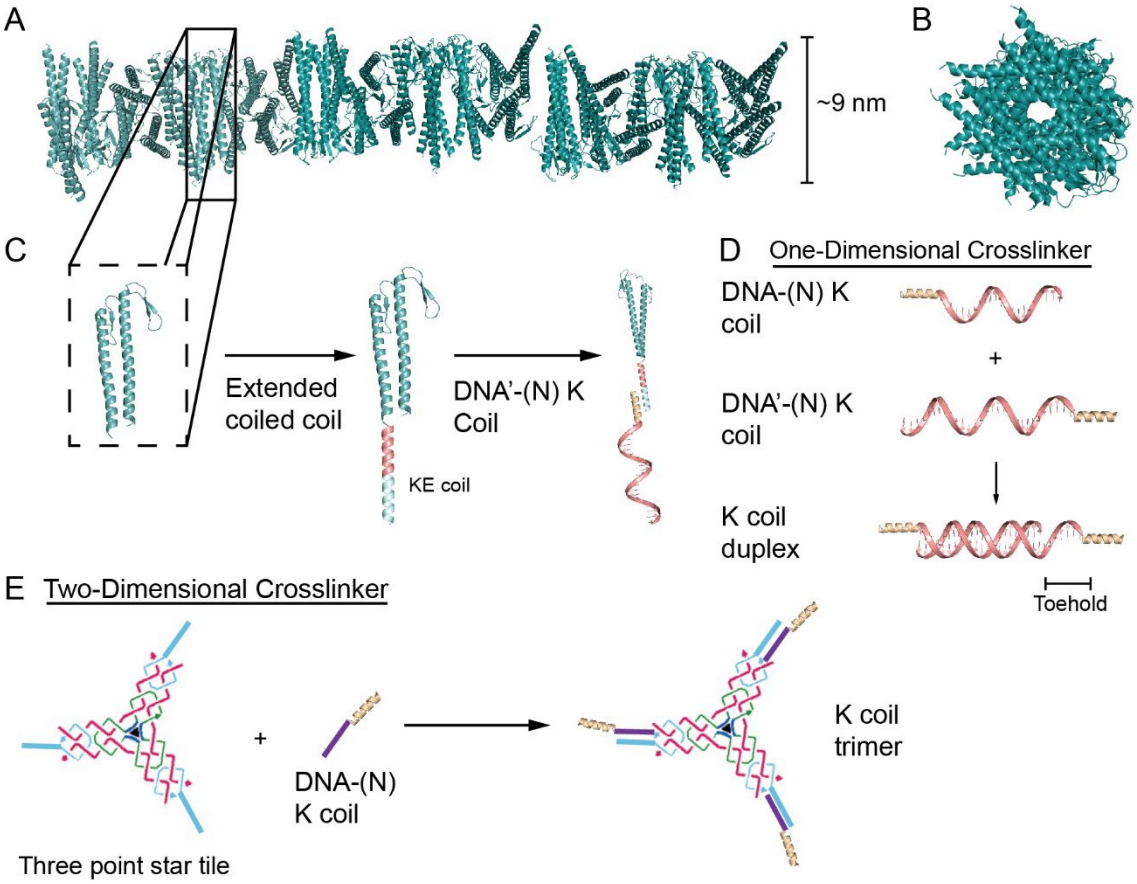

Figure 4.1. Overview of the crosslinking approach of prefoldin-KE filaments. A) The crystal structure of native γPFD filaments, highlight the repeat pattern and width of the filament. **B)** Cross-sectional view of the γPFD filaments. **C)** Schematic highlighting the extension of a γPFD monomer with the KE coil through genetic fusion. **D)** Schematic for the one-dimensional crosslinker, utilizing two distinct DNA-peptide conjugates. **E)** Schematic for the two-dimensional crosslinker.

concentration of protein required for this application, our intention was to create a hydrogel through the same system but at a much lower concentration. As a result, the same γPFD-

KE monomer was used, which can then bind to the complementary K coil (Figure 4.1 C). Additional functionality can be incorporated to the binding K coil, through the development of a K coil-DNA conjugate. Through this hybrid approach, the γPFD filaments can be modulated through DNA crosslinkers.

As a result, two different crosslinkers were designed. The simplest crosslinker is the K coil duplex, which can bind to two distinct γPFD filaments, on each end of the duplex (Figure 4.1 D). Due to the simplicity of the design, a toehold was designed into the duplex, which can result in the disruption of the crosslinks through toehold-mediated strand displacement.[74] The second crosslink was designed to be a two-dimensional crosslink structure, namely the three-point star tile (Figure 4.1 E). Due to the ease of assembly, the three-point star allows for three K coils to be tethered to the structure, increasing the crosslink density of the hybrid material.

The two DNA-peptide conjugates that were synthesized were the 3-point star-s (short)-cut N-K coil conjugate and the 3-point star-s comp toe N-K coil conjugate. For the nomenclature, the "s" stand corresponds to one of the three strands used for the assembly of the three-point star structure, notably the *short* strand. The "cut" indicate a *shorter* sequence based from an previous sequence. The N-K coil refers to the modification of the azidolysine being placed on the N-terminus of the K coil peptide. As for the second conjugate, the same nomenclature still applies but in addition, the "comp toe" indicates the *complement* to the s-cut conjugate and the "toe" portion refers to a *toehold* being present in the strand for reversibility of the crosslinks through DNA strand displacement. Both conjugates were successfully synthesized through copper-free click chemistry, purified

through RP-HPLC, and verified through mass spectrometry (Figure 4.2 A, B). Each of the mass spectra revealed correct masses with the addition of a Na^+ adduct.

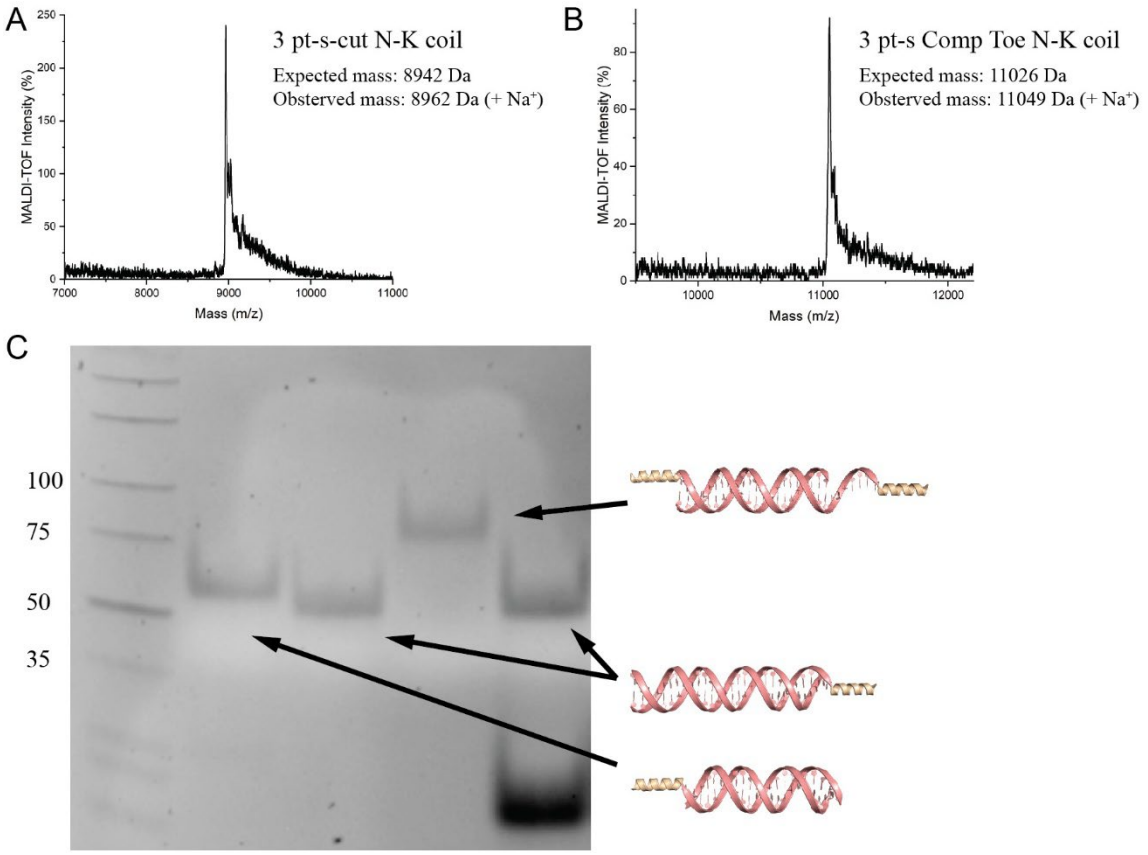

Figure 4.2. Characterization of the K coil conjugates. A) MALDI-TOF mass spectrum of the 3 pt-s-cut N-K coil peptide-DNA conjugate. **B)** MALDI-TOF mass spectrum of the 3-pt-s-comp toe N-K coil peptide-DNA conjugate. **C)** 5% native PAGE analysis of the binding of the K-coil conjugates with their DNA complements and the effectiveness of strand displacement.

Once the conjugates were synthesized, purified, and characterized, the assembly of the conjugates were monitored through native PAGE (Figure 4.2 C). The first lane shows the binding between the 3-point star-s (short)-cut N-K coil conjugate and the 3-point star-m (medium) strand. The 3-point star-m (medium) strand was chosen for hybridization due to complete complementarity to the short strand and due to native assembly of the three-point star structure. The second lane shows the binding of the 3-point star-s comp toe N-K

coil conjugate with the displacement strand due to complete complementarity. To note, this band migrates faster compared to the band in lane one due to the 3-point star-m strand being at a larger molecular weight compared to the displacement strand. Lane three shows the binding of both conjugates together, showing a clean band with a slower migration rate due to the presence of the cationic K coils on the duplex. To highlight the displacement reaction, lane four shows that the K coil duplex in lane three can be completely reversed with the molar equivalent addition of the displacement strand mediated through strand displacement. By the successful demonstration of strand displacement, the two crosslinkers were tested with the γPFD-KE to see if these components would allow for self-assembly.

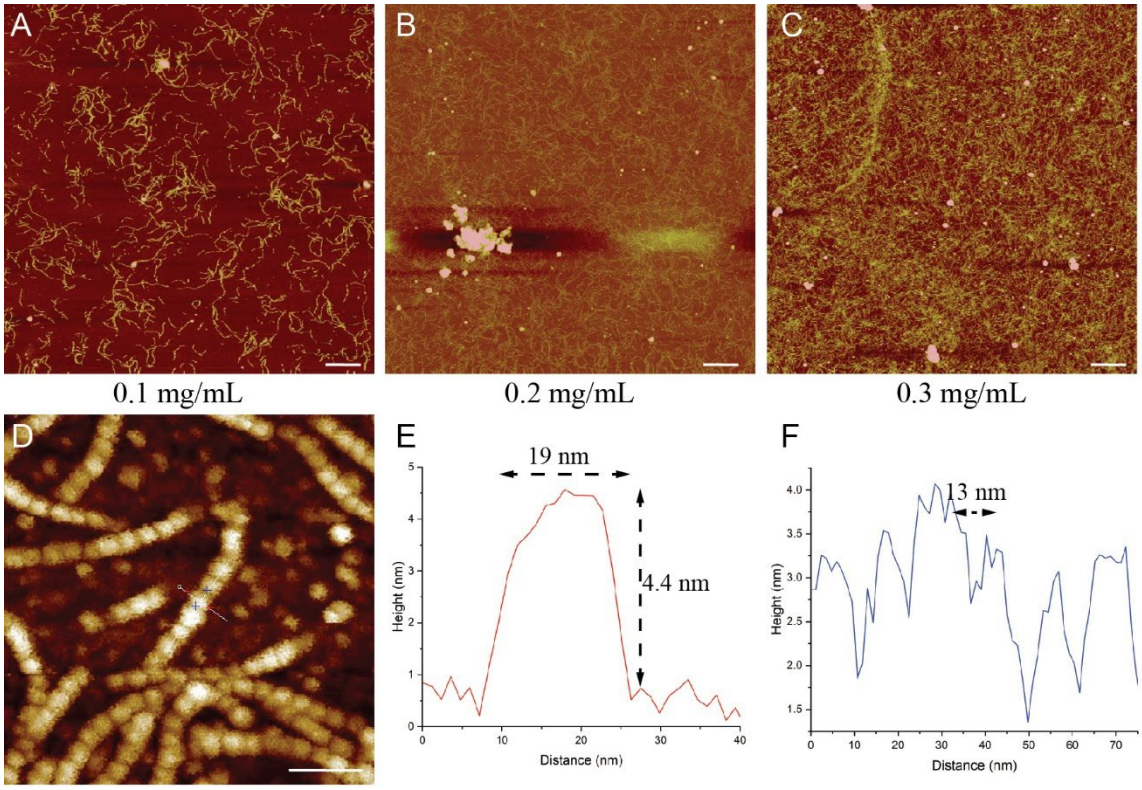

Figure 4.3. γPrefoldin-KE AFM Analysis. A-C) AFM analysis of γPFD-KE filaments at a concentration of 0.1 mg/mL, 0.2 mg/mL, and 0.3 mg/mL, respectively. Scale bar = 1 μm. **D)** Zoom-in of γPFD-KE filaments on AFM to determine physical dimensions. Scale bar = 50 nm. **E)** Cross-sectional height profile of the γPFD-KE filaments. **F)** Medial length measurements of γPFD-KE filaments.

Initially, to visualize the self-assembly process of these hybrid materials, experiments were conducted to determine the optimal conditions of the assembly process through AFM. Three different concentrations were screened under AFM to determine the number of filaments on the surface. From a concentration range of 0.1 mg/mL to 0.3 mg/mL, the optimal concentration was 0.1 mg/mL due to well-dispersed filaments on the surface (Figure 4.3 A-C). 0.2 mg/mL had a high abundance of filaments on the surface but there was visible clustering on the surface, which may prevent clear self-assembly patterns from being distinguished. Lastly, 0.3 mg/mL was too high of a concentration due to dense regions of filaments and unwanted clustering.

To further examine the γPFD-KE filaments on AFM, zoom-in micrographs were taken to obtain physical dimensions of the filaments for future reference (Figure 4.3 D). Under AFM, each γPFD-KE helical repeat can be observed. By choosing an optimal filament to analyze, lateral and medial measurements were taken. For the lateral height measurement, the observed height was 4.4 nm with a length of 19 nm (Figure 4.3 E). Based on the Cryo-EM structure, the width of the γPFD-KE filaments should be 17.4 nm, which includes the length of the PFD-monomer in addition to the KE coil extensions.[211] In addition, tip artifacts from AFM acquisition may result in broadening of the height profile, giving rise to the deviation that is observed from the height profile relative to the Cryo-EM structure. The height of the filaments was measured to be 4.4 nm. The short height of these filaments may be due to surface flattening of the structure, under air mode AFM acquisition. For the medial length measurements, each helical repeat was measured to be 13 nm (Figure 4.3 F). Based on each γPFD monomer resulting in a helical rise of 1.83 nm with a rotation of -48.9° along the helical axis, the helical repeat should be 13.47 nm. As a

result, the theoretical length of the helical repeat is in good agreement with the helical repeat measured on AFM.

After the initial round of optimization, experiments were conducted to evaluate how the K coil duplex promotes the self-assembly of the γPFD-KE filaments. As a reference, the self-assembly experiments were conducted at a concentration range of 0.1 mg/mL due to low aggregation and decent loading density on the mica surface (Figure 4.4 A). Upon

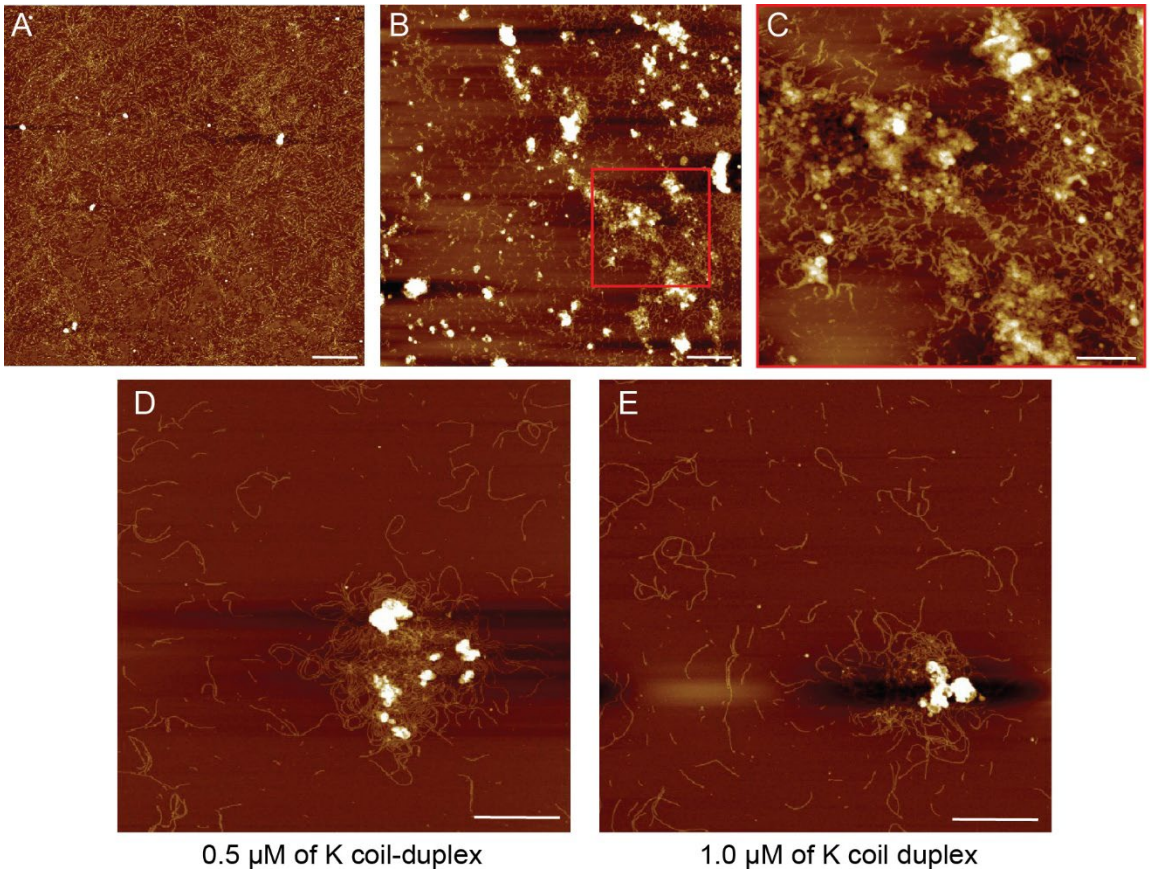

Figure 4.4. γPrefoldin-KE crosslinking with K coil duplex. A) AFM micrograph of γPFD-KE filaments at a concentration of 0.1 mg/mL as a reference. Scale bar = 1 μm. **B)** Wide-field micrograph of the γPFD-KE filaments crosslinked with the K-coil duplex at a concentration of 0.5 μM. Scale bar = 1 μm. **C)** Zoom-in micrograph of the γPFD-KE filaments crosslinked with the K-coil duplex at a concentration of 0.5 μM. Scale bar = 500 nm. **D)** AFM micrograph of the γPFD-KE filaments crosslinked with the K-coil duplex at a concentration of 0.5 μM. Scale bar = 1 μm. **E)** AFM micrograph of the γPFD-KE filaments crosslinked with the K-coil duplex at a concentration of 1.0 μM. Scale bar = 1 μm.

the addition of the pre-annealed K coil duplex, the γPFD-KE filaments appeared to aggregate to γPFD-KE clusters on surface (Figure 4.4 B). A zoom-in on the micrograph, in Figure 4.4 B, revealed cloud-like clusters that reduce the filament density on the surface, indicating that the cloud-like clusters are composed of the γPFD filaments, crosslinked with the K coil duplex. The clusters also had large height profiles, indicating extensive crosslinking. In order to try to optimize the conditions, another higher concentration was tried. By comparing two different concentrations of the K coil duplex, 0.5 μM and 1.0 μM, differences in self-assembly can be observed. The resulting AFM micrographs depicted differences in the extent of clustering using those two different concentrations of crosslinker (Figure 4.4 D, E). It appears that crosslinker resulted in larger arrays/clusters of γPFD-KE filaments when at a concentration of 0.5 μM compared to 1.0 μM. The clusters observed through the micrographs also depict better formed arrays and less clustering compared to the original crosslinking approach. In this respect, the methods to optimize the self-assembly process were conducted through annealing processes.

Due to the thermal stability of the γPFD-KE filaments,[211, 212] the γPFD-KE filaments were crosslinked with the K coil complementary DNA conjugates and annealed from 65 °C to 4 °C over 10 h. To gain a better understanding of the effect of thermal annealing, another K coil duplex titration was conducted. The concentration ranged from 0.5 μM to 1.5 μM to see if the annealing would favor a higher concentration or remain ideal at 0.5 μM. At a concentration of 0.5 μM of the K coil duplex crosslinker, there was a large thin film assembly, spanning several microns in size (Figure 4.5 A). The γPFD-KE array seems well-ordered but there were portions of the film that seemed to have been blown off, resulting in a few clusters near the thin film with an expanded height profile.

Due to air mode acquisition, it is suspected that the delicate thin film was blown off while the sample buffer was blown from the surface of the mica chip, resulting in the artifact seen in the micrograph. The higher concentrations, at 1.0 μM and 1.5 μM seemed to form well-ordered clusters but not as well-formed as the thin film assembly seen at 0.5 μM (Figure 4.5 B, C). Once again, a concentration a 0.5 μM seemed to be the most optimal for the assembly of the γPFD-KE filaments using the K coil duplex crosslinker. Based on the air mode artifact seen in these thin films, conditions were optimized to preserve the delicate structure as much as possible. As a result, these protein thin films were analyzed using liquid mode AFM.

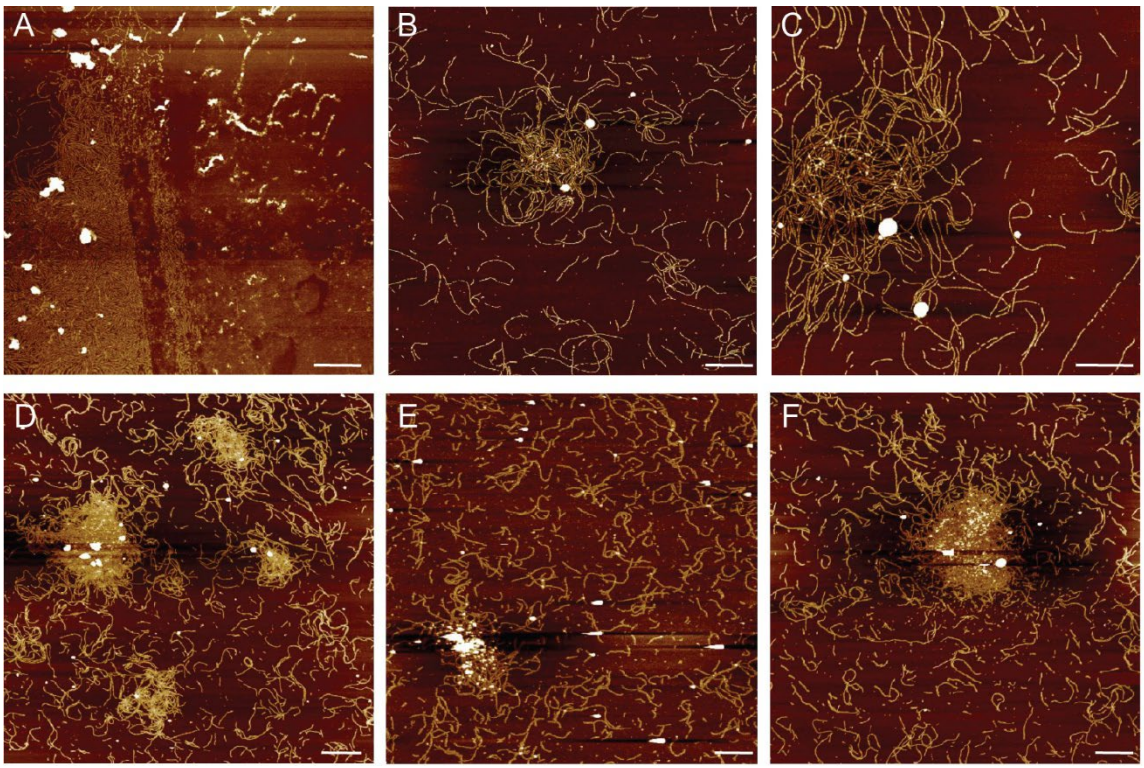

Figure 4.5. γPrefoldin-KE annealed crosslinking with the K coil duplex. A-C) AFM analysis of γPFD-KE filaments crosslinked with the K coil duplex at an increasing concentration of 0.5 μM, 1.0 μM, and 1.5 μM, respectively. The AFM micrographs were acquired through air mode acquisition. Scale bar = 500 nm. **D-F)** AFM analysis of γPFD-KE filaments crosslinked with the K coil duplex at an increasing concentration of 0.5 μM, 1.0 μM, and 1.5 μM, respectively. The AFM micrographs were acquired through liquid mode acquisition. Scale bar = 1 μm.

Liquid mode allows for the structures to be imaged in their native buffer without the need to perturb the structures on the mica surface. A similar titration was done, where the K coil duplex concentration was varied from 0.5 μM to 1.5 μM and imaged through liquid mode AFM to identify either a similar trend under air mode AFM or if the modes of acquisition results in a dramatically different result (Figure 4.5 D-F). Just as the previous titration experiment, a crosslinker concentration at 1.0 μM seemed to give minimal films and arrays, whereas a concentration at 1.5 μM resulted in films spanning several microns in size. Lastly, a concentration of 0.5 μM resulted in the highest abundance of observed arrays, with multiple patches spanning several microns. The overall difference of liquid mode acquisition was that the films were stabilized and displayed a clear two-dimensional organization without the clustering seen under air mode acquisition with and without the annealing process. There were regions where the height profile was not well-defined but that may be due to overlapping filaments, salt contaminations, or highly dense regions where the filaments start to cluster but to a minimal extent. Overall, liquid mode AFM resulted in the preservation of these delicate thin film structures, allowing for a better understanding of this self-assembling process.

Once these conditions were optimized, more deliberate measurements were taken to characterize the extent of these self-assembled thin film materials. Through much wider scan sizes, thin films up to 20 micrometers in size were visible under AFM (Figure 4.6 A). These sheets exhibited greater clustering, and the scan was not as clean as smaller scan sizes. However, this may be due to the extent of material on the surface, allowing for more protein aggregation to be seen at such a scale. However, through a zoom-in scan, the nature of ordering of these thin films were highlighted (Figure 4.6 B). As seen on the micrograph,

the γPFD-KE were seen to be well aligned, exhibiting order on a micron scale. There were instances where much smaller filaments seem to pack in areas where the longer filaments left gaps, indicating self-sorting and thermal equilibration through this annealed self-assembly process. However, throughout the scan, there were visible areas where a few filaments were duplicated, which highlights a drawback and artifact of liquid mode imaging. Due to the mobility of the structure in the buffer, minor drift is seen through this mode of acquisition.

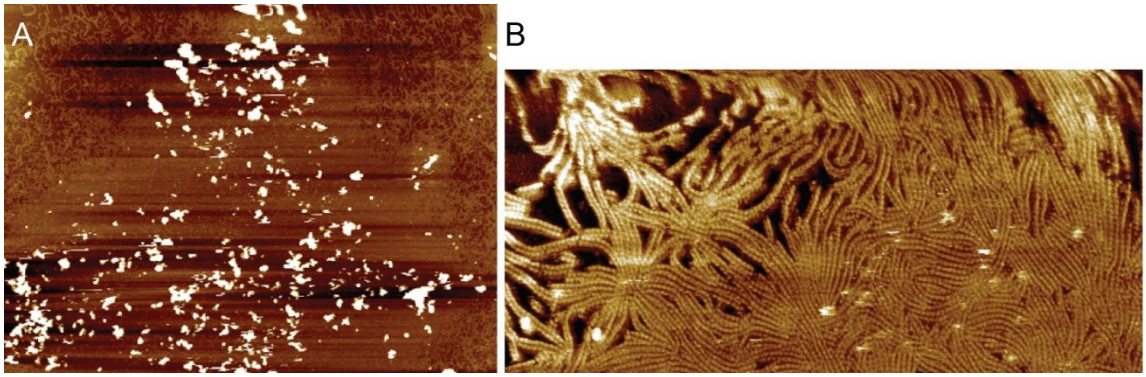

Figure 4.6. γPFD-KE thin film analysis. A) Wide-field micrograph of the γPFD-KE thin film under liquid mode AFM. Scale bar = 2 μm. **B)** Zoom in of the γPFD-KE thin film, highlighting the well-ordered array and dense packing. Scale bar = 200 nm.

To further characterize these thin-film assemblies as well as avoiding any artifacts of AFM acquisition, these materials were characterized using negative-stain TEM. Similar to the morphologies seen under AFM, there were areas of low-density crosslinking of the γPFD-KE filaments (Figure 4.7 A), where patches of these films were seen with extended filaments creating a network between thin film patches. On the other hand, there were areas of high-density crosslinking, where the γPFD-KE filaments were tightly packed, forming a dense thin film (Figure 4.7 B). γPFD-KE filaments can still be distinguished in the high-density area, highlighting the tight packing of these structures, similar to the high-density areas seen under AFM. Due to the same morphologies seen under both AFM and TEM, it

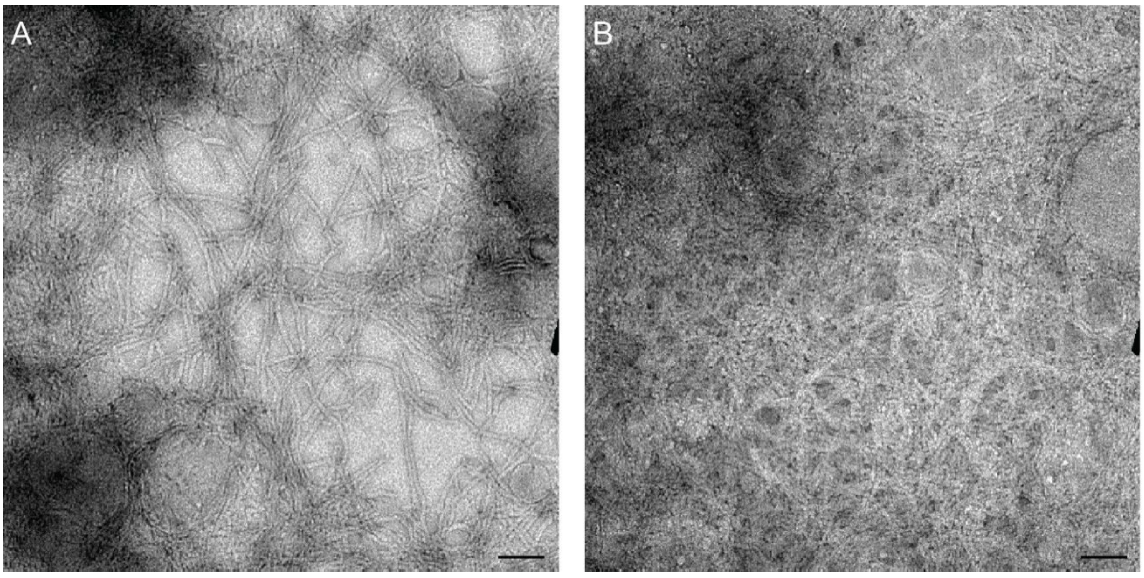

Figure 4.7. TEM characterization of γPFD-KE thin films. A) Low density area of the crosslinked γPFD-KE filaments. Scale bar = 100 nm. **B)** High density area of crosslinked γPFD-KE filaments. Scale bar = 100 nm.

is apparent that the K coil duplex is an efficient strategy to crosslink the γPFD-KE filaments into large, micrometer-sized hybrid protein-DNA thin films.

Based on the successful crosslinking by the K coil duplex to form delicate thin films, the second type of crosslinker, the 3pt-star K coil crosslinker, was used. Upon the initial addition of the 3pt-star K coil crosslinker, there were many areas where visible clusters were seen (Figure 4.8 A). These types of aggregated clusters spanned several micrometers in size, indicating higher-ordered assembly. As before, these initial experiments were conducted using air mode AFM. By zooming into these clustered areas, it can be seen that these areas are areas of high γPFD-KE filament entanglement (Figure 4.8 B, C). In figure 4.8 C, γPFD-KE filaments are packed together in a crude fashion, deviating from the type of packing seen from the K coil duplex. In addition, the small 3-pt star K coil crosslinker can be seen on the mica surface, hinting towards inefficient crosslinking.

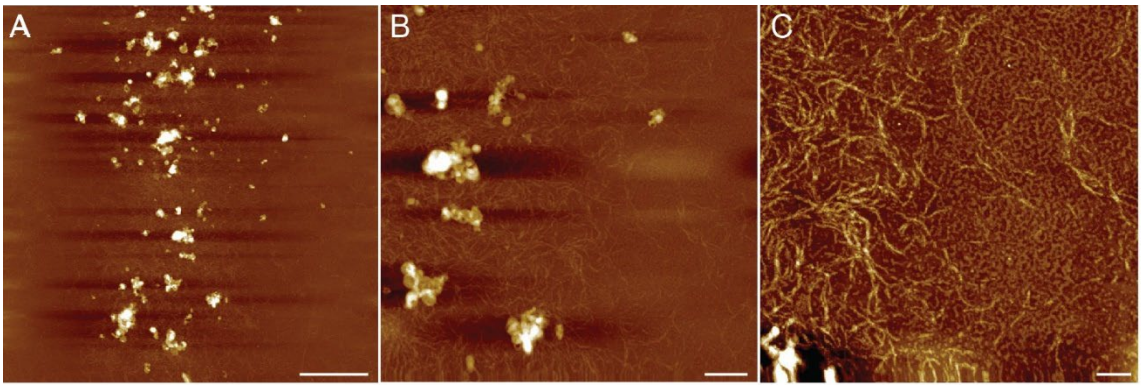

Figure 4.8. γPFD-KE crosslinking with the 3pt-star K coil linker. A) Wide-field AFM micrograph of γPFD-KE filaments crosslinked with the 3pt-star K coil linker. Scale bar = 2 μm. **B)** AFM micrograph of γPFD-KE filaments crosslinked with the 3pt-star K coil linker. Scale bar = 500 nm. **C)** Zoomed in AFM micrograph of γPFD-KE filaments crosslinked with the 3pt-star K coil linker. Scale bar = 200 nm.

To optimize the assembly process using the 3pt-star K coil crosslinker, three different concentrations were tested, ranging from 0.5 μM to 1.5 μM. Once these three different sample types were assembled, these samples were analyzed under AFM (Figure 4.9 A-C). As with the K coil duplex, the 3-pt star K coil crosslinker seemed to give the best assemblies at a concentration of 0.5 μM. Through a wide-field micrograph, there were multiple areas where the γPFD-KE filaments were crosslinked to form similar arrays to those seen with the K coil duplex. As the concentration of the crosslinker increased to 1.0 μM, the micrograph revealed less areas of densely crosslinked regions. As the concentration increased to 1.5 μM, there were even less areas of densely crosslinked regions, compared to the 0.5 μM crosslinked sample. In addition, there were more examples of areas that formed clusters rather than well-formed arrays. The increase in more aggregated clusters rather than well-defined arrays might indicate that the higher concentration results in kinetically trapped aggregate.

Due to the inability to anneal the γPFD-KE filaments with the 3pt-star K coil crosslinker, it was difficult to optimize the sample futher. The reason for the inability for

the anneals is potentially due to ill-formed 3-pt star structures. The structure does not form perfectly and requires a purification step to obtain the pure 3-pt star K coil structure. Therefore, any annealed structure may give rise to multiple γPFD-KE filaments being crosslinking through a non-homogenous crosslinker. Due to the non-homogeneity, this avenue was avoided because of the lack of well-defined assembly.

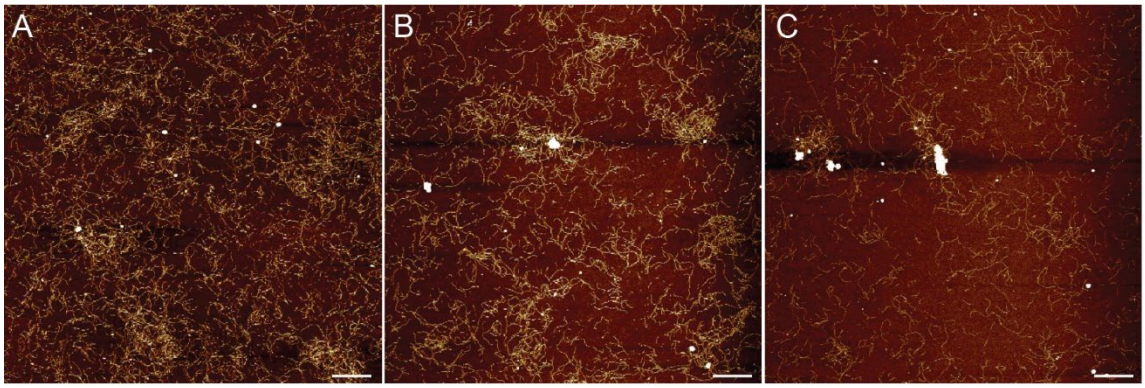

Figure 4.9. Titration of the 3pt-star K coil linker with γPFD-KE. A) γPFD-KE filaments crosslinked with the 3pt-star K coil linker at a concentration of 0.5 μM. **B)** γPFD-KE filaments crosslinked with the 3pt-star K coil linker at a concentration of 1.0 μM. **C)** γPFD-KE filaments crosslinked with the 3pt-star K coil linker at a concentration of 1.5 μM. Scale bars = 1 μm.

To continue to examine the self-assembly process, the γPFD-KE filaments crosslinked with the 3-pt star K coil linker were examined under negative-stain TEM. Under a wide-field TEM micrograph, there was clear evidence that the γPFD-KE filaments self-assembled into a well-ordered thin film, spanning several micrometers in size (Figure 4.10 A). A zoom-in on the thin film revealed remarkable ordering of the γPFD-KE filaments, into a densely packed film (Figure 4.10 B). The high-density packing and ordering seem to be more well-defined than the K coil duplex route, indicating that the multivalency of the 3-pt star might result in a better assembly. However, the interpretation of these results is due to the lack of well-defined arrays under AFM. Indeed, TEM reveals the assembly in a better light due to the wide-field analysis. Ultimately, the TEM analysis

highlights the well-defined arrays that can be achieved through the crosslinking of the γPFD-KE filaments using the 3-pt star K coil crosslinker. In the end, both types of crosslinkers proved to be excellent candidates to allow for the self-assembly of the γPFD-KE filaments into nicely defined arrays on a micrometer scale.

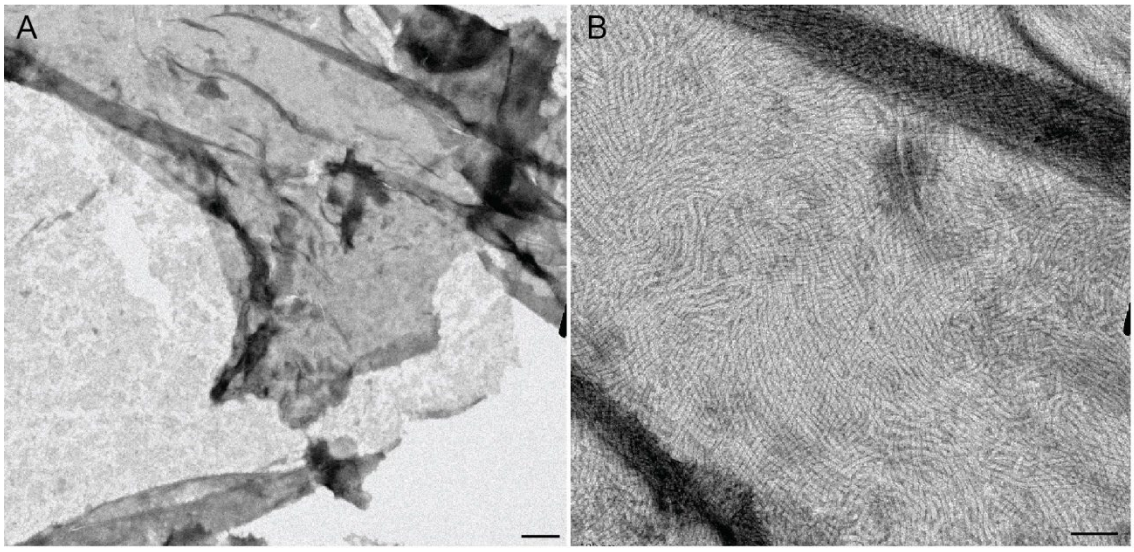

Figure 4.10. TEM analysis of γPFD-KE filaments with the 3-pt star K coil crosslinker. A) Wide-field TEM micrograph of the γPFD-KE filaments crosslinked with the 3-pt star K coil crosslinker. Visible macroscopic thin film sheets are seen. Scale bar = 0.5 μm. **B)** TEM micrograph of the γPFD-KE filaments crosslinked with the 3-pt star K coil crosslinker. Scale bar = 100 nm.

4.2.2 Reversibility of DNA Crosslinked Prefoldin-KE Filaments

Based on the K coil duplex crosslinker design, the crosslinking can be rendered reversible through the addition of the displacement strand *or* through the addition of DNase enzymes. In this manner, the crosslinkers can be disrupted through strand displacement, or the DNA crosslinker can be degraded enzymatically while preserving the protein filaments. The initial experiment that probed this reversibility was through a titration experiment on the conditions that formed reliable thin films under AFM. The γPFD-KE filaments were kept at 0.1 mg/mL and the K coil duplex was kept at a concentration of 0.5 μM. The

titration consisted of ranging the displacement molar equivalents of 1x, 4x, 10x, 20x, and 30x.

Under AFM analysis, the control sample revealed thin films on the order of microns, indicating that the self-assembly process is behaving as intended under these conditions (Figure 4.11 A). Upon an equimolar addition of the displacement strand, there were still large patches of the γPFD-KE thin films (Figure 4.11 B). Based on the

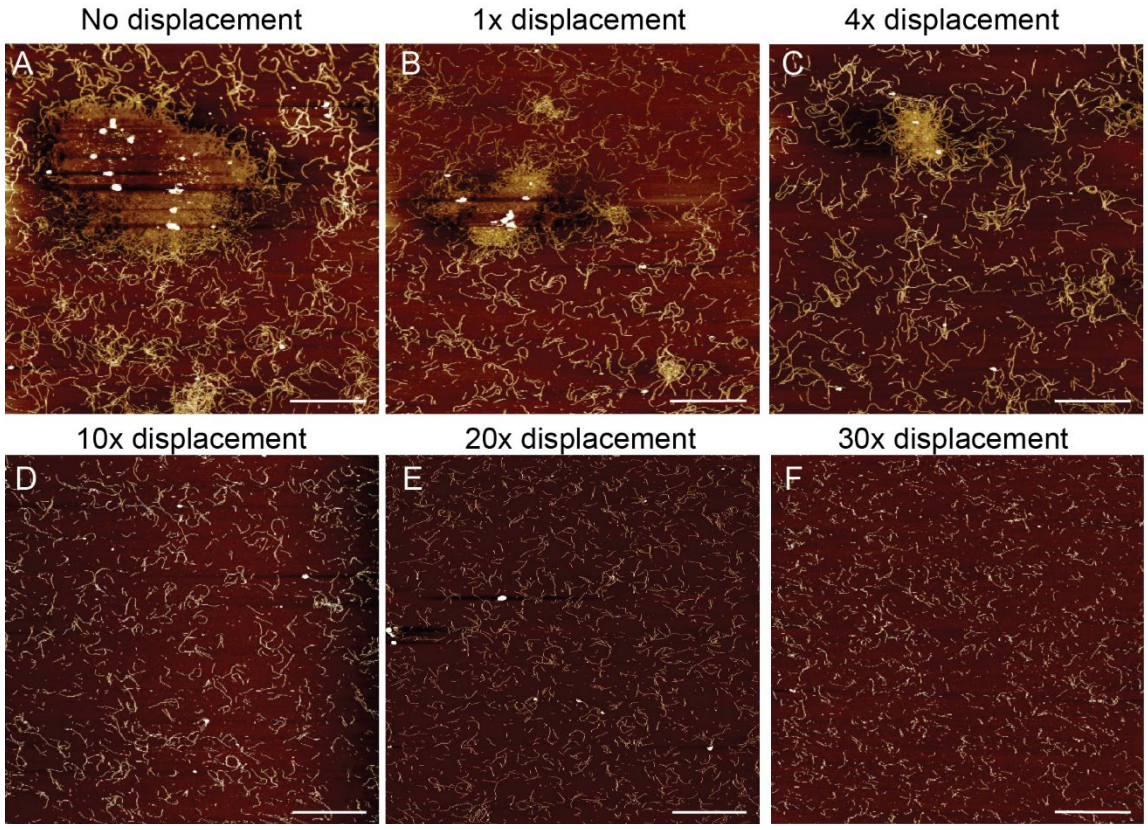

Figure 4.11. Displacement analysis of γPFD-KE K coil duplex crosslinked thin films. **A)** γPFD-KE K coil duplex crosslinked thin films without the addition of the displacement strand. **B)** γPFD-KE K coil duplex crosslinked thin films with the addition of the displacement strand at a 1x molar equivalents. **C)** γPFD-KE K coil duplex crosslinked thin films with the addition of the displacement strand at a 4x molar equivalents. **D)** γPFD-KE K coil duplex crosslinked thin films with the addition of the displacement strand at a 10x molar equivalents. **E)** γPFD-KE K coil duplex crosslinked thin films with the addition of the displacement strand at a 20x molar equivalents. **F)** γPFD-KE K coil duplex crosslinked thin films with the addition of the displacement strand at a 30x molar equivalents. Scale bars = 2 μM.

displacement gel (Figure 4. 2 C), the displacement reaction occurs quantitatively at a 1:1 molar ratio but with the dense packing of the thin film, some toehold regions might not be as accessible for the displacement strand to bind, resulting in inefficient displacement. By increasing the molar equivalents of the displacement strand to 4x, there was a reduction in the amount of thin film regions visible under AFM as well as a reduction in the size of these thin film patches (Figure 4.11 C). By dramatically increasing the molar equivalents to 10x, there were hardly any thin film patches seen under AFM (Figure 4.11 D). On the surface, most of the γPFD-KE filaments were monodispersed, indicating that the displacement strand at 10-fold molar excess is enough to completely reverse the non-covalent K coil crosslinkers. By pushing the molar ratio to 30x and 40x, the AFM micrographs revealed similar trends to the 10x sample, with no thin film patches seen on the mica surface.

Based on the titration experiment conducted using AFM analysis, it is sufficient to say that the displacement reaction was successful and represents a technique to reverse the self-assembly of the γPFD-KE filaments using the K coil duplex crosslinker. Although the concentration need for successful displacement was high, compared to standard strand displacement, the density of the self-assembled thin film might hamper the accessibility of the toehold. Despite the high molar equivalents needed for complete disruption, the reversibility of the K coil duplex with the displacement strand was successful.

To probe another avenue of reversibility, namely through enzymatic degradation of the crosslinker, DNase I was used to digest the K coil duplex. Due to DNase I being specific to accessible double-stranded DNA duplexes, this route of reversibility can enable to

control of thin film assembly while preserving the protein filaments. Initially, 0.5 µL of DNase I at a concentration of 10 mg/mL was added to the thin film assembly and allowed to incubate at 37 °C for one hour. After incubation, the thin film sample was analyzed under liquid mode AFM. The AFM micrograph revealed very few thin film patches, as compared to other sample without the addition of the DNase I (Figure 4.12 A). However, there were thin film patches observed but more so areas where the γPFD-KE filaments were binding to one another but not to a significant extent. To reduce the small patches seen under the first set on conditions, the amount of DNase I was double. Under AFM, the micrograph revealed no thin film patches, indicating successful digestion of the DNA crosslinks (Figure 4.12 B). The filaments were relatively monodispersed but there were a few areas that showed γPFD-KE filaments binding to one another but to a non-significant extent.

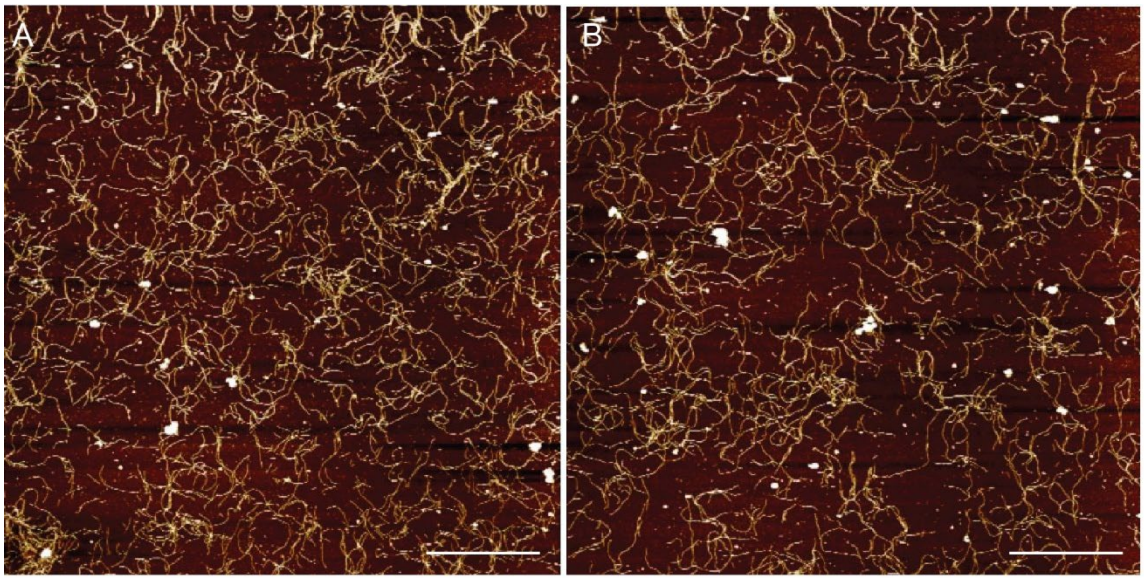

Figure 4.12. DNase I degradation of the K coil duplex crosslinked γPFD-KE thin films. A) 0.5 µL of 10 mg/mL DNase I treatment of the K coil duplex crosslinked γPFD-KE thin films. **B)** 1.0 µL of 10 mg/mL DNase I treatment of the K coil duplex crosslinked γPFD-KE thin films. Scale bars = 2 µm.

To further verify the degradation of the K coil crosslinkers, the same samples were imaged under negative stain TEM. As a control, the K coil crosslinked sample without the addition of DNase I was imaged to visualize the extent of crosslinking under the optimal conditions (Figure 4.13 A). The TEM micrograph revealed a dense network of crosslinked γPFD-KE filaments. The dense patch of filaments was heavily stained and the network had filaments extending from the periphery of the thin film patch. However, upon the addition of 0.5 μL of DNase I, the TEM micrograph revealed dispersed fibers but also areas where the filaments were still clustered in close proximity (Figure 4.13 B). There were filaments extending from this patch to create a network with other smaller patches, indicating larger films that were assembled but have been disrupted by the DNase I treatment. By doubling

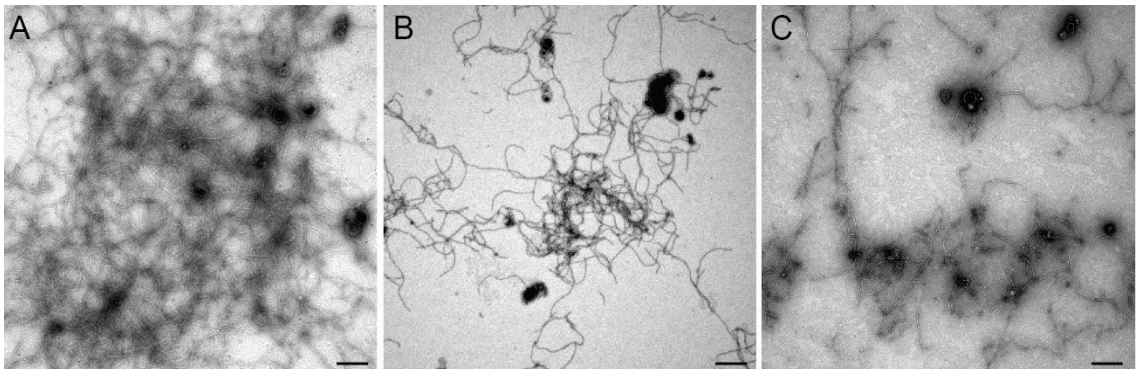

Figure 4.13. TEM analysis on DNase I degradation of the K coil duplex crosslinked γPFD-KE thin films. A) γPFD-KE thin films crosslinked with the K coil duplex. **B)** 0.5 μL of 10 mg/mL DNase I treatment of the K coil duplex crosslinked γPFD-KE thin films. **C)** 1.0 μL of 10 mg/mL DNase I treatment of the K coil duplex crosslinked γPFD-KE thin films. Scale bars = 200 nm.

the concentration of DNase I in the sample, the TEM micrograph revealed a significant decrease in the number of crosslinked filaments. Many of these filaments were well dispersed and the patches that were crosslinked were sparse and not densely clustering as seen in previous TEM micrographs. With the results corroborating the results seen under AFM, both imaging techniques reveal the successful approach to control the self-assembly of the γPFD-KE filaments through the degradation of the DNA crosslinkers.

4.2.3 Assembly of DNA Crosslinked Prefoldin-E_2/K_2 Filaments

Based on the assembly that was seen utilizing the two different K coil crosslinkers, the approach was modified to see if the γPFD-KE filaments can assemble with coil variants that are not complementary, i.e., γPFD-E_2 or γPFD-K_2 (Figure 4.14 A, B). The rationale between preventing the self-complementarity was to deduce whether the self-complementary was needed for efficient and well-defined self-assembly or if these two-heptad coiled coil system is enough for well-defined self-assembly. As a result, each of

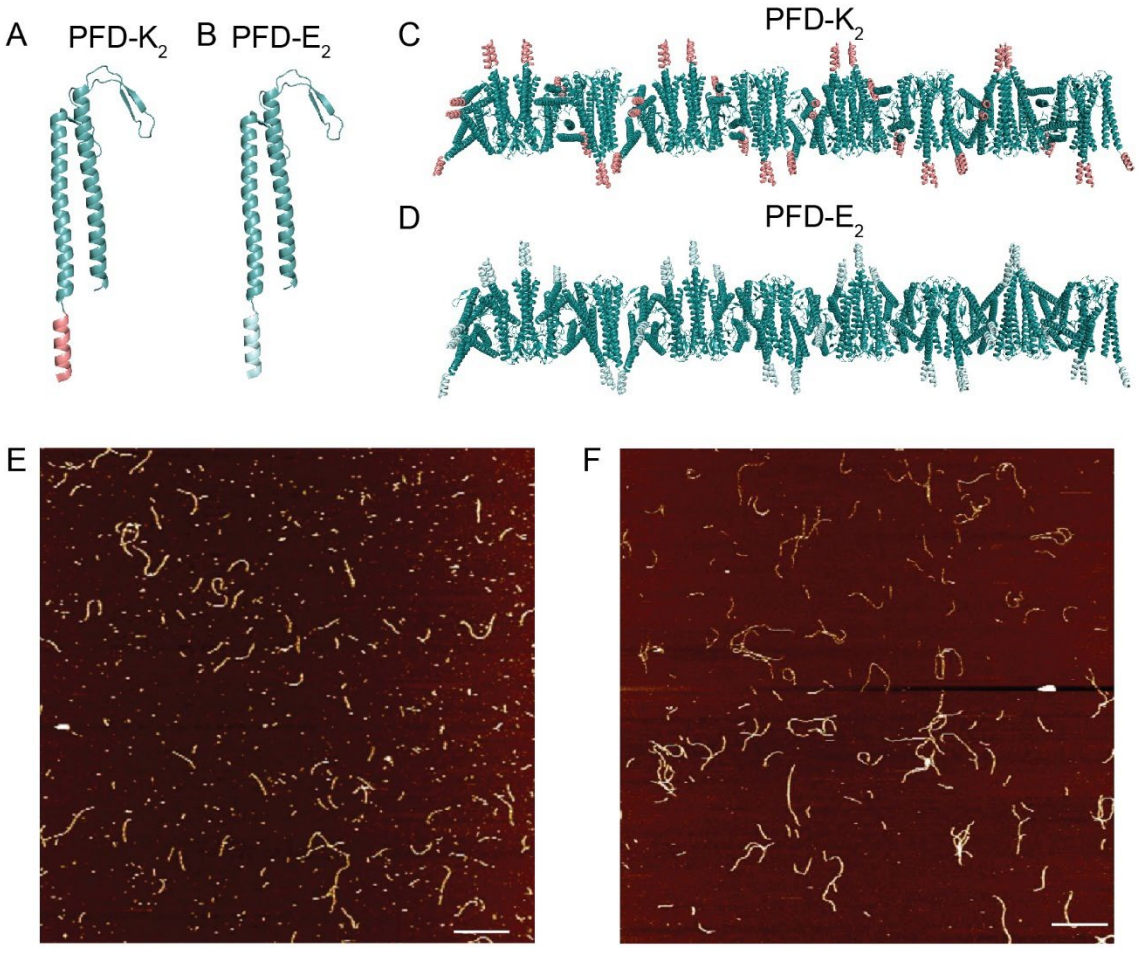

Figure 4.14. γPFD-coil variants. A) Cartoon schematic of the extension of γPFD with the two-heptad K coil. **B)** Cartoon schematic of the extension of γPFD with the two-heptad E coil. **C)** Cartoon schematic of the γPFD-K_2 filament. **D)** Cartoon schematic of the γPFD-E_2 filament. **E)** AFM micrograph of the γPFD-E_2 filaments. Scale bar = 1 μm. **F)** AFM micrograph of the γPFD-K_2 filaments. Scale bar = 1 μm.

these γPFD-coil variants were expressed and purified. The resulting protein filaments should result in a high density of the two-heptad coils (Figure 4.14 C, D). It is anticipated that the multi-valency should result in an increase in binding affinity between the K coil and the E coil, allowing for self-assembly. To make sure that the γPFD-coil variants still formed well dispersed filaments, each of these coil variants were taken to the AFM and imaged. For the γPFD-E_2 filaments, the AFM micrograph revealed protein filaments ranging from 100 nm to over micrometer in size (Figure 4.14 E). These filaments were well dispersed, with no aggregation seen. For the γPFD-K_2 filaments, the filaments were well dispersed as well but seemed a bit longer that the γPFD-E_2 filaments. The filaments were well over a micrometer in size. As for the γPFD-E_2 filaments, there was little aggregation/bundling seen with the γPFD-K_2 filaments, indicating that any bundling seen in future cross-linking experiments is due to the crosslinker and not the self-complementarity of the protein filaments. It is important to note that these protein filaments result in better dispersed filaments compared to the γPFD-KE filaments, indicating that the reduction of self-complementarity should result in more refined and distinguishable self-assembly.

Due to the nature of the coils, the K-coil crosslinkers were immediately tested to see if this route would result in similar self-assembly as the γPFD-KE filaments. If the self-assembly resulted in well-defined films, the complementary E-coil crosslinkers would be synthesized and tested as well. To obtain an initial idea of the self-assembly process of the γPFD-E_2 filaments with the K-coil duplex, a few concentrations were screened, ranging from the standard 0.5 μM to 3.0 μM (Figure 4.15 A-D). From the AFM micrographs, it was revealed that the optimal concentration of hybrid self-assembly was utilizing a 0.5 μM

concentration with 0.1 mg/mL of the γPFD-E2 filaments (Figure 4.15 A). From the AFM micrograph, there were areas of high crosslinking density and many areas with low crosslinking density, leaving a few gaps between each crosslinked patch. Most of these patches were not as large as previously seen with the γPFD-KE filaments at the same conditions. It is believed that the large disparity from the nicely formed γPFD-KE thin films and these patches of self-assembled γPFD-E2 is due to the small self-complementarity of the γPFD-KE thin films. Since these are self-complementary, the K-coil duplexes might allow for the γPFD-KE to come in close proximity, allowing for the γPFD-KE

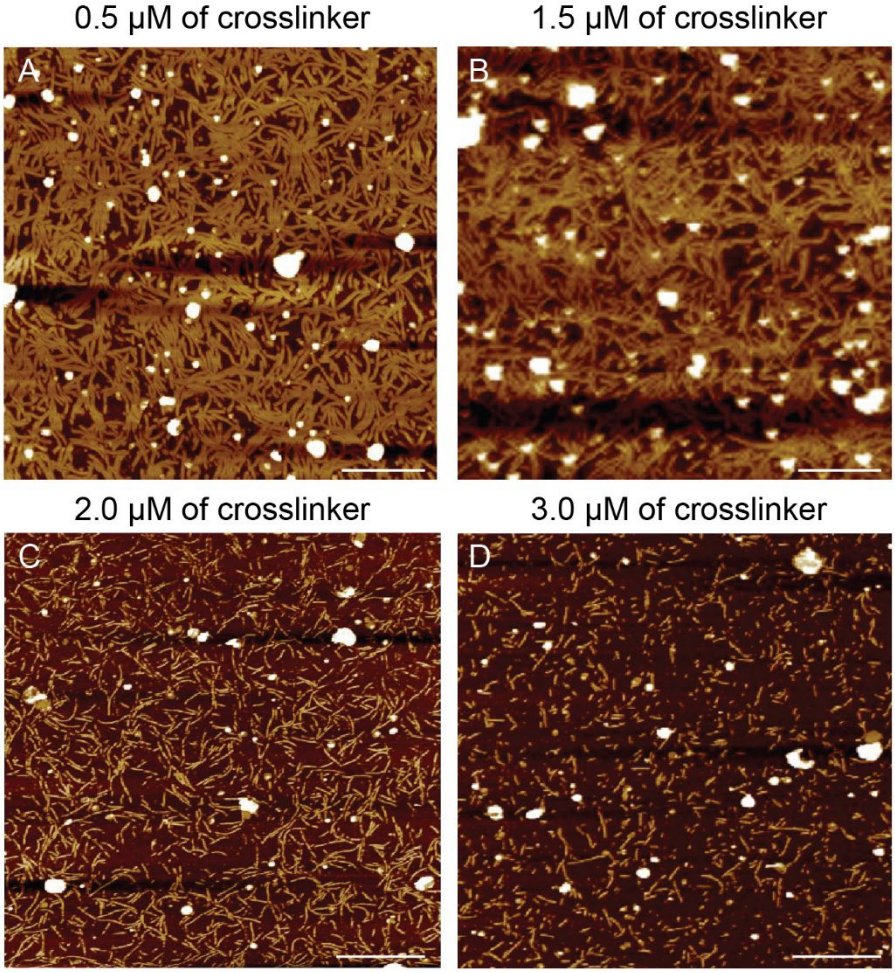

Figure 4.15. Crosslinking of γPFD-E2 with the K-coil duplex. A-D) AFM micrograph of the γPFD-E2 filaments crosslinked with the K-coil duplex. The concentration ranges from 0.5 to 3.0 μM, respectively. Scale bars = 600 nm.

complementary coils to “zip up”. Since these samples also undergo a thermal annealing process, the thermal energy might enable better film formation. As a result, the self-complementary γPFD-KE filaments form much larger and nicely defined thin films as compared to the γPFD-E_2 variants.

As the crosslinker concentration increases to 1.0 μM, crosslinked patches are observed at a high density, closing the unclosed gaps seen at the lower concentration (Figure 4.15 B). The higher concentration resulted in more crosslinking which indicates that the multi-valent mode of self-assembly occurs only when there is enough crosslinker in solution. In this regard, one would expect that by increasing the crosslinker concentration one would see much better self-assembled thin films through this coil approach. However, by increasing the crosslinker concentration by 2.0 μM, there is very little assembly of the filaments, and the majority of the filaments are well-dispersed on the surface of the mica (Figure 4.15 C). It is unclear why the increase leads to unfavorable self-assembly conditions, but some possible reasons include electrostatic repulsion, solution crowding, or steric hinderance. These results are further strengthened by the non-assembled γPFD-E_2 at a crosslinking concentration of 3.0 μM (Figure 4.15 D). Most of these filaments in the AFM micrograph were very well-dispersed, indicating little to no self-assembly. In addition, the filaments seemed much shorter compared to the γPFD-KE filaments. One can reason that if the initial protein filaments are shorter than the multi-valent approach for self-assembly would be hindered. As a result, there is less crosslinking of one specific filament to other filaments, resulting in less thin film assembly.

To ensure that the hybrid assembly is reproducible and characterized thoroughly, the γPFD-E_2 fiber sample that was set at 0.1 mg/mL and crosslinked with 0.5 μM of the K-coil crosslinker was analyzed by TEM. The TEM micrographs revealed different degrees of self-assembly, similar to what was seen with the γPFD-KE thin films, which included low-density and high-density areas of crosslinking (Figure 4.16 A-D). The initial wide-field view revealed a low-density area of crosslinking, indicating patches of crosslinked fibers that begins to branch out from these patches (Figure 4.16A). Some of these patches resulted in darkly stained areas due to the accumulation of protein filaments. By taking a closer look, the was a high overlap between these patches, where the filaments overlap with one another, creating a tightly crosslinked network (Figure 4.16 B). Due to the degree of overlap, there was a clear γPFD-E_2 filament to the top right of the micrograph, revealing the helical repeats of the protein filament.

Other areas on the TEM grid revealed much higher degrees of crosslinking density. With a wide-field view of the high-density crosslinked area, the micrograph reveals a large degree of assembly, spanning several micrometers in size (Figure 4.16 C). Due to the high degree of crosslinking, the staining revealed dark patches, obscuring some of the well-assembled thin films. To take a closer look, we zoomed into the area to see the well-ordered assembly. The zoomed-in micrograph revealed extensive crosslinking where the protein filaments are either nicely aligned or creating a dense network of overlapping filaments (Figure 4.16 D). The dense network was similar to the γPFD-KE thin films structures seen in the past, indicating similar assembly utilizing the γPFD-E_2 protein filaments. The TEM micrographs reveal similar morphologies as seen under AFM, indicating that the K-coil duplex is an effective method for the self-assembly of the γPFD-E_2 into thin film

assemblies. However, it is important to note that the TEM micrographs revealed better, and tighter assembly compared to AFM. These differences might be due to the liquid mode acquisition of AFM or different modes of surface adhesion on the mica chip or on the TEM

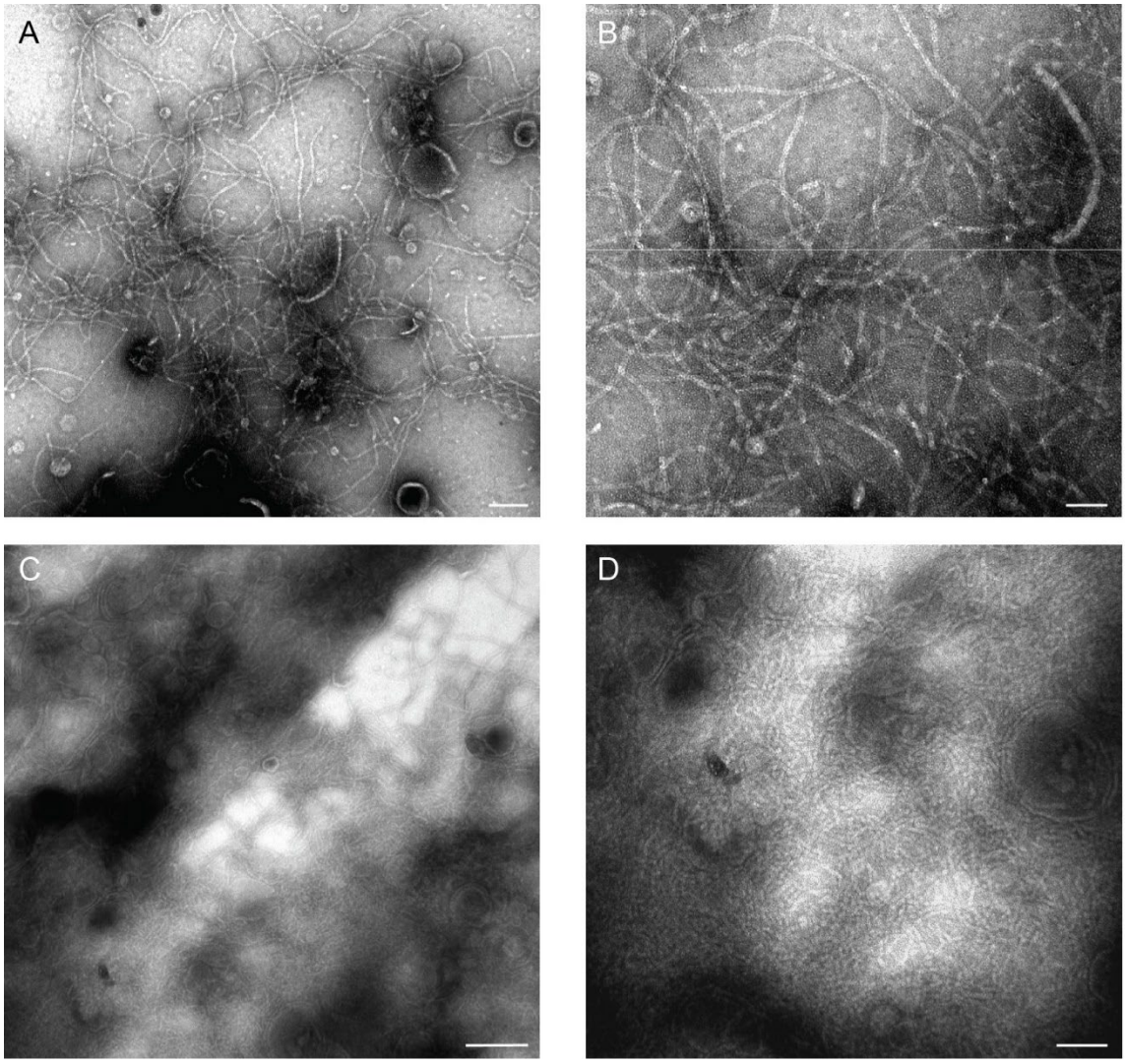

Figure 4.16. TEM analysis of the crosslinking of γPFD-E$_2$ with the K-coil duplex. **A)** Low-density TEM micrograph of the γPFD-E2 filaments crosslinked with the K-coil duplex. Scale bars = 100 nm. **B)** Zoom in of the TEM micrograph in (**A**). Scale bars = 50 nm. **C)** High-density TEM micrograph of the γPFD-E2 filaments crosslinked with the K-coil duplex. Scale bars = 200 nm. **D)** Zoom in of the TEM micrograph in (**C**). Scale bars = 100 nm.

carbon grid. Nonetheless, each of these modes of microscopy revealed extensive crosslinked protein filaments.

Based on the results of the self-assembly between the γPFD-E_2 filaments and the K-coil crosslinker, the reversibility of these assemblies was tested through strand displacement of the K coil crosslinker and the nuclease degradation of the DNA-based crosslinker. Based on the initial strand displacement reactions with the γPFD-KE system, it is known that an excess of the displacement strand should be enough to allow for the reversibility of these hybrid assemblies. As a result, the γPFD-E_2 assembly with the K-coil crosslinker was treated with 50x of the displacement strand. The resulting AFM micrograph revealed well dispersed filaments on the mica surface with little to no crosslinking seen (Figure 4.17 A). Based on the micrograph, it is revealed that the 50x addition of the displacement strand was successful in breaking apart the dense assemblies previously seen with the γPFD-E_2 system crosslinked the K-coil duplex. To further validate the reversibility of the hybrid assemblies, nuclease degradation was explored. Using 0.5 µL of DNase I (10 mg/mL) resulted in a severe reduction of γPFD-E_2 filaments with the

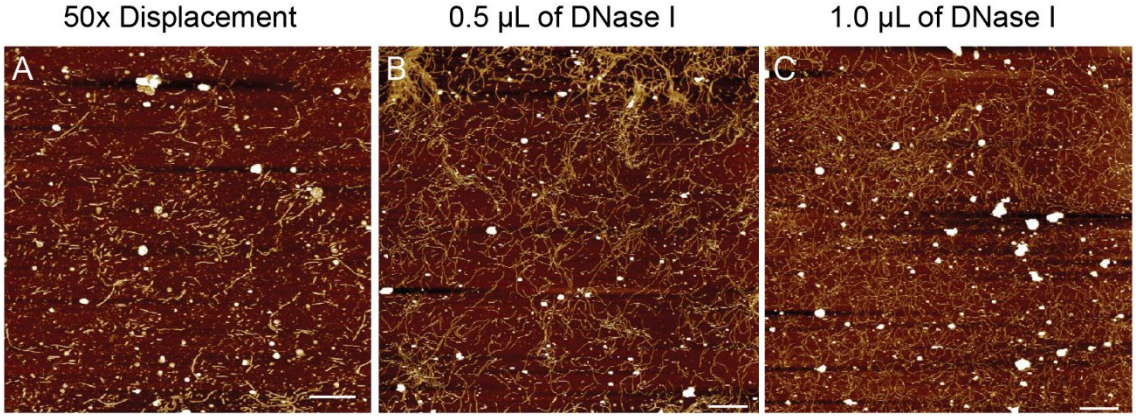

Figure 4.17. AFM analysis of the disruption of the crosslinked γPFD-E_2 filaments with the K-coil duplex. A) AFM micrograph of the crosslinked γPFD-E_2 filaments with the K-coil duplex displaced with 50x of the displacement strand. Scale bar = 500 nm. **B)** AFM micrograph of the crosslinked γPFD-E_2 filaments with the K-coil duplex disrupted by the addition of 0.5 µL of DNase I. Scale bar = 1 µm. **C)** AFM micrograph of the crosslinked γPFD-E_2 filaments with the K-coil duplex disrupted by the addition of 1.0 µL of DNase I. Scale bar = 1 µm.

K-coil crosslinker (Figure 4.17 B). However, based on the AFM micrograph, there were still visible patches of crosslinked γPFD-E_2 filaments, indicating that the concentration of the nuclease was not high enough to result in complete degradation of the DNA crosslinker. As a result, the nuclease concentration was doubled to 1.0 μL. The doubling of the nuclease concentration resulted in even more dispersed filaments on the mica surface (Figure 4.17 C). There were areas that seemed to be overlapping or crosslinked but may be due to just the concentration of the γPFD-E_2 filaments. The AFM micrograph indicated that the nuclease treatment to these hybrid assemblies result in an effective method for reversing these non-covalent crosslinks.

To further verify the reversibility of these hybrid assemblies, each of these systems were analyzed using negative-stain TEM. Upon treatment with the 50x displacement strand, the first TEM micrograph revealed heavily stained patches of filaments (Figure 4.18 A). These patches were dramatically different to what was seen under TEM before the displacement reaction, indicating that the displacement strand resulted in a significant change in the assembly process. To obtain a better understanding of the displacement reaction, a zoom-in was taken. The resulting TEM micrograph revealed dispersed γPFD-E_2 filaments, where there was some overlap, but nothing that depicted well-ordered and dense crosslinking (Figure 4.18 B). Most of the filaments that were seen were well dispersed, indicated that the assembly process was effectively disrupted through the displacement reaction. For the nuclease degradation experiment, the first sample that was treated with 0.5 μL of DNase I was analyzed under TEM. A wide-field TEM micrograph revealed clusters of heavily stained γPFD-E_2 filaments (Figure 4.18 C). There were a few filaments scattered across the carbon grid as well. The scattered filaments in addition to the

severely reduced crosslinking indicates that the nuclease was effective at degrading some of the K-coil duplex.

To obtain a better understanding of the clusters seen on the wide-field micrograph, a zoom-in was taken. The resulting micrograph revealed that the clusters were scattered filaments with some overlap and partial crosslinking between them (Figure 4.18 D). It is

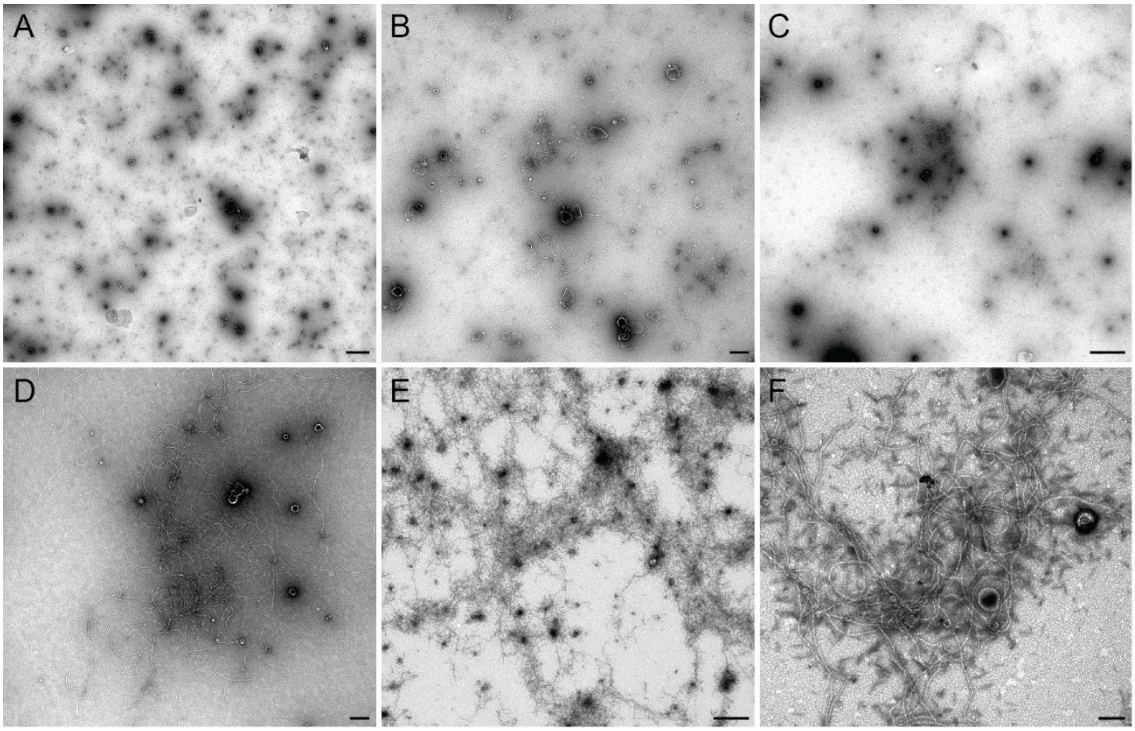

Figure 4.18. TEM analysis of the disruption of the crosslinked γPFD-E_2 filaments with the K-coil duplex. A) Wide-field TEM micrograph of the crosslinked γPFD-E_2 filaments with the K-coil duplex displaced with 50x of the displacement strand. Scale bar = 500 nm. **B)** Zoom-in on of the TEM micrograph in (**A**) of the crosslinked γPFD-E_2 filaments with the K-coil duplex displaced with 50x of the displacement strand. Scale bar = 200 nm. **C**) Wide-field TEM micrograph of the crosslinked γPFD-E_2 filaments with the K-coil duplex disrupted with 0.5 µL of DNase I. Scale bar = 1 µm. **D)** Zoom-in on of the TEM micrograph in (**C**) of the crosslinked γPFD-E_2 filaments with the K-coil duplex disrupted with 0.5 µL of DNase I. Scale bar = 200 nm. **E)** Wide-field TEM micrograph of the crosslinked γPFD-E_2 filaments with the K-coil duplex disrupted with 1.0 µL of DNase I. Scale bar = 1 µm. **F)** Zoom-in on of the TEM micrograph in (**E**) of the crosslinked γPFD-E_2 filaments with the K-coil duplex disrupted with 1.0 µL of DNase I. Scale bar = 100 nm.

difficult to say whether these filaments are indeed crosslinked with the K-coil duplex or just electrostatically bound. However, in comparison to the previous assemblies seen without the addition of the nuclease then what can be deduced is that the nuclease was effective to a certain extent to degrade the crosslink. To ensure complete degradation of the DNA-based crosslinker, the concentration of DNase I was increased to 1.0 µL. The nuclease-treated sample was analyzed under the TEM. The resulting TEM micrograph revealed entangled clusters that were speckled with these gray "shards" (Figure 4.18 E). The entangled clusters may represent patches of γPFD-E_2 filaments that are bridged with dispersed γPFD-E_2 filaments. The gray shards that were seen are possibly nuclease present at a high concentration or the remains of the degraded DNA crosslinker. To better understand these entangled patches, a zoom-in was taken to reveal the ordering of the filamentous patches. The resulting TEM micrograph revealed stained patches of filaments that were localized on the grid (Figure 4.18 F). The clusters of filaments on the grid were not interacting with each other, indicating the lack of physical crosslinking and more of a surface deposition effect. In addition, the clustering that was seen was much less ordered as compared to previously crosslinked filaments. From the micrograph, it can be deduced that the addition of the nuclease was an efficient method to degrade the DNA-based K-coil crosslinkers.

4.2.4 Improving the Self-assembly of DNA Crosslinked Prefoldin-KE Filaments

To further investigate the ability of the K-coil duplex to crosslink the γPFD-KE filaments, a new K coil crosslinker was devised. Initially, each of the oligonucleotides that were conjugated to the K coil peptides were on the N-terminus of the peptide, allowing for closer self-assembly interactions with the γPFD-KE filaments (Figure 4.19 A). The parallel

interactions of the K coils bring the K-coil duplex in closer proximity, allowing for the other K coil to interact with another γPFD-KE monomer. As seen, this method promoted the efficient crosslinking of the γPFD-KE filaments into well-defined protein-DNA thin films. The rationale between the new K-coil duplex was to see if the new directionality of crosslinking either promotes or prevents the self-assembly of the γPFD-KE filaments into the thin film structures.

As such, the new conjugate that was synthesized was the C-term K coil-3pt-s Comp, which is the complementary DNA-peptide conjugate to the N-term K coil 3-pt-s Toe. In this regard, the self-assembly would allow for the extension of the K coil duplex, increasing the length span of the K coil duplex. Through this design, there is more space between individual γPFD-KE filaments (Figure 4.19 B). The assembly of the new (N-, C-) K-coil duplex was performed using the same conditions that resulted in well-defined thin films using the previous duplex system to compare the results. Once these samples were set up, the samples were taken over to the AFM to visualize the assembly. The AFM revealed poor and inefficient crosslinking (Figure 4.19 C, D) as compared to the previous duplex system. The first AFM micrograph revealed filaments that were connected and crosslinked, but there was more space between each filament as compared to the previous results. Previously, the γPFD-KE filaments were tightly packed and nicely arranged. However, the patch that is seen in Figure 4.19 C is around 1 micrometer in size but not as tightly packed as previous self-assembled films.

The other AFM micrograph revealed plenty of dispersed filaments that were not crosslinked. However, a small patch of crosslinked filaments was seen in Figure 4.19 D.

The patch had a large area of aggregation with tightly packed filaments surrounding the aggregated spot. This patch resembled some of the initial assembly experiments with these γPFD-KE filaments without an annealing protocol, resulting in aggregation and some defined assembly. Due to optimized conditions with the new (N-, C-) K-coil duplex, the results indicated that the orientation of this new design prevents efficient assembly of the γPFD-KE filaments. From these results, it highlights the two necessary factors for the well-

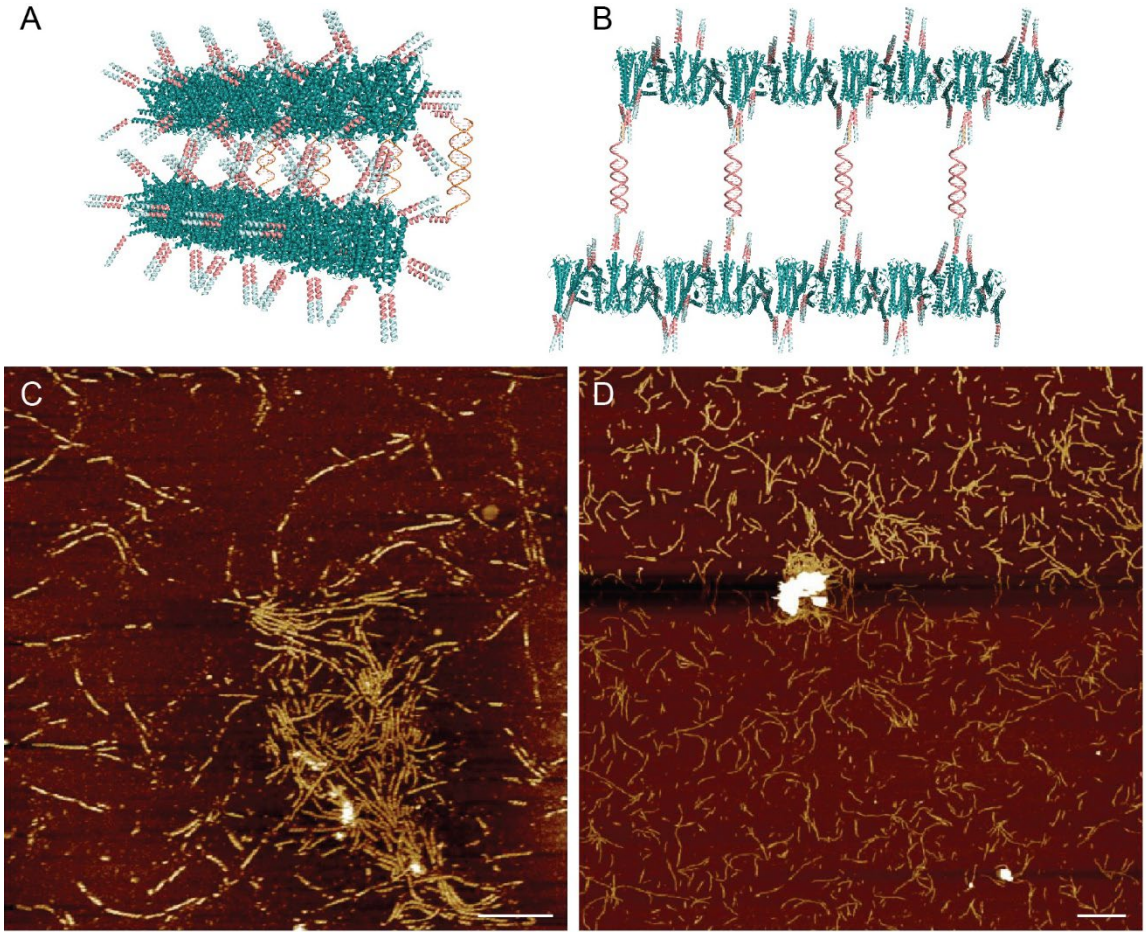

Figure 4.19. AFM analysis of the crosslinked γPFD-KE filaments with the (N-term, C-term) K-coil duplex. A) Schematic of the γPFD-KE filaments crosslinked with the K-coil duplex when the coils are both conjugated on the N-termini of the peptides. **B)** Schematic of the γPFD-KE filaments crosslinked with the N-K coil 3pt-s Cut conjugate and the C-K coil 3pt-s Complementary conjugate. **C)** AFM micrograph of the crosslinked γPFD-KE filaments with the (N,C-) K-coil duplex. Scale bar = 200 nm. **D)** AFM micrograph of the crosslinked γPFD-KE filaments with the (N,C-) K-coil duplex. Scale bar = 500 nm.

defined assembly of these protein-DNA hybrid aggregates. The first aspect is that the partial complementarity of the γPFD-KE, which, once crosslinked, allows for these filaments to "zip-up" and tightly assemble into these thin-film materials. The second aspect of the design is that the placement of the non-covalent crosslinkers is crucial for tight packing. By changing the orientation and increasing the space between each filament, the γPFD-KE filaments are prevented from tightly packing *and* zipping up, which resulted in non-tightly packed thin film structures.

To extent the self-assembly from two-dimensional thin films to three-dimensional hydrogels, the gelation of the γPFD-KE filaments was attempted with the K-coil duplex. A previous system that utilized the γPFD-K_2E_2 filaments reported the gelation at a 2 weight (wt) %.[212] Inspired from this approach, the same weight percentage was used to form a gel using the K-coil crosslinker. To test this idea, a wide variety of crosslinker concentrations was used to see if the crosslinker can promote gelation.

The first concentration that was used was 1 μM that was pre-annealed and added to the cured solution of the γPFD-KE filaments and allowed to assemble at room temperature overnight. After incubation, the two samples, one being the γPFD-KE filaments without the crosslinker and the other sample with the K-coil duplex, were inverted to test for gelation (Figure 4. 20A). The test tubes showed that most of the solutions in both test tubes flowed downward towards the cap, indicating no gelation. There was some solution at the top of the tubes but that was mainly due to surface. A four-fold increase in the crosslinker concentration resulted in a similar result, i.e., no gelation (Figure 4.20 B). The solutions in the photograph were running down the sides of the tube, indicating the liquid nature of the

samples. Increasing the concentration to 7 µM resulted in similar result, with no evidence of an increase in gelation (Figure 4.20 C). Most of the solutions in these samples were at the bottom of the tube.

Due to the negligible differences in the samples, the concentration of the crosslinker was increased to 13 µM. Once the tubes were inverted, most of the solutions still flowed to the bottom of the tube, but there was a retention of the solution at the top of the tube in both samples (Figure 4.20 D). Due to the negligible difference between the control sample and the treated sample, the results indicated a lack of gelation, requiring a higher concentration of the duplex crosslinker. An increase in the crosslinker concentration to 17 µM, the solution appeared cloudier compared to the previous samples (Figure 4.20 E).

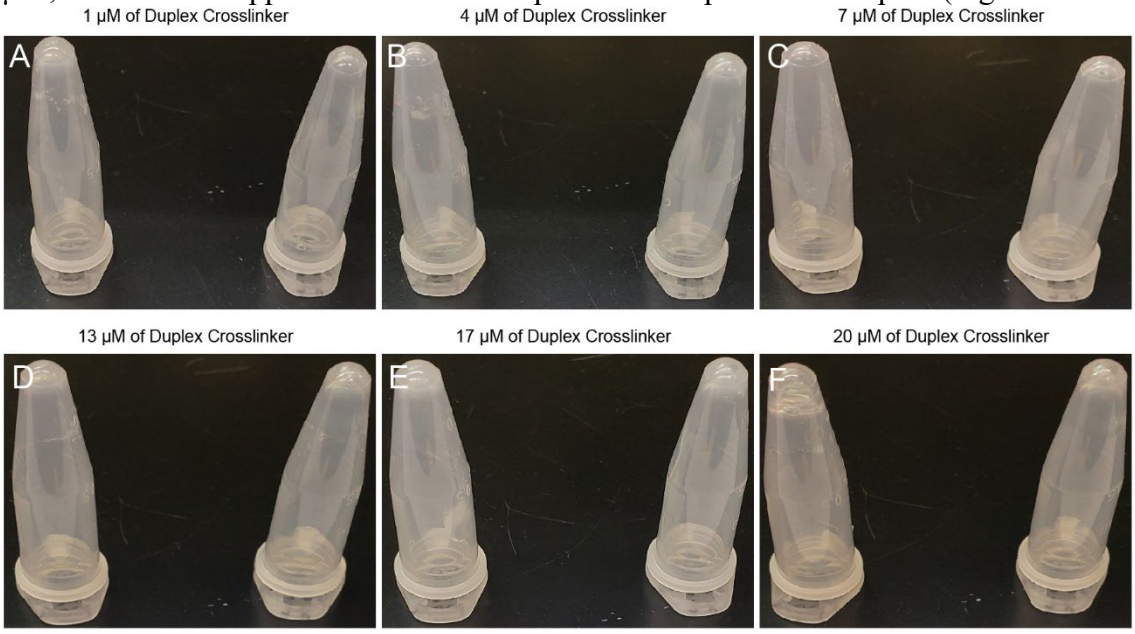

Figure 4.20. Gelation of crosslinked γPFD-KE filaments with the K-coil duplex. A-F) Digitial photograph of the γPFD-KE filaments crosslinked with the K-coil duplex at a 2 wt % with an increasing concentration of the K-coil duplex (1, 4, 7, 13, 17, 20 µM, respectively). The left sample in each photograph is the control sample without the addition of the K-coil crosslinker whereas the right tube contains the filaments with the addition of the K-coil crosslinker.

Once the tubes were inverted, there a retention of the solutions are the top of the tubes.

Each of these sample types resulted in a similar retention at the top of the tubes which indicated that there was not a change in the solution state. There was still some solution flowing to the bottom in both sample types, indicating more of a solution state compared to the gel state. Finally, in a last attempt to gel the solution, a concentration of 20 μM was used. The solution was a similar cloudiness as compared to the 17 μM sample. Upon inversion, there was still some liquid flow towards the bottom of the tube with some solution remaining at the top of the tube. The extent of solution that remained at the top was more than previous samples but there was not a discernible difference between the sample and the control. Due to the high concentration that would be required and due to the concentration of the DNA-peptide conjugates, there was no further optimization that was conducted.

To avoid the need for a high concentration of the DNA-peptide conjugate, the fraction of the γPFD-KE filaments was increased to 4 wt % to allow for a lower or similar concentration of the K-coil duplex to potentially promote gelation. The concentration is double that of the previously reported γPFD hydrogels but might facilitate more controllable gelation due to the reversible nature of the DNA crosslinker.

By curing/solvate the lyophilized γPFD-KE filaments at a concentration of 4 wt%, the resulting solution was cloudy and viscous. Upon incubation with the crosslinker, the solutions were inverted to test for gelation. Upon inversion, the control sample without the crosslinker had some liquid flow to the bottom of the tube but most of the solution stayed at the top, indicating a high viscous and possibly extensive entanglement/gelation (Figure 4.21 A). The sample with the crosslinker had more liquid characteristics, with more of the

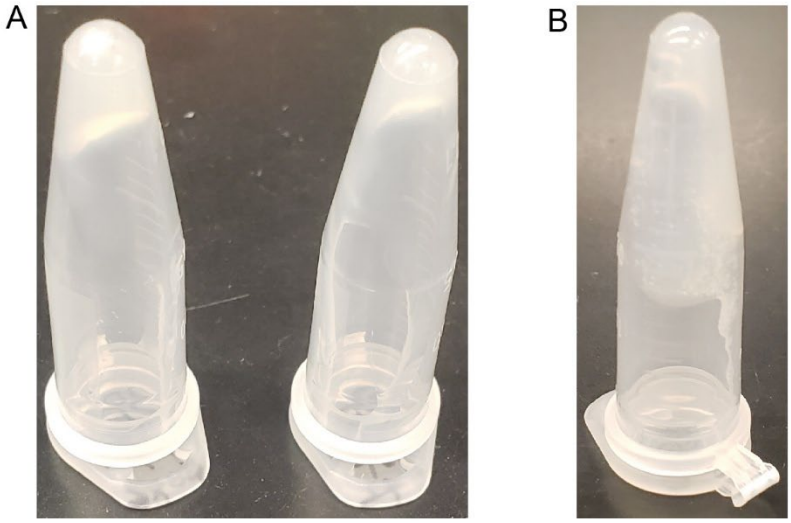

Figure 4.21. Gelation of crosslinked γPFD-KE filaments with the K-coil duplex at a higher concentration. A) Digital photograph of the γPFD-KE filaments (4 wt %) crosslinked with the K-coil duplex at a concentration of 13 μM. The left sample in each photograph is the control sample without the addition of the K-coil crosslinker whereas the right tube contains the filaments with the addition of the K-coil crosslinker. **B)** Digital photograph of the γPFD-KE filaments crosslinked with the K-coil duplex at a 4wt % with an increasing concentration of the K-coil duplex (13 μM). The sample was incubated at 37 °C overnight.

liquid flowing down to the bottom of the tube (Figure 4.21 B). Due to the increase in liquid flow, the tube-inversion experiment indicated that the crosslinker was inefficient at creating a hydrogel with the γPFD-KE filaments at a 4 wt%, when present at a 13 μM concentration. One final effort was made to reach a sol-to-gel transition, which was done by incubating the solution at 37 °C overnight. The rationale behind this was to provide some thermal energy into the system with the hopes of promoting more efficient crosslinks and better arrangement of the crosslinkers and the filaments. The resulting solution was less viscous than the initial solution, allowing for more of the solution to flow to the bottom of the tube upon inversion (Figure 4.21 C). Due to the negative results from this isothermal anneal, no further experiments were conducted.

4.3 Conclusion

The ability to generate 2D protein aggregates using designed DNA-coil crosslinkers was demonstrated in this chapter. The system exploits the ability to readily functionalize, stiff, thermostable protein filaments with self-assembling coil domains. These coil handles on the protein filaments were used for self-assembly through the synthetic DNA-peptide conjugates. The benefit of using DNA-peptides conjugates was to readily incorporate the structural benefits of DNA nanotechnology into the crosslinkers. Through this, DNA designed facilitated the development of 1D and 2D crosslinkers, which both resulted in protein thin films. In addition to the structural benefits, DNA strand displacement was easily incorporated into the design of the 1D crosslinker to promote *and* disassemble the protein thin films. Furthermore, due to the inclusion of oligonucleotide domains, the crosslinkers can be *selectively* degraded while retaining the protein filaments through DNA degradation.

Due to the reversibility displayed in this chapter, the system was tested with higher concentrations in hopes of achieving gelation. However, the results proved to be unsuccessful and require further optimization. Further experiments could involve either polarization microscopy to detect the crystallinity of these systems and SEM to detect the extent of self -assembly. Ultimately, this approach represents a way to achieve 2D arrays with superb physical properties and demonstrates two ways to modulate the self-assembly of hybrid protein-DNA nanomaterials.

4.4 Methods and Materials

Protein Expression and Purification. The gene encoding γPFD-KE/E_2/K_2 were synthesized as gBlocks gene fragments (Integrated DNA Technologies) and were inserted into the multiple cloning sites of the pET-19b plasmid (Novagen) using the Gibson assembly (New England Biolabs). The assembled plasmids were transformed into T7 Express competent cells, which were grown at 37 °C in LB Broth (Lennox) containing 100 μg/mL ampicillin up to OD600 = 0.6. γPFD-Cys protein expression was induced by adding IPTG to a final concentration of 0.5 mM and cells were grown for an additional 16 hours at 25 °C. The cells were harvested by centrifugation at 5000 rpm for 20 min, lysed by French press, and centrifuged at 13,000 rpm for 60 min. For all the γPFD variants, the resulting supernatant was then purified by multimodal chromatography resin (Capto Core 700, GE healthcare) using an AKTA FPLC. The proteins were loaded on the column with the equilibrium buffer (100 mM NaCl, 50mM Tris, pH 7.4). The elution peak was inspected using SDS-PAGE and SimplyBlue staining (Invitrogen), and the pure target protein was dialyzed overnight against water. Finally, the purified proteins were flash-frozen with liquid N2 and lyophilized for storage at -80 °C.

Peptide Synthesis and Characterization. Peptides were obtained using solid phase peptide synthesis (SPPS) on a CEM Liberty Blue instrument. Synthesis was performed on a solid phase Rink-Amide resin (0.78 mmol/g) at a 0.1 mmol scale, using a standard Fmoc protocol and deprotected in 20% piperidine in DMF. Amino acids, coupling agents, N,N'-Diisopropylcarbodiimide (DIC) and Oxyma, were added in a 10-fold molar excess. Crude peptides were cleaved by shaking the resin by in a solution containing trifluoroacetic acid (TFA), triisopropylsilane (TIPS), and water in a ratio of 95:2.5:2.5 for 3.5 h. The resin was

washed with TFA and concentrated under nitrogen. The solution was then added to 40 mL of cold diethyl ether to precipitate the peptide. The solution was centrifuged at 4200 rpm for 10 min, the supernatant was removed, and the pellet was allowed to dry overnight. The dried pellet was dissolved in a mixture of water and acetonitrile (50:50) and 0.1% TFA. Peptides were purified via reverse phase chromatography on a Waters HPLC using a Phenomenex column with C18 resin. A linear gradient was generated using water/acetonitrile + 0.1% TFA, from 10% to 100% acetonitrile over 50 min. Peak fractions were collected based upon their absorbance at 230 nm and tested for purity by MALDI-TOF mass spectrometry on a Bruker microflex LRF MALDI using α-cyano-4-hydroxycinnamic acid matrix (Sigma). Pure fractions were pooled and lyophilized, and peptides were stored at -20 °C until use.

Synthesis of DNA-Peptide Conjugates. DNA-peptide conjugates were prepared via strain-promoted azide-alkyne cycloaddition (SPAAC) following reported protocols.[111, 112] Briefly, amine modified oligonucleotides were dissolved in phosphate buffered saline (PBS) to a concentration of 1 mM. 5 aliquots of 100 mM DBCO-sulfo-NHS dissolved in DMSO were then added to the DNA and agitated at R.T. overnight. The reaction mixture was washed six times with a 3 kDa molecular weight cutoff (MWCO) filter (Amicon) to remove any excess DBCO. The peptide bearing azidolysine (azK) were added in 3-fold molar excess to DNA-DBCO. Reactions were heated to 37 °C and shaken overnight. Following the reaction, samples were exchanged into 50 mM triethyleammonium acetate (TEAA) using a 3 kDa MWCO filter and purified by reverse phase HPLC on an Agilent 1220 Infinity LC HPLC with a Zorbax Eclipse XDB-C18 column. A Linear gradient was generated using 50 mM TEAA/Methanol from 10% to 100% methanol over 60 minutes.

Peak fractions were collected based upon their absorbance at 260 nm, and tested for purity by MALDI-TOF mass spectrometry on a Bruker microflex LRF MALDI in 3-Hydropicolinic acid (HPA) matrix (Sigma). Pure fractions were pooled, and buffer exchanged into water using a 3 kDa MWCO filter.

Protein Nanofiber Assembly Using Peptide Linker. The fusion protein was added with the peptide linker at a 1:1 molar ratio in a 1x phosphate buffer at a pH = 8.0. The unannealed samples were allowed to incubate on the benchtop overnight without any additional manipulation. For the annealed samples, the thermal protocol consisted of incubating the sample at 37 °C for 10 minutes and then a gradual decrease to 12 °C, with a ramp rate of 0.5 °C/30 min. Once the ramp was completed, the sample was incubated at 4 °C until the sample was ready for imaging.

γPFD-KE/E_2/K_2 Assembly with the K-coil Linkers. The γPFD filaments were added with the K-coil crosslinkers at a 1:1 molar ratio in a 1x PBS buffer at a pH = 8.0. The samples were allowed to incubate on the benchtop overnight without any additional manipulation before imaging.

Annealed γPFD-KE/E_2/K_2 Assembly with the K-coil Linkers. The γPFD filaments were added with the K-coil crosslinkers at a 1:1 molar ratio in a 1x PBS buffer at a pH = 8.0. The samples were allowed to anneal in a thermal cycler from 65 °C to 12 °C with a gradient of 30 min/°C. Once 12 °C was reached, the sample cooled to 4 °C and was held at this temperature before imaging.

PAGE Analysis of Peptide-DNA Assemblies. Peptide-DNA assemblies (both individual

conjugates and the DX tile system) were analyzed using 8% native PAGE. 20 µl of a 1 µM sample were added to each lane and electrophoresed at 150 V for 4 h, then stained with ethidium bromide and imaged with a Bio-Rad Molecular Imager GelDOC XR+ system.

Atomic Force Microscopy (AFM) Characterization. All AFM micrographs were collected within 24 h of sample preparation. AFM micrographs were captured on a Veeco DI MultiMode V instrument in air using scan assist mode with SCANASYST-AIR tips (Bruker). 2 µL of sample was deposited on freshly cleaved mica followed by the addition of 2 µL of 0.2 M NiCl and allowed to incubate for 30 seconds. After the 30 s incubation, 56 µL of 1x 50 mM Tris, pH=8.0 was added and allowed to incubate for 3 mins. The buffer was blown off and washed with 60 µL of nanopure water to remove excess salts.

Transmisison Electron Microscopy (TEM) Characterization. All TEM micrographs were collected within 24 h of sample preparation. 5 µL of the sample were adsorbed onto a glow discharged formvar stabilized carbon type-B, 400 mesh copper grid (Ted Pella, 01814-F), at a concentration of 500 nM, and allowed to incubate for 2 mins. The buffer was wicked off, washed twice with 5 uL of 50 mM Tris, pH = 8.0 and quickly wicked off. Lastly, the grid was stained twice with 5 µL of a 2% uranyl acetate stain for 20 s and quickly wicked off. The samples were imaged on a Talos L120C TEM with 120 kEV.

CHAPTER 5

INCORPORATION OF PROTEIN FILAMENTS INTO BIOMATERIALS SCAFFOLDS

5.1 Introduction

As the field of stem cell therapies and tissue engineering continues to grow, there is a continuous effort to control the phenotypic and genotypic behavior of cells. As for stem cells, due to their promiscuous ability to differentiate and self-renew into a wide variety of cell lineages, the regulation of these properties are vital for their translation into therapeutics.[215] To this end, it has been shown that biomaterials are an effective tool that not only can culture and sustain cell but can act as designed micro-environments to regulate stem cell fate. To emphasize the importance of biomaterials, it has been shown that biomaterials can supersede genotypic behavior solely through cellular interactions with its microenvironment, highlighting that the importance of biomimetic ECM materials for stem cell engineering.[216] Lastly, due to the system being examined (i.e, a 3-D cell), the dimensionality of the scaffold has shown to be critical, where a 2-D substrate is inefficient in replicating native conditions *in vivo*.[217, 218] Therefore, the ability to create a scaffold that can direct cell fate through a variety of biochemical, biomechanical, and structural factors is highly desirable.

To access the advantages of 3D scaffolds, hydrogel fabrication has branched into two major categories of materials: either (1) composed of synthetic polymers, such as polyethylene glycol (PEG),[219] or (2) using naturally derived biopolymers, such as collagen.[148] Each of these building materials comes with different benefits and drawbacks, such as ease of functionality, biocompatibility and suitable mechanical properties. For

natural polymer system, researchers have successfully fabricated hydrogels through the use of collagen,[148] fibrin,[220, 221] fibronectin,[151, 155, 222, 223] and hyaluronic acid.[187, 224] The benefit of naturally-derived components are biocompatibility and native bioactivity. However, due to the heterogeneity of the biopolymer, the resulting cell signals are often obscured. Lastly, the mechanics of these systems are often difficult to modulate.[225]

On the other hand, synthetic hydrogels offer a highly reproducible platform for cell culturing. Synthetic hydrogels have been composed of PEG,[219] poly(vinyl alcohol),[226] and even co-block polymers systems, such as Poly(lactic-co-glycolic acid) (PLGA)-PEG systems.[227] Due to the ease of chemical manufacturing of these synthetic scaffolds, these systems are highly reproducible and the mechanical properties can be easily tuned. However, due to the synthetic nature of these scaffolds, these scaffolds lack endogenous bioactivity, rendering these synthetic minimalist platforms for designer ECM mimics, which must be further elaborated with peptides or proteins.

Regardless of which type of biomaterial is chosen for the fabrication of the hydrogel, there are other factors to consider in order to engineer an ECM mimic, such as ligand presentation and density, mechanical properties, porosity, and molecular and cellular diffusion. Out of these factors, hydrogels allow for porous structures to be obtained, which are more suited to encapsulate cells, which have an average size of 10 μm. In addition, the nature of hydrogels (being mainly composed of water) allows for effective diffusion of nutrients within the scaffold. From an engineering perspective, the factors that are difficult to obtain are a spatiotemporal presentation of bioactive ligands, the ability to

modulate the mechanical stiffness of these hydrogel systems, and the ability to incorporate the fibrous morphologies into designer hydrogel systems.

The fibrous morphology of ECM mimics plays a vital role in cellular tethering and encapsulation and helps to mimic the fibrous morphology that is seen in the native microenvironment of cells.[14, 228] However, nanofiber platforms alone do not provide the sufficient biomechanical properties to allow for proper mechanotransduction. To overcome this, researchers have incorporated fibrous building blocks into hydrogel scaffolds, such as collagen-alginate hydrogels,[176] fibronectin-hyaluronan hydrogels,[222] fibronectin-alginate hydrogels,[229] and even *de novo* designed protein hydrogels.[230] However, one of the main drawbacks to protein nanofiber incorporation is the instability of proteins and their possible aggregation. Therefore, implementing a stable protein building block to introduce a fibrous morphology into a non-fibrous hydrogel is desirable.

To this end, two different hydrogel scaffolds were tested and incorporated with a thermostable protein filament, γPFD, which was described in Chapter 4. To reiterate the benefits of the protein filament, the γPFD protein filaments have a T_m of 93 °C, overcoming the instability of protein nanofibers in traditional hydrogels. Furthermore, these protein filaments have been shown amendable to genetic fusion of specific proteins of interest,[213] which can be exploited to incorporate bioactive protein domains. Due to the native function of the filaments as chaperone proteins (in the native extremophile from which they are derived), these proteins can further stabilize bioactive proteins-of-interest.[212] However, based on previous reports, the hydrogels that were fabricated relied on a weak coiled coil

association of fibers, resulting in extremely softs gels (<1 kPa) without an achievable broad range of stiffness.

Therefore, to highlight the versatility of the γPFD filaments to modulate the mechanical stiffness of hydrogels as well as to incorporate a fibrous morphology into the scaffold, a biologically derived polymer, NorHA (Figure 5.1 A), and a synthetic scaffold, tetra-arm PEG_{10k}, was used to highlight the versatility of this approach. In order to allow for chemical conjugation to these scaffolds, a γPFD-Cys mutant was expressed and isolated, which can allow for chemical conjugation through the Cys residues (Figure 5.1

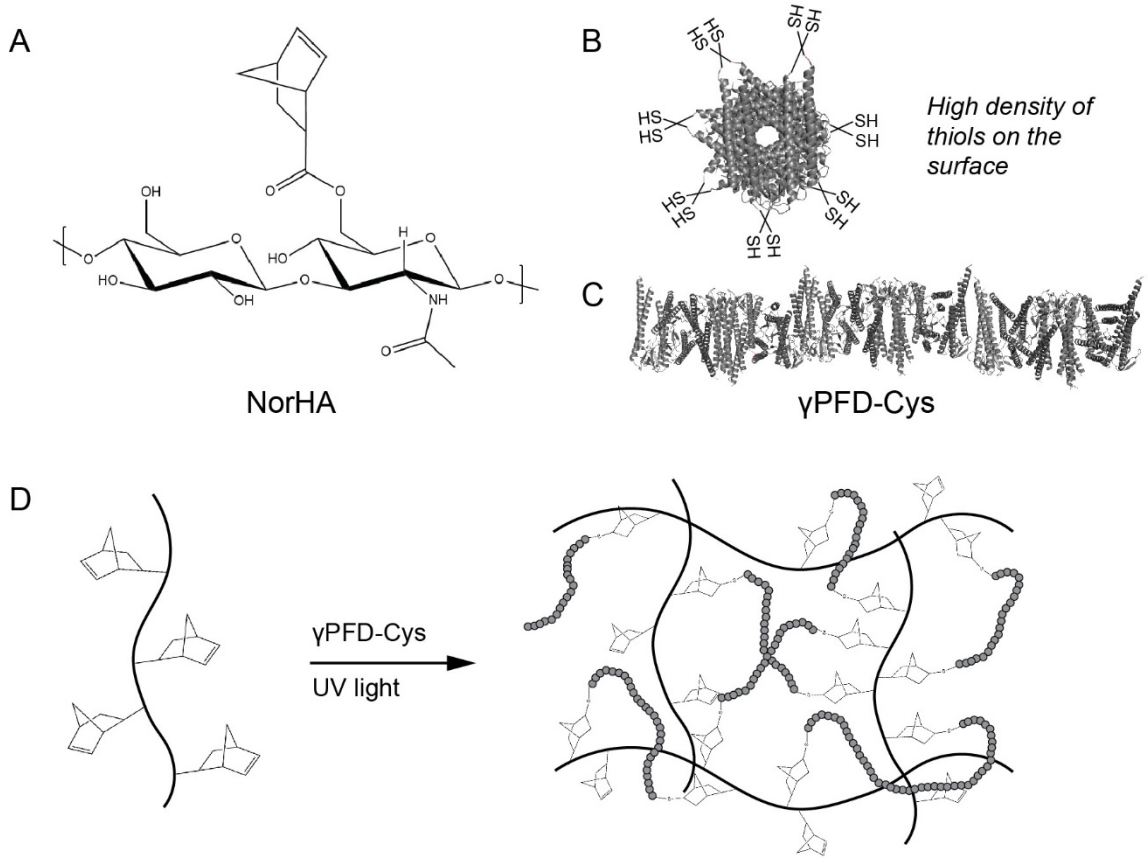

Figure 5.1. Schematic for the γPFD-Cys crosslinking into a hyaluronic acid-based hydrogel. A) Chemical structure of the norbornene-modified hyaluronic acid. **B)** View of the thiol functional groups on the protein filament, looking down the filament axis. **C)** Length view of the γPFD-Cys. **D)** Schematic for the formation of the γPFD-Cys-NorHA hydrogel through UV irradiation.

B, C). For the NorHA scaffold, photocrosslinking of the Norbornene groups with the Cys residues of the filaments allowed for gelation (Figure 5.1 D), whereas for the maleimide tetra-arm PEG_{10k}, the Cys was able to crosslink via Michael addition to allow for gelation. This approach was shown to exhibit a wide range of stiffnesses with both the NorHA and the PEG scaffolds and the fibrous morphologies were also observed through SEM analysis. Ultimately, the use of γPFD-Cys filaments allows for a versatile approach to modulate the mechanical properties of various hydrogel systems while incorporating a fibrous morphology into these scaffolds, allowing for engineered hydrogels to more closely replicate the nature of the ECM.

5.2. Results and Discussion

5.2.1 Material Characterization of the Fibrous NorHA Hydrogels

Due to the lack of a fibrous nature in the hyaluronan hydrogel system, it was envisioned that Cys-rich protein filaments can be photo-polymerized in a NorHA scaffold to overcome this issue. Therefore, γPFD-Cys was used to solve this drawback. The lyophilized protein was initially dissolved in a TBS solution, at a pH = 8.0, at 2 wt% and incubated overnight. The incubation process is performed with the lyophilized γPFD to ensure that the protein is efficiently hydrated and solubilized. After this process, the solubilized γPFD-Cys was mixed with the lyophilized NorHA and vortexed gently to ensure complete dispersion of the NorHA. After the NorHA was completely solubilized, the photoinitiator I2959 was added to the solution, and 30 μL of the final mixture was added to four cylindrical molds. The solutions in the molds were covered with a glass coverslip and irradiated with a UV lamp source for four minutes at a power of 10 mW. After the solutions were crosslinked, the coverslip was removed to reveal the gels on the

coverslip. The resulting gels were relatively flat and lacked sufficient stiffness for easy mechanical handling of the gel (Figure 5.2 A). In addition, the gels were cloudy and translucent, capturing some of the translucency of the initial γPFD-Cys solution.

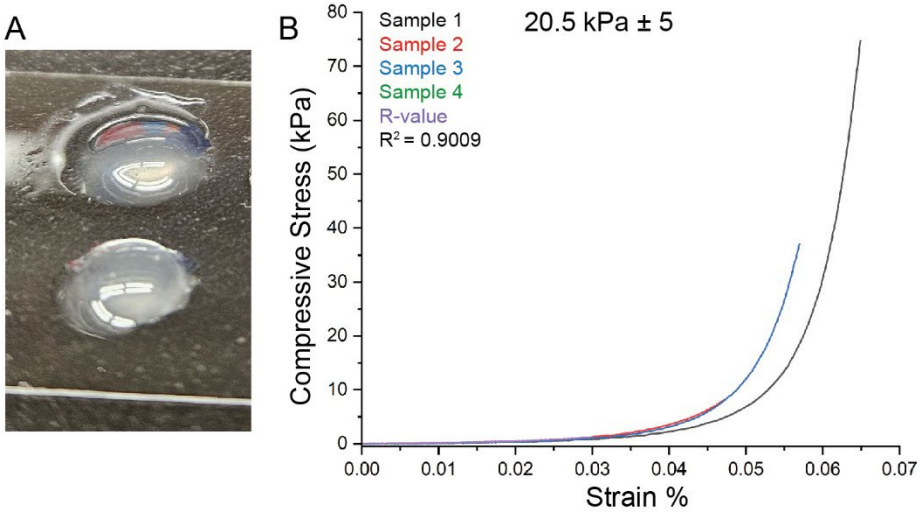

Figure 5.2. Initial gelation of crosslinked γPFD-Cys filaments with hyaluronic acid based scaffold. A) Photograph of the γPFD-Cys filaments (2 wt%) photo-crosslinked with NorHA for 4 mins, I2959, and no DTT. **B)** Compressive stress versus stress % curve of the crosslinked gels. N = 4.

Once the gels were formed, the mechanical properties were tested using a compression tester. As mentioned, the gels were quite soft, making it difficult to transfer them onto instrument. However, each sample was tested and the resulting compressive stress vs strain % curves revealed some deviations from each sample (Figure 5.2 B). The curves revealed a range for the strain % from ~0.055% to 0.065 %. In addition, the range for the compressive stress for each of these samples were from 10 kPa to 75 kPa, indicating a large range for the compressive stress. Samples 2, 3, and 4 had similar stress vs strain profiles, whereas sample 1 ended later than the rest of the samples. To passivate the deviations seen from these curves, a linear region from 0.1 – 0.5 strain % was used to obtain the compressive modulus. The linear region had a R^2 value of 0.9003, indicating that these samples had decent linearity in this strain region, mainly due to the last three samples. Due

to the suitable R^2 value, the compressive modulus was calculated to be 20.5 kPa ± 5.0. The compressive modulus of the gels was surprising due to the lack of structural stability seen in these gels after photo-crosslinking. Due to their flatness, it was expected that these gels would result in a much lower stiffness. However, the γPFD-Cys filaments might provide enough structural stiffness that once the gels were finally compressed, they possessed the observed level of stiffness.

To investigate the incorporation of the γPFD-Cys filaments in the NorHA scaffold, the hydrogel was analyzed using scanning electron microscopy (SEM). Due to the lack of a critical point dehydrator to preserve the native structure, the samples were fixed using 2% paraformaldehyde, and the water content was buffer exchanged to ethanol. After the buffer exchange, the hydrogel was further dehydrated in a desiccator overnight. After desiccation, the sample was sputter coated with carbon and analyzed by SEM. The SEM revealed several types of morphologies from a smooth, wrinkled surface and a flaky, fibrous core (Figure 5.3 A). There seemed to be a thick upper layer that was surrounding the flaky core. In this smooth layer, it was difficult to distinguish any fibrous morphology. Therefore, the flaky core was examined in closer detail. By taking a closer look at the flaky core, pores and cavities can be seen (Figure 5.3 B). The flakes form an extensive network, forming dense pillars and dense areas. However, there are also areas where the flakes seem to branch off into individual flakes, creating the pores in the hydrogel. By taking a closer look at the flaky core, individual filaments that interpenetrate through the flaky scaffold were seen in abundance (Figure 5.3 C, D). The filaments were seen crosslinking many

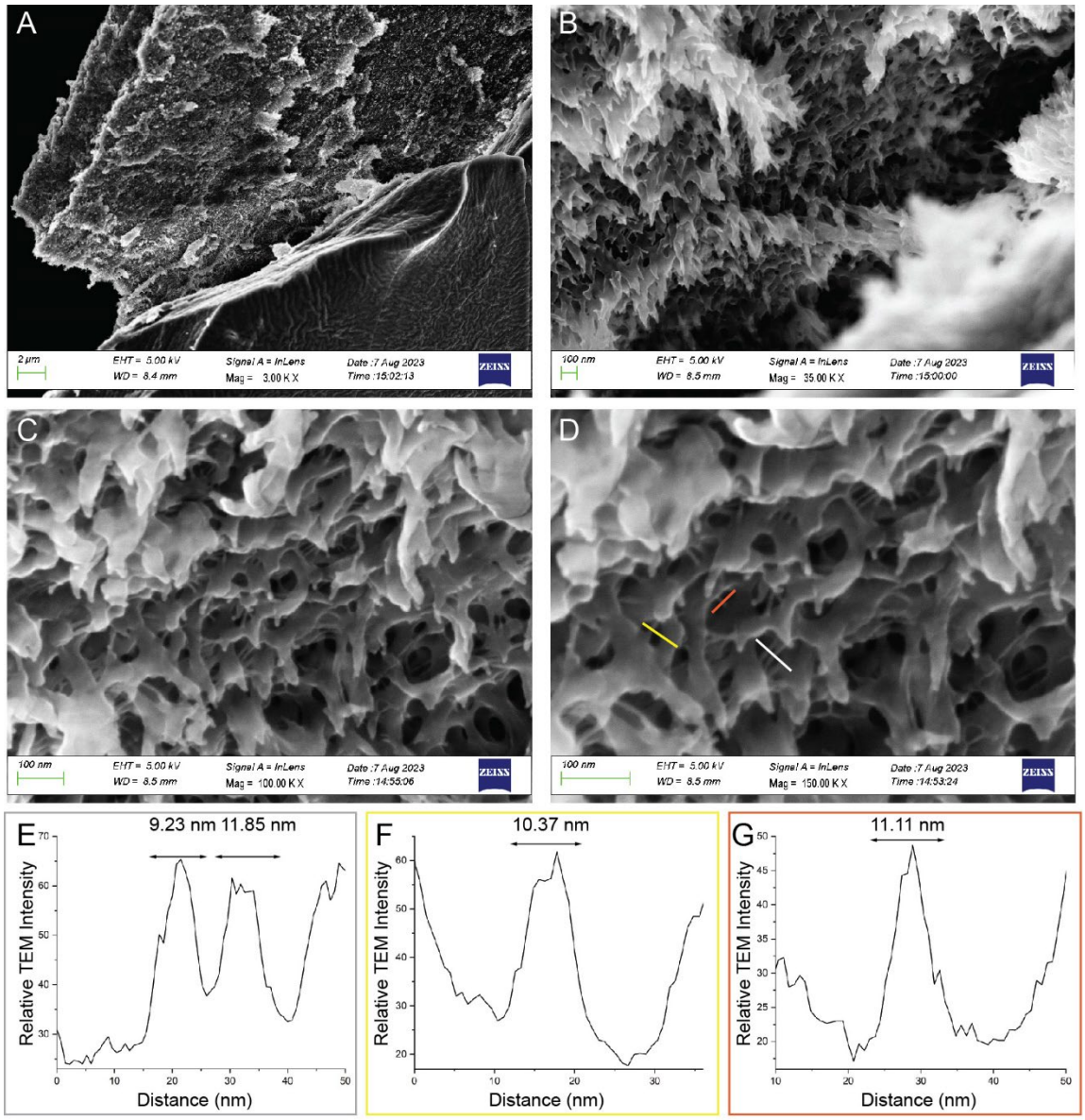

Figure 5.3. SEM analysis of the γPFD-Cys NorHA hydrogel. A) Wide-field SEM micrograph of the γPFD-Cys NorHA hydrogel. **B)** SEM micrograph of the γPFD-Cys NorHA hydrogel highlighting the NorHA morphology. **C)** SEM micrograph of the γPFD-Cys NorHA hydrogel highlighting the fibrous incorporation of the protein filaments in the scaffold. **D)** A zoomed-in SEM micrograph of the γPFD-Cys NorHA hydrogel revealing the fibers embedded in the hydrogel. The lines depict the sections that were measured in the width traces. **E)** Width profile of the γPFD-Cys nanofibers in (**D**), traced with the white line. **F)** Width profile of the γPFD-Cys nanofibers in (**D**), traced with the yellow line. **G)** Width profile of the γPFD-Cys nanofibers in (**D**), traced with the orange line.

areas of the scaffold, where the base scaffold formed a dense and porous network. Due to

the stability of the hydrogel under high magnification, we took a closer look to reveal the protein nanofibers with better resolution. The filaments seem to have a stiff and rigid morphology in the scaffold, where they penetrate the scaffold without any collimating effects at the entrance/exit points from where the fibers are sticking out.

To better understand the incorporation of these fibers, width measurements of these fibers were taken from the SEM micrograph in Figure 5.3 D. The expected width of these protein filaments is ~ 9 nm but they are expected to appear wider under SEM due to the carbon coating, which imparts a few nanometers to the overall width of the protein filaments. To characterize these filaments, three regions were measured, highlighted on the micrograph by different line segments (white, yellow, and orange). The first width trace was done in the middle of the micrograph due to the clear morphology and the good contrast between the filaments and the black cavities (Figure 5.3 E). The measured width of the two filaments in this region were 9.2 nm and 11.9 nm, the width of these filaments is relatively close to the expected width of the filaments, where the filament measuring to 11.9 nm gives room for a roughly 2 nm coating of carbon. The other width trace was taken near the center, due to the stark contrast between the filament and the black background again (Figure 5.3 F). This isolated filament measured 10.4 nm, which is in close alignment with the previously measured filaments. This filament also gives room a few nanometers of coated carbon. Lastly, the last filament that was measured was near the other measured filaments. The proximity ensures that the measurements are not distorted due to them being farther away from the plane of the other measured fibers. The resulting trace revealed a width of 11.1 nm, which is also in close agreement with the other measured filaments. Overall, the measured filaments gave an average filament width of 10.6 nm, which is close

to the expected width of the protein filaments and can account for a thin nanometer coating of carbon on the hydrogel surface. Through these measurements and SEM micrographs, the data indicates that the γPFD-Cys filaments have been successfully incorporated into the hydrogel scaffold, creating a fibrous network *within* the hydrogel.

To ascertain whether the compression modulus of the γPFD-Cys and NorHA system can be modulated, a new type of gel was fabricated. The new gel consisted of the same wt% of γPFD-Cys (2 wt%), with I2959 and NorHA but the solution was doped with 0.1 molar equivalents of DTT. The amount added is relative to the norbornene functional groups on the modified HA, allowing for a small percentage of the gel to be crosslinked with a small molecule linker. The fabrication was similar to the previous system, with an exposure time of 4 min. The resulting gel was distinctly different than the previous system, due to the physical robustness of the gel (Figure 5.4 A). The gel conserved the physical structure of the mold, which is a small cylindrical disk. In addition, the gel appeared to be translucent. In addition, the tops of the gels remained flat, not rounded, indicating that the

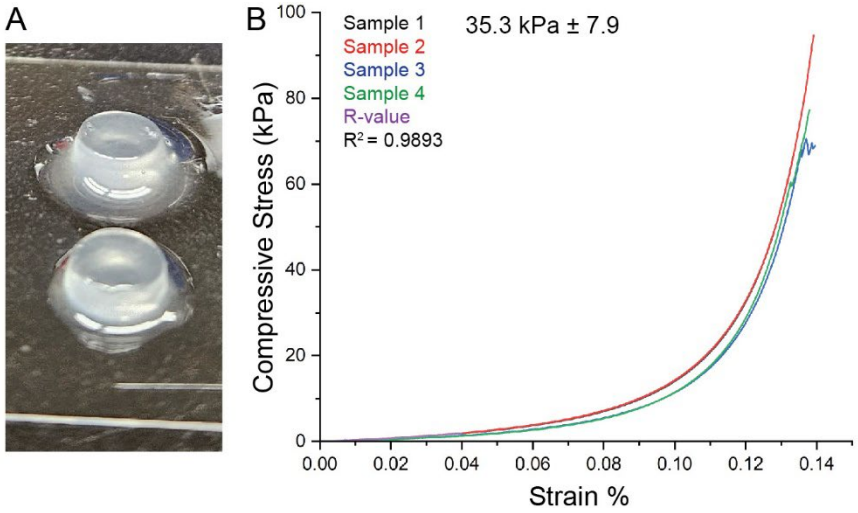

Figure 5.4. Gelation of crosslinked γPFD-Cys filaments with hyaluronic acid-based scaffold. A) Digitial photograph of the γPFD-Cys filaments (2 wt %) photo-crosslinked with NorHA for 4 mins, I2959, and DTT. **B)** Compressive stress versus stress % curve of the crosslinked gels. N = 4.

structure was stiff enough to preserve the structure of the mold. After four of these samples were fabricated, the gels were measured using a compression tester. The compressive stress versus strain % curves for all of the four gels gave consistent curves (Figure 5.4 B). These reproducible curves hint towards the structural stability of these types of hydrogels, where the protein filaments and the DTT allow for efficient and reliable crosslinking of the NorHA. For the stress vs. strain curves, the curves had a narrow stress % range of 0.135-0.140, further confirming the consistent nature of the gel system. In addition, the compressive stress for these four gels ranged from 60 kPa to 90 kPa. The range for these gels is much wider than the strain % but the results are interesting, nonetheless. This observed stress is five times greater than the highest recorded compressive stress for the previous system without DTT.

From the compressive stress vs. strain % curves, the resulting compressive modulus for the gel system was calculated using the strain % from 0.0 – 0.05 %. The linearity of this region was calculated with an R^2 value of 0.9893, indicating good linearity for this system (Figure 5.4 B). For comparison, for the previous system, the linearity of the system was 0.9336, which reaffirms the consistency of the dataset. The resulting compression modulus of this gel system was 35.4 kPa ± 7.9 (Figure 5.4 C). The calculated compression modulus was significantly different than the previous system, with almost a 1.5x increase in the value. From the mechanical analysis of this gel system, the results indicate that doping in of DTT can increase the modulus of the γPFD-Cys-NorHA hydrogel system by providing structural robustness and physically stiffer gels.

After the mechanical testing of the γPFD-Cys-NorHA hydrogels, the samples were fixed, similar to the previous gel for SEM imaging. Due to the increase in mechanical stiffness, the fixed and subsequent dehydrated gels maintain some structural composition, making them easier to handle. Under the SEM, the sputter-coated hydrogel revealed many fibrous-like areas, where the gel had hair-like features (Figure 5.5 A). Due to the fibrous morphology of the imaged area, a zoom-in was taken to analyze the widths of the fibers (Figure 5.5 B). The zoom-in revealed an assortment of fibers ranging in their width. Many of the fibers seemed to stick out from the gel matrix. Based on the scale bar, most of these imaged fibers were far too large to be the γPFD-Cys filaments. However, there was an instance where there was a smaller fiber sticking out closer to the field of view. The fiber was measured and revealed a width of 33.7 nm (Figure 5.5 E). The measure width is approximately three times larger than the expected width of the γPFD-Cys filaments, indicating that the fiber that was measured was mainly from the NorHA scaffold.

Due to the width measurements of the previous scan, another area of the hydrogel was imaged to see the incorporation of the γPFD-Cys filaments. The next area that was scanned was an area that seemed to be two different ends of the NorHA scaffold that was "connected" together by thin filaments (Figure 5.5 C). There are a number of notable features of this specific area. Firstly, the scaffold seemed to have fibers embedded in the surface, giving off an etched surface. Secondly, there were many filaments connecting two areas of the NorHA scaffold, with a similar width. To note, there were some filaments that have a wider width and even some "tape-like" filaments with bulges going along the tape-like structure. A closer look was taken in this area, and the resulting SEM micrograph plenty of filaments that appeared to have a similar width and a consistent diameter coming

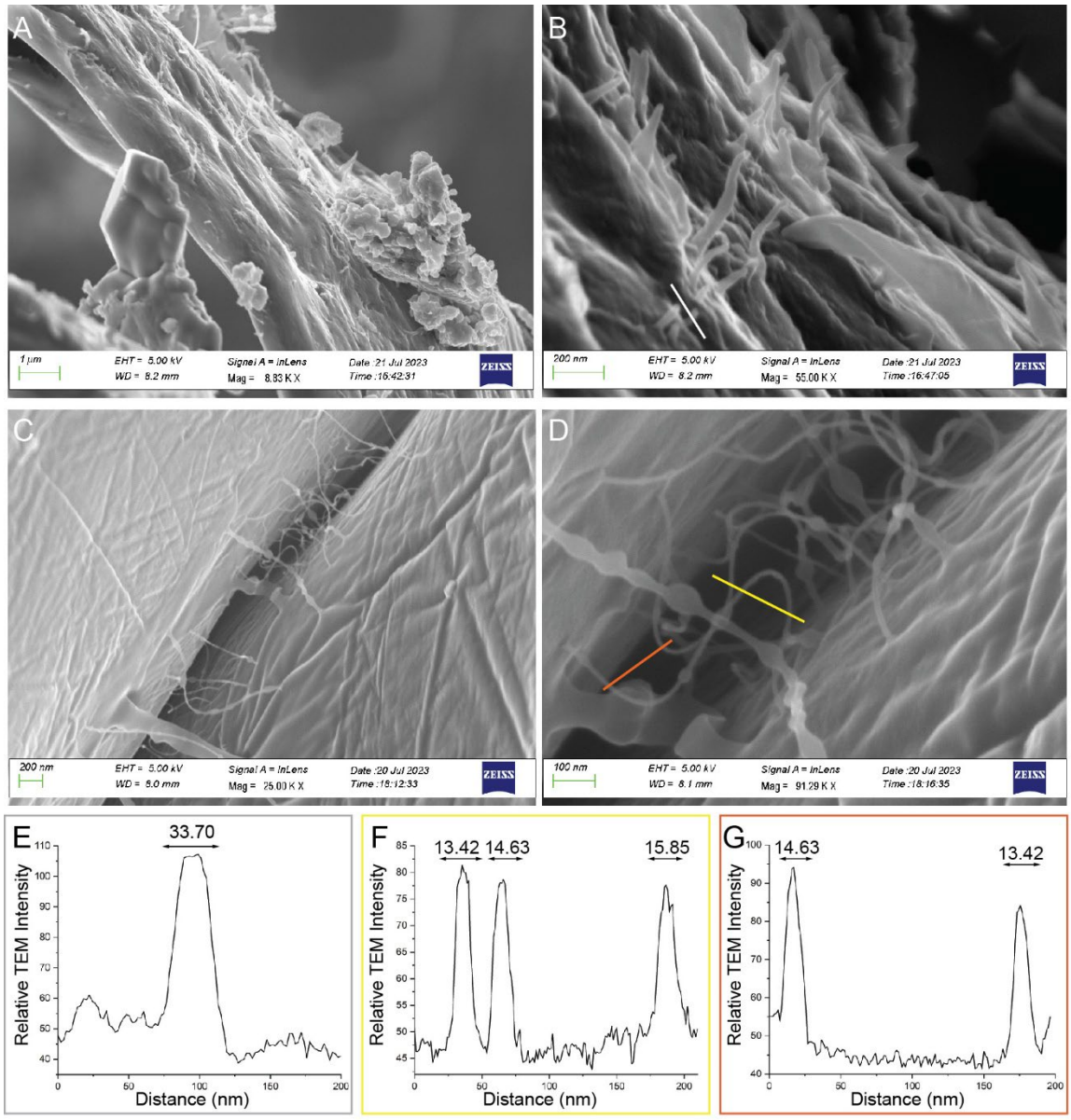

Figure 5.5. SEM analysis of the γPFD-Cys NorHA hydrogel doped with DTT. A) Wide-field SEM micrograph of the γPFD-Cys NorHA hydrogel. **B)** SEM micrograph of the γPFD-Cys NorHA hydrogel highlighting fibrous morphology. The line depicts the sections that was measured in the width trace below. **C)** SEM micrograph of the γPFD-Cys NorHA hydrogel highlighting the fibrous incorporation of the protein filaments in the scaffold. **D)** A zoomed-in SEM micrograph of the γPFD-Cys NorHA hydrogel revealing the fibers interpenetrating two areas within the hydrogel. The lines depict the sections that were measured in the width traces below. **E)** Width profile of the γPFD-Cys nanofibers in (**B**), traced with the white line. **F)** Width profile of the γPFD-Cys nanofibers in (**D**), traced with the yellow line. **G)** Width profile of the γPFD-Cys nanofibers in (**D**), traced with the orange line.

out of the scaffold until the filaments goes back in the scaffold (Figure 5.5 D). As mentioned previously, the consistent diameter of the filaments indicates a higher likelihood of these structures being a protein filament and *not* the hydrogel scaffold due to the lack of the fiber diameter becoming narrower from the base.

To further probe the presence of these filaments, several areas were measured, depicted by the orange and yellow lines in the micrograph. The first section that was measured was the yellow line, measuring three distinct portions of the filaments. The filaments gave an average width of 14.6 nm, which is closer to the expected width of the γPFD-Cys filaments. Based on the expected width of the filaments (~9 nm), these results imply a few nanometers of carbon coating. In addition, each of the three segments gave a relatively similar measurement, showing some consistency in the width as well as being more reasonable compared to the previous filament in Figure 5.5 B. The other measured area was sectioned by the orange line, which measured two distinct filaments. The average width of these filaments was 14.0 nm, which is also close to the expected width of the γPFD-Cys filaments. In addition, the average width of these filaments was close to the average width of the previous measured area, indicating good consistency. These measured filaments were in close agreement with the measured filaments in the hydrogel from Figure 5.3 D. The discrepancy between these measurements is that the micrograph in Figure 5.3 D was obtained at a higher magnification (150k X), which would allow for better and more reliable width measurements. All in all, the SEM micrographs and their resulting width measurements provided convincing evidence of the incorporation of the γPFD-Cys filaments in the NorHA scaffold.

To further verify the incorporation of the protein filaments, Energy-Dispersive X-ray Spectroscopy (EDS) SEM was conducted on the γPFD-Cys-NorHA hydrogel. The technique was used to verify the elemental incorporation of nitrogen (N) and sulfur (S), which is present in the γPFD-Cys filaments. On an elemental basis, the N signal should be more abundant due to the peptide backbone in addition to the various amino acid residues that contain nitrogen. In addition, there should only be one sulfur on each γPFD-Cys monomer, indicating a much lower presence of sulfur in the hydrogel. The elemental composition is distinctly different because the NorHA scaffold should not contain any nitrogen atoms or sulfur atoms. However, due to the small doping of the DTT crosslinker, there should be an increase in the sulfur signal. Other than that, most of the nitrogen N $K\alpha_{1,2}$ and the sulfur N $K\alpha_1$ spectroscopic signals that were observed should result from the crosslinker and/or the γPFD-Cys filaments. To note, the N $K\alpha_{1,2}$ signal should only be derived from the γPFD-Cys filaments.

To obtain an EDS-SEM micrograph of the sample, an area that seemed filamentous was imaged using a low electron voltage (5 KeV). Once an appropriate area was found, the electron voltage was increased to 20 KeV to ensure appropriate inner-shell electron dispersion. Upon increasing the electron voltage and inserting the EDS detector, the elemental composition of the area was obtained. The elemental composition is obtain as a measurement of X-ray counts vs energy (KeV). The signals depend on the elemental abundance, the heaviness of the atom, and can be used to obtain *qualitative* information about the elemental composition. The sensitivity of the detection can be measured to 0.1% of the composition and the measurements exhibit a high degree of precision, around 2-4 %. The resulting EDS-SEM micrograph was made selective for the N $K\alpha_{1,2}$ signal and the

S Kα1 due to those being the distinguishing elements for the experiment (Figure 5.6 A). The EDS-SEM micrograph displayed the S Kα1 signal at a high abundance (green signal)

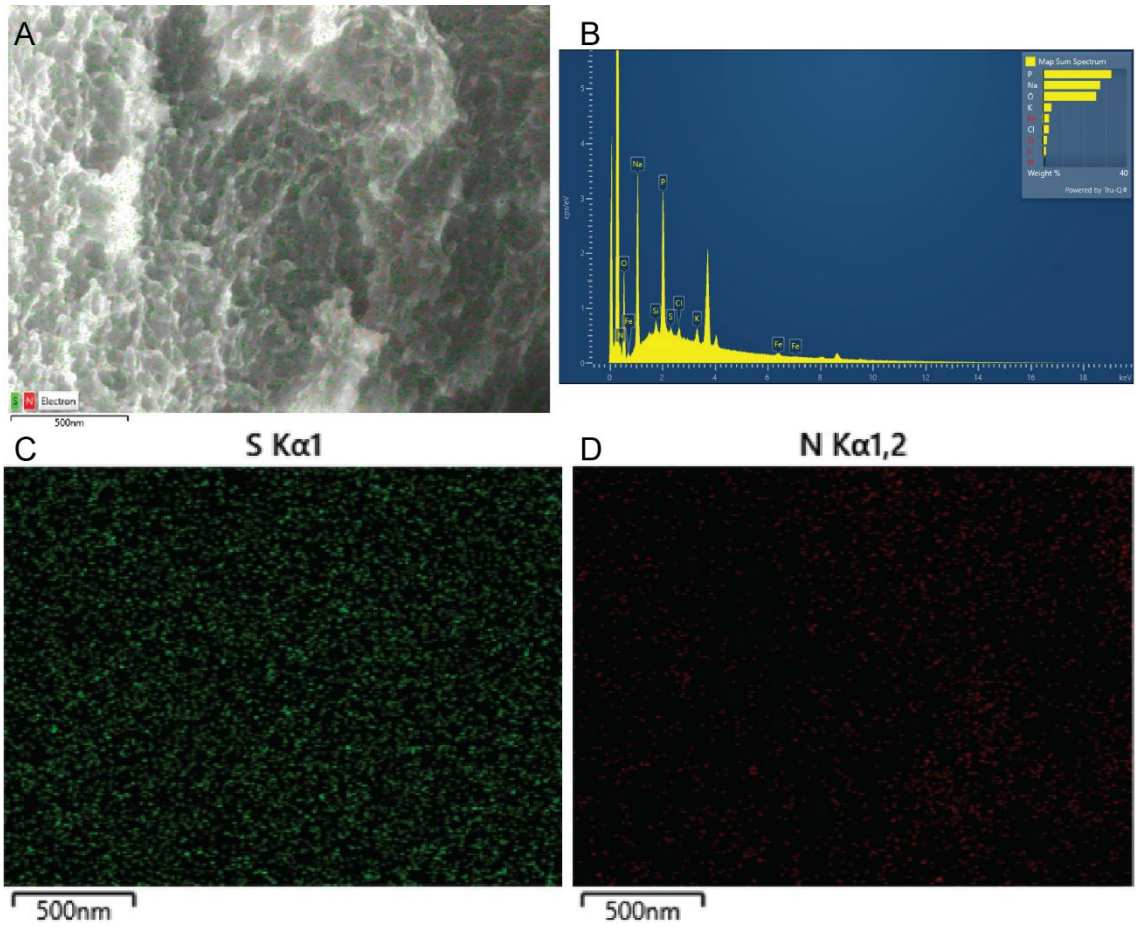

Figure 5.6. SEM-EDS analysis of the γPFD-Cys NorHA hydrogel doped with DTT. **A)** SEM-EDS micrograph of the γPFD-Cys NorHA hydrogel, inlaid with the S and N elemental signals. **B)** EDS spectrum of the SEM micrograph in (**A**). **C)** Elemental mapping of the sulfur Kα1 signal from the SEM micrograph in (**A**). **D)** Elemental mapping of the nitrogen Kα1,2 signal from the SEM micrograph in (**A**).

whereas the N Kα1,2 signal was scattered throughout (red signal). There were also many areas that exhibited an overlap between the S Kα1 signal and the N Kα1,2 signal, suggesting the presence of a species that consists of both elements (i.e., the γPFD-Cys filaments).

In addition to the EDS-SEM micrograph, the EDS spectrum was obtained to gather the entire elemental composition of the imaged area in the hydrogel (Figure 5.6 B). From

the EDS spectrum, the most abundant elements were carbon, phosphorus, sodium, and oxygen. The high carbon signal is due to the carbon sputter coating, which would create an abundantly high-intensity peak. The high sodium and phosphorous peaks are not present in the biochemical make-up of either the γPFD-Cys filaments of the NorHA but the hydrogel was made in a phosphate buffer saline, which contains both of these elements. As a result, these signals are most likely derived from residue salt that was captured during the fixing and dehydration treatment of the gel. The high O $K\alpha_1$ signal is derived from the NorHA scaffold due to the oxygen in the hyaluronic acid *and* due to the high presence of oxygen in the protein filaments.

Due to the high C $K\alpha_1$ signal, the N $K\alpha_1$ that was received by the detector was masked. The N $K\alpha_1$ signal appeared near 0.4 KeV, with an intensity of 0.3 cps/KeV. Although this signal was low and masked by the C $K\alpha_1$ signal, it was still registered by the detector and was visualized by the N $K\alpha_1$ EDS-SEM micrograph (Figure 5.6 D). The red dots from the EDS-SEM micrograph depict areas of scattered N in the area, where there are some bright red spots, indicating a high abundance of N in that localized area. As for the S $K\alpha_1$ signal, it was more dominant in the EDS spectrum compared to the N $K\alpha_{1,2}$ signal, at 2.3 KeV with an intensity of 0.7 cps/KeV. Once again, the high intensity of the S $K\alpha_1$ signal is more likely derived due to the DTT crosslinker but is contributed by the Cys-residue in the protein filaments. However, it is difficult to distinguish between the two. In addition, the EDS-SEM micrograph of just the S $K\alpha_1$ displayed well-scattered dispersion spots, with areas of high, localized intensity and even black-out areas. Due to the high intensity of the S $K\alpha_1$ signal, the EDS dispersion spots are easily depicted in the EDS-SEM micrograph, which makes the incorporation easier to distinguish.

Finally, concentration-dependent EDS-SEM micrographs were obtained from the hydrogel area to ascertain the relative abundance of each elemental signal. For the S $K\alpha_1$ signal, there signal was well-scattered throughout the surface and most of the concentration values, relative to 899, ranged from 150-449 (Figure 5.7 A). The dispersion spots did not tread to such high intensity values but there were a few instances where spots indicative of a intensity of 674 were detected, relative to the concentration of the sample. As for the N $K\alpha_{1,2}$ signal, the scattering of dispersion peaks was low, as compared to the S $K\alpha_1$ signal (Figure 5.7 B). In addition, the concentration values remained on the lower end, ranging from 150-449. There were hardly any peaks seen in the 674-value range, but a few were scattered throughout the SEM imaging area. Overall, the concentration-dependent EDS-SEM micrograph depicts a higher S concentration relative to the N signal, perhaps due to the additional DTT that was added to the hydrogel.

To further confirm the EDS results, a zoom-in EDS-SEM micrograph was taken of the similar spot. Upon increasing the electron voltage and inserting the EDS detector, the elemental composition of the area was retrieved. The resulting EDS-SEM micrograph was made selective for the N $K\alpha_{1,2}$ signal and the S $K\alpha_1$ due to those being the distinguishing elements for the experiment (Figure 5.8 A). The EDS-SEM micrograph displayed the N $K\alpha_{1,2}$ signal at a high abundance (red signal) whereas the S $K\alpha_1$ signal was harder to interpret due to the low intensity. There were also many areas that exhibited an overlap between the S $K\alpha_1$ signal and the N $K\alpha_{1,2}$ signal, indicating the presence of a species that consists of both elements (i.e., the γPFD-Cys filaments).

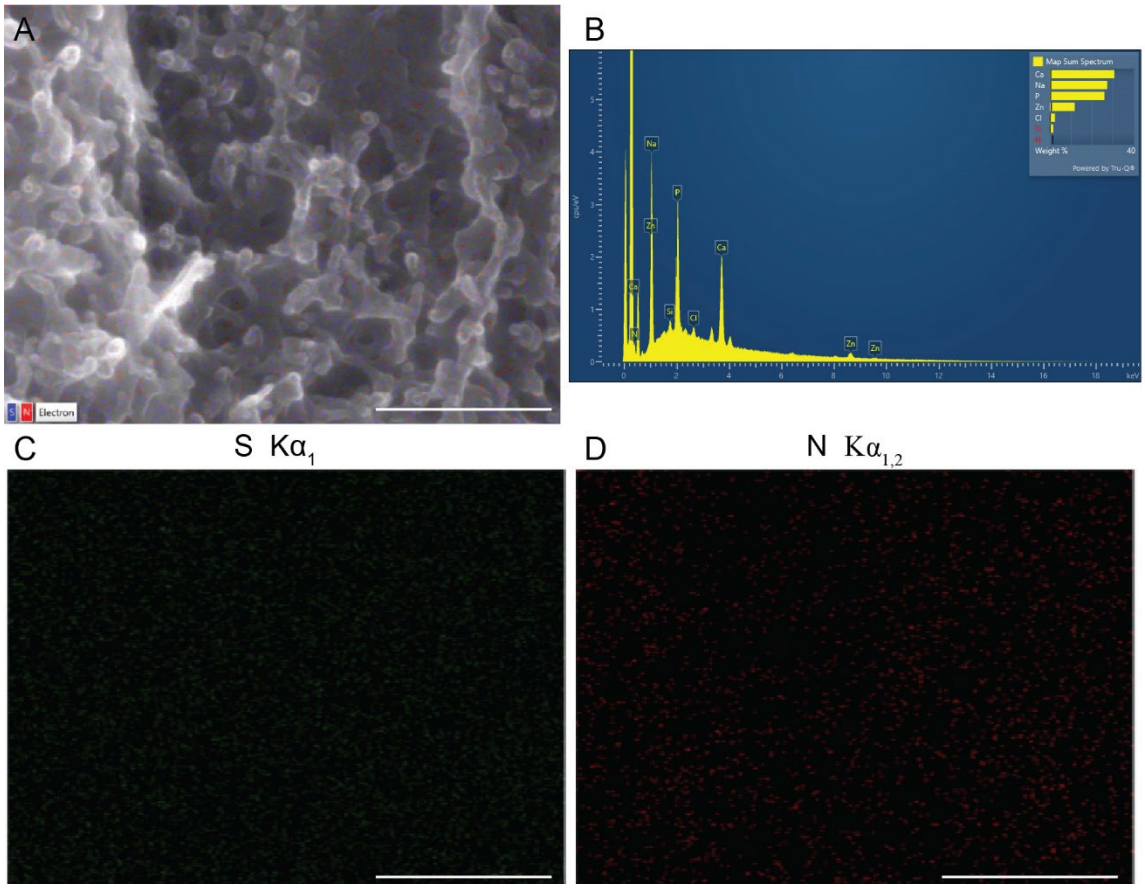

Figure 5.8. Zoomed-in SEM-EDS analysis of the γPFD-Cys NorHA hydrogel doped with DTT. A) SEM-EDS micrograph of the γPFD-Cys NorHA hydrogel, inlaid with the S and N elemental signals. Scale bar = 250 nm. **B)** EDS spectrum of the SEM micrograph in (**A**). **C)** Elemental mapping of the sulfur $K\alpha_1$ signal from the SEM micrograph in (**A**). Scale bar = 250 nm. **D)** Elemental mapping of the nitrogen $K\alpha_{1,2}$ signal from the SEM micrograph in (**A**). Scale bar = 250 nm.

In addition to the EDS-SEM micrograph, the EDS spectrum was obtained to gather the entire elemental composition of the imaged area in the hydrogel (Figure 5.8 B). From the EDS spectrum, the most abundant elements were carbon, phosphorus, sodium, oxygen, and calcium. Once again, the high carbon signal is due to the carbon sputter coating, the high sodium and phosphorous peaks are most likely derived from residual buffer during the fixing and dehydration treatment of the gel. The high Ca $K\alpha_1$ signal is most likely derived from environmental contamination since there should not have been any Ca in the

buffers. Lastly, the O peak is still present due to the oxygen in the hyaluronic acid *and* due to the high presence of oxygen in the protein filaments.

Due to the high C $K\alpha_1$ signal, the N $K\alpha_1$ that was received by the detector was masked. The N $K\alpha_1$ signal appeared near 0.4 KeV, with an intensity of 0.3 cps/KeV. Although this signal was low and masked by the C $K\alpha_1$ signal, it was still registered by the detector and was visualized by the N $K\alpha_1$ EDS-SEM micrograph (Figure 5.8 D). The red dots from the EDS-SEM micrograph depict areas of scatter N in the area, where there are some bright red spots, indicating a high abundance of N in that localized area. As for the S $K\alpha_1$ signal, it was slightly more dominant in the EDS spectrum compared to the N $K\alpha_{1,2}$ signal, at 2.2 KeV with an intensity of 0.6 cps/KeV but was hardly detectable due to the signal being masked by the P signal. Once again, the high intensity of the S $K\alpha_1$ signal is more likely derived due to the DTT crosslinker but should have some contribution by the Cys-residue in the protein filaments, although it is not possible to definitively attribute the fraction of each contribution. In addition, the EDS-SEM micrograph of just the S $K\alpha_1$ displayed well-scattered dispersion spots, with areas of high, localized intensity and even black-out areas. Due to the high intensity of the S $K\alpha_1$ signal, the EDS dispersion spots are easily depicted in the EDS-SEM micrograph, which makes the incorporation easier to distinguish.

Finally, concentration-dependent EDS-SEM micrographs were obtained from the hydrogel area to ascertain the relative abundance of each elemental signal. For the S $K\alpha_1$ signal, their signal was well-scattered throughout the surface and most of the concentration values, relative to 899, ranged from 150-449 (Figure 5.9 A). In comparison to the previous

concentration-dependent S EDS-SEM micrograph, there were more dispersion spots were at a higher concentration of 674. The higher instance of more localized and concentrated S

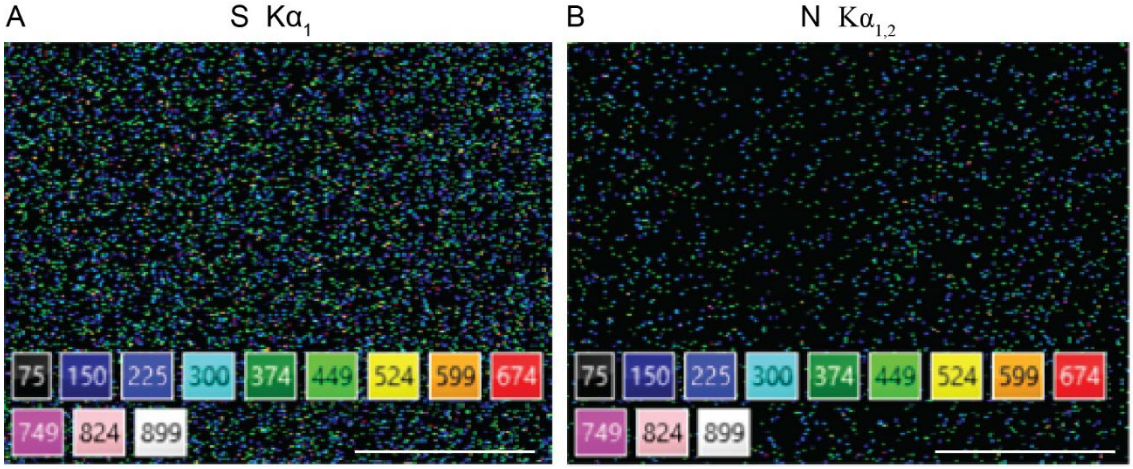

Figure 5.9. Zoomed-in concentration-dependent elemental mapping of γPFD-Cys NorHA hydrogel doped with DTT. A) Concentration-dependent elemental mapping of the sulfur Kα1 signal from the SEM micrograph in (**Figure 5.8 A**). Scale bar = 250 nm. **B)** Concentration-dependent elemental mapping of the nitrogen Kα1,2 signal from the SEM micrograph in (**Figure 5.8 A**). Scale bar = 250 nm.

dispersion peaks may be due to the higher magnification that the scan was taken, allowing for the signal to be detected more reliably. As for the N Kα1,2 signal, the scattering of dispersion peaks was low, as compared to the S Kα1 signal (Figure 5.9 B). In addition, the concentration values remained on the lower end, ranging from 150-449. There were hardly any peaks seen in the 674-value range, but a few were scattered throughout the SEM imaging area. There were also more black-out regions, indicating the absence of N in this specific scanned region. Overall, the concentration-dependent EDS-SEM micrograph depicts a higher S concentration relative to the N signal, mainly due to the additional DTT that was added to the hydrogel.

To further extend the utility of the γPFD-Cys-NorHA hydrogel system, additional protein decoration was tested once the gels were formed. This approach allows for the

modulation of bio-active signals at a temporal manner mainly imparted by the high density of norbornene groups on the HA scaffold. To allow for a temporal incorporation of a protein-of-interest into the gel post-gelation, a Cys-mutant can be used. Through this method, the Cys-protein can be photochemically modified onto the gel scaffold, in a facile manner. To demonstrate this idea, we used a cysteine mutant of super-folder green fluorescent protein (sfGFP). This protein was used because the ease of visualization through fluorescence imaging, the protein is stable at room temperature, and due to the stability, the expression of this protein construct is facile. In addition, the benefit of the radical crosslinking of a thiol to a norbornene functional group is that the protein does *not* need to be reduced prior to the addition. Any disulfides in the solution will be cleaved through radical formation to allow for efficient covalent immobilization of the sfGFP to the scaffold.

The γPFD-Cys NorHA gel that was doped with DTT was formed in the molds, crosslinked with an irradiation time of 4 mins and removed from the mold. Once formed, a solution of the sfGFP in PBS was added on top of the pre-formed gel and additionally crosslinked for another minute. After irradiation, the gel was washed three times with PBS to ensure any biomolecule that was not covalently tethered to the gel was removed. The gel was subsequently imaged by fluorescence microscopy to determine the efficiency of incorporation. Under fluorescence imaging, the gel was appeared to be effectively impregnated with the fluorescent protein, as evidences a well-dispersed fluorescence signal (Figure 5.10 A). Barring a few minor inhomogeneities, the fluorescence was well-dispersed through the γPFD-Cys NorHA gel. Lastly, to measure the physical stability of the protein incorporation, the gel was washed six times overnight and kept at 4 °C. After the

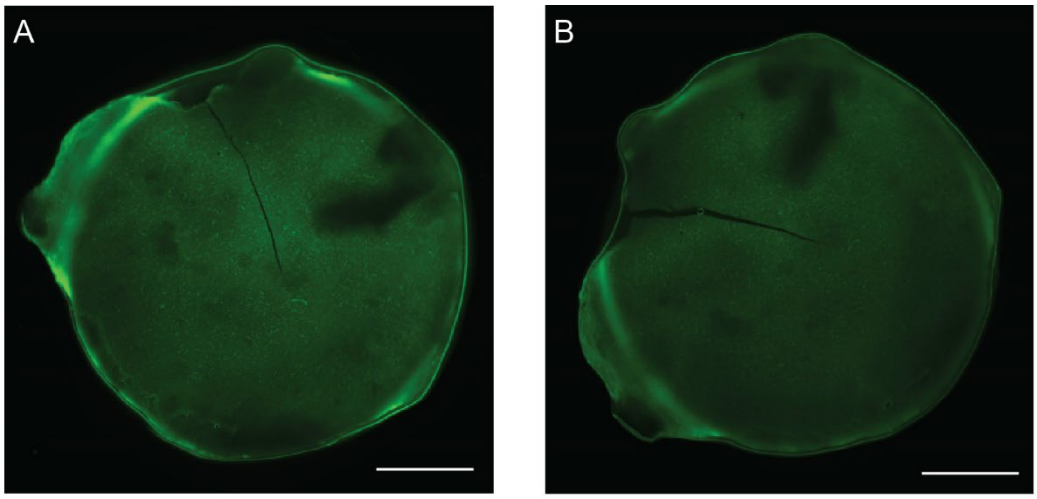

Figure 5.10. Fluorescence microscopy analysis of the γPFD-Cys NorHA hydrogel doped with DTT and the stable incorporation of sfGFP. A) Fluorescence micrograph of the γPFD-Cys NorHA hydrogel embedded with sfGFP. **B)** Fluorescence micrograph of the γPFD-Cys NorHA hydrogel embedded with sfGFP with overnight washes to highlight the stability of the protein. Scale bars = 1 mm.

subsequent washes, the gel was imaged to see if the fluorescence signal was maintained. The resulting gel showed similar well-distributed fluorescence, similar to the original fluorescent signal (Figure 5.10 B). Overall, the γPFD-Cys NorHA hydrogel platform represents a viable option to include both a filamentous nature to non-fibrous hydrogel *and* to allow for the incorporation of proteins-of-interest post-gelation (e.g., to attach bioactive proteins to the scaffold).

To better understand how the inclusion of the γPFD-Cys filaments affected the mechanical properties of the gel, we devised a negative control: formation of a NorHA gel, without the addition of DTT, and just the photoinitiator, I2959. Upon photo-crosslinking, the resulting gels seemed to have a better structural composition than the gel with the γPFD-Cys filaments included (Figure 5.11 A). The structural rigidity of the resulting gel provided a better formed gel that resembled the shape of the mold that was used. One thing

to note is that the tops of the gels were rounded, indicating a certain degree of softness to the gel, preventing the gels from completely recapitulating the shape of the mold.

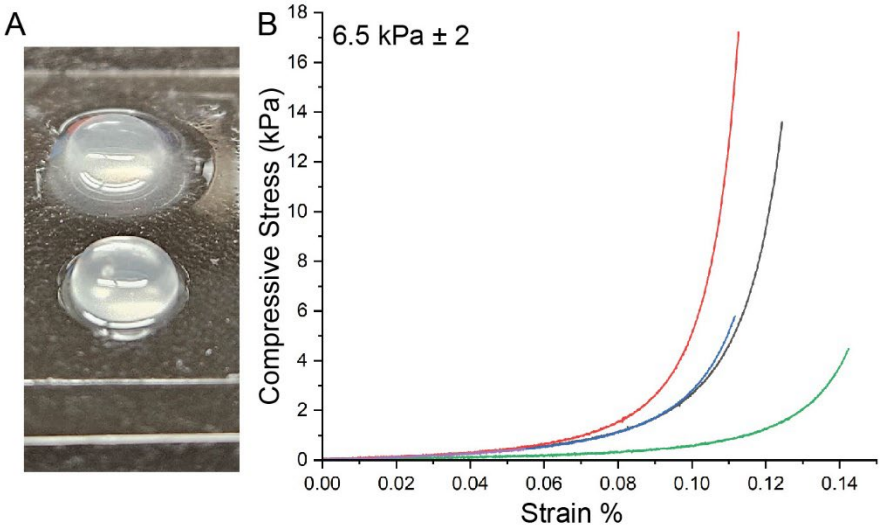

Figure 5.11. Gelation of the photo-crosslinked NorHA scaffold. A) Digital photograph of the photo-crosslinked NorHA for 6 mins, I2959, and no DTT. **B)** Compressive stress versus stress % curve of the crosslinked gels. N = 4.

Following gel fabrication, the mechanical properties were measured with a compression tester. Four samples were tested, and there was a fair degree of variability between gels. The range of the strain % for all the samples that were tested was 0.11 – 0.14 %, whereas the compressive stress ranged from 4 to 17 kPa (Figure 5.11 B). The dramatic range in the measured compressive stress indicates a large degree of variability in the sample type, possibly due to inhomogeneity in the nature of the crosslinking (which, in the absence of DTT, is presumed to be directly norbornene-to-norbornene linking via radical formation). The samples that gave similar measurements were samples 1 and 3, where the compressive strain was similar until sample 3 ended with a smaller compressive stress (~ 5 kPa). Sample 2 had the highest measured compressive stress of about ~ 17 kPa, whereas sample 4 had a compressive stress of about ~4 kPa, which resulted in a large standard deviation for the four samples.

From these compression results, the modulus for this system was calculated to be 6.45 kPa ± 1.99 kPa. The calculated compression modulus was dramatically different than the compression modulus of the same gel type but with the γPFD-Cys filaments included. The difference between the compression moduli is 14.01 kPa, which is about a three-fold increase in the compression modulus due to the incorporation of the γPFD-Cys filaments. With a large degree of areas in the gel that is not crosslinked, that would result in a gel with a smaller compression modulus. The nature of the crosslinker is also dramatically different. The γPFD-Cys filaments are micrometers in size, with a multi-valent presentation of cysteine residues, which can allow for a large degree of crosslinking, ranging throughout a large area of the biomaterial scaffold due to the size of the filaments. However, for the crosslinked NorHA just with I2959, the crosslinking is derived from norbornene-norbornene crosslinking, which limits the effective range of crosslinking. Due to the limited effective crosslinking range, that might result in a certain degree of crosslinking but may not efficiently crosslink the gel as compared to the γPFD-Cys filaments.

To more directly probe the microstructure of the NorHA only system, the gel was fixed, buffer exchanged in ethanol, dehydrated in a dessicator overnight and sputter coated with carbon. The resulting carbon-coated hydrogel was analyzed under the SEM to understand the native morphology of the NorHA scaffold. With a wide-field view of the hydrogel, the gel revealed a smooth surface but with a flakey and granular interior (Figure 5.12 A, B). Taking a closer look in the granular and flakey nature of the NorHA scaffold revealed a similar morphology seen in previous NorHA SEM micrographs, but lacking any fibrous morphology (Figure 5.12 C). There were areas in the hydrogel that appeared slightly fibrous but upon closer examination, these morphologies appeared to be more like

pillars of the NorHA scaffold that rose from the base of the scaffold. In addition, these pillars narrowed, with a wider base compared to the tip of the pillar, indicating a lack of a homogeneous width. From these SEM micrographs, the native morphology of the NorHA scaffold provides a clear contrast compared to the gels that have been incorporated with the γPFD-Cys filaments.

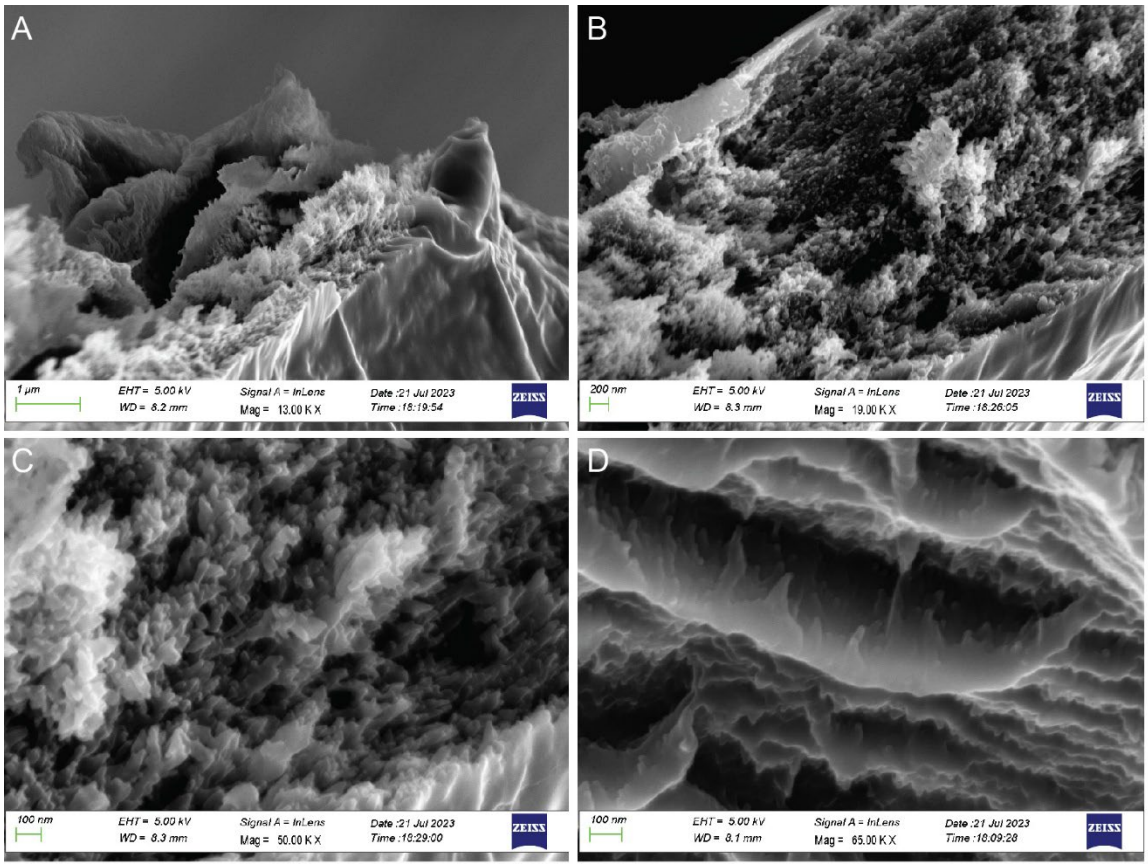

Figure 5.12. SEM analysis of the photo-crosslinked NorHA hydrogel without DTT. A) Wide-field SEM micrograph of the NorHA hydrogel. **B)** SEM micrograph of the NorHA hydrogel highlighting the flaky morphology. **C)** SEM micrograph of the NorHA hydrogel highlighting the flaky morphology throughout the scaffold. **D)** A zoomed-in SEM micrograph of the NorHA hydrogel revealing amorphous pillars within the hydrogel.

To test the gelation of the γPFD-Cys filaments with another system, a madeimide-tetra-arm PEG_{10k} was used. The lyophilized madeimide-tetra-arm PEG_{10k} was dissolved in water and vortexed until the powder was completely dissolved. Once dissolved, an

equivalent volume of the the γPFD-Cys filaments were mixed with the madeimide-tetra-arm PEG_{10k} but no gelation was observed. However, upon the small volume addition of 2 µL of DTT in the mixture, the sample did indeed gel. Three other samples were generated from through this process, where 4 µL of DTT was added, 6 µL of DTT was added and lastly, the PEG-DTT sample was generated *without* the addition of the γPFD-Cys filaments.

The mechanical properties of the resulting PEG-based hydrogels were probed by compression testing. Due to material limitation, only two of each sample type was tested. The resulting strain % vs. compresssive stress plot revealed a strain % range of 0.07 – 0.14 % (Figure 5.13 A). In addition, the compressive stress had a range from ~0.6 kPa to 1.5 kPa, with the PEG-DTT, without the protein filaments having the highest measured compressive stress and strain %. For the PEG-DTT gels that contained the protein

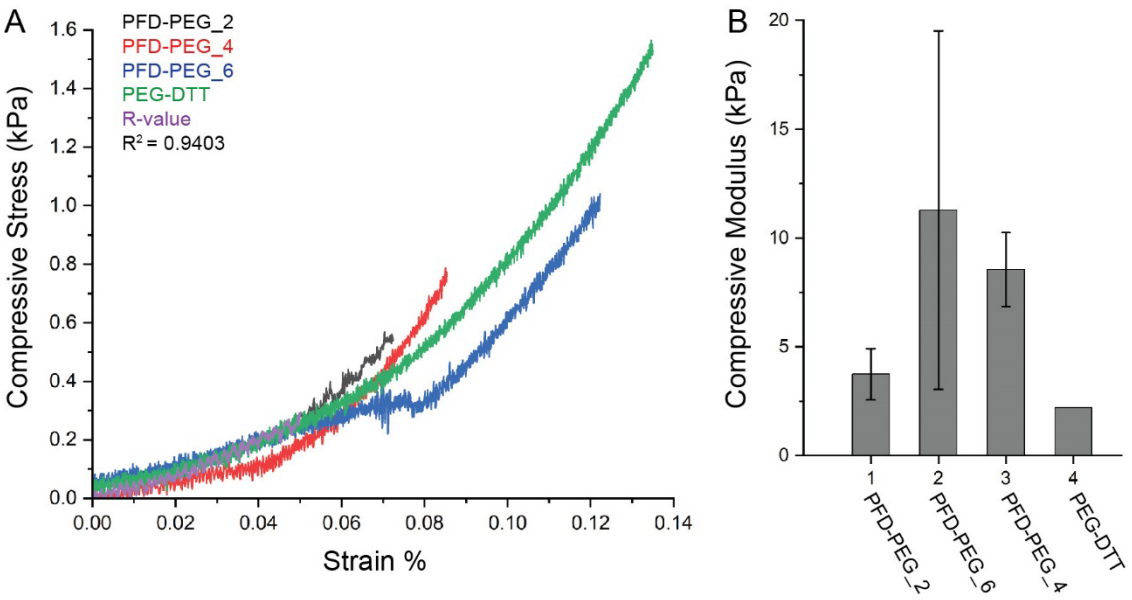

Figure 5.13. Gelation of the crosslinked γPFD-Cys $TetraPEG_{10k}$ scaffold. A) Compressive stress versus stress % curve of the crosslinked gels. N = 2. **B)** Calculated average compressive moduli from the compressive strain vs. stress % curves for all four types of PEG gels.

filaments, there was an observed increase in the compressive stress when the amount of DTT in the hydrogel increased from 2 μL to 6 μL. From the compressive stress plots, the compression moduli for each sample type was calculated. For the PEG-DTT control, the resulting compression modulus was 2.02 kPa. Due to material restrictions, there was no standard deviation that was obtained from this sample type. However, for the calculated compression modulus, this is a significant reduction compared to the NorHA system, which highlights the softness of PEG-based gel system. For the PEG gels with the γPFD-Cys filaments included, the first sample (2 μL) had a calculated compression modulus of 3.7 ± 1.2 kPa. Based on the slight increase in the compression modulus, it highlights the potential for the γPFD-Cys filaments to stiffen the gel, similarly to the NorHA system; however, given the potentially high variabilility in modulus of these systems,it will be necessary to reproduce this result to say this with certainty. By increasing the additon of DTT to 4 μL, the calculated compression modulus increased to 11.3 ± 8.2 kPa. The calculated modulus results in a significant increase in the storage modulus, an increase of about six-fold compared to the based PEG scaffold. However, due to the large standard deviation, it is hard to say for certain that the calculated compression modulus is accurately reflected. Lastly, an increase to 6 μL of DTT resulted in a calculated compression modulus of 8.6 ± 1.7 kPa. This represents a four-fold increase in the compression modulus compared to the base scaffold, with a more reliable standard deviation. From these mechanical studies, the results indicate that the γPFD-Cys filaments as well as the addition of the DTT crosslinker can promote gelation and can be used to modulate the stiffness of a PEG-based gel. However, the results also indicate that the range of moduli is rather limited, based on the

small set of sample types, as compared to the NorHA, which ranged from approximately 6 kPa to 35 kPa.

To examine the PEG-based gels further, each gel type was fixed, buffer exchanged into ethanol, dried overnight in a dessicator, and sputter coated with carbon. The resulting carbon-coated hydrogel were analyzed under SEM to determine their morphology. The first PEG-system that was analyzed was the PEG gel crosslinked with DTT *without* the addition of the γPFD-Cys filaments. An initial wide-field SEM micrograph was taken to observe the large-scale morpolohy of the gel (Figure 5.14 A). The SEM micrograph revealed a smooth but striated scaffold, where the striations indicate ridges where the hydrated gel folded on itself during the dehyradation process. To note, there is a region towards the bottom right of the micrograph which depicts some cracking of the gel. The crack is due to the physical instability of the PEG gel under the electron beam. Even through the electron beam was at a low dose (5 KeV), the strength of the beam was strong enough to deteriorate the surface of the sample.

Taking a closer look at the surface revealed areas that seemed filamentous in nature (Figure 5.14 B), the micrograph revealed an area that formed pillars of the scaffold. The pillars in this micrograph appeared to have similar widths, where the pillars started with a larger base, narrowed in the middle, and then broadened out again as it was penetrating the other area of the PEG scaffold. Physical measurements of these pillars revealed a wide range of widths, from 30 nm to 18 nm (Figure 5.14 E). Based on the measuremnts and the micrograph, it highlights the ability of the PEG scaffold to form these filamentous-like structures in the gel, which exhibit inhomogeneous dimension and morphology.

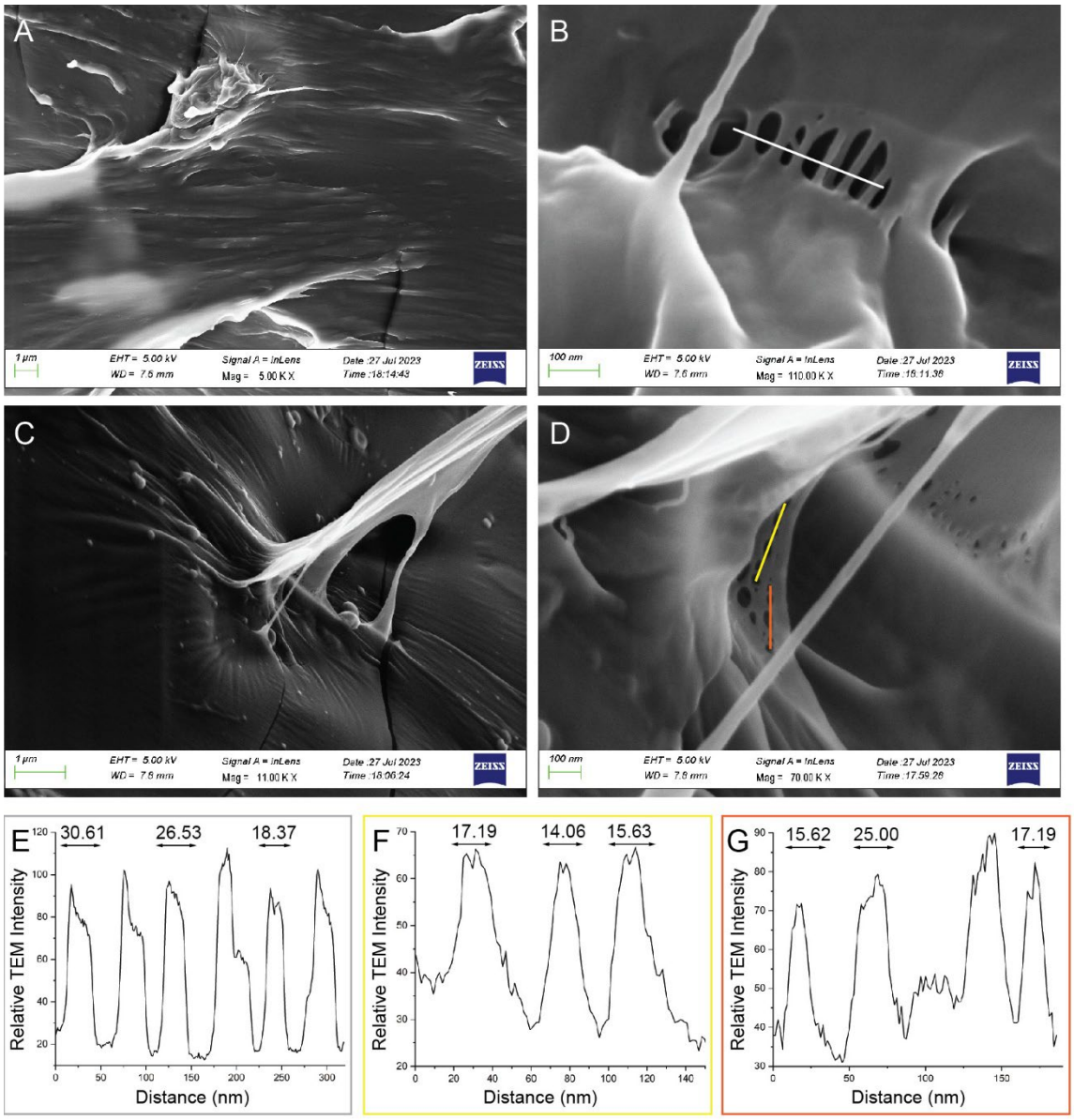

Figure 5.14. SEM analysis of the tetraPEG$_{10k}$ hydrogel crosslinked with DTT. A) Wide-field SEM micrograph of the PEG-DTT hydrogel. **B)** SEM micrograph of the PEG-DTT hydrogel highlighting filamentous-like morphology. The line depicts the sections that was measured in the width trace below. **C)** SEM micrograph of the PEG-DTT hydrogel highlighting the smooth but brittle morphology in the scaffold. **D)** A zoomed-in SEM micrograph of the PEG-DTT hydrogel revealing the fibrous network within the hydrogel. The lines depict the sections that were measured in the width traces below. **E)** Width profile of the PEG filaments in (**B**), traced with the white line. **F)** Width profile of the PEG filaments in (**D**), traced with the yellow line. **G)** Width profile of the PEG filaments in (**D**), traced with the orange line.

Another scan of the sample revealed an area where it looked like a portion of the

PEG gel was being pulled apart, and due to the viscosity of the PEG solution, appears to

be an “elastic” fiber (Figure 5.14 C). The micrograph nicely depicts the “elastic”, smooth, and brittle nature of the PEG hydrogel. There is also another crack in the micrograph, once again highlighting the instability of the PEG sample under SEM conditions. Lastly, by taking a closer look at this specific region in the gel, mutliple unique morphologies are seen in the SEM micrograph (Figure 5.14 D). In terms of the morphologies that are seen, there are areas where the scaffold appears very smooth, areas where the scaffold seems amorphous, areas where there is some web-like morphologies, and lastly, areas where the scaffold appears to be fibrous. To better understand the web-like features, a couple of physical measurements were taken, depicted by the yellow and orange lines in the micrograph. The first measurement depicted by the yellow line revealed a smaller range of widths for the “filaments”, where there widths measured out as 17.2 nm, 14.1 nm, and 15.6 nm. The other region that was measured was highlighted by the orange line, which had a much broader width range. The structures that were measured has widths of 15.6 nm, 25.0 nm, and 17.2 nm. These three measurements in conjuncton with the three previous measurements revealed that these fibrous/web-like structures are very inhomogeneous in their dimensions and emphasizes the vicous nature of the biomaterial scaffold. Overall, the micrographs of the base scaffold shows that the PEG is brittle, sticky, and smooth in nature, and where the “fibers/pillars” that are seen have inhomogeneous physical dimensions.

Once a morphological view of the PEG-based system was observed, the next sample that was analyzed was the PEG-DTT gel with the addition of the γPFD-Cys filaments to observe differences that could be attributed to the incorporation of the protein filaments. The sample that was analyzed next was doped with 4 μL of DTT, yielding the slightly stiffer gel. The 2 μL DTT gel sample was not taken over to the SEM due to

complete collapse of the gel struture under dehydration conditions, percluding transfer to an SEM pillar. By contrast, the 4 μL DTT sample resulted in a pliable, dehydrated gel that was suitable for sputter coating with carbon. After sputter coating, the sample was analyzed with a wide-field view to achieve a better understanding of the morphology involved.

The wide-field view of the gel sample revealed a more fibrous type of morphology, where the smoothness of the PEG scaffold was accented with more intense ridges and striations (Figure 5.15 A). In the micrograph, there was also an interesting ribbon-like structure, which may be derived from the PEG scaffold. By zooming into a region where there seemed to be fibrous, it was revealed that there were large fibers sticking out of the base scaffold (Figure 5.15 B). Based on the scale bar of the micrograph, the fibers were too large to be the γ-PFD-Cys filaments. However, to ensure the width of these surface filaments, one of them were measured, highlighted by the white line in the micrograph. The resulting measurement indicated a width of 168.07 nm, which is significanty larger than the expected width of the protein filaments. In this regard, the fibers that appear to penetrate out from the surface of the gel may be due to fibrous PEG-like structures.

By scouring other regions of the gel sample, there were more instances of pillar-like structure that may indicate the introduction of the γPFD-Cys filaments (Figure 5.15 C, D). For the pillars in Figure 5.15 C, the basal region seemed to have a similar width through the entirety of the filament, indicating homogeneous physical dimensions, which would indicate the presence of well-formed protein filaments. Physical measurements were taken to determine the width of each of these pillars (along the yellow line in the micrograph). The resulting measurements revealed widths ranging from 26.82 nm to 34.57 nm (Figure 5.15 F). The measurements are too large to be the protein filaments and the variability of

the measurements indicates that these pillars are most likely due to the PEG scaffold, based on previous measurements.

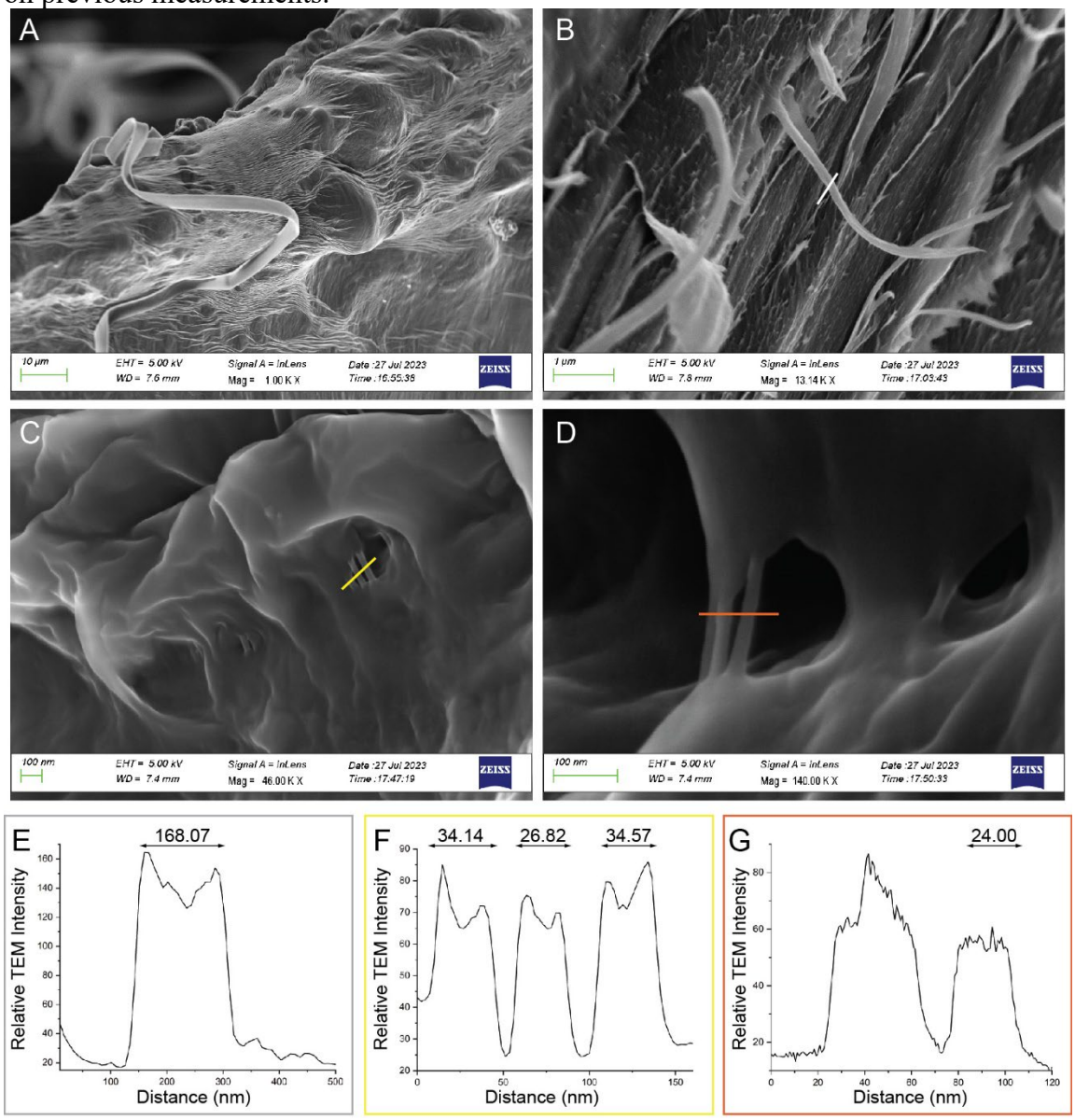

Figure 5.15. SEM analysis of the γPFD-Cys-tetraPEG$_{10k}$ hydrogel. A) Wide-field SEM micrograph of the PFD-Cys-tetraPEG$_{10k}$ hydrogel. **B)** SEM micrograph of the PFD-Cys-tetraPEG$_{10k}$ hydrogel highlighting fibrous-like morphology. The line depicts the sections that was measured in the width trace below. **C)** SEM micrograph of the PFD-Cys-tetraPEG$_{10k}$ hydrogel highlighting smooth and filamentous morphologies in the scaffold. **D)** A zoomed-in SEM micrograph of the PFD-Cys-tetraPEG$_{10k}$ hydrogel revealing fibrous branches within the hydrogel. The lines depict the sections that were measured in the width traces below. **E)** Width profile of the filaments in (**B**), traced with the white line. **F)** Width profile of the filaments in (**C**), traced with the yellow line. **G)** Width profile of the filaments in (**D**), traced with the orange line.

The other SEM micrograph also revealed pillar-like structures but based on previous SEM micrographs, these pillars had large basal regions which collimated towards the center, suggesting that these structures are derived from the base scaffold (Figure 5.15 D). To obtain a better understanding of these pillars, measurements were taken (along the orange line in the micrograph). The measurements revealed pillars with dimensions greater than 24 nm, which again deviates greatly from the expected width of the protein filaments (Figure 5.15 G). From the SEM microgaphs that were obtained from the PEG-DTT (4 μL) sample doped with the γPFD-Cys filaments, there was little evidence of the incorporation of these protein filaments.

To obtain better evidence of the incorporation of the γPFD-Cys filaments, the other PEG-DTT (6 μL) sample with the filaments were analyzed under SEM. The gel was subjected to similar fixing and dehydrating conditions for SEM preparation. After the sample was sufficiently dehydrated, the gel was sputter coated with carbon and taken over to the SEM. A wide-field view of the gel revealed similar morphological features that have been seen with the other previous PEG samples, such as a smooth surface, pillaring, and web-like features (Figure 5.16 A). Once again, there was an area to the right of the micrograph that depicted a severed region of the gel, which cracked due to the power of the electron beam. By examining other areas of the gel sample, a region that appeared to be stitched together was captured on the SEM (Figure 5.16 B). The regions were smooth folds that were speckled with white dots. The smooth folds were stitched together by numerous, thin filaments, which appeared to have similar physical dimensions. With the current magnification, one of these filamentous regions were measured with respect to the white line on the SEM micrograph. The measurement revealed distinct peaks that

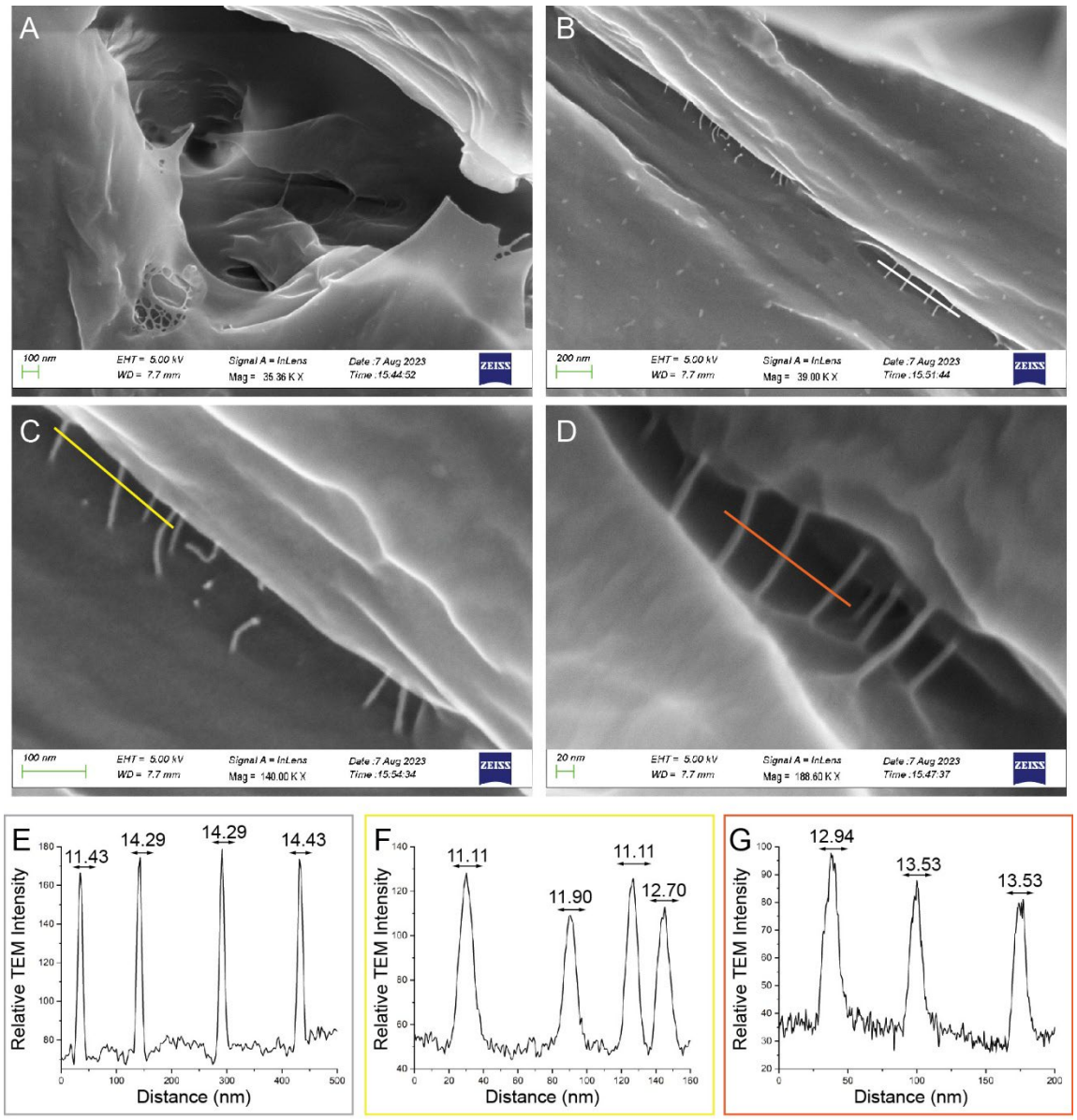

Figure 5.16. Filamentous SEM analysis of the γPFD-Cys-tetraPEG$_{10k}$ hydrogel. A) Wide-field SEM micrograph of the PFD-Cys-tetraPEG$_{10k}$ hydrogel highlighting the PEG scaffold. **B)** SEM micrograph of the PFD-Cys-tetraPEG$_{10k}$ hydrogel highlighting fibrous-like morphology. The line depicts the sections that was measured in the width trace below. **C)** SEM micrograph of the PFD-Cys-tetraPEG$_{10k}$ hydrogel highlighting smooth and filamentous morphologies in the scaffold. The line depicts the sections that was measured in the width trace below. **D)** A zoomed-in SEM micrograph of the PFD-Cys-tetraPEG$_{10k}$ hydrogel revealing filaments interconnected within the hydrogel. The lines depict the sections that were measured in the width traces below. **E)** Width profile of the filaments in (**B**), traced with the white line. **F)** Width profile of the filaments in (**C**), traced with the yellow line. **G)** Width profile of the filaments in (**D**), traced with the orange line.

accounted for thin filaments with a tight width range, from 11.4 nm to 14.4 nm, deviating

only by 2 nm from the width of the γPFD-Cys filaments. These measurements also agree with the previous filaments that were measured in Figure 5.3 and Figure 5.4. In addition, since these measurements did not have such major width deviations, the consistency hints towards well-defined structures that may correspond to protein filaments.

A closer examination into the filamentous region showcased well-defined filaments penetrating one region of the PEG scaffold to another. To highlight a few interesting observations from the zoomed-in micrograph, there was two filaments that appeared to be "snapped" in half, where the filaments where the filaments were almost floating in space. In addition to these filaments, the regions that were torn off appeared to leave white specs on the surface of the PEG gel. These white specs resemble some of the specs that were coating the surface in figure 5.16 B. If the specs in fig. 5.16 B are due to γPFD-Cys surface blemishes, then that would indicate that this specific region under examination would be littered with the filaments, highlighting the incorporation of the γPFD filaments. These well-defined filaments were measured (along the yellow line in the micrograph), yielding 11.1 nm to 12.7 nm, which is much closer to the expected value of the protein fibers.

To further verify the incorporation of the protein filaments, EDS-SEM was conducted on the γPFD-Cys-PEG hydrogel. Once again, the technique was used to probe the elemental incorporation of nitrogen (N) and sulfur (S), which is present in the γPFD-Cys filaments. EDS-SEM should selectively distinguish the γPFD-Cys monomer, based on their S and N content, which differ dramatically from the PEG scaffold due to the lack of any nitrogen atoms or sulfur atoms. However, due to the small doping of the DTT crosslinker, there should be an increase in the sulfur signal. Other than that, most of the nitrogen N $K\alpha_{1,2}$ and the sulfur N $K\alpha_1$ spectroscopic signals that are observed should be

derived from the crosslinker and/or the γPFD-Cys filaments. To note, the N $K\alpha_{1,2}$ signal should only be derived from the γPFD-Cys filaments.

To obtain an EDS-SEM micrograph of the sample, an area that seemed to have clear filaments filamentous was imaged used a low electron voltage (5 KeV). Once an appropriate area was found, the electron voltage as increased to 20 KeV to allow for enough energy to be applied to the sample to ensure appropriate inner-shell electron dispersion. Upon increasing the electron voltage and inserting the EDS detector, the elemental composition of the area was determined. The resulting EDS-SEM micrograph was probed for the N $K\alpha_{1,2}$ signal and the S $K\alpha_1$ due to those being the distinguishing elements for the experiment (Figure 5.17 A). The EDS-SEM micrograph displayed the S $K\alpha_1$ signal at a high abundance (red signal) whereas the N $K\alpha_{1,2}$ signal was scattered throughout (blue signal). Due to the high abundance of the S $K\alpha_1$ signal, there N $K\alpha_{1,2}$ signal was difficult to distinguish.

In addition to the EDS-SEM micrograph, the EDS spectrum was obtained to gather the entire elemental composition of the imaged area in the hydrogel (Figure 5.17 B). The most abundant elements were carbon, oxygen, sulfur, and sodium. As before, the high carbon signal is due to the carbon sputter coating, which would create an abundantly high-intensity peak. The high sodium peak does not reflect the biochemical make-up of either the γPFD-Cys filaments or the PEG scaffold, but the hydrogel was made in a phosphate buffer saline, which contains a high concentration of sodium resulting in residual salt that was captured during the fixing and dehydration treatment of the gel. The high O $K\alpha_1$ signal is derived from the PEG scaffold due to the oxygen in the PEG monomer *and* due to the

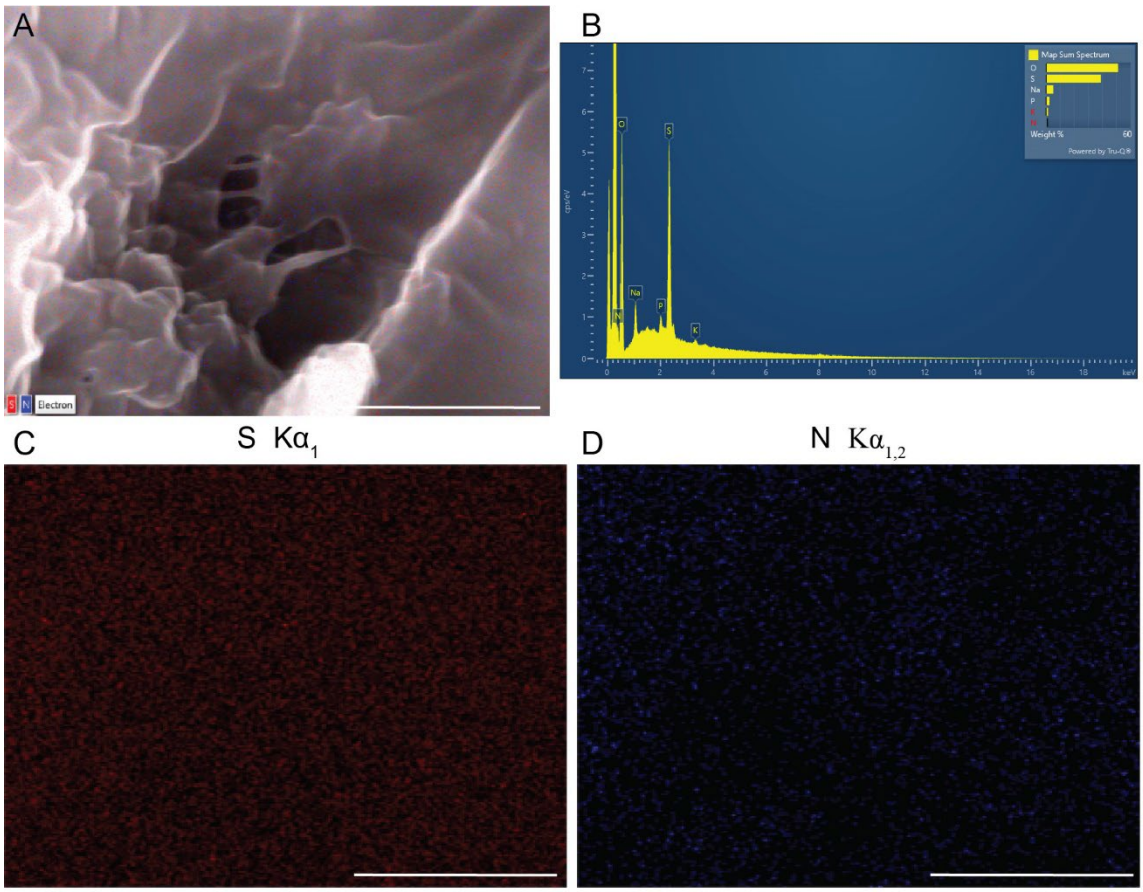

Figure 5.17. SEM-EDS analysis of the γPFD-Cys-tetraPEG$_{10k}$ hydrogel doped with DTT. A) SEM-EDS micrograph of the γPFD-Cys-tetraPEG$_{10k}$ hydrogel, inlaid with the S and N elemental signals. **B)** EDS spectrum of the SEM micrograph in (**A**). **C)** Elemental mapping of the sulfur Kα$_1$ signal from the SEM micrograph in (**A**). **D)** Elemental mapping of the nitrogen Kα$_{1,2}$ signal from the SEM micrograph in (**A**). Scale bars = 500 nm

high presence of oxygen in the protein filaments. The high sulfur content is the highest sulfur Kα$_1$ signal seen in any EDS-SEM micrograph seen thus far, and represents the portion of S on the protein filaments and due to the thiols, that are present in the DTT crosslinker.

Due to the high C Kα$_1$ signal, the N Kα$_1$ that was received by the detector was masked. The N Kα$_1$ signal appeared near 0.4 KeV, with an intensity of 0.8 cps/KeV. Although this signal was low and masked by the C Kα$_1$ signal, it was still registered by the

detector and was visualized by the N $K\alpha_1$ EDS-SEM micrograph (Figure 5.17 D). The bleu dots from the EDS-SEM micrograph depict areas of scatter N in the area, where there are some bright red spots, indicating a high abundance of S in that localized area. As for the S $K\alpha_1$ signal, it was more dominant in the EDS spectrum compared to the N $K\alpha_{1,2}$ signal, at 2.3 KeV with an intensity of 5.4 cps/KeV. Once again, the high intensity of the S $K\alpha_1$ signal is partly derived from the DTT crosslinker but includes contribution by the Cys-residue in the protein filaments. However, it is not possible to determine the relative contribution of the two. In addition, the EDS-SEM micrograph of just the S $K\alpha_1$ displayed well-scattered dispersion spots, with areas of high, localized intensity and even black-out areas. Due to the high intensity of the S $K\alpha_1$ signal, the EDS dispersion spots are easily depicted in the EDS-SEM micrograph, which makes the incorporation easier to distinguish. One of the downsides of EDS-SEM is the high intensity of the electron beam (20 KeV), which resulted in major deterioration of the PEG scaffold. Only areas that did not deteriorate under the electron beam could be probed.

Finally, concentration-dependent EDS-SEM micrographs were obtained from the hydrogel area to ascertain the relative abundance of each elemental signal. For the S $K\alpha_1$ signal, their signal was well-scattered throughout the surface and most of the concentration values, relative to 3179, ranged from 530-1589 (Figure 5.18 A). The dispersion spots did trend towards high concentration values and there were a few instances where red spots indicative of a concentration of 2384 was detected. As for the N $K\alpha_{1,2}$ signal, the scattering of dispersion peaks was low, as compared to the S $K\alpha_1$ signal (Figure 5.18 B). In addition, the concentration values were much lower compared to the S $K\alpha_1$ values, ranging from 150-749. There were hardly any peaks seen in the 674-749 value range, but a few were

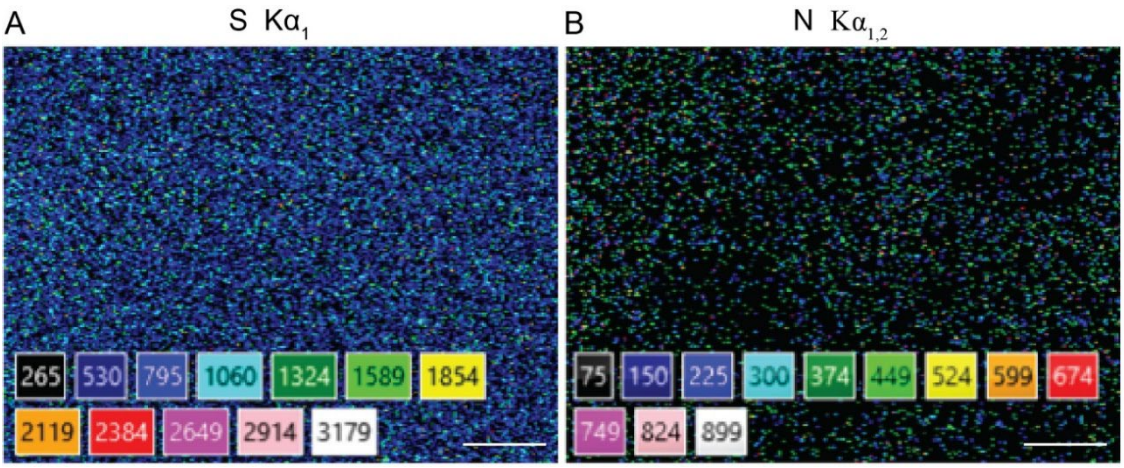

Figure 5.18. Concentration-dependent elemental mapping of the γPFD-Cys-tetraPEG$_{10k}$ hydrogel doped with DTT. **A)** Concentration-dependent elemental mapping of the sulfur Kα$_1$ signal from the SEM micrograph in (**Figure 5.17A**). **B)** Concentration-dependent elemental mapping of the nitrogen Kα$_{1,2}$ signal from the SEM micrograph in (**Figure 5.17 A**). Scale bars = 200 nm.

scattered throughout the SEM imaging area. Overall, the concentration-dependent EDS-SEM micrograph depicts a higher S concentration relative to the N signal, mainly due to the additional DTT that was added to the hydrogel.

5.3 Conclusion

To circumvent the need for a high protein concentration to obtain a γPFD hydrogel and to more reliably tune the hydrogel mechanical properties through the use of a crosslinker, a filler hydrogel, NorHA, was used to promote gelation with the protein filaments. The addition of 2 wt% γPFD-Cys was shown to be enough to achieve gelation with the NorHA through photochemical crosslinking. The wt% is dramatically lower than other reported systems and provides a facile method to achieve filamentous morphologies into scaffolds that lack those structural parameters. This method was demonstrated incorporation of protein filaments the NorHA scaffold as well as a PEG scaffold, demonstrating these results in both a natural polymer system as well as a synthetic one.

The inclusion of the γPFD filaments in either scaffold yielded an increase in compression modulus, with a broader range of moduli that can be achieved. In addition to the increase in structural stiffness, the NorHA platform provided a means to further functionalize these protein filament hydrogels through the photochemical crosslinking of Cys-GFP, post gelation. Lastly, the inclusion of the protein filaments was characterized through SEM to observe filaments scattered throughout the hydrogel, in addition with EDS-SEM to detect the elemental inclusions of the protein filaments. This approach highlights the utility of such a system and can be a useful tool for fundamental biology or for regenerative medicine applications.

5.4 Methods and Materials

Protein Expression and Purification. The gene encoding γPFD-Cys were synthesized as gBlocks gene fragments (Integrated DNA Technologies) and were inserted into the multiple cloning sites of the pET- 19b plasmid (Novagen) using the Gibson assembly (New England Biolabs). The assembled plasmids were transformed into T7 Express competent cells, which were grown at 37°C in LB Broth (Lennox) containing 100 μg/mL ampicillin up to OD600 = 0.6. γPFD-Cys protein expression was induced by adding IPTG to a final concentration of 0.5 mM and cells were grown for an additional 16 hours at 25°C. The cells were harvested by centrifugation at 5000 rpm for 20 minutes, lysed using a French press, and centrifuged at 13,000 rpm for 60 minutes. For γPFD-Cys, the resulting supernatant was then purified using a multimodal chromatography resin (Capto Core 700, GE healthcare) using an AKTA FPLC. The proteins were loaded on the column with the equilibrium buffer (100 mM NaCl, 50mM Tris, pH 7.4). The elution peak was identified using SDS-PAGE and SimplyBlue staining (Invitrogen), and the pure target protein was dialyzed overnight

against water. Finally, the purified proteins were flash-frozen with liquid N2 and lyophilized for storage at -80°C.

Norbornene-functionalized Hyaluronic Acid (NorHA) Synthesis. NorHA for the gel construction was provided by the Holloway lab. Their protocol for making it is as follows: sodium hyaluronate (HA, Lifecore Biomedical, 60 kDa) was converted to its tetrabutylammonium salt (HA-TBA) using the Dowex 50 x 200 ion exchange resin, frozen, and lyophilized and characterized by ^{1}H NMR (Bruker). HA-TBA carboxylic acid groups were then modified with norbornene groups via amidation with 5-norbornene-2-methylamine (Tokyo Chemical Industry), anhydrous dimethyl sulfoxide (DMSO), and benzotriazole-1-yl-oxy-tris-(dimethylamino)-phosphonium hexafluorophosphate (BOP) under nitrogen at room temperature for 4 h. The reaction was quenched with cold water, purified via dialysis (SpectraPor, 6–8 kDa molecular weight cutoff) for 7 days at room temperature, frozen, and lyophilized. The degree of modification was ~92% as measured by ^{1}H NMR (Bruker).

NorHA Hydrogel Fabrication. Hydrogels were fabricated with 4 wt % of NorHA macromer in phosphate-buffered saline (PBS). NorHA with approximately 92% norbornene functionalization was dissolved in PBS containing a non-degradable dithiol crosslinker (1,4-dithiothreitol), and 0.05% w/v photoinitiator (Irgacure-2959). DTT was added a stoichiometric molar ratio of 0.2:1 thiol to norbornene functional groups, leaving 80% of the original norbornene groups available for photoconjugation. The pre-gel solution was transferred into a custom cylindrical acrylic mold (SYLGARD 184, Dow), covered

with a glass slide, and crosslinked via ultraviolet (UV) light at 10 mW/cm^2 (Omnicure S1500, 320–390 nm) for 4 minutes.

To create protein nanofiber embedded throughout the NorHA hydrogels, NorHA was completely dissolved with the γPFD-Cys filaments at a concentration of 2 wt%. Once dissolved, 0.05 wt% of photoinitiator I2959 in PBS was added into the solution. The solution was pipetted into the custom silicone mold and exposed to UV light (10 mW/cm^2) for 6 min. The mold was removed to retrieve the fabricated gel. The gel was washed with three rounds of PBS to ensure removal of non-crosslinked material.

Secondly, to create a stiffer γPFD-Cys hydrogel, NorHA was completely dissolved in a PBS solution containing the 2wt% γPFD-Cys filaments and vortexed. DTT was added at a 0.1 equivalents relative to the norbornene groups, and 0.05 wt% of photoinitiator I2959 in PBS was added into the solution. The solution was pipetted into the custom silicone mold and exposed to UV light (10 mW/cm^2) for 4 min. The mold was removed to retrieve the fabricated gel. The gel was washed with three rounds of PBS to ensure removal of non-crosslinked material.

Tetra-PEG$_{10k}$ Hydrogel Fabrication. Hydrogels were fabricated with 1 wt% of Tetra-PEG$_{10k}$ (Sigma Aldrich) macromer in phosphate-buffered saline (PBS). First, the maleimide-tetra-PEG$_{10k}$ powder was dissolved in PBS and vortexed aggressively. The 2 wt% γPFD-Cys filaments were added to obtain a concentration of 1 wt% and then vortexed. DTT was then added at an equimolar concentration to the maleimide groups on the tetra-PEG$_{10k}$. The solution was quickly vortexed, which immediately resulted in gelation.

Hydrogel Mechanical Property Characterization. Compression mechanical properties were assessed at room temperature immediately after gelation using a benchtop mechanical testing machine (Instron Materials Testing System Series 5943, 50 N load cell) in unconfined compression. Compression was performed at 24% strain per minute and the compressive modulus was calculated from the initial linear region of the stress vs strain curve. The compressive modulus was determined for each individual hydrogel construct.

Fluorescent Protein Incorporation into the NorHA Hydrogels. For the washed NorHA hydrogels that have been modified with γPFD-Cys filaments, a solution of sf-GFP with 0.05% of the photoinitiator was added on top of the modified gel. The gel was exposed to UV light (10 mW/cm^2) for 1 min. The mold was removed to retrieve the fabricated gel. The gel was washed with three rounds of PBS to ensure removal of non-crosslinked material. The gel was then imaged under bright-field and fluorescence microscopy (Leica DMI6000 B). Once characterized, the gel was washed six times with 1x PBS, at a pH of 7.4, overnight and allowed to shake at room temperature overnight. After incubation, the gels were imaged with bright-field and fluorescence microscopy.

Scanning Electron Microscopy Characterization. The γPFD-Cys filament-embedded hydrogels were prepared in two fashions: through ethanol replacement and subsequent dehydration, or through lyophilization. For the ethanol buffer exchange, the hydrogel was washed three times with 1x, PBS, at a pH = 7.4, and aspirated. Once washed, the gel was incubated with 400 μL of 4 % paraformaldehyde (Electron Microscopy Sciences) dissolved in 1x PBS, pH = 7.4, and allowed to be fixed for 20 mins. Once fixed, the gel was washed three times with 1x, PBS, at a pH = 7.4, and aspirated. The PBS buffer was then exchanged

into 100% ethanol over serial dilutions (10%, 20%, 30%, 50%, 70%, 95%, and 100%), where the gel was incubated in each buffer system for 10 mins. After the buffer exchange, the ethanol was removed, and the gel was dehydrated under vacuum overnight.

For the lyophilization preparation, the hydrogel was washed with 1x PBS, at a pH = 7.4, and flash frozen in a slurry of dry ice in 100% ethanol. Once frozen, the gels were immediately transferred into a lyophilizer and lyophilized for four hours. The samples were promptly removed to prevent structural compression, and were sealed and stored.

For each dried sample, the sample was immobilized on an SEM stub through double-sided carbon tape. Once immobilized, the sample was sputter coated with carbon using a carbon sputter coated. Once the samples were sputter coated, the samples were analyzed using secondary electron detection using a Zeiss Auriga Focused-Ion Beam Scanning Electron Microscope. The sample was analyzed with an electron voltage of 5 KeV.

Energy-Dispersive Spectroscopy-Scanning Electron Microscopy Characterization. For the sputter coated hydrogel samples, the samples were initially imaged using a Zeiss Auriga Focused-Ion Beam Scanning Electron Microscope at an electron voltage of 5 KeV. Once an optimal area was found, the electron voltage was increased to 20 KeV and subsequently analyzed with an Oxford X-Max Energy Dispersive X-ray Spectrometer (EDS). The elemental composition was obtained, where the Carbon, Nitrogen, Oxygen, and Sulfur signals were the main elements of focus. The data was acquired using the Oxford AZTec App.

CHAPTER 6

OUTLOOK AND CONCLUDING REMARKS

6.1 Future Directions

The work that was completed in this dissertation has demonstrated the self-assembly and utility of protein nanofibers for the generation of dynamic and fibrous biomaterials. As mentioned through the dissertation, the generation of true biomimetic ECM materials enables a spatiotemporal display of protein fibers, a cell-dependent regulation of bioactive signals, and suitable biomechanical properties. Chapter 2 described a way to self-assemble multiple protein domains into micrometer-sized nanofibers, which can be reversed through two mechanisms. In addition, Chapter 3 described a means of introducting a reversible, modular protein nanofiber into a hyaluronan scaffold, incorporating multiple components of the ECM. Thorugh this fibronectin-hyaluronan biomaterial approach, a temporal display of the nanofibers were achieved through a chemical reductant and through peptide displacement. In additon, distinct fibronectin architectures were fabricated through the selective photopolymerization of various gel layers. However, this approach has not yet been implemented and tested with cellular systems.

The ability to generate a nanofiber layer on the NorHA hydrogel system allows for easy coating of a material surface. Therefore, to test the ability of these bioactive nanofibers to regulate cell activity, the NorHA gel can be coated one- or two *distinct* nanofibers, allowing for complex regulation of the cell activity. Due to the ability for the $FN(10)_{III}$ nanofibers to promote cell adhesion, the cells can be adhered on the NorHA gel while promoting the differentiation or selective growth of stem cells due to the $FN(12\text{-}14)_{III}$

domain nanofibers (Figure 6.1 A). In addition, to selective and *temporally* remove one bioactive signal from another, distinct *orthogonal* displacment coils can be used to remove either the $FN(10)_{III}$ nanofibers or the $FN(12\text{-}14)_{III}$ nanofibers to promote specific cellular responses (Figure 6.1 B, C). The outlined approach can provide a dramatic insight on how spatiotemporal effects dictate cell fate, especially for stem cell engineering.

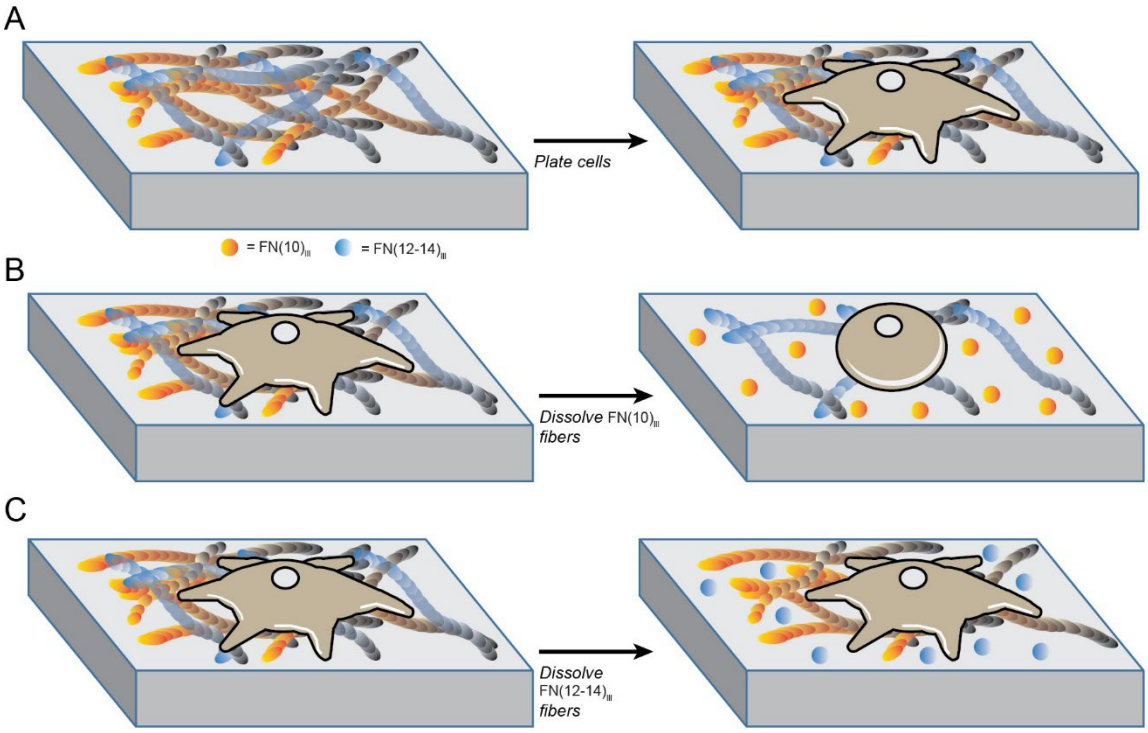

Figure 6.1. Schematic for cell spreading and differentiation studies on a hydrogel surface. A) Two protein nanofibers plated on a hydrogel surface, each with distinct bioactivity. Once plated, cells can be seed and respond accordingly. **B)** Adhered cells can be selectively detached from the surface by the temporal removal of the $FN(10)_{III}$ nanofibers. **C)** The ability of the $FN(12\text{-}14)_{III}$ nanofibers to bind growth factors can be temporally modulated, potentially allowing for selective differentiation while allowing the cells to remain adhered onto the surface.

In addition to surface coating of the protein nanofibers, a way to grow and dissolve the protein nanofibers within the NorHA scaffold would enable a powerful technique to modulate the fiber composition, ligand display, and mechanical properties within one hydrogel system. This approach would require coil handles to be modified on the gel

scaffold, then protein/peptide components would need to be incubated with the peptide-modified hydrogel (Figure 6.2 A). Through this approach, a wide variety of protein compositions can be achieved through the explicit use of orthogonal coils. Additionally,

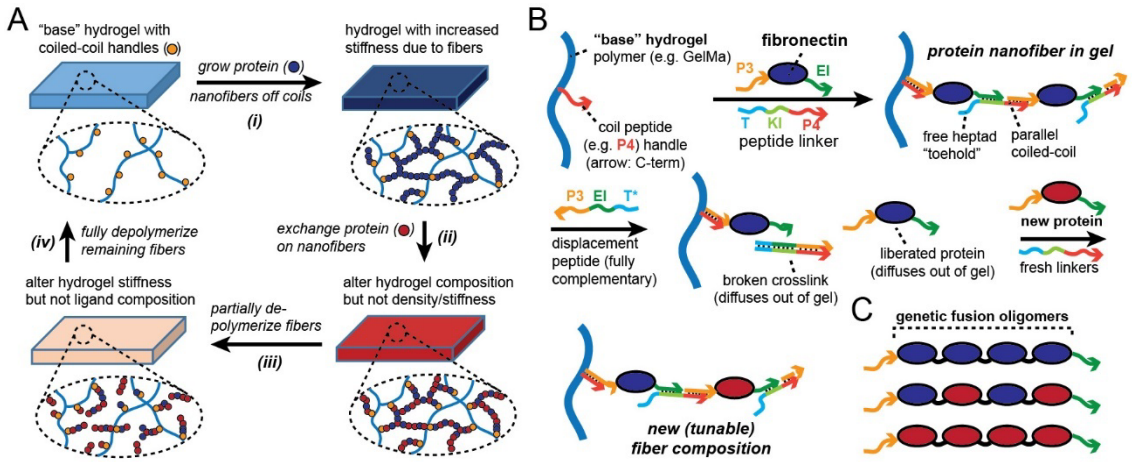

Figure 6.2. Schematic for a tunable protein hydrogel. A) A base hydrogel with coiled-coil handles will be used to grow fibronectin fibers in the vacant space. The growth of the protein filaments will increase the stiffness of the gel (**i**), where the composition can be altered (**ii**) or the stiffness can be reduced (**iii**) through coiled-coil strand displacement. If desired, the original state can be achieved (**iv**) through the reversibility and tunability of the gel platform. **B)** Mechanism of protein fiber formation: The fusion proteins will be seeded from the base hydrogel through free coil handles, where the growth will be mediated through orthogonal coil peptide linkers. The peptide linkers will exhibit a peptide "toehold", which can be used to disassemble the fibers by adding a complementary displacement peptide. The composition of the gel can be altered by adding a new set of fusion proteins and their respective peptide linkers. **C)** The expression of fusion oligomers will limit the necessary amount of peptide linkers needed for filament growth.

this approach can made into a reversible process through the use of displacements coils (Figure 6.2 B). Lastly, to allow for well-defined, spatial control of the bioactive ligands, different fusion oligomers can be expressed to understand how the placement of each ligand, on a nanometer level, changes cellular activity (Figure 6.2 C). These approaches enable a powerful tool to revolutionize the fabrication of ECM mimics to encapsulate some of the protein complexity seen in the native ECM microenvironment.

Chapter 4 outlined another approach for the fibrous inclusion of protein-based hydrogels. As highlighted, various other proteins can be easily introduced through their respective cys-mutants. The ability to modulate the mechanical properties of two distinct hydrogel system also adds an additional benefit for the inclusion of the γPFD filaments. Future work would involve the cell viability of such a system and then introduce other proteins, such as $Fn(10)_{III}$-Cys, to allow for additional bioactivity to be included.

6.2 Concluding Remarks

The use of coiled coils as a self-assembling protein motif, in conjunction with protein domains offers a powerful and rational approach for the the development of protein-based nanofiber biomaterials systems. The utility of these materials can offer an unprecedented insight on how protein signals direct cell fate and can be applied to a wide variety of biomedical applications such as tissue and stem cell engineering. The self-assembly design principles and methods that have been outlined in this dissertation sets the groundwork for a novel nanomaterial. However, due to the infancy of the design, many addition structural parameters can be investigated to ensure stability, robustness, better bioactivity, enhanced reversibility kinetics, and much more. The chapters related to the self-assembly and material incorporation of self-assembled nanofibers aims to illuminate the potential of such systems and hopefully allow the integration of these materials for applications such as fundamental biology, stem and tissue engineering.

Additionally, the development of the thermally stable protein-DNA thin films in Chapter 4 paves a new method for novel, hybrid materials. Through this approach, the structural benefits of DNA nanotechnology, and the functional utility of protein nanofibers

can be explored to fabricate materials with unmatched physical and biochemical properties. The system that was explored exemplified ways to generate well-ordered 2D proteins arrays, whose assembly was made reversible through DNA strand displacement. This approach sets the starting ground to develop complex thin films, and upon further exploration, may be used as 2D films for anti-fouling, sensing, and catalysis.

REFERENCES

(1) Feynman, R. P. There's plenty of room at the bottom. *Feynman and computation* **2018**, *63*, 76.

(2) Taniguchi, N. On the basic concept of'nano-technology'. In *Proc. Intl. Conf. Prod. Eng. Tokyo, Part II, 1974*, 1974; Japan Society of Precision Engineering.

(3) Binnig, G.; Rohrer, H.; Gerber, C.; Weibel, E. Surface Studies by Scanning Tunneling Microscopy. *Physical Review Letters* **1982**, *49* (1), 57-61. DOI: 10.1103/physrevlett.49.57 (acccessed 2023-10-03T21:50:16).

(4) Steed, J. W.; Atwood, J. L. *Supramolecular chemistry*; John Wiley & Sons, 2022.

(5) Whitesides, G. M.; Grzybowski, B. Self-assembly at all scales. *Science* **2002**, *295* (5564), 2418-2421. DOI: 10.1126/science.1070821.

(6) Branden, C. I.; Tooze, J. *Introduction to protein structure*; Garland Science, 2012.

(7) Benyus, J. M. *Biomimicry: Innovation inspired by nature*; Morrow New York, 1997.

(8) Khan, I.; Khan, M.; Umar, M. N.; Oh, D. H. Nanobiotechnology and its applications in drug delivery system: a review. *IET Nanobiotechnology* **2015**, *9* (6), 396-400. DOI: 10.1049/iet-nbt.2014.0062 (acccessed 2023-10-04T20:28:37).

(9) Anfinsen, C. B. Principles that Govern the Folding of Protein Chains. *Science* **1973**, *181* (4096), 223-230. DOI: doi:10.1126/science.181.4096.223.

(10) Dill, K. A.; Ozkan, S. B.; Shell, M. S.; Weikl, T. R. The Protein Folding Problem. *Annual Review of Biophysics* **2008**, *37* (1), 289-316. DOI: 10.1146/annurev.biophys.37.092707.153558 (acccessed 2023-10-04T22:17:27).

(11) Jumper, J.; Evans, R.; Pritzel, A.; Green, T.; Figurnov, M.; Ronneberger, O.; Tunyasuvunakool, K.; Bates, R.; Žídek, A.; Potapenko, A.; et al. Highly accurate protein structure prediction with AlphaFold. *Nature* **2021**. DOI: 10.1038/s41586-021-03819-2 (acccessed 2021-08-19T06:25:49).

(12) Baek, M.; Dimaio, F.; Anishchenko, I.; Dauparas, J.; Ovchinnikov, S.; Lee, G. R.; Wang, J.; Cong, Q.; Kinch, L. N.; Schaeffer, R. D.; et al. Accurate prediction of protein structures and interactions using a three-track neural network. *Science* **2021**, eabj8754. DOI: 10.1126/science.abj8754 (acccessed 2021-08-19T06:27:04).

(13) Ulijn, R. V.; Smith, A. M. Designing peptide based nanomaterials. *Chemical Society Reviews* **2008**, *37* (4), 664. DOI: 10.1039/b609047h (acccessed 2023-10-04T22:36:57).

(14) Zhang, S. G. Fabrication of novel biomaterials through molecular self-assembly. *Nature Biotechnology* **2003**, *21* (10), 1171-1178. DOI: 10.1038/nbt874.

(15) Truebestein, L.; Leonard, T. A. Coiled-coils: The long and short of it. *BioEssays* **2016**, *38* (9), 903-916. DOI: 10.1002/bies.201600062 (acccessed 2023-10-04T23:31:40).

(16) Crick, F. H. C. The packing of α-helices: simple coiled-coils. *Acta Crystallographica* **1953**, *6* (8), 689-697. DOI: 10.1107/s0365110x53001964 (acccessed 2023-10-04T23:37:19).

(17) Aronsson, C.; Danmark, S.; Zhou, F.; Oberg, P.; Enander, K.; Su, H. B.; Aili, D. Self-sorting heterodimeric coiled coil peptides with defined and tuneable self-assembly properties. *Scientific Reports* **2015**, *5*, 10, Article. DOI: 10.1038/srep14063.

(18) Apostolovic, B.; Danial, M.; Klok, H.-A. Coiled coils: attractive protein folding motifs for the fabrication of self-assembled, responsive and bioactive materials. *Chemical Society Reviews* **2010**, *39* (9), 3541. DOI: 10.1039/b914339b (acccessed 2022-03-30T20:33:40).

(19) Gradišar, H.; Jerala, R. De novodesign of orthogonal peptide pairs forming parallel coiled-coil heterodimers. *Journal of Peptide Science* **2011**, *17* (2), 100-106. DOI: 10.1002/psc.1331 (acccessed 2022-03-30T20:46:05).

(20) Parry, D. A.; Fraser, R. B.; Squire, J. M. Fifty years of coiled-coils and α-helical bundles: A close relationship between sequence and structure. *Journal of structural biology* **2008**, *163* (3), 258-269.

(21) Mason, J. M.; Arndt, K. M. Coiled Coil Domains: Stability, Specificity, and Biological Implications. *ChemBioChem* **2004**, *5* (2), 170-176. DOI: 10.1002/cbic.200300781 (acccessed 2023-10-05T16:23:29).

(22) Wood, C. W.; Bruning, M.; Ibarra, A. A.; Bartlett, G. J.; Thomson, A. R.; Sessions, R. B.; Brady, R. L.; Woolfson, D. N. CCBuilder: an interactive web-based tool for building, designing and assessing coiled-coil protein assemblies. *Bioinformatics* **2014**, *30* (21), 3029-3035. DOI: 10.1093/bioinformatics/btu502 (acccessed 2022-03-30T20:28:52).

(23) Chothia, C.; Levitt, M.; Richardson, D. Helix to helix packing in proteins. *Journal of molecular biology* **1981**, *145* (1), 215-250.

(24) Lupas, A. N.; Gruber, M. The structure of α-helical coiled coils. *Advances in protein chemistry* **2005**, *70*, 37-38.

(25) Pauling, L.; Corey, R. B.; Branson, H. R. The structure of proteins: Two hydrogen-bonded helical configurations of the polypeptide chain. *Proceedings of the National Academy of Sciences* **1951**, *37* (4), 205-211. DOI: 10.1073/pnas.37.4.205 (acccessed 2023-10-05T17:28:49).

(26) Pauling, L.; Corey, R. B. Two hydrogen-bonded spiral configurations of the polypeptide chain. *Journal of the American Chemical Society* **1950**, *72* (11), 5349-5349.

(27) Scheib, K. A.; Tavenor, N. A.; Lawless, M. J.; Saxena, S.; Horne, W. S. Understanding and controlling the metal-directed assembly of terpyridine-functionalized coiled-coil peptides. *Chemical Communications* **2019**, *55* (54), 7752-7755. DOI: 10.1039/c9cc03496j (acccessed 2023-10-05T18:49:36).

(28) Kumita, J. R.; Flint, D. G.; Woolley, G. A.; Smart, O. S. Achieving photo-control of protein conformation and activity: producing a photo-controlled leucine zipper. *Faraday Discussions* **2003**, *122*, 89-103. DOI: 10.1039/b200897a (acccessed 2023-10-05T18:52:00).

(29) Thomson, A. R.; Wood, C. W.; Burton, A. J.; Bartlett, G. J.; Sessions, R. B.; Brady, R. L.; Woolfson, D. N. Computational design of water-soluble α-helical barrels. *Science* **2014**, *346* (6208), 485-488. DOI: doi:10.1126/science.1257452.

(30) Scott, A. J.; Niitsu, A.; Kratochvil, H. T.; Lang, E. J. M.; Sengel, J. T.; Dawson, W. M.; Mahendran, K. R.; Mravic, M.; Thomson, A. R.; Brady, R. L.; et al. Constructing ion channels from water-soluble α-helical barrels. *Nature Chemistry* **2021**, *13* (7), 643-650. DOI: 10.1038/s41557-021-00688-0 (acccessed 2023-10-05T19:06:38).

(31) Thomas, F.; Dawson, W. M.; Lang, E. J. M.; Burton, A. J.; Bartlett, G. J.; Rhys, G. G.; Mulholland, A. J.; Woolfson, D. N. De Novo-Designed α-Helical Barrels as Receptors for Small Molecules. *ACS Synthetic Biology* **2018**, *7* (7), 1808-1816. DOI: 10.1021/acssynbio.8b00225 (acccessed 2023-10-05T19:06:24).

(32) Dong, H.; Paramonov, S. E.; Hartgerink, J. D. Self-assembly of alpha-helical coiled coil nanofibers. *Journal of the American Chemical Society* **2008**, *130* (41), 13691-13695. DOI: 10.1021/ja8037323.

(33) Hill, L. K.; Meleties, M.; Katyal, P.; Xie, X.; Delgado-Fukushima, E.; Jihad, T.; Liu, C.-F.; O'Neill, S.; Tu, R. S.; Renfrew, P. D.; et al. Thermoresponsive Protein-Engineered Coiled-Coil Hydrogel for Sustained Small Molecule Release. *Biomacromolecules* **2019**, *20* (9), 3340-3351. DOI: 10.1021/acs.biomac.9b00107 (acccessed 2023-10-06T04:13:43).

(34) Wu, D.; Sinha, N.; Lee, J.; Sutherland, B. P.; Halaszynski, N. I.; Tian, Y.; Caplan, J.; Zhang, H. V.; Saven, J. G.; Kloxin, C. J.; et al. Polymers with controlled assembly and rigidity made with click-functional peptide bundles. *Nature* **2019**, *574* (7780), 658-662. DOI: 10.1038/s41586-019-1683-4 (acccessed 2023-10-06T04:28:06).

(35) Kim, K.; Kloxin, C. J.; Saven, J. G.; Pochan, D. J. Nanofibers Produced by Electrospinning of Ultrarigid Polymer Rods Made from Designed Peptide Bundlemers. *ACS Applied Materials & Interfaces* **2021**, *13* (22), 26339-26351. DOI: 10.1021/acsami.1c04027 (acccessed 2023-10-06T04:29:23).

(36) Groger, K.; Gavins, G.; Seitz, O. Strand Displacement in Coiled-Coil Structures: Controlled Induction and Reversal of Proximity. *Angewandte Chemie-International Edition* **2017**, *56* (45), 14217-14221. DOI: 10.1002/anie.201705339.

(37) Riker, K. D.; Daly, M. L.; Papanikolas, M. J.; Jian, T.; Klawa, S. J.; Shin (Sahin), J. Y. S.; Liu, D.; Singh, A.; Miller, A. G.; Freeman, R. A Programmable Toolkit to Dynamically Signal Cells Using Peptide Strand Displacement. *ACS Applied Materials & Interfaces* **2021**, *13* (18), 21018-21029. DOI: 10.1021/acsami.1c03370 (acccessed 2022-03-30T22:16:40).

(38) Mueller, C.; Grossmann, T. N. Coiled-Coil Peptide Beacon: A Tunable Conformational Switch for Protein Detection. *Angewandte Chemie International Edition* **2018**, *57* (52), 17079-17083. DOI: 10.1002/anie.201811515 (acccessed 2023-10-06T17:02:00).

(39) Gradisar, H.; Bozic, S.; Doles, T.; Vengust, D.; Hafner-Bratkovic, I.; Mertelj, A.; Webb, B.; Sali, A.; Klavzar, S.; Jerala, R. Design of a single-chain polypeptide tetrahedron assembled from coiled-coil segments. *Nature Chemical Biology* **2013**, *9* (6), 362-+. DOI: 10.1038/nchembio.1248.

(40) Ljubetic, A.; Lapenta, F.; Gradisar, H.; Drobnak, I.; Aupic, J.; Strmsek, Z.; Lainscek, D.; Hafner-Bratkovic, I.; Majerle, A.; Krivec, N.; et al. Design of coiled-coil protein-origami cages that self-assemble in vitro and in vivo. *Nature Biotechnology* **2017**, *35* (11), 1094-+, Article. DOI: 10.1038/nbt.3994.

(41) Monera, O. D.; Kay, C. M.; Hodges, R. S. Electrostatic interactions control the parallel and antiparallel orientation of. alpha.-helical chains in two-stranded. alpha.-helical coiled-coils. *Biochemistry* **1994**, *33* (13), 3862-3871.

(42) Myszka, D. G.; Chaiken, I. M. Design and characterization of an intramolecular antiparallel coiled coil peptide. *Biochemistry* **1994**, *33* (9), 2363-2372.

(43) Oakley, M. G.; Kim, P. S. A Buried Polar Interaction Can Direct the Relative Orientation of Helices in a Coiled Coil. *Biochemistry* **1998**, *37* (36), 12603-12610. DOI: 10.1021/bi981269m (acccessed 2023-10-06T18:09:44).

(44) Gurnon, D. G.; Whitaker, J. A.; Oakley, M. G. Design and Characterization of a Homodimeric Antiparallel Coiled Coil. *Journal of the American Chemical Society* **2003**, *125* (25), 7518-7519. DOI: 10.1021/ja0357590 (acccessed 2023-10-06T18:10:12).

(45) Mcclain, D. L.; Woods, H. L.; Oakley, M. G. Design and Characterization of a Heterodimeric Coiled Coil that Forms Exclusively with an Antiparallel Relative Helix Orientation. *Journal of the American Chemical Society* **2001**, *123* (13), 3151-3152. DOI: 10.1021/ja004099l (acccessed 2023-10-06T18:10:31).

(46) Apgar, J. R.; Gutwin, K. N.; Keating, A. E. Predicting helix orientation for coiled-coil dimers. *Proteins: Structure, Function, and Bioinformatics* **2008**, *72* (3), 1048-1065. DOI: 10.1002/prot.22118 (acccessed 2023-10-06T18:09:20).

(47) Seeman, N. C. Biochemistry and structural DNA nanotechnology: An evolving symbiotic relationship. *Biochemistry* **2003**, *42* (24), 7259-7269, Editorial Material. DOI: 10.1021/bi030079v.

(48) Watson, J. D.; Crick, F. H. C. Molecular Structure of Nucleic Acids: A Structure for Deoxyribose Nucleic Acid. *Nature* **1953**, *171* (4356), 737-738. DOI: 10.1038/171737a0 (acccessed 2023-10-06T20:10:34).

(49) Qiu, H.; Dewan, J. C.; Seeman, N. C. A DNA decamer with a sticky end: The crystal structure of d-CGACGATCGT. *Journal of Molecular Biology* **1997**, *267* (4), 881-898.

(50) DąBkowska, I.; Gonzalez, H. V.; Jurečka, P.; Hobza, P. Stabilization Energies of the Hydrogen-Bonded and Stacked Structures of Nucleic Acid Base Pairs in the Crystal Geometries of CG, AT, and AC DNA Steps and in the NMR Geometry of the 5‘-d(GCGAAGC)-3‘ Hairpin: Complete Basis Set Calculations at the MP2 and. *The Journal of Physical Chemistry A* **2005**, *109* (6), 1131-1136. DOI: 10.1021/jp046738a (acccessed 2023-10-06T20:35:12).

(51) Hays, F. A.; Teegarden, A.; Jones, Z. J. R.; Harms, M.; Raup, D.; Watson, J.; Cavaliere, E.; Ho, P. S. How sequence defines structure: A crystallographic map of DNA structure and conformation. *Proceedings of the National Academy of Sciences of the United States of America* **2005**, *102* (20), 7157-7162. DOI: 10.1073/pnas.0409455102.

(52) Kowalczykowski, S. C.; Dixon, D. A.; Eggleston, A. K.; Lauder, S. D.; Rehrauer, W. M. Biochemistry of homologous recombination in Escherichia coli. *Microbiological reviews* **1994**, *58* (3), 401-465.

(53) Holliday, R. A mechanism for gene conversion in fungi. *Genetics Research* **2007**, *89* (5-6), 285-307.

(54) Clegg, R. M.; Murchie, A. I. H.; Zechel, A.; Carlberg, C.; Diekmann, S.; Lilley, D. M. J. Fluorescence resonance energy transfer analysis of the structure of the four-way DNA junction. *Biochemistry* **1992**, *31* (20), 4846-4856. DOI: 10.1021/bi00135a016 (acccessed 2023-10-06T21:38:28).

(55) Duckett, D. R.; Murchie, A. I.; Diekmann, S.; von Kitzing, E.; Kemper, B.; Lilley, D. M. The structure of the Holliday junction, and its resolution. *Cell* **1988**, *55* (1), 79-89.

(56) Seeman, N. C.; Kallenbach, N. R. DESIGN OF IMMOBILE NUCLEIC-ACID JUNCTIONS. *Biophysical Journal* **1983**, *44* (2), 201-209. DOI: 10.1016/s0006-3495(83)84292-1.

(57) Simmons, C. R.; Macculloch, T.; Krepl, M.; Matthies, M.; Buchberger, A.; Crawford, I.; Šponer, J.; Šulc, P.; Stephanopoulos, N.; Yan, H. The influence of Holliday junction sequence and dynamics on DNA crystal self-assembly. *Nature Communications* **2022**, *13* (1). DOI: 10.1038/s41467-022-30779-6 (acccessed 2023-10-06T22:23:13).

(58) Seeman, N. C. NUCLEIC-ACID JUNCTIONS AND LATTICES. *Journal of Theoretical Biology* **1982**, *99* (2), 237-247, Article. DOI: 10.1016/0022-5193(82)90002-9.

(59) Ma, R.-I.; Kallenbach, N. R.; Sheardy, R. D.; Petrillo, M. L.; Seeman, N. C. Three-arm nucleic acid junctions are flexible. *Nucleic Acids Research* **1986**, *14* (24), 9745-9753. DOI: 10.1093/nar/14.24.9745 (acccessed 2023-10-06T22:48:39).

(60) Wang, X.; Seeman, N. C. Assembly and Characterization of 8-Arm and 12-Arm DNA Branched Junctions. *Journal of the American Chemical Society* **2007**, *129* (26), 8169-8176. DOI: 10.1021/ja0693441 (acccessed 2023-10-06T22:44:46).

(61) Wang, Y.; Mueller, J. E.; Kemper, B.; Seeman, N. C. Assembly and characterization of five-arm and six-arm DNA branched junctions. *Biochemistry* **1991**, *30* (23), 5667-5674. DOI: 10.1021/bi00237a005 (acccessed 2023-10-06T22:41:43).

(62) Zhang, C.; He, Y.; Su, M.; Ko, S. H.; Ye, T.; Leng, Y.; Sun, X.; Ribbe, A. E.; Jiang, W.; Mao, C. DNA self-assembly: from 2D to 3D. *Faraday Discussions* **2009**, *143*, 221. DOI: 10.1039/b905313c (acccessed 2023-10-06T22:45:02).

(63) Zhang, F.; Jiang, S. X.; Wu, S. Y.; Li, Y. L.; Mao, C. D.; Liu, Y.; Yan, H. Complex wireframe DNA origami nanostructures with multi-arm junction vertices. *Nature Nanotechnology* **2015**, *10* (9), 779-+, Article. DOI: 10.1038/nnano.2015.162.

(64) He, Y.; Tian, Y.; Ribbe, A. E.; Mao, C. Highly Connected Two-Dimensional Crystals of DNA Six-Point-Stars. *Journal of the American Chemical Society* **2006**, *128* (50), 15978-15979. DOI: 10.1021/ja0665141 (acccessed 2023-10-06T22:48:22).

(65) Fu, T. J.; Seeman, N. C. DNA double-crossover molecules. *Biochemistry* **1993**, *32* (13), 3211-3220. DOI: 10.1021/bi00064a003 (acccessed 2023-10-06T23:06:43).

(66) Winfree, E.; Liu, F.; Wenzler, L. A.; Seeman, N. C. Design and self-assembly of two-dimensional DNA crystals. *Nature* **1998**, *394* (6693), 539-544. DOI: 10.1038/28998 (acccessed 2023-10-06T23:01:38).

(67) Pinheiro, A. V.; Han, D. R.; Shih, W. M.; Yan, H. Challenges and opportunities for structural DNA nanotechnology. *Nature Nanotechnology* **2011**, *6* (12), 763-772, Review. DOI: 10.1038/nnano.2011.187.

(68) Rothemund, P. W. K. Folding DNA to create nanoscale shapes and patterns. *Nature* **2006**, *440* (7082), 297-302, Article. DOI: 10.1038/nature04586.

(69) Douglas, S. M.; Dietz, H.; Liedl, T.; Högberg, B.; Graf, F.; Shih, W. M. Self-assembly of DNA into nanoscale three-dimensional shapes. *Nature* **2009**, *459* (7245), 414-418. DOI: 10.1038/nature08016 (acccessed 2023-10-07T00:30:20).

(70) Douglas, S. M.; Marblestone, A. H.; Teerapittayanon, S.; Vazquez, A.; Church, G. M.; Shih, W. M. Rapid prototyping of 3D DNA-origami shapes with caDNAno. *Nucleic Acids Research* **2009**, *37* (15), 5001-5006. DOI: 10.1093/nar/gkp436 (acccessed 2023-10-07T00:34:34).

(71) Dietz, H.; Douglas, S. M.; Shih, W. M. Folding DNA into Twisted and Curved Nanoscale Shapes. *Science* **2009**, *325* (5941), 725-730. DOI: 10.1126/science.1174251.

(72) Ke, Y.; Ong, L. L.; Shih, W. M.; Yin, P. Three-Dimensional Structures Self-Assembled from DNA Bricks. *Science* **2012**, *338* (6111), 1177-1183. DOI: doi:10.1126/science.1227268.

(73) Han, D.; Qi, X.; Myhrvold, C.; Wang, B.; Dai, M.; Jiang, S.; Bates, M.; Liu, Y.; An, B.; Zhang, F.; et al. Single-stranded DNA and RNA origami. *Science* **2017**, *358* (6369), eaao2648. DOI: doi:10.1126/science.aao2648.

(74) Zhang, D. Y.; Seelig, G. Dynamic DNA nanotechnology using strand-displacement reactions. *Nature Chemistry* **2011**, *3* (2), 103-113, Review. DOI: 10.1038/nchem.957.

(75) Yurke, B.; Turberfield, A. J.; Mills, A. P.; Simmel, F. C.; Neumann, J. L. A DNA-fuelled molecular machine made of DNA. *Nature* **2000**, *406* (6796), 605-608. DOI: 10.1038/35020524 (acccessed 2023-10-07T18:59:06).

(76) Zhang, D. Y.; Winfree, E. Control of DNA Strand Displacement Kinetics Using Toehold Exchange. *Journal of the American Chemical Society* **2009**, *131* (47), 17303-17314. DOI: 10.1021/ja906987s (acccessed 2023-10-07T18:59:19).

(77) Liu, H.; Hong, F.; Smith, F.; Goertz, J.; Ouldridge, T.; Stevens, M. M.; Yan, H.; Šulc, P. Kinetics of RNA and RNA:DNA Hybrid Strand Displacement. *ACS Synthetic Biology* **2021**, *10* (11), 3066-3073. DOI: 10.1021/acssynbio.1c00336 (acccessed 2023-10-07T19:08:18).

(78) Liu, M.; Jiang, S.; Loza, O.; Fahmi, N. E.; Šulc, P.; Stephanopoulos, N. Rapid Photoactuation of a DNA Nanostructure using an Internal Photocaged Trigger Strand. *Angewandte Chemie International Edition* **2018**, *57* (30), 9341-9345. DOI: 10.1002/anie.201804264 (acccessed 2023-10-07T19:15:11).

(79) Agarwal, S.; Klocke, M. A.; Pungchai, P. E.; Franco, E. Dynamic self-assembly of compartmentalized DNA nanotubes. *Nature Communications* **2021**, *12* (1). DOI: 10.1038/s41467-021-23850-1 (acccessed 2023-10-07T19:18:53).

(80) Li, S.; Jiang, Q.; Liu, S.; Zhang, Y.; Tian, Y.; Song, C.; Wang, J.; Zou, Y.; Anderson, G. J.; Han, J.-Y.; et al. A DNA nanorobot functions as a cancer therapeutic in response to a molecular trigger in vivo. *Nature Biotechnology* **2018**, *36* (3), 258-264. DOI: 10.1038/nbt.4071 (acccessed 2023-10-07T19:30:57).

(81) Funke, J. J.; Ketterer, P.; Lieleg, C.; Schunter, S.; Korber, P.; Dietz, H. Uncovering the forces between nucleosomes using DNA origami. *Science Advances* **2016**, *2* (11), e1600974. DOI: doi:10.1126/sciadv.1600974.

(82) Zhang, F.; Nangreave, J.; Liu, Y.; Yan, H. Structural DNA Nanotechnology: State of the Art and Future Perspective. *Journal of the American Chemical Society* **2014**, *136* (32), 11198-11211. DOI: 10.1021/ja505101a (acccessed 2023-10-07T23:39:38).

(83) Seeman, N. C.; Sleiman, H. F. DNA nanotechnology. *Nature Reviews Materials* **2017**, *3* (1), 1-23.

(84) Zahid, M.; Kim, B.; Hussain, R.; Amin, R.; Park, S. H. DNA nanotechnology: a future perspective. *Nanoscale Research Letters* **2013**, *8* (1), 119. DOI: 10.1186/1556-276x-8-119 (acccessed 2023-10-07T23:42:56).

(85) Aldaye, F. A.; Palmer, A. L.; Sleiman, H. F. Assembling Materials with DNA as the Guide. *Science* **2008**, *321* (5897), 1795-1799. DOI: doi:10.1126/science.1154533.

(86) Aldaye, F. A.; Sleiman, H. F. Supramolecular DNA nanotechnology. *Pure and Applied Chemistry* **2009**, *81* (12), 2157-2181.

(87) Madhanagopal, B. R.; Zhang, S.; Demirel, E.; Wady, H.; Chandrasekaran, A. R. DNA nanocarriers: programmed to deliver. *Trends in biochemical sciences* **2018**, *43* (12), 997-1013.

(88) Zhang, Q.; Jiang, Q.; Li, N.; Dai, L.; Liu, Q.; Song, L.; Wang, J.; Li, Y.; Tian, J.; Ding, B.; et al. DNA Origami as an In Vivo Drug Delivery Vehicle for Cancer Therapy. *ACS Nano* **2014**, *8* (7), 6633-6643. DOI: 10.1021/nn502058j (acccessed 2023-10-07T23:58:03).

(89) Liu, M. H.; Fu, J. L.; Hejesen, C.; Yang, Y. H.; Woodbury, N. W.; Gothelf, K.; Liu, Y.; Yan, H. A DNA tweezer-actuated enzyme nanoreactor. *Nature Communications* **2013**, *4*, 5, Article. DOI: 10.1038/ncomms3127.

(90) Liu, M.; Fu, J.; Qi, X.; Wootten, S.; Woodbury, N. W.; Liu, Y.; Yan, H. A Three-Enzyme Pathway with an Optimised Geometric Arrangement to Facilitate Substrate Transfer. *ChemBioChem* **2016**, *17* (12), 1097-1101. DOI: 10.1002/cbic.201600103 (acccessed 2023-10-07T23:54:09).

(91) Fu, J. L.; Yang, Y. R.; Johnson-Buck, A.; Liu, M. H.; Liu, Y.; Walter, N. G.; Woodbury, N. W.; Yan, H. Multi-enzyme complexes on DNA scaffolds capable of substrate channelling with an artificial swinging arm. *Nature Nanotechnology* **2014**, *9* (7), 531-536, Article. DOI: 10.1038/nnano.2014.100.

(92) Aldaye, F. A.; Senapedis, W. T.; Silver, P. A.; Way, J. C. A Structurally Tunable DNA-Based Extracellular Matrix. *Journal of the American Chemical Society* **2010**, *132* (42), 14727-14729, Article. DOI: 10.1021/ja105431h.

(93) Fern, J.; Schulman, R. Modular DNA strand-displacement controllers for directing material expansion. *Nature Communications* **2018**, *9* (1). DOI: 10.1038/s41467-018-06218-w (acccessed 2023-10-07T23:51:22).

(94) Peng, Y.-H.; Hsiao, S. K.; Gupta, K.; Ruland, A.; Auernhammer, G. K.; Maitz, M. F.; Boye, S.; Lattner, J.; Gerri, C.; Honigmann, A.; et al. Dynamic matrices with DNA-encoded viscoelasticity for cell and organoid culture. *Nature Nanotechnology* **2023**. DOI: 10.1038/s41565-023-01483-3 (acccessed 2023-10-07T23:51:09).

(95) Rosales, A. M.; Anseth, K. S. The design of reversible hydrogels to capture extracellular matrix dynamics. *Nature Reviews Materials* **2016**, *1* (2). DOI: 10.1038/natrevmats.2015.12.

(96) Hu, Y.; Niemeyer, C. M. From DNA Nanotechnology to Material Systems Engineering. *Advanced Materials* **2019**, *31* (26), 1806294. DOI: 10.1002/adma.201806294 (acccessed 2023-10-07T23:47:39).

(97) Fröhlich, E. The role of surface charge in cellular uptake and cytotoxicity of medical nanoparticles. *International Journal of Nanomedicine* **2012**, 5577. DOI: 10.2147/ijn.s36111 (acccessed 2023-10-08T00:20:39).

(98) Lou, C.; Martos-Maldonado, M. C.; Madsen, C. S.; Thomsen, R. P.; Midtgaard, S. R.; Christensen, N. J.; Kjems, J.; Thulstrup, P. W.; Wengel, J.; Jensen, K. J. Peptide–oligonucleotide conjugates as nanoscale building blocks for assembly of an artificial three-helix protein mimic. *Nature Communications* **2016**, *7* (1), 12294. DOI: 10.1038/ncomms12294.

(99) Kye, M.; Lim, Y.-B. Reciprocal Self-Assembly of Peptide-DNA Conjugates into a Programmable Sub-10-nm Supramolecular Deoxyribonucleoprotein. *Angewandte Chemie International Edition* **2016**, *55* (39), 12003-12007. DOI: 10.1002/anie.201605696.

(100) Patutina, O. A.; Bichenkova, E. V.; Miroshnichenko, S. K.; Mironova, N. L.; Trivoluzzi, L. T.; Burusco, K. K.; Bryce, R. A.; Vlassov, V. V.; Zenkova, M. A. miRNases: Novel peptide-oligonucleotide bioconjugates that silence miR-21 in lymphosarcoma cells. *Biomaterials* **2017**, *122*, 163-178.

(101) Zubin, E. M.; Romanova, E. A.; Volkov, E. M.; Tashlitsky, V. N.; Korshunova, G. A.; Shabarova, Z. A.; Oretskaya, T. S. Oligonucleotide-peptide conjugates as potential antisense agents. *FEBS letters* **1999**, *456* (1), 59-62.

(102) Arar, K.; Aubertin, A.-M.; Roche, A.-C.; Monsigny, M.; Mayer, R. Synthesis and Antiviral Activity of Peptide-Oligonucleotide Conjugates Prepared by Using N.alpha.-(Bromoacetyl)peptides. *Bioconjugate Chemistry* **1995**, *6* (5), 573-577. DOI: 10.1021/bc00035a011 (acccessed 2023-10-08T01:26:04).

(103) Astakhova, K.; Ray, R.; Taskova, M.; Uhd, J.; Carstens, A.; Morris, K. "Clicking" Gene Therapeutics: A Successful Union of Chemistry and Biomedicine for New Solutions. *Molecular Pharmaceutics* **2018**, *15* (8), 2892-2899. DOI: 10.1021/acs.molpharmaceut.7b00765 (acccessed 2023-10-08T01:26:58).

(104) Charbgoo, F.; Alibolandi, M.; Taghdisi, S. M.; Abnous, K.; Soltani, F.; Ramezani, M. MUC1 aptamer-targeted DNA micelles for dual tumor therapy using doxorubicin and KLA peptide. *Nanomedicine: Nanotechnology, Biology and Medicine* **2018**, *14* (3), 685-697.

(105) Ponnuswamy, N.; Bastings, M. M. C.; Nathwani, B.; Ryu, J. H.; Chou, L. Y. T.; Vinther, M.; Li, W. A.; Anastassacos, F. M.; Mooney, D. J.; Shih, W. M. Oligolysine-based coating protects DNA nanostructures from low-salt denaturation and nuclease degradation. *Nature Communications* **2017**, *8* (1), 15654. DOI: 10.1038/ncomms15654 (acccessed 2022-03-30T20:21:48).

(106) Wang, S.-T.; Gray, M. A.; Xuan, S.; Lin, Y.; Byrnes, J.; Nguyen, A. I.; Todorova, N.; Stevens, M. M.; Bertozzi, C. R.; Zuckermann, R. N.; et al. DNA origami protection and molecular interfacing through engineered sequence-defined peptoids. *Proceedings of the National Academy of Sciences* **2020**, *117* (12), 6339-6348. DOI: 10.1073/pnas.1919749117 (acccessed 2023-10-08T01:37:12).

(107) Spruijt, E.; Tusk, S. E.; Bayley, H. DNA scaffolds support stable and uniform peptide nanopores. *Nature Nanotechnology* **2018**, *13* (8), 739-745. DOI: 10.1038/s41565-018-0139-6 (acccessed 2023-10-08T01:28:04).

(108) Bruick, R. K.; Dawson, P. E.; Kent, S. B.; Usman, N.; Joyce, G. F. Template-directed ligation of peptides to oligonucleotides. *Chemistry & biology* **1996**, *3* (1), 49-56.

(109) Dovgan, I.; Koniev, O.; Kolodych, S.; Wagner, A. Antibody–Oligonucleotide Conjugates as Therapeutic, Imaging, and Detection Agents. *Bioconjugate Chemistry* **2019**, *30* (10), 2483-2501. DOI: 10.1021/acs.bioconjchem.9b00306 (acccessed 2023-10-08T01:29:49).

(110) Gavins, G. C.; Gröger, K.; Bartoschek, M. D.; Wolf, P.; Beck-Sickinger, A. G.; Bultmann, S.; Seitz, O. Live cell PNA labelling enables erasable fluorescence imaging of

membrane proteins. *Nature Chemistry* **2021**, *13* (1), 15-23. DOI: 10.1038/s41557-020-00584-z (acccessed 2023-06-07T05:45:00).

(111) Stephanopoulos, N.; Freeman, R.; North, H. A.; Sur, S.; Jeong, S. J.; Tantakitti, F.; Kessler, J. A.; Stupp, S. I. Bioactive DNA-Peptide Nanotubes Enhance the Differentiation of Neural Stem Cells Into Neurons. *Nano Letters* **2015**, *15* (1), 603-609, Article. DOI: 10.1021/nl504079q.

(112) Freeman, R.; Stephanopoulos, N.; Alvarez, Z.; Lewis, J. A.; Sur, S.; Serrano, C. M.; Boekhoven, J.; Lee, S. S.; Stupp, S. I. Instructing cells with programmable peptide DNA hybrids. *Nature Communications* **2017**, *8*. DOI: 10.1038/ncomms15982.

(113) Stephanopoulos, N.; Ortony, J. H.; Stupp, S. I. Self-assembly for the synthesis of functional biomaterials. *Acta Materialia* **2013**, *61* (3), 912-930. DOI: 10.1016/j.actamat.2012.10.046 (acccessed 2021-08-19T06:23:39).

(114) Stephanopoulos, N. Peptide–Oligonucleotide Hybrid Molecules for Bioactive Nanomaterials. *Bioconjugate Chemistry* **2019**, *30* (7), 1915-1922. DOI: 10.1021/acs.bioconjchem.9b00259 (acccessed 2023-10-08T01:33:10).

(115) Nazari, Z.; Gomez Herrero, J.; Fojan, P.; Gurevich, L. Formation of Conductive DNA-Based Nanowires via Conjugation of dsDNA with Cationic Peptide. *Nanomaterials* **2017**, *7* (6), 128. DOI: 10.3390/nano7060128 (acccessed 2023-10-08T01:34:07).

(116) Flory, J. D.; Shinde, S.; Lin, S.; Liu, Y.; Yan, H.; Ghirlanda, G.; Fromme, P. PNA-Peptide Assembly in a 3D DNA Nanocage at Room Temperature. *Journal of the American Chemical Society* **2013**, *135* (18), 6985-6993. DOI: 10.1021/ja400762c (acccessed 2023-10-08T01:38:23).

(117) Janssen, B. M. G.; Lempens, E. H. M.; Olijve, L. L. C.; Voets, I. K.; Van Dongen, J. L. J.; De Greef, T. F. A.; Merkx, M. Reversible blocking of antibodies using bivalent peptide–DNA conjugates allows protease-activatable targeting. *Chemical Science* **2013**, *4* (4), 1442. DOI: 10.1039/c3sc22033h (acccessed 2023-10-08T01:39:14).

(118) Marczynke, M.; Gröger, K.; Seitz, O. Selective Binders of the Tandem Src Homology 2 Domains in Syk and Zap70 Protein Kinases by DNA-Programmed Spatial Screening. *Bioconjugate Chemistry* **2017**, *28* (9), 2384-2392. DOI: 10.1021/acs.bioconjchem.7b00382 (acccessed 2023-10-08T01:39:51).

(119) Eberhard, H.; Diezmann, F.; Seitz, O. DNA as a Molecular Ruler: Interrogation of a Tandem SH2 Domain with Self-Assembled, Bivalent DNA-Peptide Complexes. *Angewandte Chemie International Edition* **2011**, *50* (18), 4146-4150. DOI: 10.1002/anie.201007593 (acccessed 2023-10-08T01:40:18).

(120) Kong, D.; Lei, Y.; Yeung, W.; Hili, R. Enzymatic Synthesis of Sequence-Defined Synthetic Nucleic Acid Polymers with Diverse Functional Groups. *Angewandte Chemie International Edition* **2016**, *55* (42), 13164-13168. DOI: 10.1002/anie.201607538 (acccessed 2023-10-08T06:05:22).

(121) Williams, B. A. R.; Diehnelt, C. W.; Belcher, P.; Greving, M.; Woodbury, N. W.; Johnston, S. A.; Chaput, J. C. Creating Protein Affinity Reagents by Combining Peptide Ligands on Synthetic DNA Scaffolds. *Journal of the American Chemical Society* **2009**, *131* (47), 17233-17241. DOI: 10.1021/ja9051735 (acccessed 2023-10-08T06:09:58).

(122) Williams, B. A. R.; Lund, K.; Liu, Y.; Yan, H.; Chaput, J. C. Self-Assembled Peptide Nanoarrays: An Approach to Studying Protein–Protein Interactions. *Angewandte Chemie International Edition* **2007**, *46* (17), 3051-3054. DOI: 10.1002/anie.200603919 (acccessed 2023-10-08T06:11:45).

(123) Harrison, J. Synthesis and hybridization analysis of a small library of peptide-oligonucleotide conjugates. *Nucleic Acids Research* **1998**, *26* (13), 3136-3145. DOI: 10.1093/nar/26.13.3136 (acccessed 2023-10-08T06:12:44).

(124) Merg, A. D.; Thaner, R. V.; Mokashi-Punekar, S.; Nguyen, S. T.; Rosi, N. L. Triblock peptide–oligonucleotide chimeras (POCs): programmable biomolecules for the assembly of morphologically tunable and responsive hybrid materials. *Chemical Communications* **2017**, *53* (90), 12221-12224. DOI: 10.1039/c7cc07708d (acccessed 2023-10-08T06:20:12).

(125) Abraham, J. N.; Gour, N.; Bolisetty, S.; Mezzenga, R.; Nardin, C. Controlled aggregation of peptide–DNA hybrids into amyloid-like fibrils. *European Polymer Journal* **2015**, *65*, 268-275.

(126) Carter, J. D.; Labean, T. H. Coupling Strategies for the Synthesis of Peptide-Oligonucleotide Conjugates for Patterned Synthetic Biomineralization. *Journal of Nucleic Acids* **2011**, *2011*, 1-8. DOI: 10.4061/2011/926595 (acccessed 2023-10-08T06:26:56).

(127) Lu, K.; Duan, Q.-P.; Ma, L.; Zhao, D.-X. Chemical Strategies for the Synthesis of Peptide−Oligonucleotide Conjugates. *Bioconjugate Chemistry* **2010**, *21* (2), 187-202. DOI: 10.1021/bc900158s (acccessed 2023-10-08T17:57:17).

(128) Gogoi, K.; Mane, M. V.; Kunte, S. S.; Kumar, V. A. A versatile method for the preparation of conjugates of peptides with DNA/PNA/analog by employing chemo-selective click reaction in water. *Nucleic acids research* **2007**, *35* (21), e139-e139.

(129) Buchberger, A.; Simmons, C. R.; Fahmi, N. E.; Freeman, R.; Stephanopoulos, N. Hierarchical Assembly of Nucleic Acid/Coiled-Coil Peptide Nanostructures. *Journal of the American Chemical Society* **2020**, *142* (3), 1406-1416. DOI: 10.1021/jacs.9b11158.

(130) Xu, Y.; Jiang, S. X.; Simmons, C. R.; Narayanan, R. P.; Zhang, F.; Aziz, A. M.; Yan, H.; Stephanopoulos, N. Tunable Nanoscale Cages from Self-Assembling DNA and Protein Building Blocks. *Acs Nano* **2019**, *13* (3), 3545-3554, Article. DOI: 10.1021/acsnano.8b09798.

(131) Forget, D.; Boturyn, D.; Defrancq, E.; Lhomme, J.; Dumy, P. Highly efficient synthesis of peptide–oligonucleotide conjugates: chemoselective oxime and thiazolidine formation. *Chemistry–A European Journal* **2001**, *7* (18), 3976-3984.

(132) Serva, S.; Lagunavičius, A. N. Direct Conjugation of Peptides and 5-Hydroxymethylcytosine in DNA. *Bioconjugate Chemistry* **2015**, *26* (6), 1008-1012. DOI: 10.1021/acs.bioconjchem.5b00165 (acccessed 2023-10-08T18:31:51).

(133) Rogers, F. A. Peptide conjugates for chromosomal gene targeting by triplex-forming oligonucleotides. *Nucleic Acids Research* **2004**, *32* (22), 6595-6604. DOI: 10.1093/nar/gkh998 (acccessed 2023-10-08T18:32:32).

(134) Stanojevic, D.; Verdine, G. L. Deconstruction of GCN4/GCRE into a monomeric peptide-DNA complex. *Nature Structural & Molecular Biology* **1995**, *2* (6), 450-457. DOI: 10.1038/nsb0695-450 (acccessed 2023-10-08T18:33:20).

(135) Chotera, A.; Sadihov, H.; Cohen-Luria, R.; Monnard, P.-A.; Ashkenasy, G. Functional Assemblies Emerging in Complex Mixtures of Peptides and Nucleic Acid-Peptide Chimeras. *Chemistry - A European Journal* **2018**, *24* (40), 10128-10135. DOI: 10.1002/chem.201800500.

(136) Pazos, E.; Portela, C.; Penas, C.; Vázquez, M. E.; Mascareñas, J. L. Peptide–DNA conjugates as tailored bivalent binders of the oncoprotein c-Jun. *Organic & Biomolecular Chemistry* **2015**, *13* (19), 5385-5390. DOI: 10.1039/c5ob00318k (acccessed 2023-10-08T18:34:18).

(137) Ruff, Y.; Moyer, T.; Newcomb, C. J.; Demeler, B.; Stupp, S. I. Precision Templating with DNA of a Virus-like Particle with Peptide Nanostructures. *Journal of the American Chemical Society* **2013**, *135* (16), 6211-6219. DOI: 10.1021/ja4008003.

(138) Jin, J.; Baker, E. G.; Wood, C. W.; Bath, J.; Woolfson, D. N.; Turberfield, A. J. Peptide Assembly Directed and Quantified Using Megadalton DNA Nanostructures. *ACS Nano* **2019**, *13* (9), 9927-9935. DOI: 10.1021/acsnano.9b04251.

(139) Jiang, T.; Meyer, T. A.; Modlin, C.; Zuo, X.; Conticello, V. P.; Ke, Y. Structurally Ordered Nanowire Formation from Co-Assembly of DNA Origami and Collagen-Mimetic Peptides. *Journal of the American Chemical Society* **2017**, *139* (40), 14025-14028. DOI: 10.1021/jacs.7b08087.

(140) Smith, C. K.; Regan, L. Construction and Design of β-Sheets. *Accounts of Chemical Research* **1997**, *30* (4), 153-161. DOI: 10.1021/ar9601048.

(141) Albert, S. K.; Lee, S.; Durai, P.; Hu, X.; Jeong, B.; Park, K.; Park, S. J. Janus Nanosheets with Face-Selective Molecular Recognition Properties from DNA–Peptide Conjugates. *Small* **2021**, *17* (12), 2006110. DOI: 10.1002/smll.202006110.

(142) Hendricks, M. P.; Sato, K.; Palmer, L. C.; Stupp, S. I. Supramolecular Assembly of Peptide Amphiphiles. *Accounts of Chemical Research* **2017**, *50* (10), 2440-2448. DOI: 10.1021/acs.accounts.7b00297.

(143) Freeman, R.; Han, M.; Alvarez, Z.; Lewis, J. A.; Wester, J. R.; Stephanopoulos, N.; McClendon, M. T.; Lynsky, C.; Godbe, J. M.; Sangji, H.; et al. Reversible self-assembly of superstructured networks. *Science* **2018**, *362* (6416), 808-+. DOI: 10.1126/science.aat6141.

(144) Hartgerink, J. D.; Beniash, E.; Stupp, S. I. Peptide-amphiphile nanofibers: A versatile scaffold for the preparation of self-assembling materials. *Proceedings of the National Academy of Sciences of the United States of America* **2002**, *99* (8), 5133-5138. DOI: 10.1073/pnas.072699999.

(145) Álvarez, Z.; Ortega, J. A.; Sato, K.; Sasselli, I. R.; Kolberg-Edelbrock, A. N.; Qiu, R.; Marshall, K. A.; Nguyen, T. P.; Smith, C. S.; Quinlan, K. A. Artificial extracellular matrix scaffolds of mobile molecules enhance maturation of human stem cell-derived neurons. *Cell stem cell* **2023**, *30* (2), 219-238. e214.

(146) Hartgerink, J. D.; Beniash, E.; Stupp, S. I. Self-assembly and mineralization of peptide-amphiphile nanofibers. *Science* **2001**, *294* (5547), 1684-1688. DOI: 10.1126/science.1063187.

(147) Silva, G. A.; Czeisler, C.; Niece, K. L.; Beniash, E.; Harrington, D. A.; Kessler, J. A.; Stupp, S. I. Selective differentiation of neural progenitor cells by high-epitope density nanofibers. *Science* **2004**, *303* (5662), 1352-1355.

(148) O'Leary, L. E. R.; Fallas, J. A.; Bakota, E. L.; Kang, M. K.; Hartgerink, J. D. Multi-hierarchical self-assembly of a collagen mimetic peptide from triple helix to nanofibre and hydrogel. *Nature Chemistry* **2011**, *3* (10), 821-828. DOI: 10.1038/nchem.1123 (acccessed 2023-08-05T23:17:58).

(149) Lopez-Silva, T. L.; Cristobal, C. D.; Lai, C. S. E.; Leyva-Aranda, V.; Lee, H. K.; Hartgerink, J. D. Self-assembling multidomain peptide hydrogels accelerate peripheral nerve regeneration after crush injury. *Biomaterials* **2021**, *265*, 120401.

(150) Aota, S.; Nomizu, M.; Yamada, K. M. THE SHORT AMINO-ACID-SEQUENCE PRO-HIS-SER-ARG-ASN IN HUMAN FIBRONECTIN ENHANCES CELL-ADHESIVE FUNCTION. *Journal of Biological Chemistry* **1994**, *269* (40), 24756-24761.

(151) Martino, M. M.; Tortelli, F.; Mochizuki, M.; Traub, S.; Ben-David, D.; Kuhn, G. A.; Muller, R.; Livne, E.; Eming, S. A.; Hubbell, J. A. Engineering the Growth Factor Microenvironment with Fibronectin Domains to Promote Wound and Bone Tissue Healing. *Science Translational Medicine* **2011**, *3* (100). DOI: 10.1126/scitranslmed.3002614.

(152) Wang, R.; Li, J.; Li, X.; Guo, J.; Liu, J.; Li, H. Engineering protein polymers of ultrahigh molecular weight via supramolecular polymerization: towards mimicking the giant muscle protein titin. *Chemical Science* **2019**, *10* (40), 9277-9284. DOI: 10.1039/c9sc02128k (acccessed 2023-07-26T17:35:38).

(153) Buchberger, A.; Riker, K.; Bernal-Chanchavac, J.; Narayanan, R. P.; Simmons, C. R.; Fahmi, N. E.; Freeman, R.; Stephanopoulos, N. Bioactive Fibronectin-III10–DNA Origami Nanofibers Promote Cell Adhesion and Spreading. *ACS Applied Bio Materials* **2022**, *5* (10), 4625-4634. DOI: 10.1021/acsabm.2c00303.

(154) Gibson, D. G.; Young, L.; Chuang, R. Y.; Venter, J. C.; Hutchison, C. A.; Smith, H. O. Enzymatic assembly of DNA molecules up to several hundred kilobases. *Nature Methods* **2009**, *6* (5), 343-U341. DOI: 10.1038/nmeth.1318.

(155) Martino, M. M.; Hubbell, J. A. The 12th–14th type III repeats of fibronectin function as a highly promiscuous growth factor-binding domain. *The FASEB Journal* **2010**, *24* (12), 4711-4721.

(156) Jasaitis, L.; Silver, C. D.; Rawlings, A. E.; Peters, D. T.; Whelan, F.; Regan, L.; Pasquina-Lemonche, L.; Potts, J. R.; Johnson, S. D.; Staniland, S. S. Rational design and self-assembly of coiled-coil linked SasG protein fibrils. *ACS Synthetic Biology* **2020**, *9* (7), 1599-1607.

(157) Dietz, H.; Bornschlögl, T.; Heym, R.; König, F.; Rief, M. Programming protein self assembly with coiled coils. *New Journal of Physics* **2007**, *9* (11), 424.

(158) Jha, A. K.; Xu, X.; Duncan, R. L.; Jia, X. Controlling the adhesion and differentiation of mesenchymal stem cells using hyaluronic acid-based, doubly crosslinked networks. *Biomaterials* **2011**, *32* (10), 2466-2478. DOI: 10.1016/j.biomaterials.2010.12.024 (acccessed 2023-06-07T00:47:36).

(159) Langer, R.; Tirrell, D. A. Designing materials for biology and medicine. *Nature* **2004**, *428* (6982), 487-492. DOI: 10.1038/nature02388 (acccessed 2023-06-07T04:09:11).
(160) Langer, R.; Vacanti, J. P. Tissue Engineering. *Science* **1993**, *260* (5110), 920-926. DOI: doi:10.1126/science.8493529.

(161) Freed, L. E.; Vunjak-Novakovic, G. Culture of organized cell communities. *Advanced drug delivery reviews* **1998**, *33* (1-2), 15-30.

(162) Ghosh, K.; Ingber, D. E. Micromechanical control of cell and tissue development: implications for tissue engineering. *Advanced drug delivery reviews* **2007**, *59* (13), 1306-1318.

(163) Place, E. S.; Evans, N. D.; Stevens, M. M. Complexity in biomaterials for tissue engineering. *Nature Materials* **2009**, *8* (6), 457-470. DOI: 10.1038/nmat2441 (acccessed 2023-06-07T04:17:08).

(164) Chen, X.; Thibeault, S. L. Novel Isolation and Biochemical Characterization of Immortalized Fibroblasts for Tissue Engineering Vocal Fold Lamina Propria. *Tissue Engineering Part C: Methods* **2009**, *15* (2), 201-212. DOI: 10.1089/ten.tec.2008.0390 (acccessed 2023-06-07T04:25:19).

(165) Pittenger, M. F.; Mackay, A. M.; Beck, S. C.; Jaiswal, R. K.; Douglas, R.; Mosca, J. D.; Moorman, M. A.; Simonetti, D. W.; Craig, S.; Marshak, D. R. Multilineage potential of adult human mesenchymal stem cells. *science* **1999**, *284* (5411), 143-147.

(166) Jiang, Y.; Jahagirdar, B. N.; Reinhardt, R. L.; Schwartz, R. E.; Keene, C. D.; Ortiz-Gonzalez, X. R.; Reyes, M.; Lenvik, T.; Lund, T.; Blackstad, M.; et al. Pluripotency of mesenchymal stem cells derived from adult marrow. *Nature* **2002**, *418* (6893), 41-49. DOI: 10.1038/nature00870 (acccessed 2023-06-07T04:29:30).

(167) Caplan, A. I. Adult mesenchymal stem cells for tissue engineering versus regenerative medicine. *Journal of Cellular Physiology* **2007**, *213* (2), 341-347. DOI: 10.1002/jcp.21200 (acccessed 2023-06-07T04:29:54).

(168) Engler, A. J.; Sen, S.; Sweeney, H. L.; Discher, D. E. Matrix Elasticity Directs Stem Cell Lineage Specification. *Cell* **2006**, *126* (4), 677-689. DOI: 10.1016/j.cell.2006.06.044 (acccessed 2022-03-30T20:45:04).

(169) Discher, D. E.; Mooney, D. J.; Zandstra, P. W. Growth Factors, Matrices, and Forces Combine and Control Stem Cells. *Science* **2009**, *324* (5935), 1673-1677. DOI: 10.1126/science.1171643 (acccessed 2023-06-07T04:37:03).

(170) Saha, K.; Pollock, J. F.; Schaffer, D. V.; Healy, K. E. Designing synthetic materials to control stem cell phenotype. *Current Opinion in Chemical Biology* **2007**, *11* (4), 381-387. DOI: 10.1016/j.cbpa.2007.05.030 (acccessed 2023-06-07T04:42:36).

(171) Dawson, E.; Mapili, G.; Erickson, K.; Taqvi, S.; Roy, K. Biomaterials for stem cell differentiation. *Advanced drug delivery reviews* **2008**, *60* (2), 215-228.

(172) Lutolf, M. P.; Gilbert, P. M.; Blau, H. M. Designing materials to direct stem-cell fate. *Nature* **2009**, *462* (7272), 433-441. DOI: 10.1038/nature08602 (acccessed 2023-06-07T04:46:45).

(173) Caliari, S. R.; Burdick, J. A. A practical guide to hydrogels for cell culture. *Nature Methods* **2016**, *13* (5), 405-414. DOI: 10.1038/nmeth.3839 (acccessed 2023-06-07T00:53:58).

(174) Tibbitt, M. W.; Anseth, K. S. Hydrogels as extracellular matrix mimics for 3D cell culture. *Biotechnology and Bioengineering* **2009**, *103* (4), 655-663. DOI: 10.1002/bit.22361 (acccessed 2023-06-07T04:53:33).

(175) Trappmann, B.; Gautrot, J. E.; Connelly, J. T.; Strange, D. G. T.; Li, Y.; Oyen, M. L.; Cohen Stuart, M. A.; Boehm, H.; Li, B.; Vogel, V.; et al. Extracellular-matrix tethering regulates stem-cell fate. *Nature Materials* **2012**, *11* (7), 642-649. DOI: 10.1038/nmat3339 (acccessed 2023-09-26T17:20:42).

(176) da Cunha, C. B.; Klumpers, D. D.; Li, W. A.; Koshy, S. T.; Weaver, J. C.; Chaudhuri, O.; Granja, P. L.; Mooney, D. J. Influence of the stiffness of three-dimensional alginate/collagen-I interpenetrating networks on fibroblast biology. *Biomaterials* **2014**, *35* (32), 8927-8936.

(177) Gilbert, P. M.; Havenstrite, K. L.; Magnusson, K. E. G.; Sacco, A.; Leonardi, N. A.; Kraft, P.; Nguyen, N. K.; Thrun, S.; Lutolf, M. P.; Blau, H. M. Substrate Elasticity Regulates Skeletal Muscle Stem Cell Self-Renewal in Culture. *Science* **2010**, *329* (5995), 1078-1081. DOI: doi:10.1126/science.1191035.

(178) Vega, S. L.; Kwon, M. Y.; Song, K. H.; Wang, C.; Mauck, R. L.; Han, L.; Burdick, J. A. Combinatorial hydrogels with biochemical gradients for screening 3D cellular microenvironments. *Nature Communications* **2018**, *9* (1). DOI: 10.1038/s41467-018-03021-5 (acccessed 2023-09-26T17:28:46).

(179) Hall, P. A.; Watt, F. M. Stem cells: the generation and maintenance of cellular diversity. *Development* **1989**, *106* (4), 619-633. DOI: 10.1242/dev.106.4.619 (acccessed 2023-09-26T17:37:10).

(180) Watt, F. M.; Hogan, a. B. L. M. Out of Eden: Stem Cells and Their Niches. *Science* **2000**, *287* (5457), 1427-1430. DOI: doi:10.1126/science.287.5457.1427.

(181) Shah, N. M.; Groves, A. K.; Anderson, D. J. Alternative Neural Crest Cell Fates Are Instructively Promoted by TGFβ Superfamily Members. *Cell* **1996**, *85* (3), 331-343. DOI: 10.1016/s0092-8674(00)81112-5 (acccessed 2023-09-26T18:11:37).

(182) Peifer, M. Neither straight nor narrow. *Nature* **1999**, *400* (6741), 213-215. DOI: 10.1038/22214 (acccessed 2023-09-26T17:48:14).

(183) Wong, M. H.; Rubinfeld, B.; Gordon, J. I. Effects of Forced Expression of an NH2-terminal Truncated β-Catenin on Mouse Intestinal Epithelial Homeostasis. *The Journal of Cell Biology* **1998**, *141* (3), 765-777. DOI: 10.1083/jcb.141.3.765 (acccessed 2023-09-26T17:48:01).

(184) Zhu, A. J.; Haase, I.; Watt, F. M. Signaling via β1 integrins and mitogen-activated protein kinase determines human epidermal stem cell fate

in vitro. *Proceedings of the National Academy of Sciences* **1999**, *96* (12), 6728-6733. DOI: 10.1073/pnas.96.12.6728 (acccessed 2023-09-26T18:14:54).

(185) Quesenberry, P. J.; Becker, P. S. Stem cell homing: Rolling, crawling, and nesting. *Proceedings of the National Academy of Sciences* **1998**, *95* (26), 15155-15157. DOI: 10.1073/pnas.95.26.15155 (acccessed 2023-09-26T18:14:42).

(186) Highley, C. B.; Prestwich, G. D.; Burdick, J. A. Recent advances in hyaluronic acid hydrogels for biomedical applications. *Current opinion in biotechnology* **2016**, *40*, 35-40.

(187) Burdick, J. A.; Prestwich, G. D. Hyaluronic Acid Hydrogels for Biomedical Applications. *Advanced Materials* **2011**, *23* (12), H41-H56. DOI: 10.1002/adma.201003963 (acccessed 2023-06-07T05:02:07).

(188) Fraser, J. R. E.; Laurent, T. C.; Laurent, U. B. G. Hyaluronan: its nature, distribution, functions and turnover. *Journal of Internal Medicine* **1997**, *242* (1), 27-33. DOI: 10.1046/j.1365-2796.1997.00170.x (acccessed 2023-06-07T05:03:04).

(189) Chen, W. Y. J.; Abatangelo, G. Functions of hyaluronan in wound repair. *Wound Repair and Regeneration* **1999**, *7* (2), 79-89. DOI: 10.1046/j.1524-475x.1999.00079.x (acccessed 2023-06-07T05:04:39).

(190) Hoyle, C. E.; Bowman, C. N. Thiol-Ene Click Chemistry. *Angewandte Chemie International Edition* **2010**, *49* (9), 1540-1573. DOI: 10.1002/anie.200903924 (acccessed 2023-06-07T05:17:24).

(191) Fairbanks, B. D.; Schwartz, M. P.; Halevi, A. E.; Nuttelman, C. R.; Bowman, C. N.; Anseth, K. S. A Versatile Synthetic Extracellular Matrix Mimic via Thiol-Norbornene Photopolymerization. *Advanced Materials* **2009**, *21* (48), 5005-5010. DOI: 10.1002/adma.200901808 (acccessed 2023-06-07T05:18:00).

(192) Fox, C. H.; Johnson, F. B.; Whiting, J.; Roller, P. P. Formaldehyde fixation. *Journal of Histochemistry & Cytochemistry* **1985**, *33* (8), 845-853. DOI: 10.1177/33.8.3894502 (acccessed 2023-09-22T18:35:35).

(193) Wegst, U. G. K.; Bai, H.; Saiz, E.; Tomsia, A. P.; Ritchie, R. O. Bioinspired structural materials. *Nature Materials* **2015**, *14* (1), 23-36. DOI: 10.1038/nmat4089 (acccessed 2023-10-02T00:54:39).

(194) Meyers, M. A.; McKittrick, J.; Chen, P.-Y. Structural Biological Materials: Critical Mechanics-Materials Connections. *Science* **2013**, *339* (6121), 773-779. DOI: doi:10.1126/science.1220854.

(195) Kan, A.; Joshi, N. S. Towards the directed evolution of protein materials. *MRS Communications* **2019**, *9* (2), 441-455. DOI: 10.1557/mrc.2019.28 (acccessed 2023-10-02T01:13:03).

(196) Garcia-Seisdedos, H.; Empereur-Mot, C.; Elad, N.; Levy, E. D. Proteins evolve on the edge of supramolecular self-assembly. *Nature* **2017**, *548* (7666), 244-247. DOI: 10.1038/nature23320 (acccessed 2023-10-02T01:14:22).

(197) Wu, J.; Li, P.; Dong, C.; Jiang, H.; Xue, B.; Gao, X.; Qin, M.; Wang, W.; Chen, B.; Cao, Y. Rationally designed synthetic protein hydrogels with predictable mechanical properties. *Nature Communications* **2018**, *9* (1). DOI: 10.1038/s41467-018-02917-6 (acccessed 2023-10-02T01:15:39).

(198) D'Amone, L.; Matzeu, G.; Quijano-Rubio, A.; Callahan, G. P.; Napier, B.; Baker, D.; Omenetto, F. G. Reshaping de Novo Protein Switches into Bioresponsive Materials for Biomarker, Toxin, and Viral Detection. *Advanced Materials* **2023**, *35* (11), 2208556. DOI: 10.1002/adma.202208556 (acccessed 2023-10-02T01:19:24).

(199) Mcmillan, J. R.; Hayes, O. G.; Winegar, P. H.; Mirkin, C. A. Protein Materials Engineering with DNA. *Accounts of Chemical Research* **2019**, *52* (7), 1939-1948. DOI: 10.1021/acs.accounts.9b00165 (acccessed 2021-07-14T01:18:06).

(200) Studart, A. R. Towards High-Performance Bioinspired Composites. *Advanced Materials* **2012**, *24* (37), 5024-5044. DOI: 10.1002/adma.201201471 (acccessed 2023-10-02T01:22:50).

(201) Doolan, J. A.; Alesbrook, L. S.; Baker, K.; Brown, I. R.; Williams, G. T.; Hilton, K. L. F.; Tabata, M.; Wozniakiewicz, P. J.; Hiscock, J. R.; Goult, B. T. Next-generation protein-based materials capture and preserve projectiles from supersonic impacts. *Nature Nanotechnology* **2023**, *18* (9), 1060-1066. DOI: 10.1038/s41565-023-01431-1 (acccessed 2023-10-02T01:29:17).

(202) Fang, J.; Mehlich, A.; Koga, N.; Huang, J.; Koga, R.; Gao, X.; Hu, C.; Jin, C.; Rief, M.; Kast, J.; et al. Forced protein unfolding leads to highly elastic and tough protein hydrogels. *Nature Communications* **2013**, *4* (1). DOI: 10.1038/ncomms3974 (acccessed 2023-10-02T01:30:46).

(203) Zhong, C.; Gurry, T.; Cheng, A. A.; Downey, J.; Deng, Z.; Stultz, C. M.; Lu, T. K. Strong underwater adhesives made by self-assembling multi-protein nanofibres. *Nature Nanotechnology* **2014**, *9* (10), 858-866. DOI: 10.1038/nnano.2014.199 (acccessed 2023-10-02T01:33:46).

(204) Sleytr, U. B.; Schuster, B.; Egelseer, E.-M.; Pum, D. S-layers: principles and applications. *FEMS Microbiology Reviews* **2014**, *38* (5), 823-864. DOI: 10.1111/1574-6976.12063 (acccessed 10/2/2023).

(205) Cox, P.; Hooley, P. Hydrophobins: New prospects for biotechnology. *Fungal Biology Reviews* **2009**, *23* (1-2), 40-47.

(206) Buchko, C. J.; Chen, L. C.; Shen, Y.; Martin, D. C. Processing and microstructural characterization of porous biocompatible protein polymer thin films. *Polymer* **1999**, *40* (26), 7397-7407.

(207) Mcmillan, R. A.; Howard, J.; Zaluzec, N. J.; Kagawa, H. K.; Mogul, R.; Li, Y.-F.; Paavola, C. D.; Trent, J. D. A Self-Assembling Protein Template for Constrained Synthesis and Patterning of Nanoparticle Arrays. *Journal of the American Chemical Society* **2005**, *127* (9), 2800-2801. DOI: 10.1021/ja043827s (acccessed 2023-10-02T02:05:39).

(208) Liu, Y.; Tao, F.; Miao, S.; Yang, P. Controlling the Structure and Function of Protein Thin Films through Amyloid-like Aggregation. *Accounts of Chemical Research* **2021**, *54* (15), 3016-3027. DOI: 10.1021/acs.accounts.1c00231 (acccessed 2023-10-02T02:09:09).

(209) Whitehead, T. A.; Boonyaratanakornkit, B. B.; Höllrigl, V.; Clark, D. S. A filamentous molecular chaperone of the prefoldin family from the deep-sea hyperthermophile Methanocaldococcus jannaschii. *Protein Science* **2007**, *16* (4), 626-634. DOI: 10.1110/ps.062599907 (acccessed 2023-10-02T03:44:49).

(210) Glover, D. J.; Giger, L.; Kim, S. S.; Naik, R. R.; Clark, D. S. Geometrical assembly of ultrastable protein templates for nanomaterials. *Nature Communications* **2016**, *7* (1), 11771. DOI: 10.1038/ncomms11771 (acccessed 2023-10-02T03:49:23).

(211) Chen, Y. X.; Ing, N. L.; Wang, F.; Xu, D.; Sloan, N. B.; Lam, N. T.; Winter, D. L.; Egelman, E. H.; Hochbaum, A. I.; Clark, D. S. Structural determination of a filamentous chaperone to fabricate electronically conductive metalloprotein nanowires. *ACS nano* **2020**, *14* (6), 6559-6569.

(212) Xu, D.; Lim, S.; Cao, Y.; Abad, A.; Kang, A. N.; Clark, D. S. Filamentous chaperone protein-based hydrogel stabilizes enzymes against thermal inactivation. *Chemical Communications* **2021**, *57* (45), 5511-5513. DOI: 10.1039/d1cc01288f (acccessed 2023-08-19T22:05:56).

(213) Lim, S.; Jung, G. A.; Muckom, R. J.; Glover, D. J.; Clark, D. S. Engineering bioorthogonal protein–polymer hybrid hydrogel as a functional protein immobilization platform. *Chemical Communications* **2019**, *55* (6), 806-809. DOI: 10.1039/c8cc08720b (acccessed 2023-10-01T01:12:20).

(214) Sahoo, J. K.; Xu, D.; Falcucci, T.; Choi, J.; Hasturk, O.; Clark, D. S.; Kaplan, D. L. Horseradish Peroxidase Catalyzed Silk–Prefoldin Composite Hydrogel Networks. *ACS Applied Bio Materials* **2023**, *6* (1), 203-208. DOI: 10.1021/acsabm.2c00836 (acccessed 2023-10-02T03:54:29).

(215) Schaffer, V., David; O'Neill, A. The biology and engineering of stem-cell control. *Biotechnology and Applied Biochemistry* **2004**, *40* (1), 5. DOI: 10.1042/ba20030195 (acccessed 2023-09-29T21:35:06).

(216) Lebeyec, J.; Xu, R.; Lee, S.; Nelson, C.; Rizki, A.; Alcaraz, J.; Bissell, M. Cell shape regulates global histone acetylation in human mammary epithelial cells. *Experimental Cell Research* **2007**, *313* (14), 3066-3075. DOI: 10.1016/j.yexcr.2007.04.022 (acccessed 2023-09-29T21:49:07).

(217) Petersen, O. W.; Rønnov-Jessen, L.; Howlett, A. R.; Bissell, M. J. Interaction with basement membrane serves to rapidly distinguish growth and differentiation pattern of normal and malignant human breast epithelial cells. *Proceedings of the National Academy of Sciences* **1992**, *89* (19), 9064-9068. DOI: 10.1073/pnas.89.19.9064 (acccessed 2023-09-29T21:56:59).

(218) Tanaka, H.; Murphy, C. L.; Murphy, C.; Kimura, M.; Kawai, S.; Polak, J. M. Chondrogenic differentiation of murine embryonic stem cells: Effects of culture conditions and dexamethasone. *Journal of Cellular Biochemistry* **2004**, *93* (3), 454-462. DOI: 10.1002/jcb.20171 (acccessed 2023-09-29T21:56:54).

(219) Sawhney, A. S.; Pathak, C. P.; Hubbell, J. A. Bioerodible hydrogels based on photopolymerized poly(ethylene glycol)-co-poly(.alpha.-hydroxy acid) diacrylate macromers. *Macromolecules* **1993**, *26* (4), 581-587. DOI: 10.1021/ma00056a005 (acccessed 2023-09-29T22:10:47).

(220) Snyder, T. N.; Madhavan, K.; Intrator, M.; Dregalla, R. C.; Park, D. A fibrin/hyaluronic acid hydrogel for the delivery of mesenchymal stem cells and potential for articular cartilage repair. *Journal of Biological Engineering* **2014**, *8* (1), 10. DOI: 10.1186/1754-1611-8-10 (acccessed 2023-06-07T00:48:43).

(221) Eyrich, D.; Brandl, F.; Appel, B.; Wiese, H.; Maier, G.; Wenzel, M.; Staudenmaier, R.; Goepferich, A.; Blunk, T. Long-term stable fibrin gels for cartilage engineering. *Biomaterials* **2007**, *28* (1), 55-65.

(222) Trujillo, S.; Vega, S. L.; Song, K. H.; San Félix, A.; Dalby, M. J.; Burdick, J. A.; Salmeron-Sanchez, M. Engineered Full-Length Fibronectin–Hyaluronic Acid Hydrogels for Stem Cell Engineering. *Advanced Healthcare Materials* **2020**, *9* (21), 2000989. DOI: 10.1002/adhm.202000989 (acccessed 2023-06-07T00:00:29).

(223) Trujillo, S.; Gonzalez-Garcia, C.; Rico, P.; Reid, A.; Windmill, J.; Dalby, M. J.; Salmeron-Sanchez, M. Engineered 3D hydrogels with full-length fibronectin that sequester and present growth factors. *Biomaterials* **2020**, *252*, 120104.

(224) Mohand-Kaci, F.; Assoul, N.; Martelly, I.; Allaire, E.; Zidi, M. Optimized Hyaluronic Acid–Hydrogel Design and Culture Conditions for Preservation of Mesenchymal Stem Cell Properties. *Tissue Engineering Part C: Methods* **2013**, *19* (4), 288-298. DOI: 10.1089/ten.tec.2012.0144 (acccessed 2023-06-07T00:48:06).

(225) Cushing, M. C.; Anseth, K. S. Hydrogel Cell Cultures. *Science* **2007**, *316* (5828), 1133-1134. DOI: doi:10.1126/science.1140171.

(226) Martens, P.; Anseth, K. Characterization of hydrogels formed from acrylate modified poly (vinyl alcohol) macromers. *Polymer* **2000**, *41* (21), 7715-7722.

(227) Ghahremankhani, A. A.; Dorkoosh, F.; Dinarvand, R. PLGA-PEG-PLGA tri-block copolymers as in situ gel-forming peptide delivery system: effect of formulation properties on peptide release. *Pharmaceutical development and technology* **2008**, *13* (1), 49-55.

(228) Nur-E-Kamal, A.; Ahmed, I.; Kamal, J.; Schindler, M.; Meiners, S. Three-Dimensional Nanofibrillar Surfaces Promote Self-Renewal in Mouse Embryonic Stem Cells. *Stem Cells* **2005**, *24* (2), 426-433. DOI: 10.1634/stemcells.2005-0170 (acccessed 9/30/2023).

(229) Choi, S.; Lee, K. Y.; Kim, S. L.; Macqueen, L. A.; Chang, H.; Zimmerman, J. F.; Jin, Q.; Peters, M. M.; Ardoña, H. A. M.; Liu, X.; et al. Fibre-infused gel scaffolds guide cardiomyocyte alignment in 3D-printed ventricles. *Nature Materials* **2023**, *22* (8), 1039-1046. DOI: 10.1038/s41563-023-01611-3 (acccessed 2023-09-30T00:29:08).

(230) Liu, Y.; Chen, X.; Yin, S.; Chang, X.; Lv, C.; Zang, J.; Leng, X.; Zhang, T.; Zhao, G. Directed Self-Assembly of Dimeric Building Blocks into Networklike Protein Origami to Construct Hydrogels. *ACS Nano* **2022**, *16* (11), 19472-19481. DOI: 10.1021/acsnano.2c09391 (acccessed 2023-09-30T01:06:51).

APPENDIX A

SUPPLEMENTAL MATERIAL FOR CHAPTER 2

S1. DNA Sequences for Protein Constructs:

Gene sequence P3-FN (10)$_{III}$-EK (pQE-80L):

ATGAGAGGATCGCATCACCATCACCATCACGGATCCGAAATCCAGCAGCTTG
AGGAAGAAATCGCACAGTTGGAGCAAAAAAATGCGGCTTTAAAAGAAAAAA
ATCAGGCACTGAAGTATGCAGCCTCTGCGGCATCTGCGGCCAGTCGTGACCT
GGAGGTAGTCGCAGCAACTCCGACATCGCTGCTGATCTCCTGGGACGCGCCG
GCTGTAACAGTCCGTTACTACCGCATTACATATGGTGAAACGGGTGGCAACA
GTCCGGTTCAGGAGTTTACAGTACCCGGATCGAAGAGCACTGCGACCATTAG
TGGGCTTAAACCCGGTGTGGACTATACTATTACTGTGTACGCTGTAACTGGTC
GCGGAGATTCGCCCGCGTCTTCCAAACCTATTAGCATTAACTATCGTACTGCC
GCCTCCGCAGCTTCTGCAGCATctGAGATCGCGGCTCTTGAGCAAGAAAATGC
GGCTTTAGAACAAAAAATCGCAGCTCTTAAATGGAAGAATGCGGCTTTGAAG
CAA

Gene sequence P3-FN (9-10)$_{III}$-EK (pQE-80L):

ATGAGAGGATCGCATCACCATCACCATCACGGATCCGAAATCCAGCAGCTTG
AGGAAGAAATCGCACAGTTGGAGCAAAAAAATGCGGCTTTAAAAGAAAAAA
ATCAGGCACTGAAGTATGCAGCCTCTGCGGCATCTGCGGCCAGTGGTTTGGA
TTCTCCGACCGGAATTGACTTTAGTGACATCACTGCTAATTCTTTCACTGTGC
ATTGGATCGCTCCCCGCGCAACAATTACAGGTTACCGTATTCGCCATCATCCC
GAACATTTCTCCGGGCGTCCCCGTGAGGATCGCGTACCACATAGCCGCAACT
CTATCACGCTTACCAATTTGACCCCCGGCACAGAGTATGTGGTATCAATTGTC
GCCTTAAACGGACGCGAGGAGTCACCGCTTCTGATTGGGCAACAGTCAACTG

TGTCCGACGTGCCCCGCGACCTGGAAGTAGTGGCGGCCACCCCAACTAGTCT

TCTTATCTCGTGGGATGCTCCAGCCGTCACCGTCCGCTATTATCGCATCACAT

ACGGCGAGACTGGTGGAAATAGTCCCGTACAGGAGTTCACTGTCCCTGGGTC

AAAGTCAACCGCAACCATTTCAGGTTTGAAACCTGGAGTCGATTACACGATC

ACGGTATATGCAGTGACTGGCCGCGGCGATAGTCCGGCATCGTCTAAACCCA

TTAGCATCAACTATCGCACGGCCGCCTCCGCAGCTTCTGCAGCATctGAGATC

GCGGCTCTTGAGCAAGAAAATGCGGCTTTAGAACAAAAAATCGCAGCTCTTA

AATGGAAGAATGCGGCTTTGAAGCAA

Gene sequence P3-FN (12-14)$_{III}$-EK (pQE-80L):

ATGAGAGGATCGCATCACCATCACCATCACGGATCCGAAATCCAGCAGCTTG

AGGAAGAAATCGCACAGTTGGAGCAAAAAAATGCGGCTTTAAAAGAAAAAA

ATCAGGCACTGAAGTATGCAGCCTCTGCGGCATCTGCGGCCAGTGCAGCGAC

AGCGATTCCTGCTCCAACGGATTTAAAATTCACGCAAGTTACCCCCACCAGC

CTTTCAGCACAGTGGACTCCACCCAATGTGCAGCTGACTGGGTACCGCGTCC

GTGTGACGCCGAAAGAAAAGACAGGGCCTATGAAGGAGATCAATCTTGCGC

CGGATTCGTCTAGCGTTGTCGTGAGCGGCTTGATGGTCGCTACTAAATACGAA

GTATCCGTATACGCTCTTAAAGATACCCTTACGTCCCGTCCCGCCCAAGGGGT

TGTGACAACTTTGGAGAACGTTTCGCCTCCACGCCGTGCCCGCGTGACCGAC

GCTACCGAGACGACGATCACAATTTCCTGGCGCACTAAGACAGAAACCATTA

CCGGATTCCAGGTTGACGCCGTCCCAGCCAACGGACAAACCCCCATTCAGCG

TACGATTAAGCCCGATGTCCGCAGTTATACCATCACTGGGCTTCAGCCCGGC

ACGGACTACAAGATTTATCTTTACACCCTTAATGATAATGCCCGCAGTTCGCC

CGTCGTTATTGATGCTTCCACTGCCATTGATGCGCCAAGCAACTTGCGTTTTC

TTGCCACAACACCGAACTCCCTGCTTGTTTCGTGGCAACCTCCGCGTGCGCGT

ATCACAGGCTACATCATCAAATATGAGAAGCCAGGGTCTCCCCCCCGTGAAG

TGGTTCCCCGTCCGCGCCCTGGCGTTACGGAGGCCACTATCACAGGGTTAGA

GCCCGGTACGGAGTACACAATCTACGTGATTGCTTTGAAAAATAATCAAAAG

TCAGAACCGTTAATCGGACGCAAAAAGACTTTCAAGGCCGCCTCCGCAGCTT

CTGCAGCATCTGAGATCGCGGCTCTTGAGCAAGAAAATGCGGCTTTAGAACA

AAAAATCGCAGCTCTTAAATGGAAGAATGCGGCTTTGAAGCAA

Gene sequence P3-mCherry-EK (pQE-80L):

ATGAGAGGATCGCATCACCATCACCATCACGGATCCGAAATCCAGCAGCTTG

AGGAAGAAATCGCACAGTTGGAGCAAAAAAATGCGGCTTTAAAAGAAAAAA

ATCAGGCACTGAAGTATGCAGCCTCTGCGGCATCTGCGGCCAGTGGCGAAGA

AGATAACATGGCCATCATCAAGGAGTTCATGCGCTTCAAGGTTCACATGGAG

GGCTCCGTGAACGGCCACGAGTTCGAGATCGAGGGCGAGGGCGAGGGCCGC

CCCTACGAGGGCACCCAGACCGCCAAGCTGAAGGTGACCAAGGGTGGCCCC

CTGCCCTTCGCCTGGGACATCCTGTCCCCTCAGTTCATGTACGGCTCCAAGGC

CTACGTGAAGCACCCCGCCGACATCCCCGACTACTTGAAGCTGTCCTTCCCCG

AGGGCTTCAAGTGGGAGCGCGTGATGAACTTCGAGGACGGCGGCGTGGTGAC

CGTGACCCAGGACTCCTCCCTGCAAGACGGCGAGTTCATCTACAAGGTGAAG

CTGCGCGGCACCAACTTCCCCTCCGACGGCCCCGTAATGCAGAAGAAGACTA

TGGGCTGGGAGGCCTCCTCCGAGCGGATGTACCCCGAGGACGGCGCGCTGAA

GGGCGAGATCAAGCAGAGGCTGAAGCTGAAGGACGGCGGCCACTACGACGC

TGAGGTCAAGACCACCTACAAGGCCAAGAAGCCCGTGCAACTGCCCGGCGC

GTACAACGTCAACATCAAGTTGGACATCACCTCCCACAACGAGGACTACACC

ATCGTGGAACAGTACGAACGCGCCGAGGGCCGCCACTCCACCGGCGGCATG

GACGAGCTGTACAAGGCCGCCTCCGCAGCTTCTGCAGCATCTGAGATCGCGG

CTCTTGAGCAAGAAAATGCGGCTTTAGAACAAAAAATCGCAGCTCTTAAATG

GAAGAATGCGGCTTTGAAGCAA

Gene sequence KE_3H-FN(10)$_{III}$-P4 (pQE-80L):

ATGAGAGGATCGCATCACCATCACCATCACGGATCCGAGATTGCAGCTCTGG

AGAAGAAAAATGCAGCGTTAAAATATGAGATCGCGGCCTTGGAACAAGAGA

ATGCAGCGTTGGAGCAGGCAGCCTCTGCGGCATCTGCGGCCAGTCGTGACCT

GGAGGTAGTCGCAGCAACTCCGACATCGCTGCTGATCTCCTGGGACGCGCCG

GCTGTAACAGTCCGTTACTACCGCATTACATATGGTGAAACGGGTGGCAACA

GTCCGGTTCAGGAGTTTACAGTACCCGGATCGAAGAGCACTGCGACCATTAG

TGGGCTTAAACCCGGTGTGGACTATACTATTACTGTGTACGCTGTAACTGGTC

GCGGAGATTCGCCCGCGTCTTCCAAACCTATTAGCATTAACTATCGTACTGCC

GCCTCCGCAGCTTCTGCAGCATCTAGCCCGGAAGATAAAATCGCCCAGTTAA

AACAGAAAATCCAGGCCCTGAAACAAGAGAATCAGCAGCTGGAAGAGGAAA

ATGCAGCACTGGAATAT

Primer sequences:

pQE-80L FWD BB:

TAAAAGCTTAATTAGCTGAGCTTGGACTCCTGTTGATAGATC

pQE-80L REV MBP BB: GCTGGATCCCTGAAAATACAGGTTTTCGGTC

pQE-80L REV BB:

TAAAAGCTTAATTAGCTGAGCTTGGACTCCTGTTGATAGATC

pBR-ECO-FWD SEQ: AATAGGCGTATCACGAGGC

T0-TERM REV SEQ: GAACGCTCGGTTGCCGC

Ins P3-FN10-EK FWD pQE80L:

CATCACCATCACCATCACGGATCCGAAATCCAGCAGCTT

Ins P3-FN10-EK Rev pQE80L:

GGAGTCCAAGCTCAGCTAATTAAGCTTTTATTGCTTCAAAGCCGCATTC

Ins KE_3HI_FN FWD pQE80L:

CATCACCATCACCATCACGGATCCGAGATTGCAGCTCTG

Ins KE_3HI_FN REV pQE80L:

GGAGTCCAAGCTCAGCTAATTAAGCTTTTAATATTCCAGTGCTGC

S2. Amino Acid Sequences for Protein Constructs:

Amino Acid sequence P3-FN(10)$_{III}$-EK (pQE-80L):

MRGSHHHHHHGSEIQQLEEEIAQLEQKNAALKEKNQALKYAASAASAASRDLE
VVAATPTSLLISWDAPAVTVRYYRITYGETGGNSPVQEFTVPGSKSTATISGLKPG
VDYTITVYAVTGRGDSPASSKPISINYRTAASAASAASEIAALEQENAALEQKIAA
LKWKNAALKQ

Amino Acid sequence P3-FN(9-10)$_{III}$-EK (pQE-80L):

MRGSHHHHHHGSEIQQLEEEIAQLEQKNAALKEKNQALKYAASAASAASGLDSP

TGIDFSDITANSFTVHWIAPRATITGYRIRHHPEHFSGRPREDRVPHSRNSITLTNL

TPGTEYVVSIVALNGREESPLLIGQQSTVSDVPRDLEVVAATPTSLLISWDAPAVT

VRYYRITYGETGGNSPVQEFTVPGSKSTATISGLKPGVDYTITVYAVTGRGDSPA

SSKPISINYRTAASAASAASEIAALEQENAALEQKIAALKWKNAALKQ

Amino Acid sequence P3-FN(12-14)$_{III}$-EK (pQE-80L):

MRGSHHHHHHGSEIQQLEEEIAQLEQKNAALKEKNQALKYAASAASAASAATAI

PAPTDLKFTQVTPTSLSAQWTPPNVQLTGYRVRVTPKEKTGPMKEINLAPDSSSV

VVSGLMVATKYEVSVYALKDTLTSRPAQGVVTTLENVSPPRRARVTDATETTITI

SWRTKTETITGFQVDAVPANGQTPIQRTIKPDVRSYTITGLQPGTDYKIYLYTLND

NARSSPVVIDASTAIDAPSNLRFLATTPNSLLVSWQPPRARITGYIIKYEKPGSPPR

EVVPRPRPGVTEATITGLEPGTEYTIYVIALKNNQKSEPLIGRKKTFKAASAASAA

SEIAALEQENAALEQKIAALKWKNAALKQ

Amino Acid sequence P3-mCherry-EK (pQE-80L):

MRGSHHHHHHGSEIQQLEEEIAQLEQKNAALKEKNQALKYAASAASAASGEED

NMAIIKEFMRFKVHMEGSVNGHEFEIEGEGEGRPYEGTQTAKLKVTKGGPLPFA

WDILSPQFMYGSKAYVKHPADIPDYLKLSFPEGFKWERVMNFEDGGVVTVTQD

SSLQDGEFIYKVKLRGTNFPSDGPVMQKKTMGWEASSERMYPEDGALKGEIKQ

RLKLKDGGHYDAEVKTTYKAKKPVQLPGAYNVNIKLDITSHNEDYTIVEQYERA

EGRHSTGGMDELYKAASAASAASEIAALEQENAALEQKIAALKWKNAALKQ

Amino Acid sequence P3-mCherry-EK (pQE-80L):

MRGSHHHHHHGSEIAALEKKNAALKYEIAALEQENAALEQAASAASAAASRDLE

VVAATPTSLLISWDAPAVTVRYYRITYGETGGNSPVQEFTVPGSKSTATISGLKPG

VDYTITVYAVTGRGDSPASSKPISINYRTAASAASAASSPEDKIAQLKQKIQALKQ

ENQQLEEENAALEY

S.3 Expression Analysis:

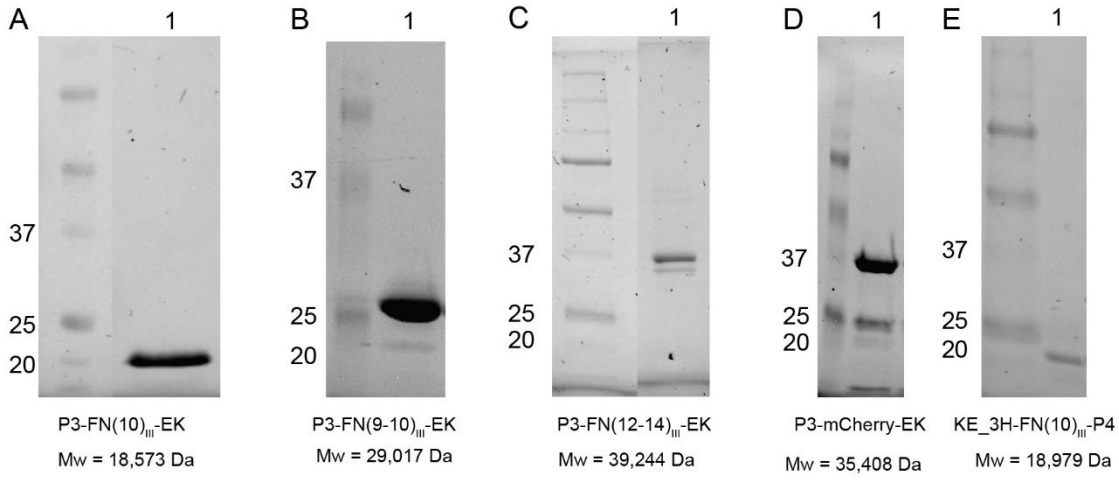

Figure S1. SDS-PAGE analysis of each purified protein. A) The fusion protein, P3-FN(10)$_{III}$-EK. **B)** The fusion protein, P3-FN(9-10)$_{III}$-EK. **A)** The fusion protein, P3-FN(12-14)$_{III}$-EK. **A)** The fusion protein, P3-mCherry-EK. **A)** The fusion protein, KE_3H-FN(10)$_{III}$-P4.

APPENDIX B

PERMISSION TO REPRODUCE FIGURES IN CHAPTER 1

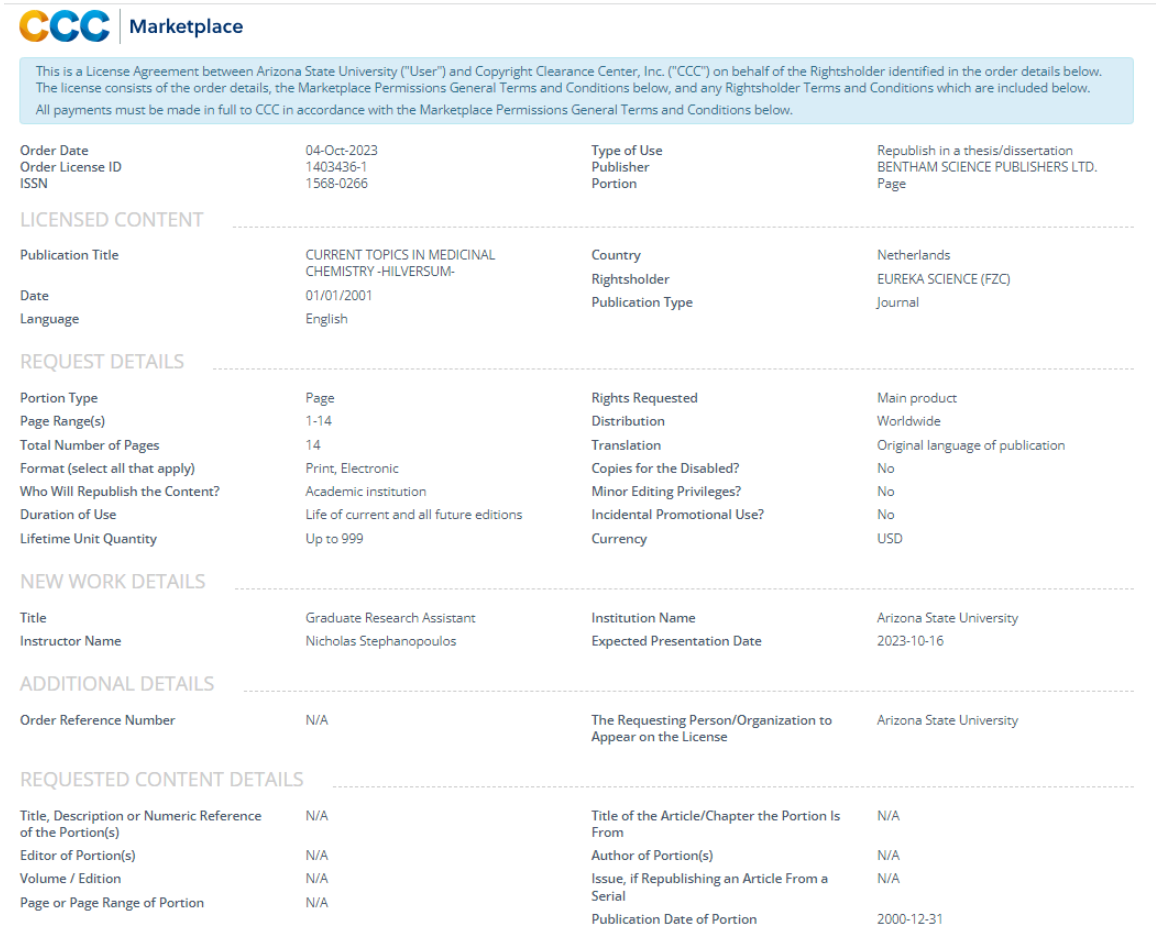

CCC Marketplace

This is a License Agreement between Arizona State University ("User") and Copyright Clearance Center, Inc. ("CCC") on behalf of the Rightsholder identified in the order details below. The license consists of the order details, the Marketplace Permissions General Terms and Conditions below, and any Rightsholder Terms and Conditions which are included below.

All payments must be made in full to CCC in accordance with the Marketplace Permissions General Terms and Conditions below.

Order Date	04-Oct-2023	Type of Use	Republish in a thesis/dissertation
Order License ID	1403436-1	Publisher	BENTHAM SCIENCE PUBLISHERS LTD.
ISSN	1568-0266	Portion	Page

LICENSED CONTENT

Publication Title	CURRENT TOPICS IN MEDICINAL CHEMISTRY -HILVERSUM-	Country	Netherlands
		Rightsholder	EUREKA SCIENCE (FZC)
Date	01/01/2001	Publication Type	Journal
Language	English		

REQUEST DETAILS

Portion Type	Page	Rights Requested	Main product
Page Range(s)	1-14	Distribution	Worldwide
Total Number of Pages	14	Translation	Original language of publication
Format (select all that apply)	Print, Electronic	Copies for the Disabled?	No
Who Will Republish the Content?	Academic institution	Minor Editing Privileges?	No
Duration of Use	Life of current and all future editions	Incidental Promotional Use?	No
Lifetime Unit Quantity	Up to 999	Currency	USD

NEW WORK DETAILS

Title	Graduate Research Assistant	Institution Name	Arizona State University
Instructor Name	Nicholas Stephanopoulos	Expected Presentation Date	2023-10-16

ADDITIONAL DETAILS

Order Reference Number	N/A	The Requesting Person/Organization to Appear on the License	Arizona State University

REQUESTED CONTENT DETAILS

Title, Description or Numeric Reference of the Portion(s)	N/A	Title of the Article/Chapter the Portion Is From	N/A
Editor of Portion(s)	N/A	Author of Portion(s)	N/A
Volume / Edition	N/A	Issue, if Republishing an Article From a Serial	N/A
Page or Page Range of Portion	N/A	Publication Date of Portion	2000-12-31

Reprinted with permission from: Bernal-Chanchavac J, Al-Amin M, Stephanopoulos N. Nanoscale Structures and Materials from the Self-assembly of Polypeptides and DNA. *Curr Top Med Chem*. 2022;22(8):699-712. Copyright Clearance Center, Inc.

SPRINGER NATURE LICENSE
TERMS AND CONDITIONS

Oct 15, 2023

This Agreement between Arizona State University -- Julio Bernal-Chanchavac ("You") and Springer Nature ("Springer Nature") consists of your license details and the terms and conditions provided by Springer Nature and Copyright Clearance Center.

License Number	5650360959859
License date	Oct 15, 2023
Licensed Content Publisher	Springer Nature
Licensed Content Publication	Nature Chemical Biology
Licensed Content Title	Design of a single-chain polypeptide tetrahedron assembled from coiled-coil segments
Licensed Content Author	Helena Gradišar et al
Licensed Content Date	Apr 28, 2013
Type of Use	Thesis/Dissertation
Requestor type	academic/university or research institute
Format	print and electronic
Portion	figures/tables/illustrations
Number of figures/tables/illustrations	1
Would you like a high resolution image with your order?	no
Will you be translating?	no
Circulation/distribution	50000 or greater
Author of this Springer Nature content	no
Title of new work	Biomimetic Design of Nucleic Acid/Protein-Based Nanomaterials
Institution name	Arizona State University
Expected presentation date	Oct 2023
Portions	Figure on Page 6 for an overview of coiled coil nanomaterials.
Requestor Location	Arizona State University 727 East Tyler St

Reprinted with permission from: Gradišar, H., Božič, S., Doles, T. *et al.* Design of a single-chain polypeptide tetrahedron assembled from coiled-coil segments. *Nat Chem Biol* **9**, 362–366 (2013). Copyright 2013 Springer Nature.

Your confirmation email will contain your order number for future reference.

Printable Details

License Number	5650361437919
License date	Oct 15, 2023

Licensed Content

Licensed Content Publisher	Springer Nature
Licensed Content Publication	Nature
Licensed Content Title	Folding DNA to create nanoscale shapes and patterns
Licensed Content Author	Paul W. K. Rothemund
Licensed Content Date	Mar 16, 2006

Order Details

Type of Use	Thesis/Dissertation
Requestor type	academic/university or research institute
Format	print and electronic
Portion	figures/tables/illustrations
Number of figures/tables/illustrations	1
Would you like a high resolution image with your order?	no
Will you be translating?	no
Circulation/distribution	50000 or greater
Author of this Springer Nature content	no

About Your Work

Title of new work	Biomimetic Design of Nucleic Acid/Protein-Based Nanomaterials
Institution name	Arizona State University
Expected presentation date	Oct 2023

Additional Data

Portions	Figure 1.2. Overview of DNA Nanotechnology.

Requestor Location

Requestor Location	Arizona State University 727 East Tyler St Tempe, AZ 85287 United States Attn: Arizona State University

Tax Details

Reprinted with permission from: Rothemund, P. Folding DNA to create nanoscale shapes and patterns. *Nature* **440**, 297–302 (2006). Copyright 2006 Springer Nature.

Lou, C., Martos-Maldonado, M., Madsen, C. *et al.* Peptide–oligonucleotide conjugates as nanoscale building blocks for assembly of an artificial three-helix protein mimic. *Nat Commun* **7**, 12294 (2016). Copyright 2016 Springer Nature.

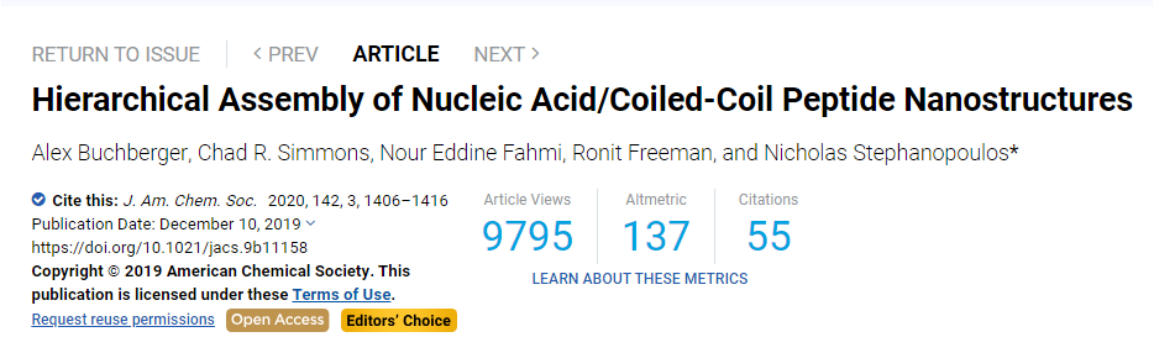

Alex Buchberger, Chad R. Simmons, Nour Eddine Fahmi, Ronit Freeman, and Nicholas Stephanopoulos. *Journal of the American Chemical Society* **2020** *142* (3), 1406-1416

Copyright 2020 ACS Publications.

License Number	5650371066139
License date	Oct 15, 2023

Printable Details

Licensed Content

Licensed Content Publisher	John Wiley and Sons
Licensed Content Publication	Small
Licensed Content Title	Janus Nanosheets with Face-Selective Molecular Recognition Properties from DNA–Peptide Conjugates
Licensed Content Author	Shine K. Albert, Sunghee Lee, Prasannavenkatesh Durai, et al
Licensed Content Date	Mar 15, 2021
Licensed Content Volume	17
Licensed Content Issue	12
Licensed Content Pages	10

Order Details

Type of use	Dissertation/Thesis
Requestor type	University/Academic
Format	Print and electronic
Portion	Figure/table
Number of figures/tables	1
Will you be translating?	No

About Your Work

Title of new work	Biomimetic Design of Nucleic Acid/Protein-Based Nanomaterials
Institution name	Arizona State University
Expected presentation date	Oct 2023

Additional Data

Portions	Figure 1.3. Overview of DNA-Peptide Nanomaterials.

Requestor Location

Requestor Location	Arizona State University 727 East Tyler St Tempe, AZ 85287 United States Attn: Arizona State University

Tax Details

Publisher Tax ID	EU826007151

Reprinted with permission from: Albert, S. K., Lee, S., Durai, P., Hu, X., Jeong, B., Park, K., Park, S.-J., Janus Nanosheets with Face-Selective Molecular Recognition Properties from DNA–Peptide Conjugates. *Small* 2021, 17, 2006110. Copyright 2021 Wiley.

Can I use AAAS material in a thesis or dissertation?

Yes, different criteria apply depending upon whether you are the author of the AAAS article being reproduced.

Authors:

If you are the author of the AAAS article being reproduced, please refer to your License to Publish for rules on reproducing your paper in a dissertation or thesis.

Others:

AAAS permits the use of content published in its journals *Science*, *Science Immunology*, *Science Robotics*, *Science Signaling*, and *Science Translational Medicine* to be used in a thesis or dissertation, but only provided the following criteria are met:

1. If you are using figure(s)/table(s), permission is granted for use in print and electronic versions of your dissertation or thesis.
2. A full-text article may be used only in print versions of a dissertation or thesis. AAAS does not permit the reproduction of full-text articles in electronic versions of theses or dissertations.
3. The following credit line must be printed along with the AAAS material: "From [Full Reference Citation]. Reprinted with permission from AAAS."
4. All required credit lines and notices must be visible any time a user accesses any part of the AAAS material and must appear on any printed copies that an authorized user might make.
5. The AAAS material may not be modified or altered, with the exception that figures and tables may be modified with permission from the author. Author permission for any such changes must be secured prior to your use.

- Reprinted with permission from: Ronit Freeman *et al.*, Reversible self-assembly of superstructured networks. *Science* **362**,8 08-813 (2018). Copyright 2019 AAAS.